Diss. ETH No. 14287

Transport Phenomena during Molten Droplet Pile-Up in Micromanufacturing

Dissertation

submitted to

The Swiss Federal Institute of Technology Zurich

for the degree of

Doctor of Technical Sciences

presented by

Stephan Eirik Ligaard Haferl
Dipl. Masch. – Ing. ETH Zurich
born 8th of March 1972
citizen of Zurich
Switzerland

Accepted on the recommendation of

Prof. Dr. D. Poulikakos, examiner
Prof. Dr. J. Dual, co-examiner

Zurich, 2001

Seite Leer /
Blank leaf

Til Mamma og Pappa

Seite Leer /
Blank leaf

It is an old maxim of mine that when you have excluded the impossible, whatever remains, however improbable, must be the truth.

Sherlock Holmes, *The Adventure of the Beryl Coronet*
Sir Arthur Conan Doyle, 1859 - 1930

Seite Leer /
Blank leaf

Table of Contents

Abstract

Over the last few years a significant research effort has been devoted to the investigation of molten droplet impact phenomena. The reason for this activity is the pressing need of an in-depth understanding of these phenomena for the successful development and implementation of a host of emerging technologies such as rapid prototyping, spray forming, spray coating and precision molten droplet dispensing in the manufacturing of microelectronics and other micromanufacturing applications. Most of the existing work has been focused on the investigation of droplet impact on planar substrates. Little information can be found in the scientific literature on the basic problem of droplet impact on non-planar substrates. With reference to molten droplets of interest to this thesis, applications include structure-building (rapid prototyping) as well as deposition of a required precise amount of material, which is larger than that of the largest single droplet that can be reliably generated; here multiple droplets are impinged one on top of the other. In addition, droplet impact on non flat surfaces finds a plethora of applications in nature and in technology (exemplified by spray coating, spray cooling, ablation technologies etc.). The limited work published to date in this challenging field consists of few oversimplified analytical or computational models (neglecting e.g. the all important effect of fluid dynamics, for example) with or without some experimental validation of only the steady state regime.

This thesis presents for the first time a detailed experimental and numerical investigation of the transient thermofluidic transport phenomena occurring during molten-microdroplet-deposition-based micromanufacturing processes. Experimental visualization of phenomena lasting a fraction of a millisecond in severely deforming domains of typical size of a fraction of a millimeter, as well as highly versatile numerical results of the thermofluidic phenomena during the axisymmetric pile up (deposition one upon another) of molten picoliter size liquid metal droplets on a substrate are presented. The numerical model thereby solves the coupled Navier-Stokes and energy equations accounting for solidification, slip at the contact line as well as thermal contact resistance at the respective interfaces. Incompressibility of the flow as well as constant thermophysical properties are assumed. The prevailing physical mechanisms of the pile up process (occurring simultaneously) are identified and quantified both experimentally and numerically. These are the fluid mechanics of the bulk liquid (controlled by the initial momentum of the impinging droplet and the free, deforming surface of the droplet), capillarity effects at the liquid-solid interface, and solidification (controlled by the initial temperature of the droplet and the substrate) and the important effect of thermal contact

resistance at the respective interfaces. The predictive capabilities of the state of the art finite element numerical model, based on a Lagrangian formulation and involving unstructured grid generation in a continuously deforming domain, are presented and discussed. Furthermore, the parametric domain in which the numerical model performs reliably is identified in terms of the relevant dimensionless groups. These are the Reynolds and the Weber number for the fluid mechanics, the Stefan and the Biot number for the heat transfer and the solidification. In terms of values of the relevant dimensionless groups the following ranges are covered in this thesis: Re = 281 – 453, We = 2.39 – 5.99, Ste = 0.187 – 0.895. This corresponds to molten solder droplets impinging at velocities ranging between 1.12 – 1.74 [m/s] having an average diameter of ≈78 [μm]. The initial substrate temperature ranges between 25 – 150 [°C]. The initial droplet temperature is kept constant at 210 [°C]. The main results of the thesis clearly add originally and significantly to the knowledge base of molten droplet pile up and solidification, a process of importance, since it is the building block to a host of micromanufacturing applications.

Zusammenfassung

Erheblicher Forschungsaufwand ist in den letzten Jahren der Untersuchung von Phänomenen im Zusammenhang mit dem Aufprall und der möglichen Erstarrung von Tropfen auf ebenen Substraten gewidmet worden. Den Hintergrund dazu bilden mannigfaltige industrielle Applikationen, die nur bei tieferem Verständnis für die auftretenden physikalischen Phänomene erfolgreich entwickelt und implementiert werden können. Zu diesen gehören u.a. Verfahren wie „Rapid Prototyping", Spritz-Formgebung, Spritz-Beschichtung sowie die Präzisionsdispensierung von Lötzinntropfen in der Herstellung von mikroelektronischen Komponenten.

Bestehende Arbeiten haben sich bisher auf den Aufprall von Tropfen auf ebenen Substraten konzentriert. In der wissenschaftlichen Literatur sind wenige Informationen zum Aufprall von Tropfen auf Substraten mit gekrümmten Oberflächen erhältlich. Mögliche industrielle Applikationen, speziell für die untersuchten Mikrotropfen in der vorliegenden Dissertation, umfassen die Herstellung von tropfen-basierten Mikrostrukturen sowie die Dispensierung von kleinsten Materialmengen auf ein festes Substrat. Für Materialmengen, welche das Volumen der grössten Tropfen, die mit der bestehenden Technologie erzeugt werden können, übersteigen, müssen mehrere Tropfen aufeinander deponiert werden. Es existieren viele Anwendungen und Erscheinungen in Natur und Technik, welche den Aufprall von Tropfen auf gekrümmten Oberflächen beinhalten. Die bis dato limitierte Anzahl an publizierten Arbeiten basiert auf ein paar wenigen, stark vereinfachenden analytischen und numerischen Modellen (unter Vernachlässigung des wichtigen Einflusses der Fluiddynamik). Diese Modelle wurden bisher nur teilweise durch Experimente im stationären Zustand validiert. Die vorliegende Arbeit präsentiert, nach bestem Wissen und Gewissen, die erste detaillierte experimentelle und numerische Untersuchung der instationären, thermodynamischen und fluidmechanischen Transportphänomene, welche beim Aufprall und der Erstarrung von Tropfen auf gekrümmten Oberflächen auftreten. Experimentelle Visualisierungen und numerische Simulationen von Phänomenen welche Bruchteile von Millisekunden dauern und in stark deformierenden, flüssigen Strukturen von der Grössenordnung eines Bruchteils eines Millimeters stattfinden, werden präsentiert und diskutiert. Das numerische Model basiert dabei auf den „Navier-Stokes"-Gleichungen und der damit gekoppelten Energiegleichung für den Wärmeaustausch. Zusätzlich sind Erstarrung, „slip" an der Kontaktlinie sowie thermischer Kontaktwiderstand modelliert. Als Annahmen werden Inkompressibilität des flüssigen Materials sowie konstante thermophysikalische Eigenschaften aller involvierter

Materiale vorausgesetzt. Die vorherrschenden physikalischen Mechanismen des „Pile Up"-Prozesses, welche simultan auftreten, werden sowohl experimentell als auch numerisch identifiziert und quantifiziert. Diese sind die Fluidmechanik (kontrolliert durch den Anfangsimpuls sowie die freie, deformierende Oberfläche des auftreffenden Tropfens), Benetzungseffekte, Erstarrung (kontrolliert durch die Anfangstemperaturen des Tropfens und des Substrates), sowie thermischer Kontaktwiderstand an den Grenzflächen. Die prädiktiven Möglichkeiten des zeitgemässen „Finite Elemente Model" werden quantifiziert und diskutiert. Letzteres basiert auf einer Lagrange-Formulierung der beschreibenden partiellen Differentialgleichungen und bezieht die Erzeugung von unstrukturierten Berechnungsgittern in einem stark deformierenden Simulationsbereich mit ein. Desweiteren wird der Parameterbereich, in welchem das numerische Model zuverlässige Resultate liefert, in Form von relevanten dimensionslosen Kennzahlen identifiziert. Diese sind die Reynolds- und die Weber-Zahl für die Fluidmechanik, die Stefan- und die Biot-Zahlen für den Wärmeaustausch und die Erstarrung. Die Parameterbereiche der dimensionslosen Kennzahlen sind dabei: Re = 281 – 453, We = 2.39 – 599, Ste = 0.187 – 0.895. Dies entspricht Aufprallgeschwindigkeiten von 1.12 – 1.74 [m/s] bei Tropfendurchmessern von ≈78 [μm]. Die Anfangstemperaturen des Substrates liegen im Bereich von 25 – 150 [°C]. Die Anfangstemperatur für die aufprallenden Tropfen beträgt konstant 210 [°C]. Die Resultate dieser Dissertation liefern wesentliche neue Beiträge zum Verständnis der Auprall- und Erstarrungsmechanik von Tropfen auf Substraten („Pile Up") und damit eine erweiterte Grundlage für zukünftige Entwicklungen in diesem Anwendungsbereich.

List of Figures


Seite Leer /
Blank leaf

List of Tables

Nomenclature

$A_{t,c}$	Thermal contact area	$[m^2]$
a_c	Arc-length of contact line radius	[m]
$B_{i,j}$	B-Spline basis functions	[-]
C_i	Dimensionless heat capacity	[-]
c	Speed of sound	[m/s]
$c_{p,i}$	Specific heat of component i	[J/kgK]
$c_{pl,i}$	Specific heat of liquid component i	[J/kgK]
d_0	Initial diameter	[m]
d_p	Diameter of the presolidified droplet	[m]
d_{il}	Interfacial layer thickness	[m]
E	Thermal energy	[J]
F_i	Component of the control point vector	[-]
g	Gravitational acceleration	$[m/s^2]$
H	Surface curvature	[1/m]
$\overline{H}$	Dimensionless surface curvature	[-]
h_p	Height of the presolidified droplet	[m]
K_i	Dimensionless thermal conductivity of component i	[-]
k_i	Thermal conductivity of component i	[W/mK]
L	Latent heat of fusion	[J/kgK]
M	Dimensionless mass	[-]
m_d	Mesh density factor	[-]
N_i	FEM basis function	[-]
n_i	Unit normal vector component	[-]
P	Dimensionless pressure	[-]
p	Pressure	[Pa]
$R_{t,c}$	Thermal contact resistance	$[m^2K/W]$
R_c	Radius of the contact line	[m]
R_i	Radius of curvature of curve i	[m]
r	Radial coordinate	[m]
r_0	Initial droplet radius	[m]
s	Arc length	[m]
T_i	Temperature of component i	[°C]

$T_{i,j}$	Temperature of component i at interface node j	[°C]
ΔT_i	Time period length	[s]
t	Time	[s]
t_β	Spreading time	[s]
t_s	Solidification time	[s]
t_i	Unit tangent vector component	[-]
U_i	Dimensionless velocity component	[-]
u_i	Velocity component	[m/s]
w	Trial function set	[-]
Y_{center}	Dimensionless pile up height at the line of symmetry	[-]
y_{center}	Pile up height at the line of symmetry	[m]
z	Axial coordinate	[m]

Greek Letters and Symbols

α	Heat transfer coefficient	[W/m^2K]
β	Spread factor	[-]
β_{max}	Maximum spread factor	[-]
β_∞	Final solidified spread factor	[-]
χ_i	Component of the coordinate vector	[-]
δ	Dirac delta function	[-]
δ_{ij}	Kronecker delta	[-]
ε	Slip parameter	[Ns/m^3]
Φ_i	Component of the free surface nodes vector	[-]
γ	Surface tension	[N/m]
φ	Angular deviation	[deg]
κ	Thermal diffusivity	[m^2/s]
λ	Orifice-Substrate pitch	[m]
μ_i	Dynamic viscosity of component i	[kg/ms]
θ	Azimuthal coordinate	[-]
ρ_i	Density of component i	[kg/m^3]

$\tilde{\sigma}$	Stress tensor	[N/m^2]
σ_{ij}	Stress component	[N/m^2]
$\overline{\sigma}$	Dimensionless stress tensor	[-]
$\overline{\sigma}_{ij}$	Dimensionless stress tensor component	[-]
τ	Dimensionless time	[-]
$\Delta\tau$	Dimensionless time step	[-]
$\Delta\tau$	Dimensionless computational time step	[-]
Θ_i	Dimensionless temperature of component i	[-]
$\Theta_{i,j}$	Dimensionless temperature of component i at interface node j	[-]
Ξ	State variable set	[-]
ψ_i	Contact angle	[deg]
Γ	Boundary	[-]
Ω	Computational domain	[-]
$\wp$	Free surface description	[-]
∂_i	Derivative with respect to the i-th variable	[-]

Dimensionless Numbers

Bi	Biot number	[-]
Fr	Froude number	[-]
Ma	Mach number	[-]
Oh	Ohnesorge number	[-]
Pe	Peclet number	[-]
Pr	Prandtl number	[-]
Re	Reynolds number	[-]
Ste	Stefan number	[-]
SHP	Superheat parameter	[-]
We	Weber number	[-]
Ca	Capillary number	[-]

Subscripts and Superscripts

c	Contact
center	Line of symmetry
e	Element/Equilibrium
exp	Experiment
GS	Gas-solid interface
h	Discretization
i	Indices
j	Indices
k	Indices
LG	Liquid-gas interface
LS	Liquid-solid interface
m	Melting
max	Maximum
num	Numerical Simulation
p	Presolidified droplet
r	Radial
z	Axial
θ	Azimuthal
S	Entropy
s	Solid
system	System (Pile up and Wafer substrate)
t	Thermal
0	Initial
1	Impinging droplet
2	Presolidified droplet
3	Artificial interface
4	Wafer substrate
∞	Final

1. Introduction

Droplets of various sizes and of a plethora of different fluids appear in many areas of modern industrial applications. Occurrences of droplet interactions with various types of substrate surfaces are manifold. To exemplify, droplets can be an intermittent form of a fluid during an industrial process such as fuel droplets in an internal combustion chamber of a car or rocket engine. In a less traditional example directly related to the work in this dissertation, droplets of a molten material can also be utilized as microscopic building blocks in the drop-wise manufacturing of structures such as in spray forming, rapid prototyping or microelectronics manufacturing. Nature itself also offers ground for countless observations and interactions with droplet phenomena. Two illustrative examples are mentioned: Rainbows appear because of optical interaction of the incident light with tiny water droplets dispersed in the atmosphere. Subcooled water droplets can cause upon impact on structures the rapid growth of dangerous ice-layers such as the "icing" problem on airplanes, marine vessels and off-shore rigs and installations. Due to the very many naturally and industrially occurring droplet phenomena it is not a surprise that great scientific interest has been generated over the years to improve our understanding of droplet behaviour, in particular in the engineering and physics communities. This interest has experienced a rapid growth recently due to the relevance of controlled microdroplet generation and deposition in a host of emerging technologies, exemplified by microelectronics manufacturing and biotechnologies.

Common to many of the above mentioned processes is the importance of the understanding of the transient behaviour of droplet interactions with substrates (surfaces) on which they are deposited. Advancement and new implementations of such processes are only possible through a rigorous enhancement of the knowledge base associated to these processes. A multiplicity of physical phenomena have to be considered. The fluid mechanics cover a severely deforming free surface interacting with the ambient environment. Furthermore, the fluid flow interacts with a solid of arbitrary shape leading to strong deformations, possible breakup (bounce off), recoalescence and oscillations. It is also necessary to confront the very intricate field of wetting in the contact line region of the droplet. Thermodynamics poses several challenges when considering multiphase and multimode heat transfer, (evaporation or, in the case of molten materials, solidification). Chemistry can also come into play through various reactions from combustion to surface oxidation. Hence, droplet physics offers a multitude of serious challenges in basic research and is, at the same time, directly related to

significant technology development. An in-depth understanding of the relevant scientific issues can lead to technological advancements with marked beneficial societal implications.

1.1 Emerging Industrial Applications in the Area of Molten Droplet Deposition

A number of different emerging technologies are based on the controlled deposition of droplets ranging from biotechnologies to microelectronics. A central example of such technologies dealing with the deposition of molten microdroplets directly related to the work in this dissertation is chip packaging in microelectronics. Chip packaging aims at sealing integrated circuits and electrically connecting them to integrated circuit boards. Simultaneously it has to reassure acceptable operating conditions and mechanical protection. Miniaturization of devices as well as of integrated circuits has concurrently lead to a shrinking of chip packaging scales as shown in Figure 1.

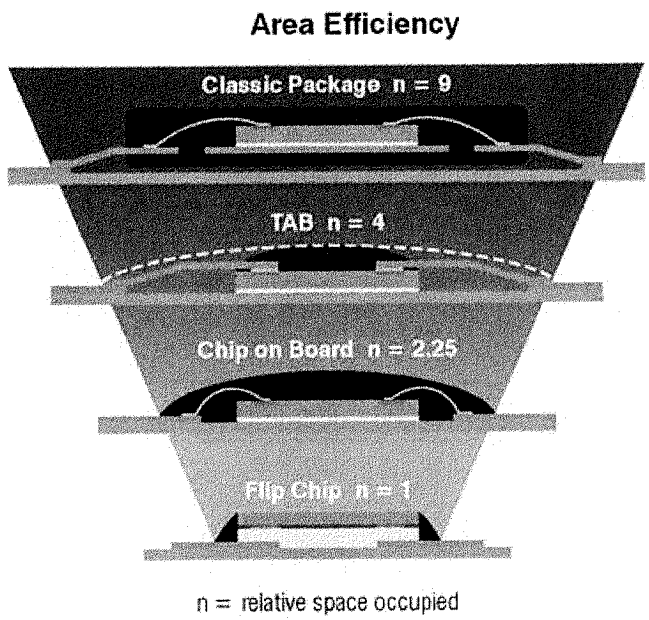

Figure 1:Evolution of the area efficiency of integrated circuit packages (WWW).

Where the area efficiency is defined as the ratio of the occupied area of a chip package to the currently smallest available chip package area. Scale reduction has predominantly been achieved by replacing wire connections from electrical connector pads by arrays of solder balls/bumps featuring a smaller pitch size and allowing for higher connector densities. A very efficient way of producing such solder bump arrays is to use solder jetting to deposit on

demand individual droplets on electrical connector pads [1,2]. However, as stated by Xiong et. al. [3] bump shape deviations of a few percent can be detrimental to the successful implementation of solder jetting in chip packaging. This was further pursued by Attinger et. al. [4] showing experimentally a strong influence of impact parameters and temperatures on final bump shapes.

A process called a host of names such as Digital Microfabrication [5], Microcasting [6], Ballistic Particle Manufacturing [7], Rapid Prototyping [7] and Solid Freeform [8-10] exemplifies a different technology based on the deposition of individual molten droplets, also directly related to the research in this dissertation. The objective of this technique is to deposit a multitude of individual molten droplets at precisely defined locations to build up layers of droplets that solidify upon impact into coherent three-dimensional structures. A schematic of such a process is shown in Figure 2.

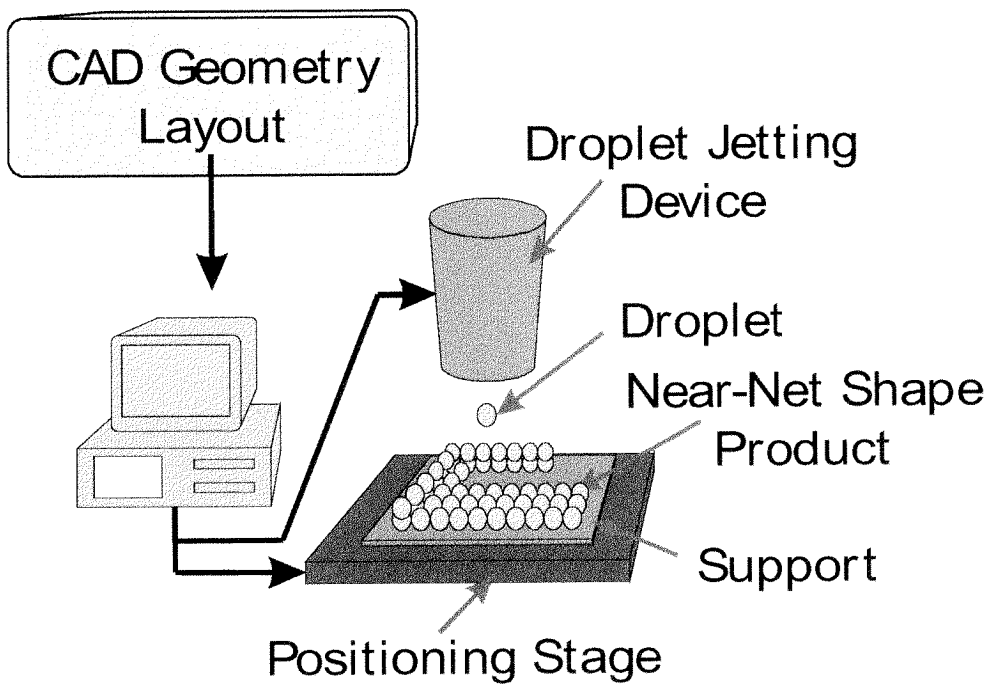

Figure 2: Schematic of a Rapid Prototyping apparatus producing near-net shape parts by ballistic droplet deposition.

This technique does not rely on a conventional cast and features high flexibility, the ability to produce near-net shape products, as well as the ability of a rapid conversion of CAD object data into a real object. Furthermore, unlike other rapid prototyping processes, such as stereolithography, selective laser sintering, and laminated object manufacturing processes

which use polymers, wood, and ceramics, processes based on molten droplet deposition produce metal parts. Preliminary experimental studies have shown that metallic objects created by digital microfabrication exhibit higher tensile strength [9] and lower porosity than objects created by conventional casting methods [11].

Both technologies described above rely on a thorough understanding of the prevailing physical phenomena during droplet deposition and interaction for a successful implementation. A potential user has to be allowed to select parameters to produce parts or single droplets with a desired shape and possibly with desired mechanical properties. This desired predictivity/reliability needs to be established through a series of fundamental studies before wide acceptance of these new technologies can be achieved.

1.2 Objectives and Definition of the Problem

The aim of this thesis, based on the described industrial processes in the foregoing section, is to shed more light on the complex interplay of the different physical phenomena occurring during the successive (one over the other) deposition (pile-up) of molten droplets. This will be pursued both experimentally and numerically. More specifically, the work is focused on the process in which a molten droplet impacts on a previously impacted and solidified droplet of the same material. In the light of the previous section, a two droplet pile up can be considered as the simplest building block in the creation of a complex three-dimensional structure as well as a special case of the general problem of a droplet impinging on a non-flat substrate (i.e. the "icing" problem). A schematic of the investigated process is shown in Figure 3. As already emphasized in Figure 3 only the axisymmetric case of the pile-up will be considered, which is of course in line with the actual printing approach where the printhead works on a "stop and drop" fashion. Furthermore, the work limits itself in investigating eutectic melts since the majority of solder materials in electronics manufacturing are eutectic, exemplified by eutectic tin-lead solder (63% Sn-37% Pb). The focus will be on the fluid mechanics of the impact process, the heat transfer between the impinging and a predeposited already solidified droplet, the subsequent solidification of the molten material, and the related wetting process. Influence of the inert, gaseous environment on the impact process has been shown to be negligible (i.e. no heat transfer from the droplet/substrate to the environment, no oxidation of the free surfaces, and no frictional drag form the gaseous environment imposed on the impacting droplet [4,12-14]).

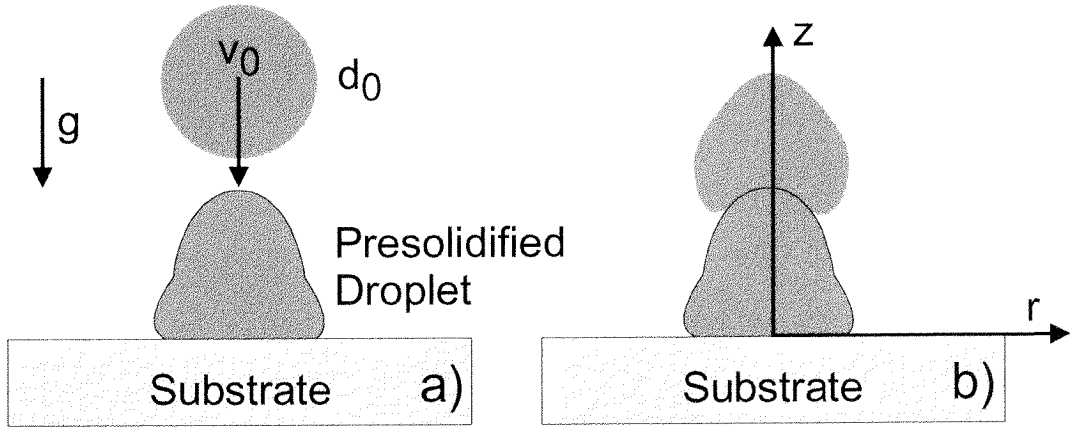

Figure 3: Schematic of the pile up process studied in this investigation. (a) The impinging droplet is deposited ballistically on top of an already solidified droplet of the same material. (b) Spreading/recoiling of the impacted droplet on the presolidified droplet.

Scale analysis as well as mathematical modelling of the pile up problem, which will be the scope in section 3, yield a set of dimensionless groups that can also serve as process parameters. These are:

Reynolds number: $$\mathrm{Re} = \frac{\rho_i u_{z0} d_0}{\mu_i} \quad (1)$$

Weber number: $$\mathrm{We} = \frac{\rho_i d_0 u_{z0}^2}{\gamma} \quad (2)$$

Ohnesorge number: $$\mathrm{Oh} = \frac{\sqrt{\mathrm{We}}}{\mathrm{Re}} \quad (3)$$

Froude number: $$\mathrm{Fr} = \frac{u_{z0}^2}{d_0 g} \quad (4)$$

Mach number: $$\mathrm{Ma} = \frac{u_{z0}}{c} \quad (5)$$

Capillary number $$\mathrm{Ca}_\beta = \frac{\mu r_0 \partial_t \beta(t)}{\gamma} \quad (6)$$

Prandtl number: $$\mathrm{Pr} = \frac{c_{pl,l}\mu_i}{k_i} \quad (7)$$

Biot number: $$Bi = \frac{\alpha_i d_0}{k_i} \quad (8)$$

Stefan number: $$Ste = \frac{c_{p1,l}\left(T_m - T_{2,0}\right)}{L} \quad (9)$$

Superheat parameter: $$SHP = \frac{T_{1,0} - T_m}{T_m - T_{2,0}} \quad (10)$$

where the different quantities and subscripts are defined in the Nomenclature. The two foremost important dimensionless numbers in droplet deposition are thereby the Reynolds number constituting the relative importance of inertial to viscous forces and the Weber number constituting the relative importance of inertial to surface tension forces. The Ohnesorge number, which is often used in droplet impact studies at low Weber number, scales viscous forces with the square root of the product of inertial forces and surface tension forces. It therefore scales the forces that resist the spreading of the droplet. The Froude and Mach number scale the relative importance of inertial to gravity forces and the initial impact velocity with the speed of sound in the molten solder droplet respectively. The Capillary number scales the viscous and the surface tension forces. The Prandtl, Biot, and Stefan numbers as well as the superheat parameter scale the heat transfer and phase change process. The order of magnitude of the two foremost important dimensionless fluid dynamics numbers, Reynolds and Weber, are O(100) and O(1) respectively. For molten eutectic solder droplets of picoliter size, this range corresponds to an order of magnitude of the impact velocity and initial diameter of O(1 m/s) and O(100 μm). This is approximately the range covered by the applications as described in section 1.1.

It has to be emphasized, that the knowledge acquired from investigating a pile up consisting of two droplets applies also to the case of multiple droplets. As a representative example, Figure 4 shows the solidified shapes of a two-droplet and a three-droplet pile up. As is apparent, the addition of more droplets changes neither the physics nor by much the details of the problem considered.

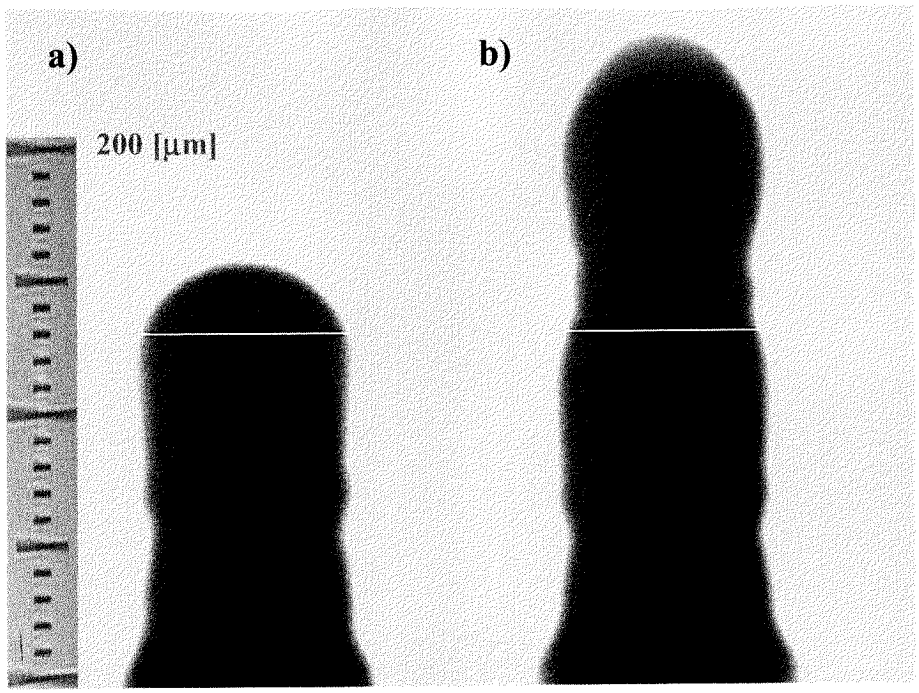

Figure 4: a) Pile up consisting of two droplets. b) Pile up consisting of three droplets. Both cases pertain to the following dimensionless impact numbers: Re = 396, We = 4.905, Fr = 3494, Ste = 0.895

1.3 Review of the Literature

The area of droplet research has received a great deal of attention in the past going back to the experimental studies of Worthington [15,16] who published one of the first works in the area of droplet deposition. Most works with focus on the deposition and the transient stages of the deformation and oscillation as well as the possible solidification process are a lot more recent and have been devoted to single droplets impinging on flat substrates. As outlined in the previous section there is also a great interest in structures built from individual droplets impacting on top of each other. In addition, there exists many times the need to place more solder material in one position than that contained in a single droplet in chip packaging applications. Since the reliable range of droplet sizes in solder jetting is rather limited, droplet pile up is a viable alternative. Unfortunately, there is almost nothing reported on such cases in the literature. To the best of our knowledge there are only publications from Che et. al. [17], Orme et. al. [8-11], Gao and Sonin [5], Liu et. al. [18] to be found in the scientific literature. Che et. al. [17] studied numerically the case of droplets impacting on top of each other. Both

for the case where a single droplet impacts on a presolidified droplet as well as the case where two molten droplets impact on a presolidified droplet and thus coalesce and subsequently form a single droplet solidifying on the latter. The solution method accounted for the conservation of mass, momentum, and energy both for the ambient, gaseous environment, the molten droplets, and the substrate. A fixed grid finite difference scheme was utilized in order to solve the equations numerically. A front-tracking method was employed in order to account for the free-surface and the solidification front. Issues like thermal contact resistance, the dynamic contact line, and the release of latent heat in the solidification process were neglected. In terms of impact parameters their Reynolds number was on the order of O(16), and the Weber number on the order of O(40). They claim that this set of dimensionless numbers is based on liquid metal properties for a 40 [μm] diameter droplet, impacting at 5 [m/s]. No experimental results were reported to compare or corroborate their numerical results. No surface structures like ripples were reported as has to be expected and has been shown for single droplets impacting on flat substrates by for instance Waldvogel et. al. [19]. The results are due to the poor grid resolution limitation of their Eulerian method as well as because they neglected the above mentioned physical issues at best descriptive or of qualitative nature. The work by Orme et. al. [8-11] is focused on the employment of molten droplets in digital microfabrication. Thus, the work reports more on methods how to create objects by drop-wise build up and deposition strategies than on the prevailing physical phenomena and neglects the fluid dynamics. However, some analytical/numerical estimations on critical issues like splat cooling, remelting and thus adhesion properties between subsequent droplets are reported. Furthermore, examples of objects built by digital microfabrication are presented. Gao and Sonin [5] reported analytical estimates of cooldown and solidification time scales for columnar wax droplet deposition (i.e. pile up of many droplets, multiple pile ups). They also presented endshapes of multiple pile ups for candelilla (a natural wax). Liu et. al. [18] reported numerical studies of droplets impacting on different non-flat substrates. The governing equations for transient, axisymmetric, viscous, incompressible flow, including surface tension effects were solved employing a modified version of RIPPLE [20]. The dynamic contact line, heat transfer and solidification were not considered. Free surfaces were modelled using the volume-of-fluid (VOF) method. Simulations of pile up similar problems were performed using tungsten droplets with diameters in the range of 10 – 60 [μm], however, at impact velocities on the order of O(100 m/s). The results show only fluid mechanical aspects of the impingement process including

the splashing of the droplets. Furthermore, only velocity fields and no droplet shapes are presented.

In contrast to multiple droplet impacts or single droplet impacts on non-flat substrates a large amount of work is reported in the scientific literature on single droplets impacting on flat substrates covering and combining the areas of analytical modelling, experimental visualization as well as numerical modelling. A very good insight to the impact of single droplets on flat substrates, which is in many respects strongly coupled to the problem of the pile up, is given in the review articles by Haferl et. al. [21], and Attinger et. al. [22]

An important very difficult sub-problem in droplet deposition problems is that of surface wetting by the droplet. This topic has received in the field of surface science a lot of attention, however, without conclusive results to date. The relevant issue is the dynamic contact line behaviour and the controversial determination of dynamic contact angles. Approaches to these connected problems span a wide area from continuum [23] down to molecular level [24-27]. Another related microscale problem that so far has not been successfully tackled is that of transient thermal contact resistance between an impacting microdroplet and a target object. With reference to the area of dynamic contact line behaviour in the presence of heat transfer and solidification, a major research effort is needed in the future, because the understanding of molecular phenomena appears to be necessary in order to provide reliable closure conditions for the continuum models.

1.4 Outline of the Present Work

The present thesis focuses on the investigation of the different phenomena occurring during the pile up of two molten solder droplets. The focus is on the influential physical mechanisms governing the entire process. This includes the transients of the impact process governed by the fluid mechanics, the wetting, the heat transfer and the simultaneous solidification, as well as the different end-shapes attained for different impact regimes and substrate temperatures. Both experimental visualization as well as numerical simulations will be reported. Results from experimental visualization and numerical simulation will be compared in order to test the modelling. Occurring phenomena with insufficient understanding and/or modelling capabilities will be identified and characterized on their respective influence on the entire impact process. Furthermore, modelling limitations stemming from the chosen numerical method will be discussed.

The thesis is structured in the following manner: First, the experimental method will be described and discussed followed by results from the impact visualization. Second, the mathematical modelling will be formulated accompanied by a description of the numerical method employed. Third, simulation results aiming at identifying the prevailing mechanisms as well as their respective importance for the process will be investigated. This also includes identifying the quality of the numerical code with respect to conservation laws, mesh and time step independence as well as limitations of the numerical method for the task of modelling the phenomena of an impacting droplet. Fourth, based on the experimentally visualized impact sequences, numerical simulations were performed which are compared to the experimental results and discussed. Fifth, an approach to identifying a refined contact line modelling will be presented and discussed. Sixth, conclusions on the experimental and numerical results as well as recommendations for future work will be discussed.

2. Experiments

2.1 Objectives and Literature Review

The objective of the realized experiments was to shed light on the transient physical phenomena occurring during a pile up of picoliter size solder droplets and to provide data for the verification of the numerical model, to be discussed later in this dissertation. To this end, a series of droplet impact experiments with varying initial conditions were performed in order to visualize the temporal evolution of the impingement process. The characteristic length scale of the investigated process is, as given in section 1.2, of the order of O(100 μm). The characteristic time-scale of the process can be estimated from experiments on flat substrates to be on the order of O(100 μs) [4,13,14,19,28,29]. The experimental accessibility to the pile up process is therefore indeed limited. Thus, the visualization and the corresponding measurements focus mostly on identifying the shapes, lengths and times characteristic of the various stages of the process in order to validate the numerical modeling.

Regarding experiments on the pile up of picoliter size droplets, these are, to the best of our knowledge, the first transient visualizations/measurements reported. Experiments by Gao and Sonin [5] show final solidified pile up wax structures as mentioned in section 1.3. The same is true for the case for the structures built using digital microfabrication by Orme et. al. [10]. No other experimental investigations on the pile up could be found in the scientific literature.

The techniques employed to visualize the pile up process herein are an extension to those used by Attinger et. al. [4] for single droplets impinging on flat wafer substrates.

2.2 Microdroplet Generation

A number of methods exist to generate monodispersed picoliter-sized droplets on demand [1,5,8,30,31]. The investigation herein utilizes a modified microdroplet jetting device manufactured by Microfab Inc., Dallas, Texas. The main concept of the method stems from ink-jet technology. A schematic of the deployed microdroplet generator device is given in Figure 5.

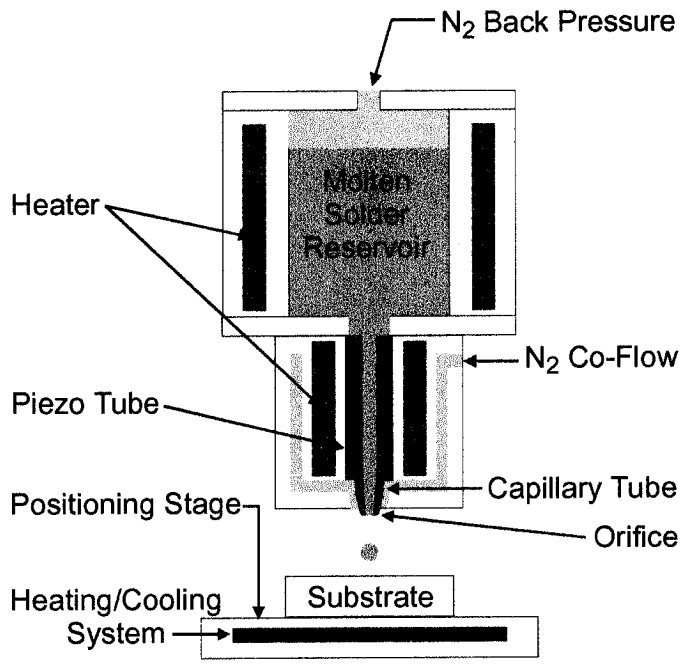

Figure 5: Schematic of the droplet generator including the positioning stage and the substrate.

The droplet generation method can be briefly summarized as follows. By applying an electric pulse on a piezoelectric tube fitted concentrically around a glass capillary, picoliter size volumes of the corresponding fluid can be ejected from the glass tube on demand. The glass capillary is filled and in contact with a temperature controlled fluid reservoir. The latter is inertized and pressurized by nitrogen gas. Backpressure is needed to force the molten solder into the thin glass capillary since solder wets glass very poorly. The glass capillary features an orifice at the open end which focuses the pressure waves generated in the glass capillary by the piezoceramic tube and thereby enables the ejection of fluid ligaments [32]. The so created fluid volume initially oscillates upon ejection and assumes a spherical shape due to minimization of the interfacial energy. For a given fluid mostly the shape and time scales of the electric pulse applied to the piezoelectric tube, the inner diameter of the glass capillary, the diameter of the orifice, as well as the pressure level in the molten solder reservoir determine the size and the velocity of the so created droplets. The present investigation employs glass capillaries with an inner diameter of approximately 500 [μm] and an orifice diameter of approximately 58 [μm], respectively. Thus, velocities and diameters can be changed by altering the driving electrical pulse and the backpressure. Respective ranges of approximately 50 – 100 [μm] for the droplet diameter and approximately 1 – 2.5 [m/s] for the impact velocity can be achieved. In order to minimize oxidation of the ejected solder droplets

a co-flow of nitrogen is applied as can also be seen in Figure 5. The solder is melted and temperature controlled in the fluid reservoir by resistance heating. The temperature of the molten solder is kept at a constant temperature of 210 [°C]. The melting temperature of the latter is 183 [°C] as can be seen in Appendix A, showing all the relevant thermophysical properties of the materials utilized in this investigation.

2.3 Visualization Method

The detailed and accurate visualization of a process taking place on a time scale on the order of O(100 [μs]) requires special attention. Conventional high-speed cameras are either limited to a certain frame acquisition frequency or the time window during which a very high acquisition frequency can be upheld. For instance, a very fast CCD camera as the KODAK EKTAPRO has a maximum acquisition rate of 40'500 frames per second at a resolution of 64x64 pixels. Apart from the poor resolution, single frames are taken approximately every 25 [μs] with an equal exposure time. This impedes the use of a conventional high-speed camera. On the other hand, intensified CCD cameras can achieve time resolutions of up to 50 [ns]. However, only a limited amount of frames (8 – 30) can be recorded from a single event [33]. This is not enough to cover the time scales of a pile up. Other visualization methods such as strobe photography/videography rely on a different approach requiring a high repeatability of the investigated process [34-39]. The difference between high-speed camera and strobe techniques is that the former records the highest number of frames of a single event (i.e. the impact of a single droplet is recorded), whereas the latter reconstructs a single event from multiple, reproducible events by patching together several frames taken at subsequent times (i.e. the impact of a droplet is visualized by recording many droplets once at subsequent times). Using this technique a time resolution on the order of O(1 [μs]) can be achieved. On this account, flash video microscopy was utilized in order to visualize the pile up process. To this end a triggered JAI M10 progressive scan CCD camera (Denmark) was employed for the digital imaging. Backlighting was provided by a triggered Xenon flash light unit (Hamamatsu L4634; Japan). The flash energy of the latter is 0.15 [J/flash] with a burst duration of 1 [μs] with less than 200 [ns] jittering. An ICI-PCI framegrabber (Stemmer Imaging; Germany) was employed for the image recording. A microscope objective (Microtech Zoom 70, USA) was

used to magnify the droplet images. An optical magnification of 29x on the CCD matrix plane was utilized giving a spatial resolution of 1.2 [μm] in the object plane.

2.4 Experimental Setup and Procedure

Based on the droplet generation and visualization methods described above, the experimental procedure consists in principle of electronically generating a sequence of pulse waveforms which is then applied on the piezoceramic tube. Each individual pulse creates thereby a single droplet. Concurrently another sequence of pulses is generated to trigger the strobe flash/camera. In order to get a pile up structure two droplets per acquired image are ejected subsequently. The first of these two droplets creates the presolidified solder droplet upon which the second droplet impacts. As substrate for the presolidified droplet serves a gold coated silicon wafer situated underneath the droplet generator device. Images are only acquired upon impact of the second droplet respectively. In order to provide a free wafer surface for each impacting droplet pair, a positioning stage is employed. The wafer substrate on which the pile ups are created is attached to a positioning stage. The stage moves the wafer substrate in the focal plane of the camera a fixed distance after the creation of each pile up, halts, remains in position until the next pile up has been created and recorded, then moves on to the next position. This stage movement is controlled by a third, concurrent trigger pulse sequence. A schematic of these somewhat intricate trigger pulse sequences is shown in Figure 6. Each experiment involves starting such a set of three trigger pulse sequences simultaneously. As shown in Figure 6 different frequencies or period lengths are associated to the three pulse sequences. The droplets are created at a fixed frequency corresponding to a period length of ΔT_1. The strobe flash and the camera are triggered at a lower frequency corresponding to a period length which is twice the period length of the droplet generation, ΔT_1, plus an adjustable time period ΔT_2. The latter determines the time lag between the subsequent recorded frames of the second droplet motion in the pile up. This enables the piecing-together of a total event of the impact of the second droplet until its complete freezing, from a sequence of such frames each corresponding to a different identical pile up.
The period length of the strobe flash/camera is approximately half the period length of the droplet generation pulses. Thus every second droplet of the pairs of a pile up is recorded as already mentioned above. The frequency of the pulse sequence driving the positioning stage is

exactly half the frequency of the droplet generation. Thus the positioning stage awaits the creation of each pile up structure until it moves into the next position.

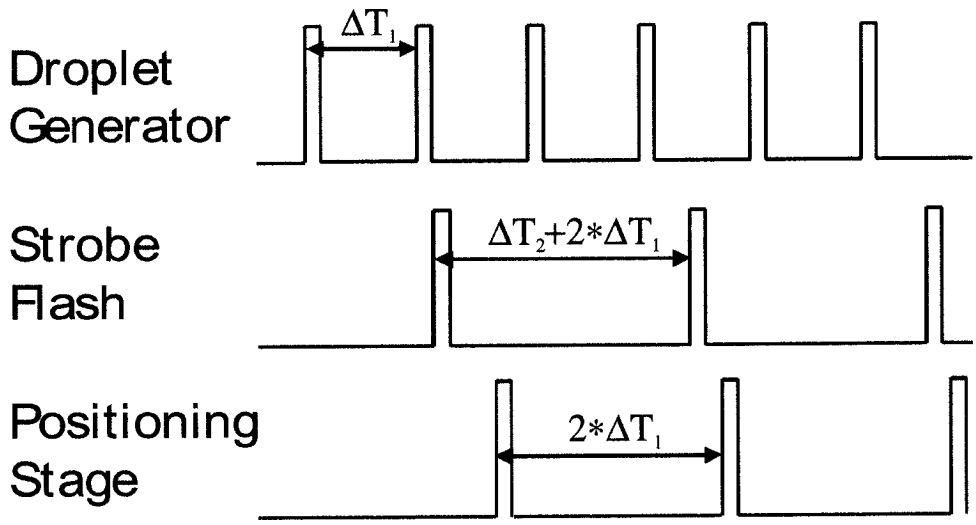

Figure 6: Schematic of the trigger pulses deployed to drive and coordinate the droplet generator, the image acquisition, and the positioning stage.

Under the conditions of the above outlined experimental procedure it has to be emphasized, that this study focuses on the investigation of pile up structures built by two solder droplets having ideally exactly the same droplet diameter and impact velocity.

A schematic of the experimental setup is shown in Figure 7. The x-y positioning is accomplished using an Aerotech MP100M (USA) and an Aerotech ALS130-150 (USA) fast precision stage. The travel distance from one pile up spot to the next is 200 [μm]. A LeCroy LW420 (USA) waveform generator is used to create the above described trigger sequences for the droplet generation and the image acquisition. Droplets are created at a frequency of 8 [Hz] (ΔT_1 = 0.125 [s]). The chosen time resolution, ΔT_2, respectively the time lag between subsequent image acquisitions is 5 [μs]. The positioning stage is triggered at a frequency of 4 [Hz]. The control of the substrate temperature involves a twofold system. The wafer substrate is heated unintentionally by the droplet generator device by radiation and most of all by the inertizing, hot nitrogen co-flow which flows at a rate of approximately 300 [cm^3/min]. In order to keep a constant and uniform wafer temperature below approximately 70 [°C] the substrate has to be cooled. This is provided using a Lauda RCS (Instrumenten Gesellschaft AG, Germany) thermostat. Wafer temperatures above 70 [°C] can be achieved using a

resistive heater, temperature controlled by a Syrelec CTD 46 (Syrelec, France) controller device.

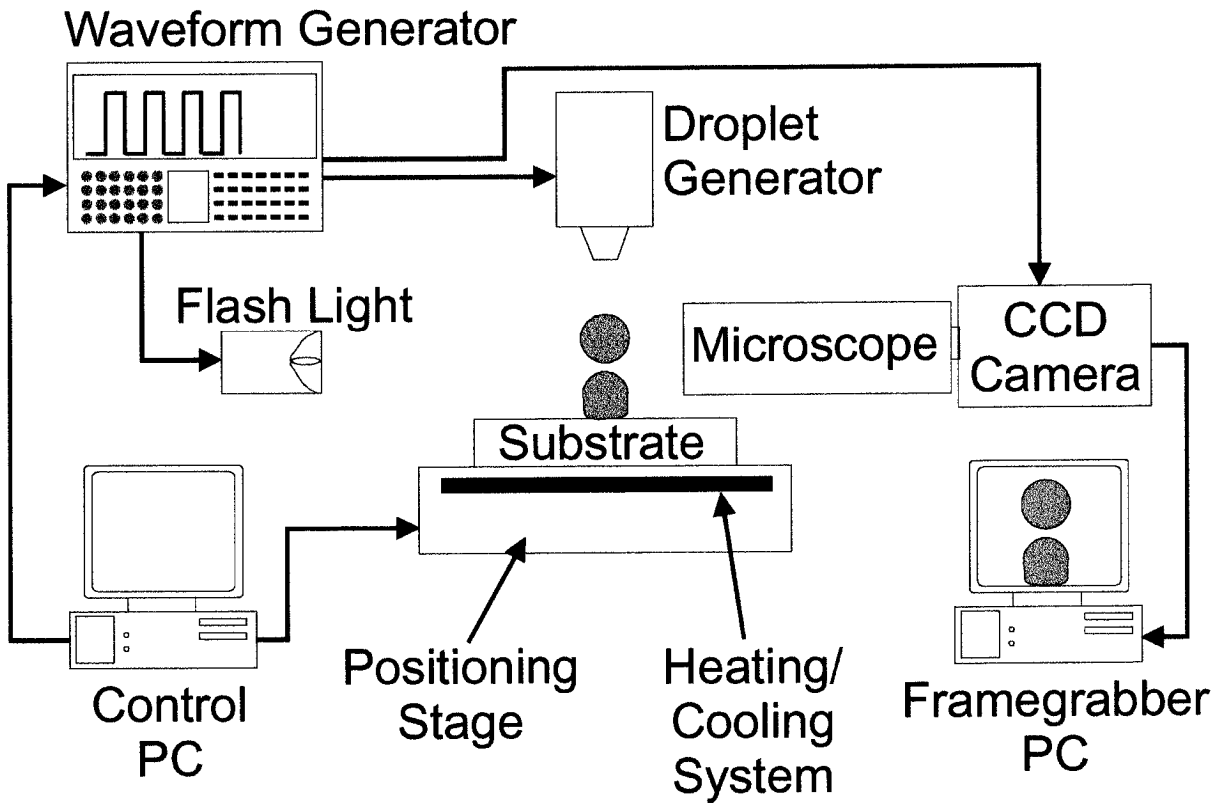

Figure 7: Schematic of the experimental setup.

To this end, the wafer substrate is fixed on a supporting copper substrate mounted on the positioning stage. The copper substrate carries a heater cartridge as well as channels for the cooling fluid from the thermostat. In order to improve thermal contact and to fix the wafer substrate on top of the supporting copper substrate a thin layer of thermal paste (HTC Electrolube, England) is inserted between the copper and the wafer substrate. The latter is a semiconductor wafer (EM Marin; Switzerland) cut to rectangular sizes of approximately 10 * 100 [mm]. The wafer consists of the following layers from top to bottom: 0.1 [μm] Au, 0.3 [μm] Ti90W alloy, 1 [μm] silicon nitride and 675 [μm] P-silicon. The corresponding material properties are given in Appendix A. The wafer surface temperature is measured using a K-type thermocouple (Omega 304 SS9). The excess back pressure level in the molten solder reservoir is kept at a constant value of $6.9*10^3$ [Pa]. The experimental setup is positioned in a dust free environment and on a vibration free table. The initial temperature of the impinging droplet is held constant at a temperature $T_{1,0}$ of 210 [°C].

2.5 Experimental Errors

A number of uncertainties and variations occur both in the postprocessing of the acquired impact sequences as well as in the experiments due to the visualization method and due to variations in the droplet generation. As can be seen from the impact sequences in the subsequent section, the experiment does not (ballistically) deliver perfect axisymmetric cases of the pile up. This is due to the circumstance that the trajectories of the ejected droplets have a slight, randomly distributed deviation from the ideal trajectory as exemplified in Figure 8.

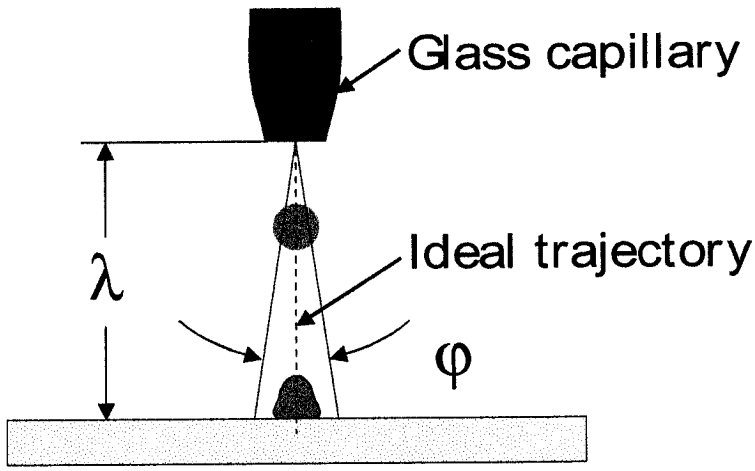

Figure 8: Angular deviation of an ejected droplet from the ideal ballisitic trajectory.

There are a number of reasons possibly responsible for this deviation. For situations where a thin liquid solder film forms non-axisymmetrically around the orifice on the outside of the glass capillary it has been observed that capillary forces deflect the ejected droplet prior to detachment from the orifice. Baggerman and Schwarzbach [40], using the same droplet generator device as employed in this study, attributed this random horizontal component of the ejected droplet to system vibrations of the capillary/piezo ensemble. It can only be speculated on further effects like accumulated impurities as oxides inside the orifice, slight irregularities of the orifice geometry, or a slightly non-axisymmetric fluid meniscus inside the orifice leading to this effect. Nonetheless, the angular deviation φ was determined for different ejection velocities and droplet diameters. This was accomplished by measuring the position of a large number of droplets at a distance of 1500 [μm] from the orifice. Independent of droplet velocity and diameter the angular deviation was determined to be $\varphi = 0.52° \pm 0.24°$. It therefore has to be emphasized, that impacts randomly distributed and

slightly off center have to be expected in the experiments. For presolidified droplet shapes not exhibiting very large radii of curvature or changes in curvature in the area of impact this is acceptable. The reason for this is the fact that the Weber number of the droplets investigated in this study is on the order of O(1). This indicates that surface tension features a large restoring force to deformations in general and specifically to slight deformations due to three-dimensional effects. This means that a droplet impinging somewhat off center will spread, recoil and solidify as if it had hit the presolidfied droplet on center. The eccentricity is only visible in an angle between the line of symmetry of the impacting droplet and the ideal trajectory as defined in Figure 8. Clearly, for an increasing distance between the orifice and the substrate λ, as defined in Figure 8, an increasing departure from the ideal trajectory is obtained leading to completely unacceptable shapes as exemplified by Figure 9.

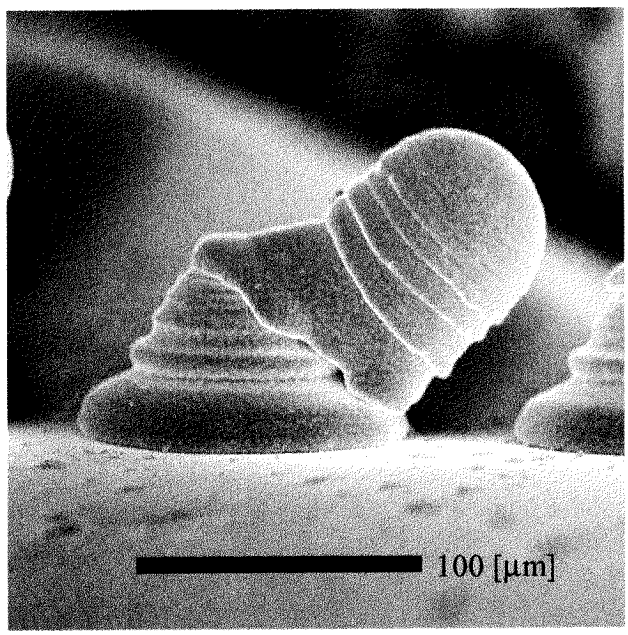

Figure 9: Scanning electron micrograph of a highly three-dimensional pile up.

A means to minimize this problem is to decrease the distance λ between the substrate and the orifice. However, it has to be kept in mind that the molten solder, when ejected from the orifice has a tear-drop shape. Surface tension forces will, in order to minimize the interfacial energy, drive an internal, oscillatory fluid motion, damped by viscosity, to attain the energetically favorable shape of a sphere. Thus, the ejected droplet suffers damped in-flight oscillations from prolate to oblate shape. The complexity of this effect is that, first, the droplet might impact in an ellipsoidal rather than a spherical shape. It has to be expected that this may

lead to changes in the results compared to the impact of an identical droplet of spherical shape since the field variables (i.e. pressure, velocities) differ from a droplet impacting in a non-oscillatory, spherical shape without gradients in the field variables [21,41,42]. However, the objective of this work is to investigate the axisymmetric pile up of a spherical droplet without residual gradients in the field variables as stated above. Therefore, a trade-off situation is encountered between angular accuracy of the impinging droplets, in order to get the postulated axisymmetric impact, and residual gradients in the field variables. It is believed, that with the chosen distance from the orifice to the substrate of $\lambda = 900$ [μm] a good compromise has been reached.

Further problems of repeatability were encountered in the experimentally obtained velocities and diameters of the ejected droplets. Velocities were determined by measuring, for a fixed time delay, the distance between two subsequent droplets. This was realized for a large number of droplets. Table I, shows the errors for some velocities employed in the present study. The velocities are thereby averages of a large number of measurements.

Velocity [m/s]	1.12	1.26	1.38	1.5	1.63	1.74
Error ± [m/s]	0.05	0.04	0.03	0.02	0.02	0.02
Error ± %	4.4	3.1	2.2	1.3	1.2	1.1

Table I: Impact velocities and respective experimental errors.

As can be seen in Table I, the error increases with decreasing droplet velocity. This is in concordance with the observation that the stability of the entire jetting process deteriorates with decreasing jetting velocity or smaller electrical pulses on the piezoceramic actuator. The velocities tabulated in Table I actually correspond to the impact velocities in the visualization experiments, section 2.6.1. Simultaneously to the velocity measurements, variations in droplet diameter were monitored. It was found that independent of a specific velocity or particular average droplet diameter, a variation of approximately 2 % of the initial droplet diameter occurred. This estimate includes the effect that the measurements are also affected by uncertainties as will be discussed briefly below.

Measurement errors also occur when evaluating distances on the acquired picture sequences. This pertains to values of, for instance, the droplet diameter, pile up height, and the spreading distance of the impacting droplet. These uncertainties are largely due to operator errors in

defining the edges of a droplet or specific points such as the contact line on the acquired image. It is very difficult to quantitatively determine this error. Therefore, an estimate for such errors of 1% of a measured distance is accepted based on repetitions of the same measurement.

A different uncertainty connected with the error in the determination of the pile up height stems from the fact that the substrate level has to be determined form the recorded pictures as well. The cause of this error is that the CCD camera, the light source and the substrate are not perfectly aligned thus leading to reflections of the pile up. As shown in Figure 10 this can induce for certain pile up geometries errors when defining the locus of the substrate level. This error is estimated to be maximum 5 % of the total pile up height including the error made when measuring distances as described above. The thin horizontal line seen in the lower part of Figure 10 is an artifact created by the CCD camera chip and can not be related to the substrate or the mirroring effect.

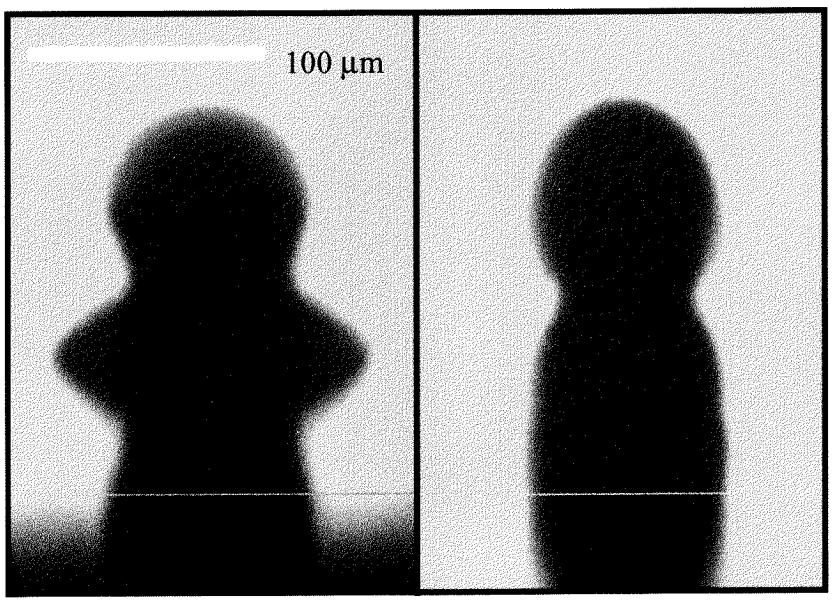

Figure 10: Unprocessed images of pile up structures showing the mirroring effect of the employed wafer substrate. The thin horizontal line in the lower part of the figure is an artifact created by the CCD camera chip.

Additional uncertainties correspond to the thermal baseline conditions for the experiments, measured as described in section 2.4. First, the droplet temperature is assumed to be the one of the jetting device. An error estimate for the initial temperature of the droplet can be given

based on the precision of the K-type thermocouple used to measure the device temperature which is approximately 1 [°C]. However, this does not account for the fact that the temperature is not measured exactly at the orifice. Due to implementation difficulties this temperature could not be measured. On the other hand, the high thermal conductivity of the liquid metal (solder) assures the acceptability of the measurement. Second, the droplet is cooled convectively in-flight. However, based on work by Kang and Poulikakos [43] as well as Bennett and Poulikakos [44], who estimated this cooling with the Ranz-Marshal correlation [45], and the fact that the droplet travels for less than a millisecond in a covering nitrogen air-flow at a temperature close to the initial droplet temperature it is assumed that this convective cooling is negligible. Third, the actively cooled substrate is locally subjected to a stream of hot nitrogen from the inertizing co-flow. Measurements of the substrate surface temperature using a K-type thermocouple with a diameter of 0.25 [mm] showed a change in temperature in areas subjected to the hot nitrogen co-flow of approximately 2 [°C], which is within the error range of the thermocouple. Changes of the thermal baseline conditions by the release of the thermal energy of the impinging droplets have found to be negligible as has been shown by Attinger et. al. [4].

Variations of impact velocity, initial diameter and also of thermal baseline conditions lead to a combined effect which becomes, compared to single droplet impacts on flat substrates, sometimes observable in visualizations of the pile up process. To summarize, the error in the measured velocity ranges, as given in Table I, between 1 – 4 % of the initial velocity. The error made in measuring the diameter is approximately 2% of the initial diameter. Spreading distances are measured with an approximate accuracy of 1% of the initial diameter. The total pile up height is measured with an accuracy of approximately 5% of the initial diameter. It has to be emphasized, that these errors also contain the variations in the droplet generator performance.

2.6 Results

2.6.1 Experimental Conditions

In terms of dimensional values, sequences at different impact velocities as well as substrate temperatures were recorded using flash video microscopy. In addition, end shapes of pile ups were imaged using a scanning electron microscope (Hitachi, S-900) in order to obtain fine

surface structures not very well visible in the recorded sequences. Basically, two series of experiments were performed covering first the influence of the impact velocity on the pile up and second, for constant impact velocity and diameter, the influence of the substrate temperature on the outcome of the pile up. For all experiments it was attempted to keep the droplet diameter at a size of approximately 80 [µm]. This is due to the fact that at this diameter the most stable droplet generation was achieved. Thus, the following array of experimental cases were visualized, Table II:

Case	Impact Velocity u_{z0} [m/s]	Droplet Diameter d_0 [µm]	Substrate Temp. $T_{2,0}$ [°C]	Reynolds Number Re [-] *	Weber Number We [-] *	Froude Number Fr [-] *	Stefan Number Ste [-] *	Ohnesorge Number Oh [-] *	Prandtl Number Pr [-]
1	1.51±0.02	76.83±1.54	25±2	363.89	4.17	3025.2	0.895	0.0056	0.025
2	1.50±0.02	77.22±1.54	50±2	363.31	4.14	2970.2	0.754	0.0056	0.025
3	1.50±0.02	77.03±1.54	75±2	362.42	4.13	2977.5	0.612	0.0056	0.025
4	1.51±0.02	76.17±1.52	100±2	360.77	4.14	3051.4	0.470	0.0056	0.025
5	1.52±0.02	75.02±1.50	125±2	357.67	4.13	3139.4	0.329	0.0056	0.025
6	1.49±0.02	76.83±1.54	150±2	359.07	4.06	2945.6	0.187	0.0056	0.025
7	1.12±0.05	80.10±1.60	25±2	281.39	2.39	1596.4	0.895	0.0054	0.025
8	1.26±0.04	76.83±1.54	25±2	303.65	2.91	2106.4	0.895	0.0056	0.025
9	1.38±0.03	79.59±1.59	25±2	344.51	3.61	2439.1	0.895	0.0055	0.025
10	1.51±0.02	76.83±1.54	25±2	363.89	4.17	3025.2	0.895	0.0056	0.025
11	1.63±0.02	77.51±1.55	25±2	396.29	4.91	3494.2	0.895	0.0056	0.025
12	1.74±0.02	83.03±1.66	25±2	453.16	5.99	3717.0	0.895	0.0054	0.025

Table II: Initial conditions of the experimental cases investigated.

* Values of the Reynolds, Weber, Froude, Stefan, and Ohnesorge number correspond to averaged values of the impact velocity, the initial diameter and the temperature.

Cases 1 – 6 represent the thermal regime with changing initial substrate temperatures and cases 7 – 12 represent the impact regime with changing impact velocities. The material properties used to form the dimensionless numbers in Table II, are taken from Appendix A.

2.6.2 The Spreading Process

Upon formation of contact between the impinging droplet and the presolidified droplet on the substrate the liquid starts to spread out. As mentioned in Rein [41], different scenarios depending on the impact kinetic energy of the droplet are possible. In the present study with We>1, spreading is greatly influenced by the kinetic energy. Concurrently, surface tension forces resist and viscous forces damp the spreading process. Furthermore, solidification influences the spreading process as well. This can take place by solidification at the wetting line as outlined by Schiaffino and Sonin [46,47] or by annihilation of kinetic energy by solidification [48]. Based on droplet impact studies on flat substrates Bennett and Poulikakos [49] proposed that surface tension effects dominate the termination of the droplet spreading over viscous effects when:

$$We << 2.8\,Re^{0.457} \tag{11}$$

In their scaling argument the effect of solidification in the droplet spreading was neglected. Based on the values of the characteristic dimensionless numbers of the pile up cases in this study, Table II, the right-hand side of Equation 11 is about an order of magnitude larger than the Weber number. This points at a dominance of the surface tension forces in the termination of the spreading process.

On the other hand, neglecting the presence of thermal contact resistance, Schiaffino and Sonin [50] derived upon scaling analysis an estimate of the ratio of the spreading time, t_β, and the solidification time, t_s:

$$\frac{t_\beta}{t_s} = \frac{OhSte}{Pr} \tag{12}$$

Based on the values of the characteristic dimensionless numbers in Table II, the ratio given by Equation 12 is in the range of 0.04 – 0.2. Accounting for thermal contact resistance it is expected that this ratio would be further decreased. This means that spreading is a process featuring a markedly shorter time scale than the solidification process. However, local freezing at the wetting line is expected to occur markedly earlier than the bulk freezing time scale. Hence, based on the above discussion, spreading arrest should be controlled by surface tension forces unless solidification at the wetting line occurs and terminates the spreading.

The low influence of viscosity is corroborated by the reconstructed pile up sequences for the cases 1, 5, 7, and 12, Figures 11-14, showing large, only weakly damped oscillations of the impacting droplet. Solidification effects become only visible after the first oscillation cycle.

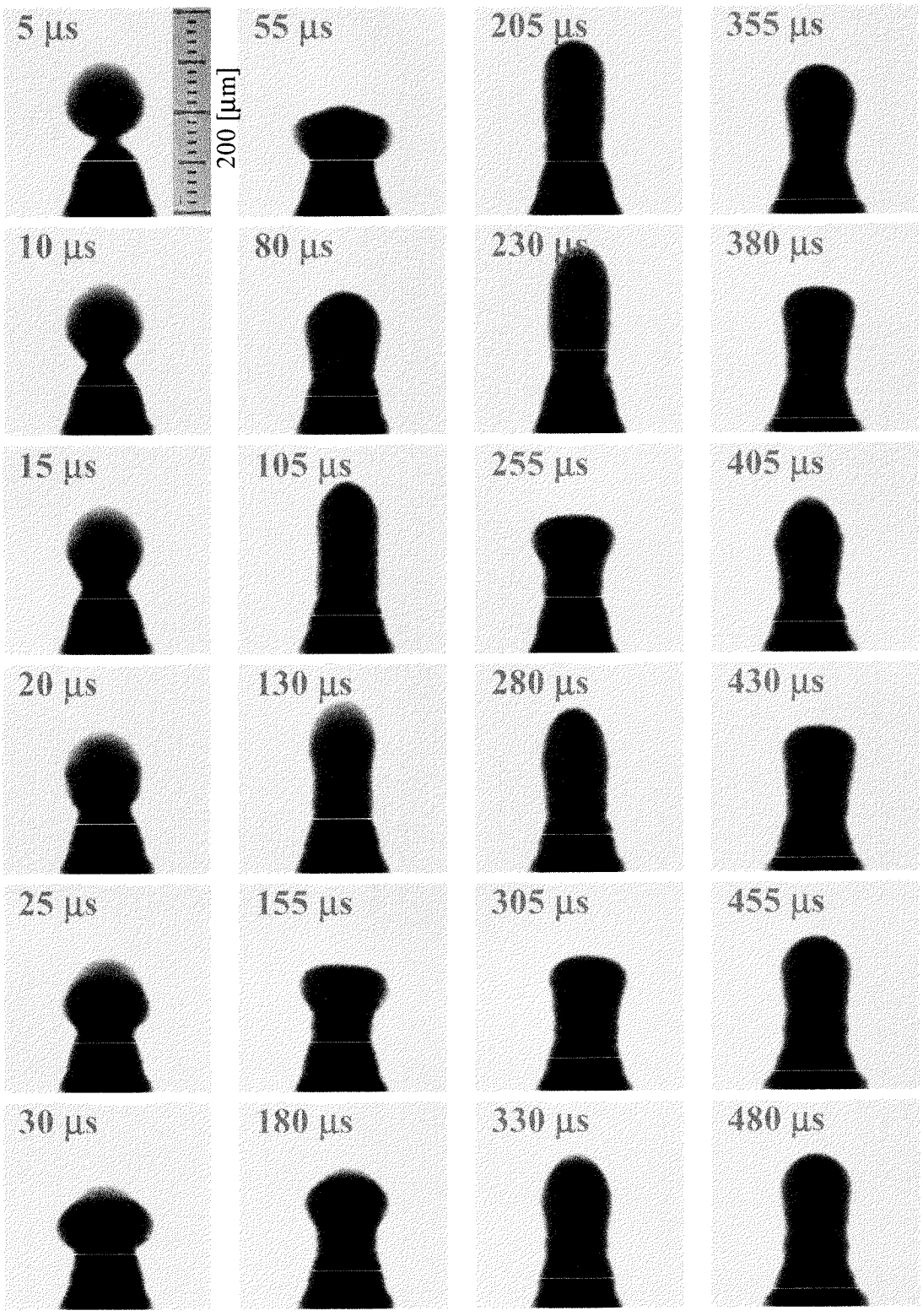

Figure 11: Case 1, spreading, oscillation, and solidification during a pile up. Initial conditions: $u_{z0} = 1.51 \pm 0.02$ [m/s], $d_0 = 76.83 \pm 1.54$ [µm], $T_{1,0} = 210$ [°C], $T_{2,0} = 25$ [°C]

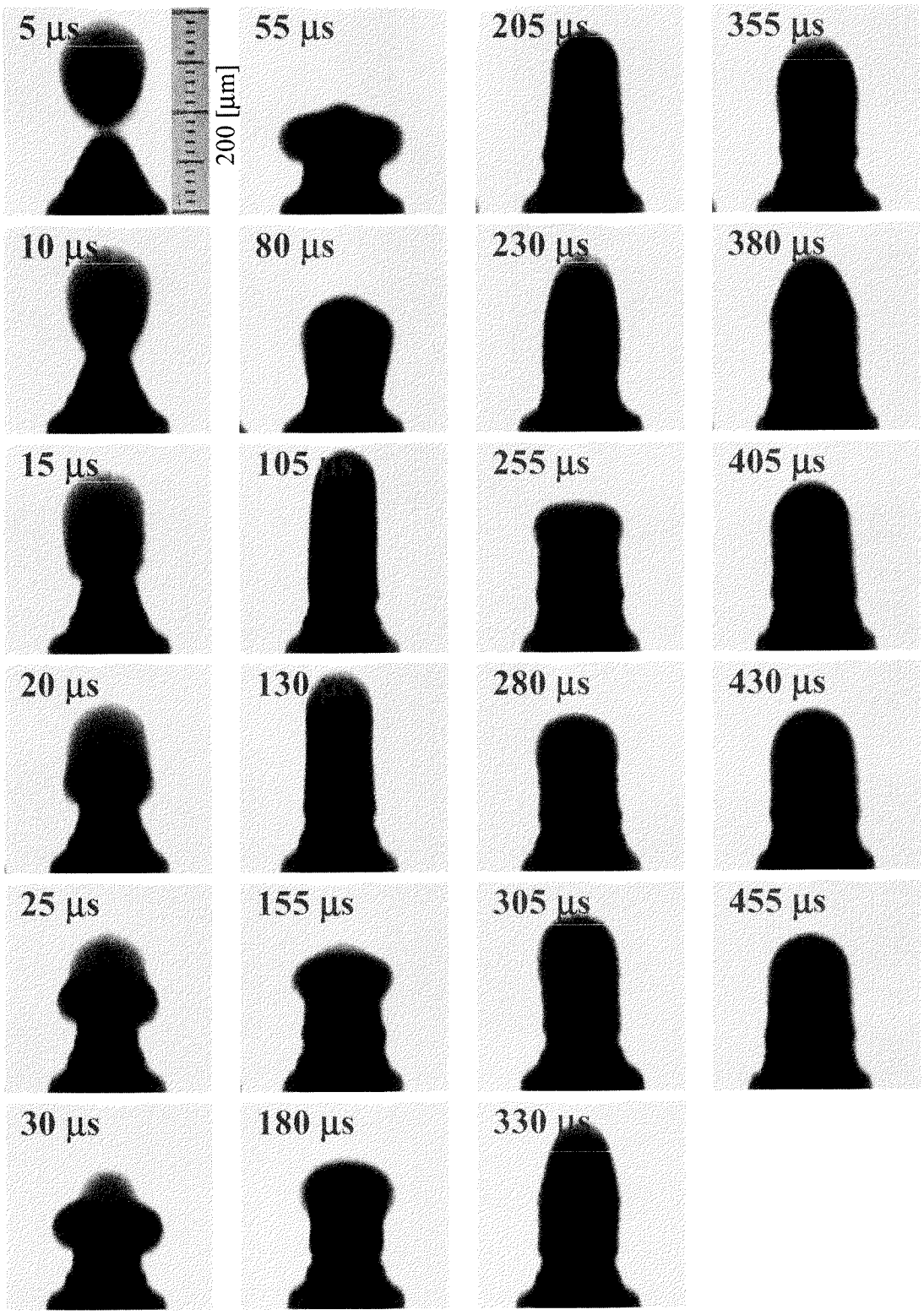

Figure 12: Case 10, spreading, oscillation, and solidification during a pile up. Initial conditions: $u_{z0} = 1.74 \pm 0.02$ [m/s], $d_0 = 83.03 \pm 1.66$ [µm], $T_{1,0} = 210$ [°C], $T_{2,0} = 25$ [°C]

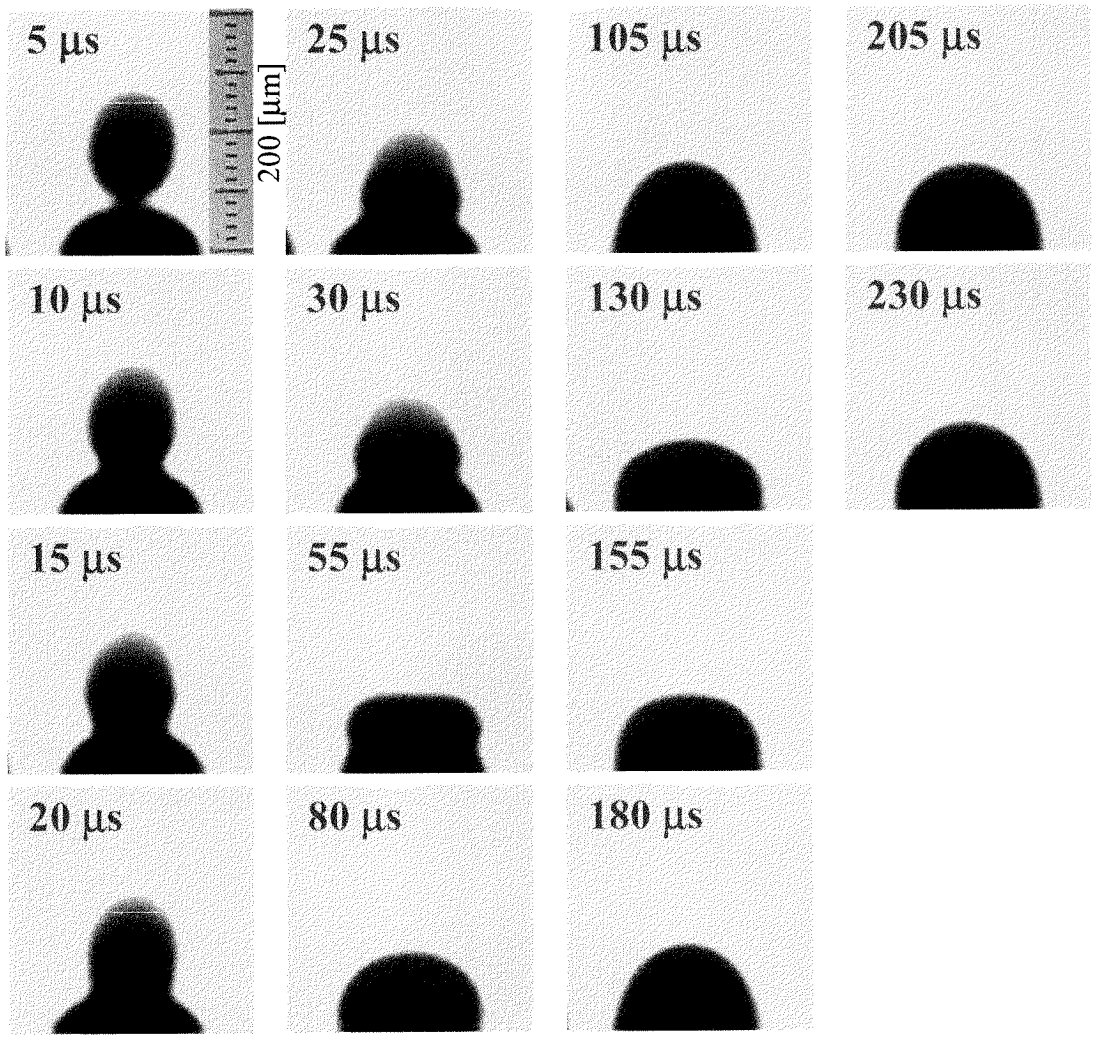

Figure 13: Case 5, spreading, oscillation, and solidification during a pile up. Initial conditions: u_{z0} = 1.52±0.02 [m/s], d_0 = 75.02±1.5 [μm], $T_{1,0}$ = 210 [°C], $T_{2,0}$ = 125 [°C]

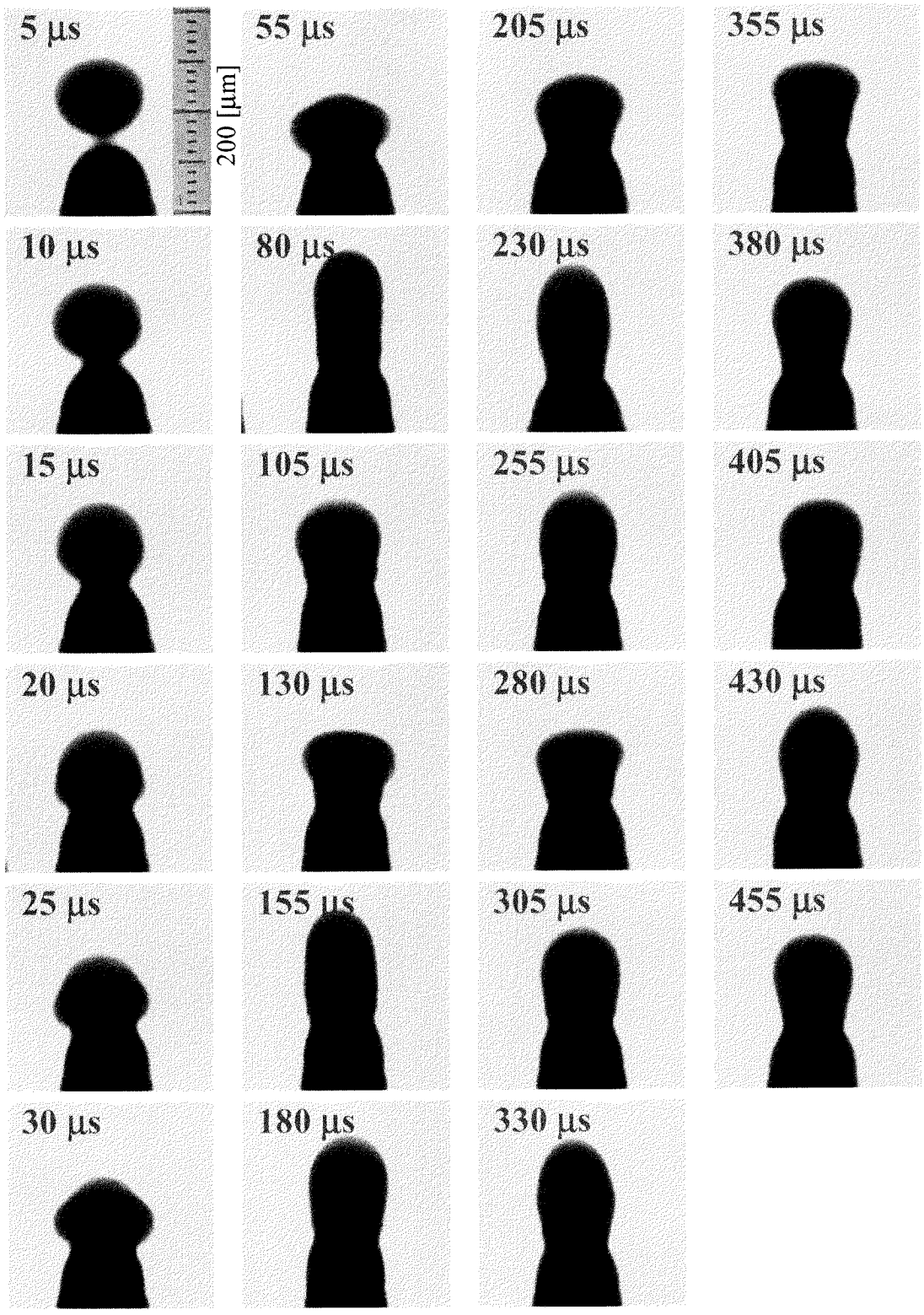

Figure 14: Case 7, spreading, oscillation, and solidification during a pile up. Initial conditions: $u_{z0} = 1.12 \pm 0.05$ [m/s], $d_0 = 80.10 \pm 1.60$ [µm], $T_{1,0} = 210$ [°C], $T_{2,0} = 125$ [°C]

The temporal evolution of the spreading process can be expressed in terms of the spread factor β:

$$\beta(t) = \frac{a_c(t)}{r_0} \tag{13}$$

where a_c is the instantaneous travel distance of the contact line, as shown in Figure 15, and r_0 is the initial droplet radius. The instantaneous travel distance of the contact line, a_c, is thereby measured in terms of the arc-length from the center of impact along the free-surface of the presolidified droplet to the contact line.

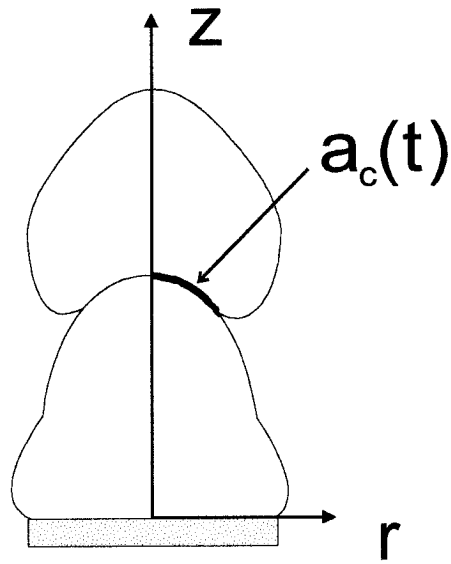

Figure 15: Definition of $a_c(t)$, the instantaneous travel distance of the contact line.

Defining the instantaneous travel distance of the contact line in this manner, takes the curvature of the presolidified droplet into account. Thus, it renders results more comparable to already existing results for droplets impacting on flat substrates. To this end, the surfaces of the presolidified droplets for all cases given in Table II were digitized in order to derive an expression for the arc-length. It has to be emphasized, that this approach is somewhat critical following the arguments on accuracy and repeatability in section 2.5. Furthermore, it has to be emphasized that in general comparability of all the cases reported herein is somewhat difficult since, as visible in Figures 11 – 14, these cases all feature a different substrate shape upon which they impact. When changing an initial condition (i.e. initial substrate temperature,

impact velocity) the effect of the altered shape of the presolidified droplet always interferes and biases the influence of for instance a higher impact velocity on another parameter such as the spread factor. With the above in mind, as follows upon inspection of Table III, the parameter changed for the thermal series (cases 1 – 6) is predominantly the Stefan number, whereas for the impact series (cases 7 – 12) the Reynolds, Weber, and Froude numbers are varied.

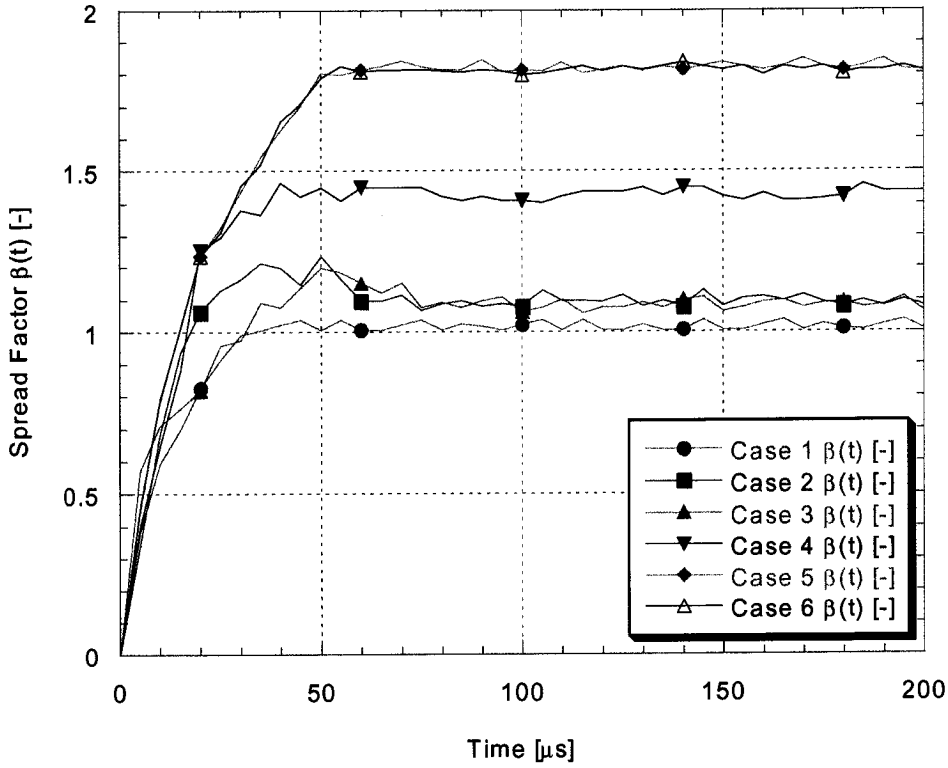

Figure 16: Spread factor β(t) for the cases pertaining to the thermal regime.

Figure 16 shows the temporal evolution of the spread factor as a function of the initial substrate temperature, cases 1 – 6. The maximum spread factor β_{max} and the final spread factor β_{∞} pertaining to the solidified contact line are additionally given in Table III.

Case	Impact Velocity u_{z0} [m/s]	Droplet Diameter d_0 [μm]	Substrate Temp. $T_{2,0}$ [°C]	Spread Factor β_{max} [-]	Spread Factor β_∞ [-]	Spread Factor Ratio β_∞/β_{max} [-]
1	1.51±0.02	76.83±1.54	25	1.0370	1.0203	0.9839
2	1.50±0.02	77.22±1.54	50	1.2329	1.0897	0.8839
3	1.50±0.02	77.03±1.54	75	1.1998	1.0829	0.9026
4	1.51±0.02	76.17±1.52	100	1.4641	1.4269	0.9746
5	1.52±0.02	75.02±1.50	125	1.8426	1.8305	0.9934
6	1.49±0.02	76.83±1.54	150	1.8374	1.8212	0.9912
7	1.12±0.05	80.10±1.60	25	1.0690	1.002	0.9373
8	1.26±0.04	76.83±1.54	25	1.0306	0.9413	0.9134
9	1.38±0.03	79.59±1.59	25	1.0916	0.9807	0.8984
10	1.51±0.02	76.83±1.54	25	1.0370	1.0203	0.9832
11	1.63±0.02	77.51±1.55	25	1.2403	1.1327	0.9132
12	1.74±0.02	83.03±1.66	25	1.8611	1.8072	0.9710

Table III: Spread factors β_{max} and β_∞ as well as the spread factor ratio β_∞/β_{max} for all experimental cases investigated.

All Cases 1 – 6 feature approximately the same impact regime (i.e. Reynolds and Weber number). Due to the different initial substrate temperatures, or Stefan numbers respectively, the presolidified droplets, upon which the second droplets in the pile up impact, feature different shapes as follows from inspection of Figures 11 and 13. As can be seen in Figure 16 the initial stage of the spreading process is already very different for all cases. After less than 10 [μs] the temporal evolution of the spread factor β diverges. This differs markedly from findings by Attinger et. al. [4] on approximately identical droplets impinging on a flat, wafer substrate (the same as deployed in this study) at different initial temperatures, respectively Stefan numbers. This divergence of the spread factor is further exemplified by Figure 17 presenting the spreading velocity. The latter is defined in terms of the Capillary number. The definition of the Capillary number, Equation 6, is determined by differentiating the measured spread factor with respect to time (It must be emphasized that the so determined Capillary number may feature large errors. The derived results are therefore only of qualitative nature).

Although the droplets impact with approximately the same velocity the spreading advances in different manner. This difference in spreading behaviour can not only be associated to the different initial temperatures or Stefan numbers as follows from inspection of [4]. It has to be due to the fact that the specific shapes of the presolidified droplets (determined of course by the different substrate temperatures), have a noticeable influence on the spreading behaviour of an impinging droplet. In other words, the substrate temperature effect on the spreading of the second droplet manifests itself in an implicit manner, through the surface curvature of the presolidified first droplet.

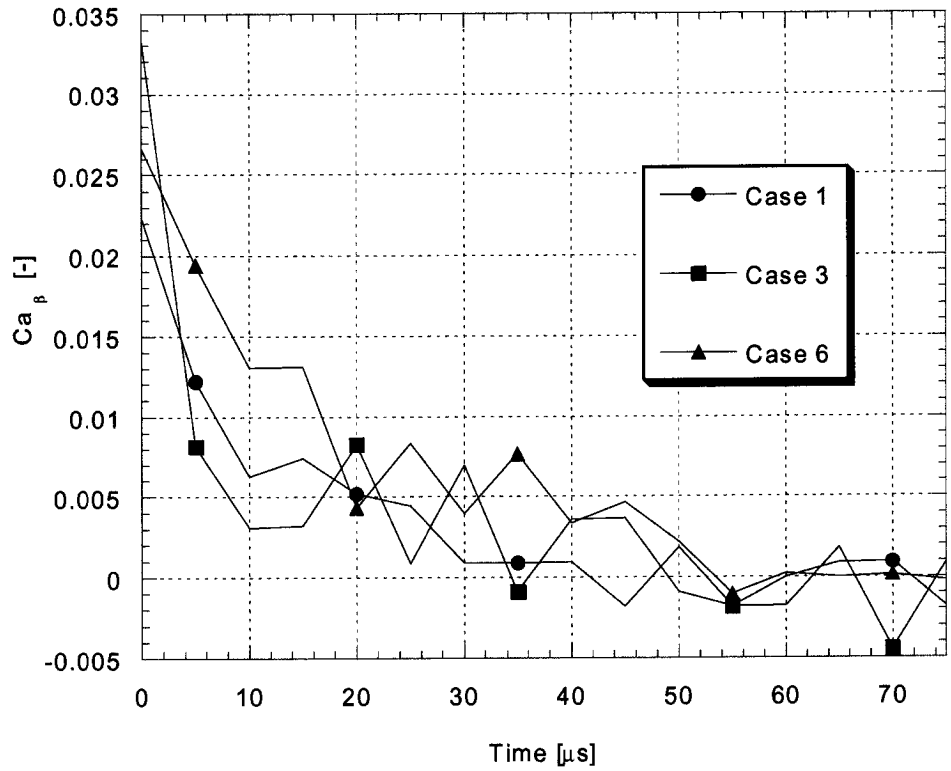

Figure 17: Temporal evolution of the Capillary number for the cases 1, 3, and 6 pertaining to the thermal regime.

In the thermal regime (cases 1 – 6), the cases 4, 5, and 6 adopt a special character. As their initial substrate temperatures lie in the range of 100 – 150 [°C] the presolidified droplet features very similar lens shapes with small curvature effects as shown in Figure 18. The spreading behaviour for these cases is comparable and not strongly dependent on the specific substrate shape, as can be seen by the less diverging evolution of the spread factor β in Figure 16. Attinger et. al. [4] reported in the above mentioned study similar behaviour for solder

droplets impacting on flat substrates. They presented results indicating that the spread factor β is independent of the Stefan number for Ste < 0.48, corresponding to an initial substrate temperature of 98 [°C]. Similar behaviour is observed in this study for cases 5, and 6, however, for Stefan numbers Ste < 0.33. A different finding of Attinger et. al. [4] was that both β_{max} and β_{∞} increase with decreasing Stefan number (increasing initial substrate temperature) until Ste ≈ 0.48. For the cases 4 – 6 in this study, a similar behaviour can be observed, however, with the difference that the characteristic Stefan number is smaller, Ste ≈ 0.33.

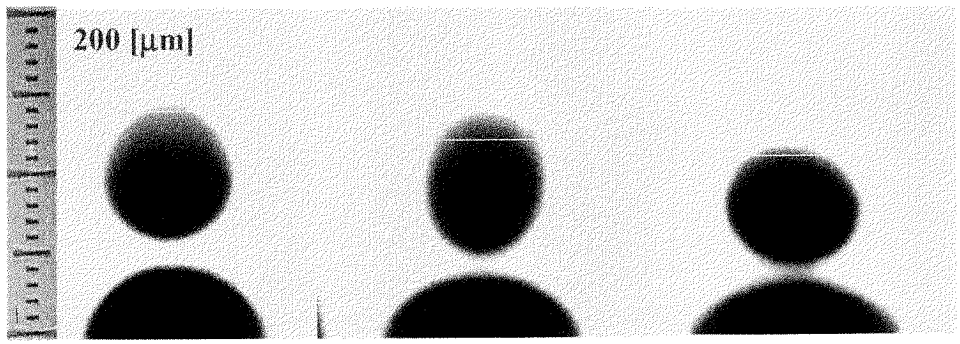

Figure 18: Shapes of the presolidified droplet prior to impact of the 2nd droplet for the cases 4, 5, and 6.

Figure 19 shows the temporal evolution of the spread factor as a function of the impact conditions (i.e. Re and We number), cases 7 – 12. The maximum spread factor β_{max} and the final spread factor β_{∞} are additionally given in Table III. As follows from inspection of Table II/III the droplets feature impact velocities in the range of 1.12 – 1.74 [m/s] with approximately the same diameter of 80 [µm]. Similarly to the thermal regime, the evolution of the spread factor between the different cases diverges shortly upon formation of contact between the impinging and the presolidified droplet. Due to the different impact velocities (impact kinetic energy) this has to be expected. Increasing the impact velocity, respectively Reynolds and Weber number, should also lead to larger values of the maximum spread factor β_{max} and the final spread factor β_{∞} [29,51,52] as in the impact of droplets on flat substrates. When comparing the values of the maximum spread factor β_{max} and the final spread factor β_{∞} for the present pile up cases of the impact regime, Figure 19/Table II, it is apparent, that this is not unequivocal. Whereas for higher impact velocities this argument holds, cases 11 and 12, at lower impact velocities, cases 7 – 10, the dependence of β_{max} on the impact velocity is

not monotonic. The maximum spread factor β_{max} and the final spread factor β_{∞} show a dependence on both the impact conditions (i.e. Re, and We number) and the substrate shape, (i.e. the shape of the presolidified droplet).

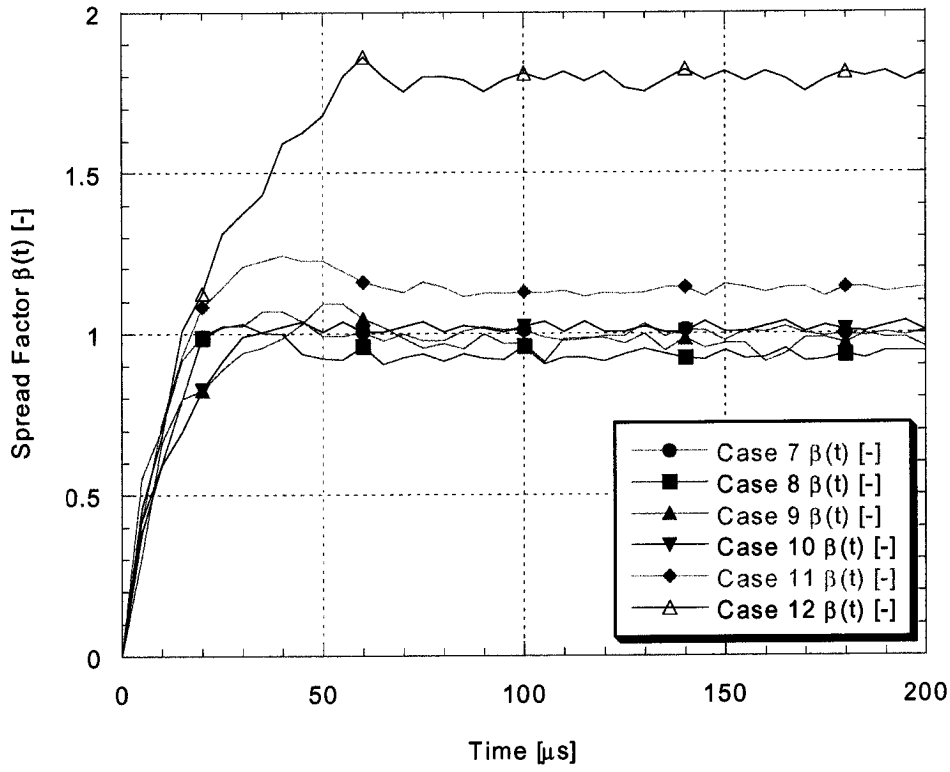

Figure 19: Spread factor $\beta(t)$ for the cases pertaining to the impact regime.

Another avenue to investigate the importance of the substrate shape on the spreading is to compare the experimentally obtained maximum spread factors β_{max} with analytical models which neglect effects of substrate curvature among other things. A large number of such approximate analytical and experimentally matched models, relating the maximum spread factor β_{max} to the predominant dimensionless numbers, exist in the literature [21,48,49,51,53]. These analytical models are derived by order of magnitude arguments scaling the effect of surface tension, viscous forces/dissipation, and some also account for solidification effects on the spreading extent. Models, deemed as predicting the maximum spread factor β_{max} reasonably well, not accounting for solidification are (Equations 14,15):

$$\frac{(\beta_{max}/1.2941)^5}{Re} + \frac{3\left[(1-\cos\psi_e)\beta_{max}^2 - 4\right]}{We} = 1 \qquad (14)$$

proposed by Bennett and Poulikakos [49]. Where ψ_e is the equilibrium contact angle.

$$\beta_{max} = \sqrt{\frac{We + 12}{3(1 - \cos\psi_a) + 4We/\sqrt{Re}}} \tag{15}$$

proposed by Pasandideh-Fard et. al. [54]. Where ψ_a is the advancing dynamic contact angle. Pasandideh-Fard et. al. [48] enhanced their model, Equation 15, to account for solidification as well:

$$\beta_{max} = \sqrt{\frac{We + 12}{3(1 - \cos\psi_a) + 4We/\sqrt{Re} + We\sqrt{(3Ste)/(4Pe)}}} \tag{16}$$

where Pe is the Peclet number (Pe = RePr). Based on the experimental baseline conditions given in Table II, these models predict the maximum spread factor β_{max} as presented in Figure 20.

As can be seen in Figure 20 the analytical models predict (for all values of the equilibrium and the advancing contact angles chosen for illustrative purposes) maximum spread factors β_{max} monotonically and slightly increasing with the Reynolds and Weber numbers. Effects of the Stefan number in Equation 16 are only weak as can be seen in Figure 20 (cases 1 – 6 correspond to values of the Reynolds and Weber number of Re ≈ 360 and We ≈ 4.1). Estimates of the equilibrium and advancing contact angles were utilized in Figure 20 for illustrative purposes because their determination is not straightforward, and in the case of the advancing contact angle, they vary with the contact line velocity [4]. Comparing the experimentally obtained values, Figure 21, with the analytical scaling laws, Figure 20, shows first that the analytical models tend to overpredict the maximum spread factor β_{max}. Much more important than this artifact is that the experimental values of β_{max} show a much more distinct trend to increase with increasing Reynolds, Weber and Stefan number than the analytical values. This further underlines the importance of the substrate shape or curvature on the spreading behaviour of an impinging droplet.

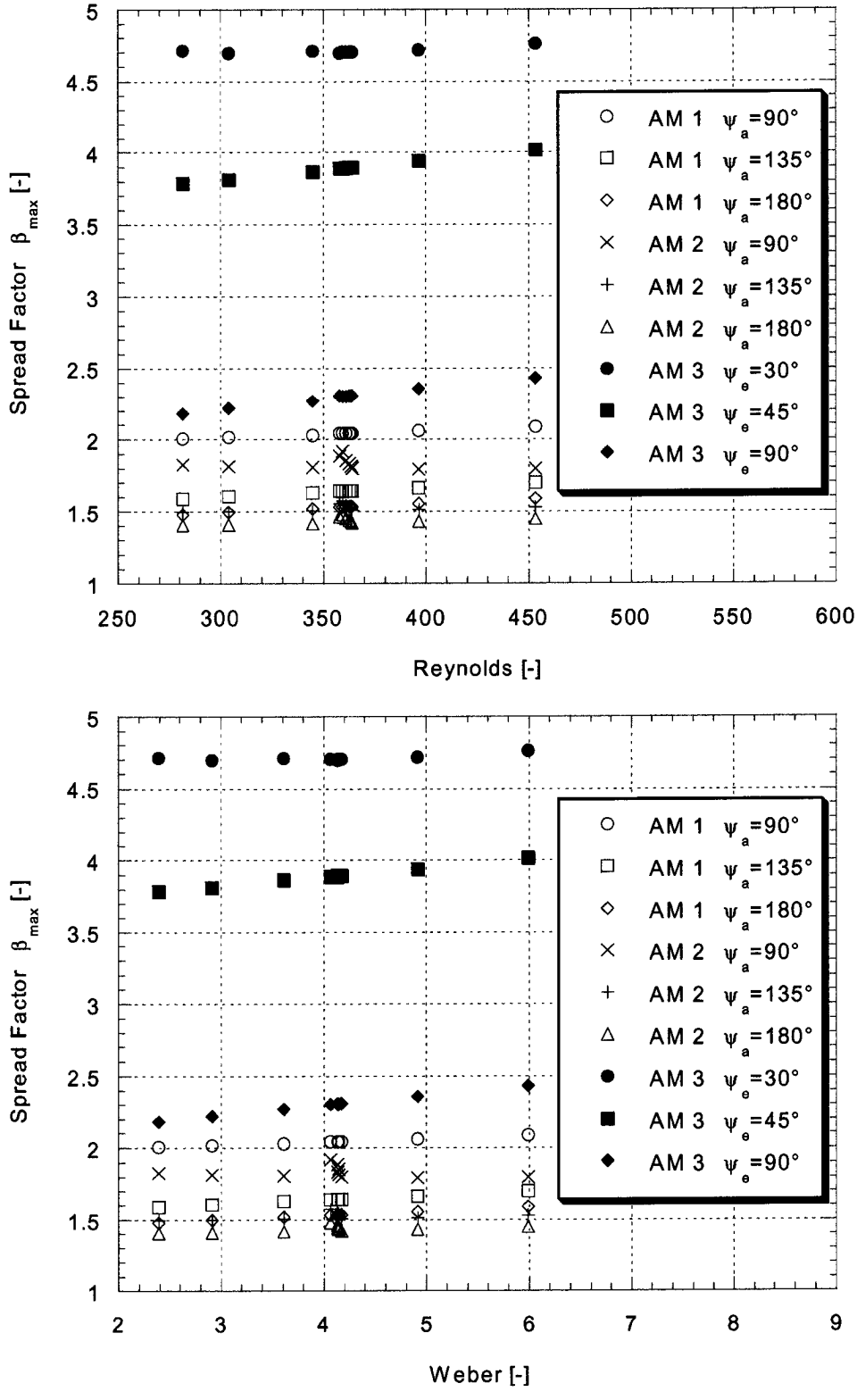

Figure 20: Maximum spread factor β_{max} in function of the Reynolds and the Weber number as predicted by analytical scaling laws. AM1 pertains to the analytical model represented by Equation 15, AM2 pertains to Equation 16, and AM3 pertains to Equation 14.

The experimentally obtained values of the maximum spread factor β_{max} as a function of the Reynolds and Weber number are shown in Figure 21.

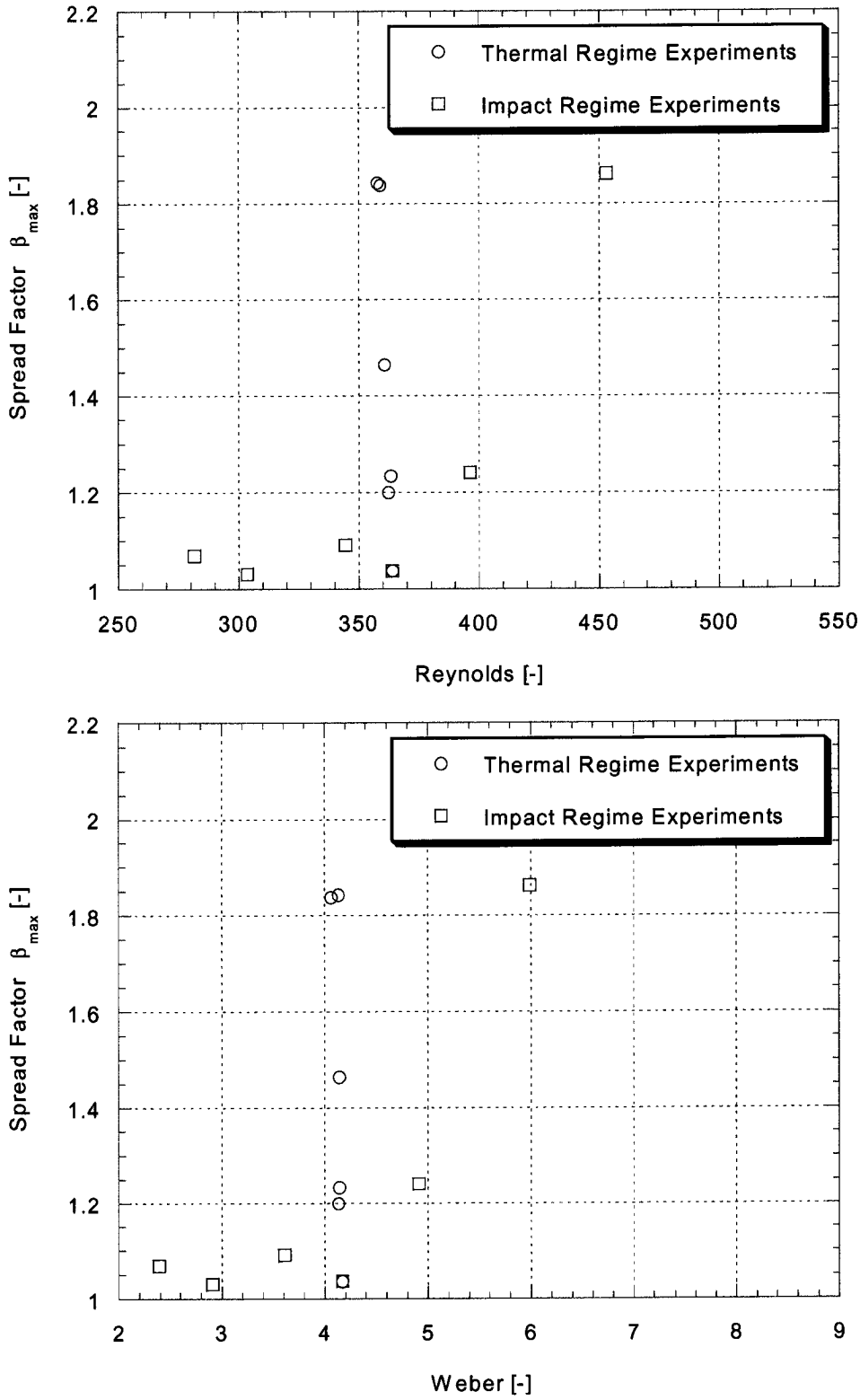

Figure 21: Maximum spread factor β_{max} in function of the Reynolds and the Weber number as determined in the experiments.

2.6.3 The Solidification Process

Solidification times are determined experimentally on a visual basis. It is commonly assumed that the motion of the impinging droplet is halted by solidification and not through viscous dissipation. The end of the droplet oscillations, as seen for instance in the pile up sequences in Figures 11 – 14, therefore indicate the termination of the solidification process. This oscillatory motion of the impinging droplet stems from the coupled interplay of the interfacial energy, and the initial kinetic impact energy. The oscillatory movement is weaky damped by viscous forces and much more important arrested by the concurrently propagating solidification front. Quantitative information on the solidification can thus be extracted from the motion of the droplet top $y_{center}(t)$. Figure 22 shows for cases 3, 6, and 9 the motion of the latter.

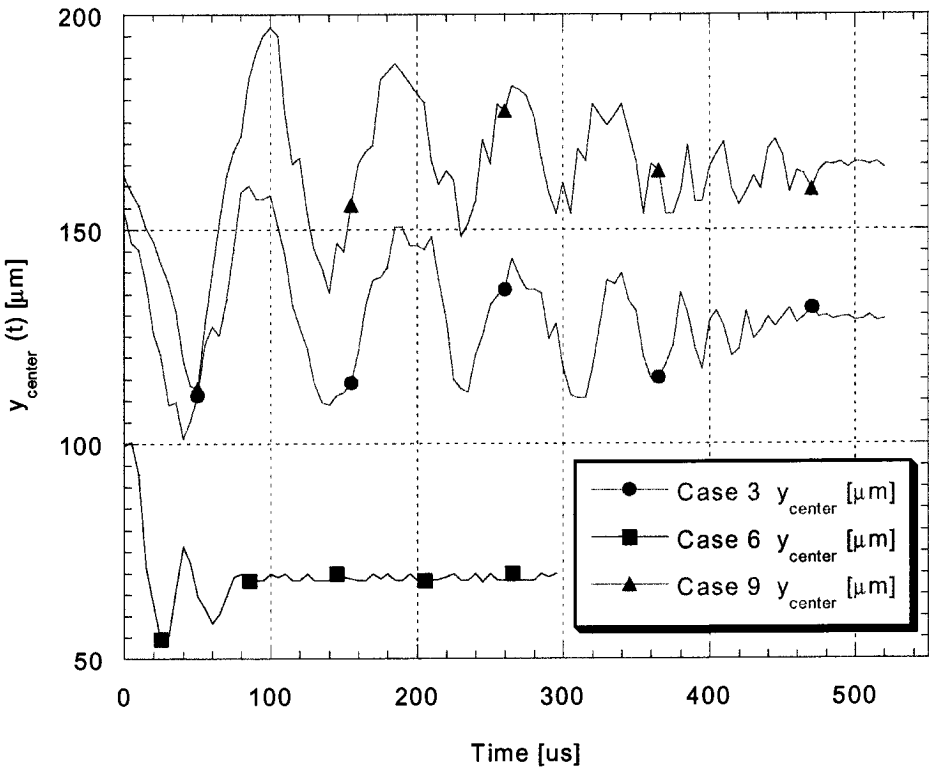

Figure 22: Damped oscillatory motion of the droplet top $y_{center}(t)$ for the cases 3, 6, and 9.

The solidification time t_s is thereby defined as the instance where the height $y_{center}(t)$ of the pile up structure remains constant (within ± 2% of the initial droplet diameter) for a time length more than half a period of its oscillations [4]. Table IV shows a compilation of the experimentally determined solidification times t_s for all experimental cases. It also includes the experimentally determined time $t_{\beta max}$ needed to reach the maximum spread factor β_{max}.

Case	1	2	3	4	5	6	7	8	9	10	11	12
t_s [μs]	440	460	475	445	270	90	450	425	480	440	500	435
$t_{\beta max}$ [μs]	45	73	74	42	72	58	50	44	74	45	70	68

Table IV: Experimentally determined solidification times t_s, and $t_{\beta max}$.

The error in determining the above solidification times is estimated to be –10/+30 [μs]. This estimate is based upon the following reasoning and on an experimental time resolution of 5 [μs] in the visualization procedure. The apparent termination of the oscillation motion can be located with an accuracy of approximately ±2 frames of the visualized pile up sequence, thus ±10 [μs]. Due to the small amplitudes of the oscillations just prior to complete solidification the final solidification time is tendentially assumed too early. Therefore, the upper limit is extended to 6 frames, thus +30 [μs].

From inspection of the solidification times measured by Attinger et. al. [4] on approximately identical droplets impacting on flat substrates and at approximately the same temperatures it is apparent that solidification times during a pile up are about 30% larger. Furthermore, it was reported that the solidification time featured a non-monotonic dependence on the Stefan number showing a single minimum at about 90 [°C] in a thermal regime ranging from 48 – 135 [°C]. The opposite evolution of the solidification times with decreasing Stefan number is observed in the present thermal regime as shown in Figure 23.

It has to be emphasized, that a difference in the solidification process during a pile up has to be expected from the outset since the geometrical shape of the substrate differs markedly from a flat substrate. A number of analytical scaling laws for the solidification time t_s, both for droplets impacting on flat substrates as well as for columnar deposition of droplets (multiple pile up), scaling mostly the effect of superheat, geometry, thermal properties, inertia and surface tension on the solidification time, are given in the literature:

$$t_s = \frac{Pr}{OhSte} t_{\beta max} \approx f\left(Pr, Oh, Ste, t_{\beta max}\right) \qquad (17)$$

proposed by Schiaffino and Sonin [50] for impacts on flat substrates. Equation 17 is just a rearrangement of Equation 12.

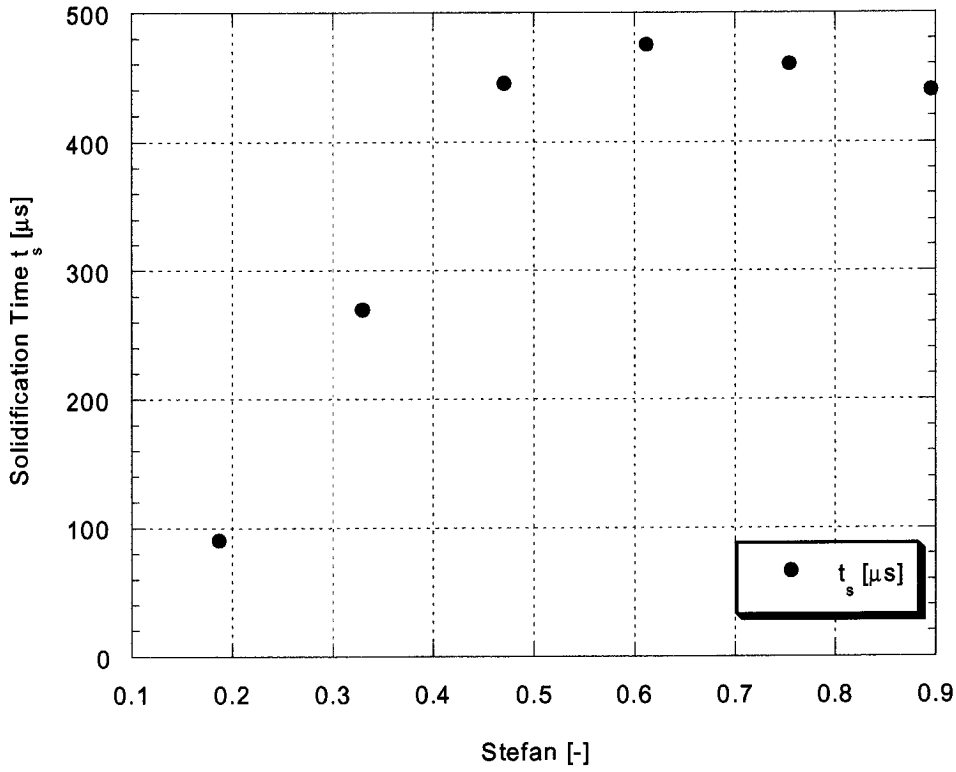

Figure 23: Solidification times in function of the Stefan number for the thermal regime, cases 1 – 6.

The following scaling law, also by Schiaffino and Sonin [50], is derived for impacts on flat substrates as well.

$$t_s = \frac{d_0^2}{4\kappa}\frac{1}{Ste} \approx f(Ste, d_0) \tag{18}$$

where κ is the thermal diffusivity of the droplet material. Both models, Equation 17 and 18, neglect thermal contact resistance. Equation 19, which was proposed by Gao and Sonin [5], is derived on the basis that the droplet impacts on a pillar/column formed by droplets of the same material. Thus, the model is based on the fin heat transfer equation for an infinitely long columnar fin, again neglecting thermal contact resistance and, more importantly, the entire complex fluid dynamics:

$$t_s = \frac{4\pi}{9}\frac{d_0^2}{4\kappa}\left(\frac{d_0}{d_p}\right)^4\left(\frac{1}{Ste}+SHP\right)^2 \approx f\left(Ste, SHP, \frac{d_0}{d_p}, d_0\right) \tag{19}$$

where d_p is the diameter of the columnar fin and SHP is the superheat parameter as defined in section 1.2. Since in the present study the height of the pile up structure is finite the above model, Equation 19, is enhanced by a factor taking the finite ratio of the masses of the droplets and the fin (presolidified droplet) into account:

$$t_s = \frac{4\pi}{9}\frac{d_0^2}{4\kappa}\left(\frac{d_0}{d_p}\right)^4\left(\frac{1}{Ste}+SHP\right)^2\left(\frac{d_0}{h_p}\right)^3 \approx f\left(Ste, SHP, \frac{d_0}{d_p}, \frac{d_0}{h_p}, d_0\right) \qquad (20)$$

where h_p is the height of the fin (presolidified droplet). The value of d_p in Equations 19 and 20 is in the present study determined as the mean of the final solidified radius of the impinging and the presolidified droplet. Figure 24 compares the above analytical scaling laws to the experimentally determined solidification times t_s for the impact regime (cases 7 – 12).

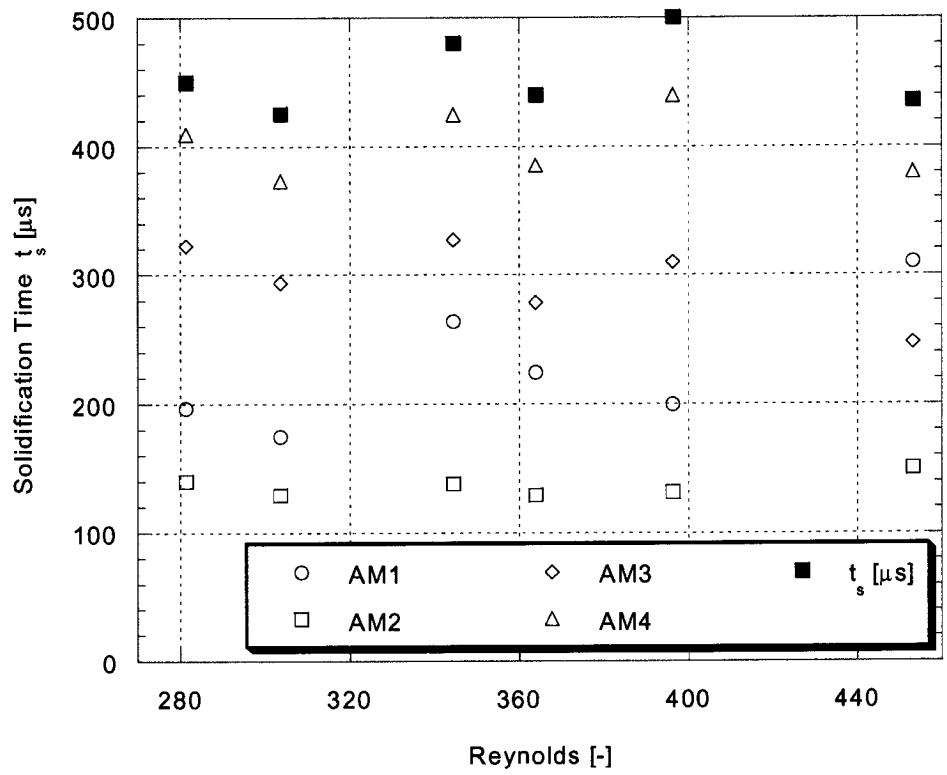

Figure 24: Comparison of the experimentally determined solidification times for the impact regime (cases 7 – 12). AM1 pertains to the analytical model represented by Equation 17, AM2 pertains to Equation 18, AM3 pertains to Equation 19, and AM4 pertains to Equation 20.

All above presented models/scaling laws underpredict solidification times. This can be explained by the fact that none of the models take neither thermal contact resistance nor the complex fluid dynamics into account. It has to be emphasized, that for the impact regime only the impact velocities vary considerably. The droplet diameter varies only very slightly and the thermal properties, the Prandtl, and the Stefan number do not vary at all. Variations of the Ohnesorge number are so small that they can be neglected as follows from inspection of Table II. The above analytical scaling laws, Equations 17 – 20, are therefore most of all functions of the following parameters: the time to reach the maximum spread factor, Equation 17, the droplet diameter, Equation 18, the droplet diameter and the diameter of the presolidified droplet, Equation 19, and the droplet diameter, the diameter of the presolidified droplet and the height of the presolidified droplet, Equation 20. As shown in Figure 24, the solidification time is not correlated to the time to reach the maximum spread factor $t_{\beta max}$, Equation 17. Taking only the droplet diameter into account, Equation 18, is not sufficient to estimate the solidification times. Taking the fin nature of the substrate into account (in a strongly simplified manner), Equations 19 and 20, give the best estimates of the solidification times, both concerning the order of magnitude as well as the trend. Accounting for the finite fin height h_p, Equation 20, yields apparently the best estimate. Interestingly enough, in the present impact regime, the initial impact velocity has no influence on the final solidification time as also follows from inspection of Figure 24. There is no correlation between the experimentally determined solidification times and the Reynolds number. The solidification time seems to depend, for cases with constant Stefan number and superheat parameter, mostly on geometrical parameters such as the initial droplet diameter, the "fin" diameter, and the height of the latter but not on the impact velocity. This is in contrast to findings by Haferl et. al. [55] on solder droplets impinging on a flat substrate in approximately the same impact and temperature regime.

The same analytical scaling laws, Equation 17 – 20, applied to the thermal regime, cases 1 – 6, is shown in Figure 25. The parameters varying in the thermal regime are most of all the Stefan number, the superheat parameter, and the time needed to reach the maximum spread factor $t_{\beta max}$. Variations in the impact velocity and the initial droplet diameter are only small. Furthermore, important for Equations 19 and 20, is the fact that the height h_p, and the diameter d_p of the presolidified droplet vary. All above models propose an inverse proportionality of the Stefan number on the solidification time. Since both Equations 17 and 18 are dominated by this inverse proportionality, both scaling laws show a trend that is opposite than the experimentally determined solidification times. Equations 19 and 20, which

account for the fin-type nature of the substrate, show a good matching at high Stefan numbers (low initial substrate temperatures). With decreasing Stefan number the inverse proportionality becomes dominant again and the analytical trend does not agree with the experimental findings.

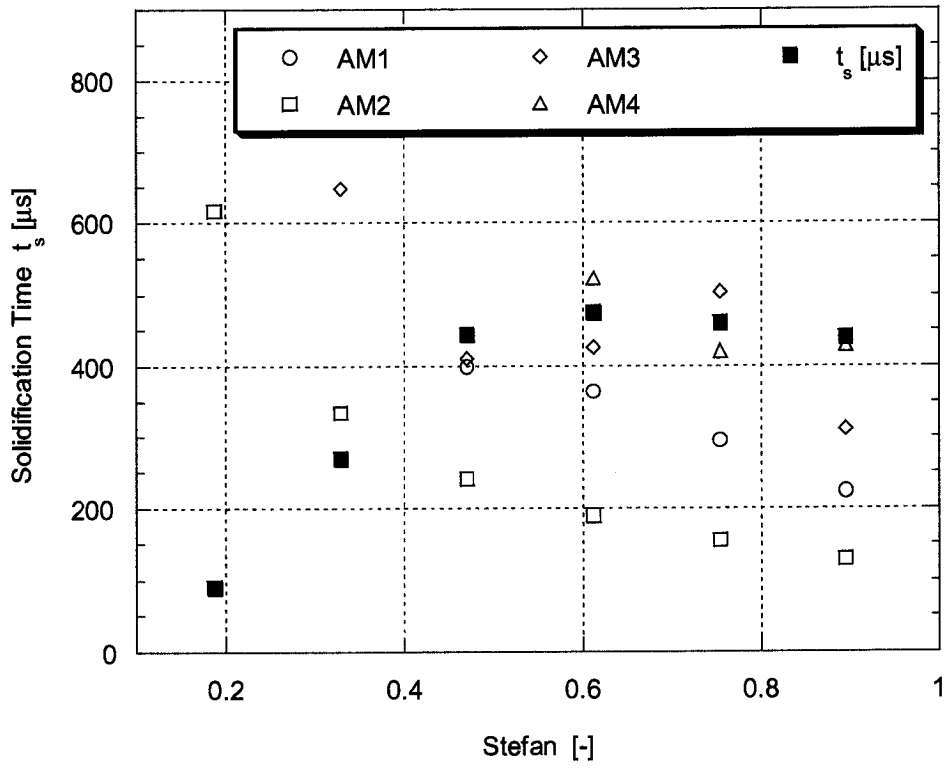

Figure 25: Comparison of the experimentally determined solidification times for the thermal regime (cases 1 – 6). AM1 pertains to the analytical model represented by Equation 17, AM2 pertains to Equation 18, AM3 pertains to Equation 19, and AM4 pertains to Equation 20. Note: Data for all analytical models, except for AM2, exceed at low Stefan number the temporal range given in this Figure.

For the analytical scaling law described by Equation 19 this becomes apparent for a Stefan number Ste < 0.47 (cases 5, 6), correspondingly for an initial substrate temperature $T_{2,0} > 100$ [°C]. On the other hand, for the analytical scaling law described by Equation 20 this becomes already apparent for a Stefan number Ste < 0.612 (cases 4 – 6)), correspondingly for an initial substrate temperature $T_{2,0} > 75$ [°C]. Inspection of Equation 19 shows that the term containing the inverse of the Stefan number is no more sufficiently balanced by the geometry term containing the droplet and the fin diameter. In other words, the Stefan number decreases faster

than the ratio of the droplet and the fin diameter. This also holds for Equation 20. However, in addition to this fact, the ratio of the droplet diameter to the height of the presolidified droplet becomes large and reduces the accuracy of the estimate for the solidification time. Thus, for low Stefan numbers analytical models neither for flat nor for fin-like substrates give a good estimate of the final solidification time. For high or moderate Stefan numbers, analytical models based on the fin heat transfer equation give a reasonable estimate of the final solidification time. As follows from inspection of Figure 18, the presolidified droplets of the cases 4 – 6 represent special cases. A description of these substrate shapes as either a flat-type substrate or a one dimensional fin-type substrate is clearly inaccurate.

The experimental finding that droplets impacting with approximately the same initial velocity and diameter solidify faster with decreasing Stefan number (decreasing the temperature difference between the warm droplet and the colder substrate) as presented in Figure 23, was initially surprising indeed. This behaviour (the corresponding trend) was rationally elucidated using a simple analytical model accounting for the physics involved. Assuming that the main resistance to solidification of the impinging droplet is the conduction of heat through the presolidified droplet, the following approximate model is postulated. The heat transfer from the impinging droplet to the much larger wafer substrate is asssumed to be of the following order of magnitude:

$$\dot{Q} = k_{eff} A_{t,c} \frac{T_{1,0} - T_{2,0}}{h_p} \tag{21}$$

where k_{eff} is an effective thermal conductivity of the presolidified droplet, $A_{t,c}$ is the area of the interface between the presolidified droplet and the wafer substrate, and h_p is the height of the presolidified droplet. The initial thermal energy of the impinging droplet can be expressed as follows:

$$E = \frac{\rho \pi d_0^3}{6} \left[c_{pl,0} \left(T_{1,0} - T_m \right) + L \right] \tag{22}$$

The solidification time can then be expressed as follows:

$$t_s = \frac{E}{\dot{Q}} = \frac{\rho \pi d_0^3 \left[c_{pl,0} \left(T_{1,0} - T_m \right) + L \right] \cdot h_p}{6 k_{eff} A_{t,c} \left(T_{1,0} - T_{2,0} \right)} \tag{23}$$

Inspection of Equation 23 clearly shows that while increasing the substrate temperature would *increase* the solidification time, there is the effect of other parameters in Equation 23, which simultaneously vary because they depend on the substrate temperature, that needs to be accounted for at the same time. An increase in the substrate temperature decreases h_p and increases $A_{t,c}$. Both these variations would tend to *reduce* the solidification time. Hence, a non monotonic behaviour of the solidification time on the substrate temperature is to be expected. Based on the values for the thermal regime (cases 1 – 6), the dependence of the solidification time on the Stefan number, as postulated by Equation 23 shows the trend plotted in Figure 26. Here, the analytical results are only meant to indicate the non-monotonic trend featuring a local maximum and explaining the surprising experimental result. The effective thermal conductivity in the model was selected arbitrarily so that the analytical result for Ste = 0.9 matched the experimental result. The so determined value of the effective thermal conductivity is thereby k_{eff} = 20.5 [W/mK]. Accounting for thermal contact resistance between the presolidified droplet and the wafer substrate this value seems reasonable compared to the thermal conductivity of solid solder (k = 48 [W/mK]).

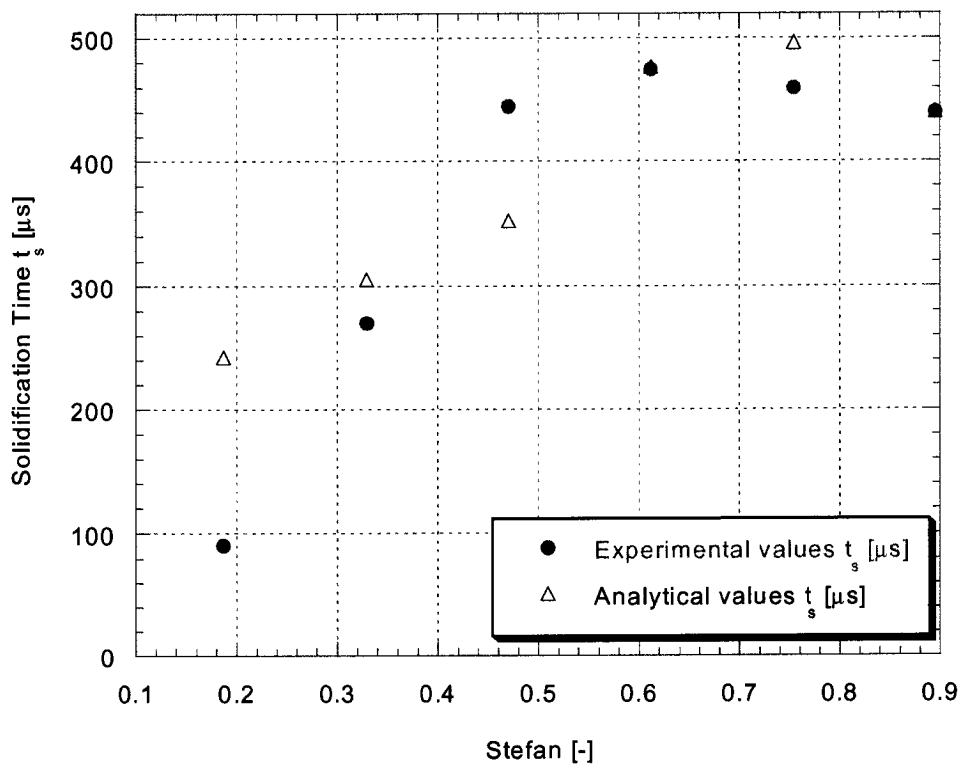

Figure 26: Experimentally determined solidification times compared to analytical values in function of the Stefan number.

2.6.4 Summary

The experimental results presented above, point to a noticeable influence of the substrate (presolidified droplet) shape on both the spreading and the solidification process occurring during a microdroplet pile up. The spreading behaviour seems to be influenced by the specific surface curvature of the presolidified droplet when comparing it to the spreading behaviour of droplets impinging on flat substrates. However, it is not possible to quantify the influence of the substrate shape or curvature on spreading with a simple model or correlation. This is due to the fact that a rich pallet of shapes of the presolidified droplet exist depending on the process parameters. These shapes affect the transport phenomena in the second droplet markedly and cannot be summarily categorized.

Accounting for a fin-type structure of the presolidified droplet yields better results (but only in an approximate sense) in the modeling prediction of the solidification time. Interesting is the fact that the influence of the initial impact velocity (within the parametric domain of interest to this study) on the solidification time is negligible as compared to the geometrical features of the presolidified droplet. The shape of the latter, and the corresponding fin type nature of the substrate causes a time lag in the solidification process as compared to the impact of a droplet on a flat, semi-infinite substrate. In all, it is clear that a thorough (and not a simple) modeling of the pile up process, including the complex fluid dynamics as well as contact resistance phenomena, is necessary in order to quantify the influence of the various intertwined physical phenomena and provide the needed engineering predictions with acceptable accuracy and reliability. The construction and solution of such a model is the main goal of the remainder of this thesis.

3. Mathematical Modeling of the Governing Equations

3.1 Outline of the Computational Domain

The computational domain of the pile up problem is shown in Figure 27. Since the problem considered is assumed axisymmetric only half of the cross-section has to be taken into account. The entire domain is divided into four regions. For the solution of the fluid mechanics equations, only the domain of the impacting droplet as well as the boundary of the presolidified droplet are considered. The solution of the energy equation covers all four regions in Figure 27. The heat transfer solution method contains special features necessitated by the two indicated interfaces, which will be discussed at length in section 3.3.3.

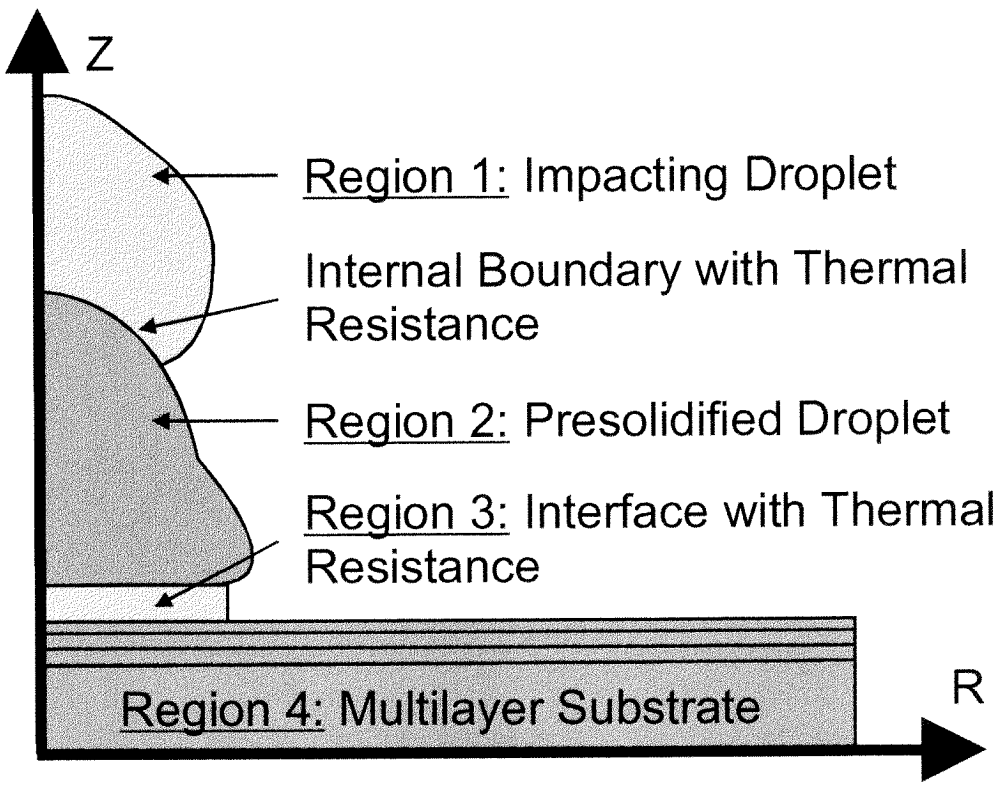

Figure 27: Schematic of the computational domain.

The multi-layer substrate is "manufactured" numerically to duplicate the gold wafer substrate employed in the experiments and thus consists of four sub-layers (i.e. gold, TiW, silicon oxide, silicon). The length scales in the computational domain are equal to the experimental cases. The substrate width is truncated at twice the droplet diameter measured from the line of symmetry. It has been shown that this is sufficient for the thermal solution [13,19,28].

3.2 Fluid Mechanics

3.2.1 Governing Equations for the Fluid Flow

The pile up is modeled as an unsteady, viscous, incompressible flow with constant density and constant dynamic viscosity. Thus, the flow is governed by the following Navier-Stokes equations, written in vector notation, and in Lagrangian form [56].

Continuity equation: $$\rho\nabla\cdot(\vec{u})=0 \tag{24}$$

Momentum equation: $$\rho\partial_t u_i+\nabla p-\mu\Delta\vec{u}-\rho\vec{g}=0,\ i\in\{r,z,\theta\} \tag{25}$$

where $\nabla\cdot,\nabla,\Delta$ denote, respectively the divergence, gradient, and the Laplacian operator, ∂_i denotes the derivative with respect to the i-th variable, r, z, and θ are, respectively the radial, axial, and azimuthal coordinates, ρ is the fluid density, $\vec{u}$ the velocity vector, $\vec{g}=(0,-g,0)^T$ the body force due to gravity, t the time, p the pressure, and μ the dynamic viscosity.
Employing the Lagrangian formulation of the Navier-Stokes equation has the advantage that no convective terms are present in the equations. Furthermore, it facilitates the handling of the free surface since boundary elements and nodes representing the free-surface are always identifiable and do not have to be determined using a front tracking scheme. Nevertheless, the solution of the Navier-Stokes equations in primitive variables is somewhat intricate because of the lack of an independent equation for the pressure variable, whose gradient influences each of the three momentum equations. There are a number of pressure solution methods at hand imposing a divergence-free velocity field [57]. One method, proposed by Chorin [58], uses the concept of artificial compressibility in order to solve the continuity equation. In order to apply the artificial compressibility method the continuity equation is re-written in compressible and axisymmetric form:

$$\partial_t\rho+\rho\left[\frac{1}{r}\partial_r(ru_r)+\partial_z u_z\right]=0 \tag{26}$$

The temporal derivative of the density term in the compressible continuity equation is replaced by the following thermodynamic expression [59], relating the density to the pressure by the speed of sound, c, in the fluid:

$$c^2 = \left(\partial_\rho p\right)\Big|_S \tag{27}$$

The appearance of the entropy S as the property held constant is the result of the fact that acoustic waves are assumed as reversible and adiabatic processes. This transformation results in a pseudo-continuity equation which contains the pressure variable explicitly.

$$\frac{1}{c^2}\partial_t p + \rho \nabla \cdot \vec{u} = 0 \tag{28}$$

The isentropic speed of sound c in Equation 28 can also be considered as an artificial compressibility parameter. The value of the latter is key for the performance of the method regarding convergence speed, accuracy and stability of the numerical scheme. It can be related to the speed of the pressure waves in the fluid stemming from the hyperbolic character of the modified equations. Clearly, the larger the value of the artificial compressibility parameter c, the more "incompressible" the equations; however, large values of c make the equations numerically very stiff with the associated problems coupled with numerical stiffness.

3.2.2 Initial and Boundary Conditions for the Fluid Flow

The initial and boundary conditions of the problem of an impacting droplet are as follows:

$$t = 0: \qquad u_r = 0,\ u_z = -u_{z0},\ p = p_0 + \frac{2\gamma}{r_0} \tag{29}$$

$$r = 0: \qquad u_r = 0,\ \partial_r u_z = 0 \tag{30}$$

$$\wp(s): \qquad u_r = 0,\ u_z = 0 \tag{31}$$

where u_{z0} is the pre-impact droplet velocity, p_0 a reference pressure (atmospheric), γ is the surface-tension coefficient of the liquid, and $\wp(s)$ describes the surface of the substrate with respect to the arc length s.

At the free surface of the impacting droplet the following balance between the viscous and the surface-tension stresses has to be satisfied [60]:

$$\tilde{\sigma} \cdot \vec{n} = -(2\gamma H + p_0) \cdot \vec{n} \tag{32}$$

where the surface tension coefficient γ is assumed constant, $\vec{n}$ is the unit normal vector, and H is the mean surface curvature defined as [61]:

$$2H = \frac{1}{R_1} + \frac{1}{R_2} \tag{33}$$

where the two radii of curvature R_1, R_2 define the curvature of the droplet surface. The latter is being calculated using a non-rational B-spline curve interpolating the free surface nodes of the fluid droplet as will be described in section 3.2.7.

3.2.3 The Boundary Condition at the Dynamic Contact Line

The treatment of the contact line needs special attention. Assuming validity of the conventional hydrodynamic no-slip boundary condition over the entire liquid-solid interface, including the contact line, leads to a force singularity at the contact line as has been shown previously by several different authors [62,63]. The modeling of the fluid behaviour in the vicinity of the contact line is therefore a delicate issue. By replacing the no-slip boundary condition by one of the various slip models postulated in the literature [21,23,64], the mathematical difficulties associated with the singularity at the contact line can be circumvented. However, they are only ad-hoc mathematical models of the physics occurring at the contact line. The method of choice in this investigation for handling the movement of the contact line numerically is to impose the Navier-Slip condition at the contact line. This particular boundary condition differs from the classical and inappropriate no-slip condition by the property that it allows the contact line to attain a velocity which is proportional to the strain rate in the vicinity of the contact-line. Thus, the Navier-slip condition is formulated as follows:

$$\vec{n} \cdot \tilde{\sigma} \cdot \vec{t} = \frac{1}{\varepsilon} \cdot \vec{u} \cdot \vec{t} \tag{34}$$

where $\vec{n}$, $\vec{t}$ are the outward directed unit normal vector and unit tangent vector to the substrate surface described by $\wp(s)$, and ε is the slip parameter, which controls the amount of slippage and has to be chosen ad hoc. Thus, at the locus of the contact line Equation 34 is applied as the appropriate boundary condition along with the no-penetration condition.

3.2.4 Dimensionless Equations, Initial and Boundary Conditions

By introducing the following dimensionless parameters the mathematical model described above is cast in dimensionless form:

$$R=\frac{r}{d_0}, Z=\frac{z}{d_0}, U_R=\frac{u_r}{u_{z0}}, U_Z=\frac{u_z}{u_{z0}},$$

$$\tau=\frac{t}{d_0/u_{z0}}, \overline{H}=\frac{H}{1/d_0}, P=\frac{p-p_0}{\rho u_{z0}^2}, \qquad (35)$$

$$\overline{\sigma}_{ij}=\left(\sigma_{ij}+\delta_{ij}p_0\right)\Big/\rho u_{z0}^2$$

where d_0 is the pre-impact droplet diameter, and $\overline{\sigma}_{ij}$ corresponds to the dimensionless stress components. The symbol δ_{ij} is the Kronecker delta which equals unity if i = j, and zero if i ≠ j. The dimensionless mathematical equations are then given by:

Continuity equation:
$$\partial_\tau P+\frac{1}{Ma^2}\left(\frac{1}{R}\partial_R\left(RU_R\right)+\partial_Z U_Z\right)=0 \qquad (36)$$

Momentum equation in radial direction:
$$\partial_\tau U_R-\frac{1}{R}\partial_R\left(R\overline{\sigma}_{RR}\right)-\partial_Z\overline{\sigma}_{RZ}+\frac{\overline{\sigma}_{\theta\theta}}{R}=0 \qquad (37)$$

Momentum equation in axial direction:
$$\partial_\tau U_Z-\frac{1}{R}\partial_R\left(R\overline{\sigma}_{RZ}\right)-\partial_Z\overline{\sigma}_{ZZ}-\frac{1}{Fr}=0 \qquad (38)$$

The dimensionless stress components $\overline{\sigma}_{ij}$ are given by:

$$\overline{\sigma}_{RR} = -P + \frac{2}{Re}\partial_R U_R \tag{39}$$

$$\overline{\sigma}_{ZZ} = -P + \frac{2}{Re}\partial_Z U_Z \tag{40}$$

$$\overline{\sigma}_{\theta\theta} = -P + \frac{2}{Re}\frac{U_R}{R} \tag{41}$$

$$\overline{\sigma}_{RZ} = \frac{1}{Re}(\partial_Z U_R + \partial_R U_Z) \tag{42}$$

The dimensionless initial and boundary conditions are respectively:

$$\tau = 0: \qquad U_R = 0,\ U_Z = -1,\ P = \frac{4}{We} \tag{43}$$

$$R = 0: \qquad U_R = 0,\ \partial_R U_Z = 0 \tag{44}$$

$$\wp(s): \qquad U_R = 0,\ U_Z = 0, \tag{45}$$

The dimensionless Navier–Slip boundary condition can be formulated as follows:

$$\overline{\sigma}_{RR} n_R + \overline{\sigma}_{RZ} n_Z = \frac{1}{\varepsilon} U_R \tag{46}$$

$$\overline{\sigma}_{RZ} n_R + \overline{\sigma}_{ZZ} n_Z = \frac{1}{\varepsilon} U_Z \tag{47}$$

The stress balance at the free surface is expressed as:

$$\overline{\sigma}_{RR} n_R + \overline{\sigma}_{RZ} n_Z = -2\frac{\overline{H}}{We} n_R \tag{48}$$

$$\overline{\sigma}_{RZ}n_R + \overline{\sigma}_{ZZ}n_Z = -2\frac{\overline{H}}{We}n_Z \tag{49}$$

The definitions of the dimensionless groups created in the course of the non-dimensionalization process are already given in section 1 (Equations 1 - 10)

3.2.5 Galerkin Finite Element Formulation

The preceding mathematical model of the fluid flow is spatially discretized using the finite element method (FEM). A weak statement, formed for the artificial compressibility conservation law system, Equations 36 - 38, is [65,66]:

$$\int_{\Omega} w(\vec{\chi})F(\Xi)d\Omega = 0 \tag{50}$$

for all test functions $w(\vec{\chi})$, where $\vec{\chi} = \{r, z, \theta\}^T$, and where $\Xi = \Xi(\vec{\chi}, t) \equiv \{p, u_i\}^T$ is the state variable, $\Omega \in R^n$ is the n-dimensional solution domain, and the superscript T denotes the transpose. The function $F(\Xi)$ in Equation 50 pertains to Equations 36 – 38. A finite element algorithm utilizes a discretization Ω^h of Ω to construct the corresponding approximate solution $\Xi^h(\vec{\chi}, t)$. Therefore,

$$\Xi(\vec{\chi}, t) \cong \Xi^h(\vec{\chi}, t) = \bigcup_{e \varepsilon \Omega^h} \sum_{i=1}^{K} N_i(\vec{\chi})\Xi_i(t) = \bigcup_{e \varepsilon \Omega^h} \{N_k(\vec{\chi})\}^T \{\Xi(t)\}_e \tag{51}$$

where N_i is a trial space basis function, K is the number of nodes per element, e denotes an element, and Ξ_i is the nodal state variable. Furthermore, $\{\Xi(t)\}_e$ is the column matrix notation for the nodal state variable array for a finite element e, $\{N_k(\vec{\chi})\}$ is the trial function basis set of degree k, and $\bigcup_e$ signifies the union over all elements of the considered domain. It is assumed that the spatial and the temporal dependency is separable, with the latter remaining within the nodal variable set $\{\Xi(t)\}$. The finite element method is thereby applied on the spatial variables only. Temporal discretization is treated separately based on a finite

difference method as will be described in section 3.2.8. By applying the Green-Gauss theorem [65,66], the resultant form of Equation 50 exposes surface integrals for enforcement of the above identified boundary conditions. Thus, for the i-th momentum equation the created surface integral yields

$$\oint_{\partial\Omega} w(\vec{\chi})(u_j n_j)u_i d\Gamma - \oint_{\partial\Omega} w(\vec{\chi})\partial_n u_i d\Gamma \qquad i,j \in \{r, z\} \qquad (52)$$

where $\partial\Omega$ symbolizes the boundary of the computational domain Ω. In the Galerkin-FEM the weak statement test function set w_i is defined identical to the trial function set. Therefore, on a finite element e, $w_i(\vec{\chi}) = N_i(\vec{\chi})$.

3.2.6 Elements, Mesh Generation, Remeshing, and Interpolation

Triangular linear elements are chosen to discretize the computational domain. To this end, a commercial mesh generator is used to mesh the computational domain (Hypermesh®, marketed by Altair Engineering). The mesh generator employs Delaunay tesselation given the surface distribution of points.

As already mentioned above the mathematical model of the pile up employs the Lagrangian formulation of the Navier-Stokes equations. This implies that the mesh nodes in the fluid domain are moving spatially in time. As the solution of the pile up advances in time the mesh is being deformed. Thus, in order to keep a good mesh quality and not to let numerical errors occur due to excessive element distortion, the mesh has to be renewed after a number of time steps. A mesh quality criterion thereby controls the remeshing activity. If the smallest angle in an element decreases below 20 [deg], a remeshing operation is induced. The angle is thereby set arbitrarily.

After a remeshing operation the values of the nodal state variables $\{\Psi\}_e$ have to be interpolated between the old mesh and the newly generated mesh. This interpolation proceeds in a node-by-node fashion using simple linear interpolation based on the element trial functions on the old mesh.

3.2.7 Free Surface Representation – Non-Rational B-Splines

The calculation of free-surface flow, accounting for surface tension and the presence of a solid substrate as an obstacle to the fluid propagation, requires accurate information on some surface properties. As outlined in the derivation of the governing conservation law system the incorporation of surface tension in the model of the fluid flow requires the calculation of the free surface curvature, Equation 33. Since the chosen elements for the numerical solution of the governing equations are of first order and thus not suited for the calculation of the curvature the needed surface information has to be enhanced. This is accomplished by interpolating the nodal points defining the free surface with a non-rational B-spline curve of order higher than unity. The radii of curvature, as defined in Equation 33, can be related to the derivative of the tangent vector by applying the first Frenet formula [61]:

$$-\frac{1}{R_i}\vec{n} = \partial_s \vec{t} \qquad i = 1, 2 \tag{53}$$

where the derivative of the tangent vector is with respect to the arc length of the curve.
A further important information is the position of the free-surface nodal points relative to the substrate. This is of considerable interest since the moving free-surface nodal points are not allowed to cross into the substrate region in order not to violate the no-penetration condition. Therefore, the respective distances of the nodal points from the substrate have to be tracked. This can easily be done using again a non-rational B-spline curve representation of the substrate surface. According to [67] a j-th degree B-spline curve is defined by:

$$\vec{B}(u) = \sum_{i=0}^{n} B_{i,j}(s)\vec{F}_i\,, \qquad a \le s \le b \tag{54}$$

where the $\{F_i\}$ are the control points, and the $\{B_{i,j}(s)\}$ are the j-th degree B-spline basis functions defined as:

$$B_{i,0}(s) = \begin{cases} 1 \rightarrow s_i \le s < s_{i+1} \\ 0 \rightarrow \text{otherwise} \end{cases} \tag{55}$$

$$B_{i,j}(s) = \frac{s - s_i}{s_{i+j} - s_i} B_{i,j-1}(s) + \frac{s_{i+j+1} - s}{s_{i+j+1} - s_{i+1}} B_{i+1,j-1}(s) \tag{56}$$

The control points $\{F_i\}$ have to be determined by solving the (n+1)×(n+1) system of linear equations defined by:

$$\{\Phi_k\} = \{B(\bar{s}_k)\} = \sum_{i=0}^{n} B_{i,j}(\bar{s}_k)\{F_i\}, \qquad k = 0,\ldots,n \tag{57}$$

where (n+1) is the number of free-surface nodal points, $\{\Phi_k\}$ is the given set of the latter, and the $\bar{s}_k$ are assigned arc-length parameter values for each element of $\{\Phi_k\}$ determined by the following expression:

$$\bar{s}_k = \bar{s}_{k-1} + \frac{\sqrt{\left|\vec{\Phi}_k - \vec{\Phi}_{k-1}\right|}}{\sum_{k=1}^{n} \sqrt{\left|\vec{\Phi}_k - \vec{\Phi}_{k-1}\right|}}, \qquad k = 1,\ldots,n\text{-}1 \tag{58}$$

where the arc lengths of the starting and the ending point are defined as: $\bar{s}_0 = 0, \bar{s}_n = 1$.

3.2.8 Solution Method

Time integration of Equations 36 – 38 is accomplished using a backward Euler finite difference scheme [57]. The coupling of fluid node locations and of the mass and momentum conservation equations is attained by employing a method proposed by Bach and Hassager [68]. Nodal locations are evaluated as follows:

$$R^{\tau+\Delta\tau} = R^{\tau} + \frac{1}{2}\left(U_R^{\tau} + U_R^{\tau+\Delta\tau}\right) \tag{59}$$

$$Z^{\tau+\Delta\tau} = Z^{\tau} + \frac{1}{2}\left(U_Z^{\tau} + U_Z^{\tau+\Delta\tau}\right) \tag{60}$$

The calculation of a time step $\Delta\tau$ features the following steps:

1. Using the velocities at time step τ as initial guesses for the velocities at time step $\tau+\Delta\tau$, the new nodal locations are calculated using Equations 59 – 60.
2. Based on the new nodal coordinates the velocity and pressure fields at time step $\tau+\Delta\tau$ are calculated using Equations 36 – 38 in their discrete form.
3. The nodal coordinates are re-calculated by inserting the newly derived velocity field in Equations 59 – 60.
4. The steps 2 and 3 are iterated until convergence is obtained. The solution is assumed to reach convergence when the maximum difference of velocity and pressure for each node is below 0.05 percent from one iteration to the next.

Equations 36 – 38 in discrete form are solved using a standard Gauss solver.

3.3 Energy Equation – Heat Transfer

3.3.1 Governing Equations for the Heat Transfer

The governing energy equations can be written in a similar form as the governing fluid mechanics equations. Whereas the governing fluid mechanics equations are only solved in the deforming domain of the impinging droplet, the energy equations are solved on the entire domain shown in Figure 27. The energy equations are thereby solved using the Galerkin finite element formulation as outlined in section 3.2.5 for the spatial discretization. Time integration is accomplished using a Crank-Nicholson scheme. The discretization of the computational domain is the same as described in section 3.2.6. The computational domain includes the liquid droplet (solidifying during the impingement process), the pre-impacted and solid droplet, and all the different layers of the supporting wafer substrate. The latter has the same dimensions and composition as the wafer substrate employed in the experiments. Furthermore, it is assumed that a very thin interface of poor thermal conductance and no specific heat capacity between the pre-impacted, solid droplet and the supporting substrate is present. This interfacial layer allows for a simple modeling of the heat transfer resistance between the wafer substrate and the presolidified droplet as will become apparent in section 3.3.3. In addition to this interfacial layer a second interface between the impinging droplet and

the presolidified droplet is assumed as indicated in Figure 27. This interface is due to modeling of the heat transfer resistance between the impinging droplet and the presolidified droplet.

Using again the Lagrangian approach the equations for all domains have the same form and can be written as follows:

$$\rho_i c_{p,i} \partial_t T_i - \nabla^2 (k_i T_i) = 0, \qquad i = 1, 2, 3, 4 \qquad (61)$$

where ρ_i is the density, $c_{p,i}$ denotes the specific heat, k_i is the thermal conductivity, and T_i is the temperature of the i-th component. The different domains, as shown in Figure 27, are numbered as: impacting droplet i = 1, presolidified droplet i = 2, interface layer i = 3, wafer substrate i = 4. The convective effect on the transfer of energy in the splat is implicit in the Lagrangian formulation. The movement of fluid particles in the deforming droplet represent this convective effect.

Three assumptions are made with regard to the solidification of the impinging droplet. First, since an eutectic solder is under study, a sharp boundary separating fluid and solid regions is incorporated. Furthermore, phase change is assumed to occur at the equilibrium freezing temperature T_m (183 [°C]). Lastly, solid and liquid densities are taken to be identical since the solder under investigation experiences only a contraction of 2.4% upon freezing [19]. The exact specific heat method proposed by Bushko and Grosse [69] is employed to model solidification. In this approach the specific heat is defined as:

$$c_{p,l}(T_l) = \{c_{ps,l}(T_l < T_m), c_{pl,l}(T_l > T_m)\} + L\int_0^T \delta(T_l - T_m)dT \qquad (62)$$

where L is the latent heat of fusion, $\delta(.)$ is the Dirac delta function and the subscripts s and l refer to solid and liquid, respectively. According to Bushko and Grosse [69] this approach leads to exact integration of the capacitance terms in the finite element formulation with linear triangle elements. Thus, conserving energy very accurately as the droplet solidifies.

The thermophysical properties (ρ_i, $c_{p,i}$, k_i) are assumed to be constant (i.e. independent of temperature) within a phase. Thus, changes of the specific heat and the thermal conductivity occur only in the computational domain of the impinging droplet due to phase change (solidification).

3.3.2 Initial and Boundary Conditions

Initial conditions in the impinging droplet, the presolidified droplet, and the wafer substrate are:

$$T_1(r,z,t=0)=T_{1,0} \tag{63}$$

$$T_2(r,z,t=0)=T_3(r,z,t=0)=T_4(r,z,t=0)=T_{2,0} \tag{64}$$

where $T_{1,0}$ and $T_{2,0}$ are the corresponding initial temperatures of the impinging droplet and the substrate (presolidified droplet and multiplayer wafer) prior to impact.
Heat transfer from the exposed droplet and substrate surfaces is neglected such that the following condition applies to all boundaries exposed to the ambient:

$$\partial_r T_i n_r + \partial_z T_i n_z = 0 \qquad i=1,2,3,4 \tag{65}$$

3.3.3 Modeling of Thermal Contact Resistance

The solidified shape of a molten droplet deposited on a substrate is not only influenced by the impact dynamics, but also by the simultaneous heat removal process from the molten material to the substrate as already mentioned by Waldvogel et. al. [14]. A key factor in this process is the resistance to the heat transfer arising through an imperfect thermal contact at the interface between the substrate and the molten, or the molten and the already solidified material, the so-called thermal contact resistance. The onset, advancement and completion of phase change are dependent on this parameter. The cause for thermal contact resistance is that when a melt spreads over a solid surface, a perfect thermal contact cannot be achieved between the liquid and the solid surface because of the substrate surface roughness, surface tension of the melt, impurities on the surface and gas entrapment [70].
Two connecting interfaces where thermal contact resistance occurs have to be taken into account in the present model as insinuated in Figure 27. An interface is present between the impinging droplet and the presolidified droplet as well as between the latter and the wafer substrate. Two different approaches are chosen to incorporate thermal contact resistance in the

present study. The contact resistance between the presolidified droplet and the wafer substrate (Region 3, Figure 27) is modeled according to Waldvogel et. al. [19] by defining a thin layer of arbitrary thickness d_{il} which attaches the two domains. It is assumed that this layer has zero heat capacity and experiences only axial conduction. The effective axial thermal conductivity $k_{z,c}$ for the layer is related to the contact resistance coefficient $R_{t,c}$ by:

$$k_{z,c} = \frac{d_{il}}{R_{t,c}} \tag{66}$$

The advantage of this approach is that it connects the sub-domains of the presolidified droplet, the interface (Region 3, Figure 27) and the wafer substrate. With all the sub-domains having essentially the same energy equation, Equation 61, the thermal solution of these sub-domains can be calculated without having to iterate. These sub-domains (from now on termed substrate domain) can be treated as a single domain having variations in heat capacity and thermal conductivity. These variations are due to the composite nature of the substrate domain consisting of different materials.

The same approach was not applied on the interface between the impinging and the presolidified droplet (Internal Boundary, Figure 27). Defining such a layer on a curved boundary is inappropriate. Furthermore, it would change the boundary curvatures of the presolidified droplet since this layer can not have an infinitesimal thickness (e.g. the layer has the characteristic thickness of an element). Thus, a change in geometry of the computational domain would have to take place, which is not acceptable. As a clearly better alternative, the interface between the impinging and the presolidified droplet is treated as an internal boundary with the following heat transfer condition:

$$k_i \partial_r T_i n_r + k_i \partial_z T_i n_z = \alpha_c \left(T_{1,j} - T_{2,j} \right) \tag{67}$$

where α_c is a heat transfer coefficient modeling the thermal contact resistance between the impinging and the presolidified droplet. The computational domains of the impinging and the presolidified droplet are connected in such a way that the boundary nodes of the respective domains overlap at the interface. Thus, the temperatures $T_{1,j}$, $T_{2,j}$ refer to boundary temperatures of the impinging droplet (1) and the presolidified droplet (2) at the j-th node of the interface.

3.3.4 Dimensionless Equations, Initial and Boundary Conditions

Using the following dimensionless parameters the mathematical model described above is cast in dimensionless form:

$$\mathrm{Pr}=\frac{\mu_1 c_{pl,1}}{k_{1,1}},\quad C_i=\frac{\rho_i c_{p,i}}{\rho_1 c_{pl,1}},\quad K_i=\frac{k_i}{k_{1,1}},\ \text{and}\quad \Theta_i=\frac{T_i-T_{2,0}}{T_{1,0}-T_{2,0}}\qquad i=1,2,3,4 \qquad (68)$$

Furthermore, the Biot number, the Stefan number and the superheat parameter SHP as defined in section 1 are employed.

Energy equation:

$$C_i\partial_\tau\Theta_i-\frac{1}{\mathrm{Pr\,Re}}\left[\frac{1}{R}\partial_R\left(K_i R\partial_R\Theta_i\right)+\partial_Z\left(K_i\Theta_i\right)\right]=0 \qquad i=1,2,3,4 \qquad (69)$$

Specific heat of the impinging droplet:

$$C_1(\Theta_1)=\left\{C_{1,s}(\Theta_1<\Theta_m),C_{1,l}(\Theta_1>\Theta_m)\right\}+\frac{1}{\mathrm{Ste}}(1-\mathrm{SHP})\int_0^{\Theta}\delta(\Theta_1-\Theta_m)\,d\Theta \qquad (70)$$

Initial conditions:

$$\tau=0:\quad \Theta_1(R,Z,\tau=0)=1,\ \Theta_i(R,Z,0)=0 \qquad i=2,3,4 \qquad (71)$$

Boundary condition at the droplet free surface and the substrate boundary surface:

$$\frac{\partial\Theta_i}{\partial R}n_R+\frac{\partial\Theta_i}{\partial Z}n_Z=0, \qquad i=1,2,3,4 \qquad (72)$$

Internal boundary condition between the impinging droplet and the presolidified droplet:

$$K_i \partial_R \Theta_i n_R + K_i \partial_Z \Theta_i n_Z = Bi\left(\Theta_{1,j} - \Theta_{2,j}\right) \qquad i = 1, 2 \qquad (73)$$

The dimensionless effective axial thermal conductivity $K_{Z,c}$ between the presolidified droplet and the wafer substrate reads:

$$K_{Z,c} = \frac{d_{il}}{R_{t,c} k_{l,l}} \qquad (74)$$

3.3.5 Solution Method and Temporal Discretization

The numerical integration of the energy equation is accomplished using the Crank-Nicholson method, which is second order, $O(\Delta\tau^2)$, accurate in time. The coupling of the energy equation of the impinging droplet and the domain including the presolidified droplet, the interface (Region 3, Figure 27), and the wafer substrate is attained by Equation 67. The calculation of a time step $\Delta\tau$ features the following steps:

1. Based on the temperature field in the substrate domain at time step τ the energy equation of the impinging droplet is solved using Equation 69.
2. Based on the new temperature field in the impinging droplet, the energy equation for the substrate domain is solved using Equation 69.
3. Based on the new temperature field in the substrate domain, the energy equation for the impinging droplet is solved using Equation 69.
4. The steps 2 and 3 are iterated until convergence is obtained. The solution is assumed to reach convergence when the maximum difference of temperature for each node is below 0.05 percent from one iteration to the next.

Equation 69 in discrete form is solved using a standard Gauss solver.

4. Simulation Results

4.1 Objectives

This section of the thesis focuses on the effect of the various influential parameters of the mathematical model described in section 3 on the results of the numerical code. This includes the Reynolds, Weber and Froude numbers for the impact regime, the Stefan number and the superheat parameter for the thermal regime, the Biot number for the influence of the thermal contact resistance, the Mach number for the behaviour of the artificial compressibility approach, and the slip parameter for the Navier-Slip model. Issues concerning mesh and time step independence as well as mass and energy conservation are also considered.

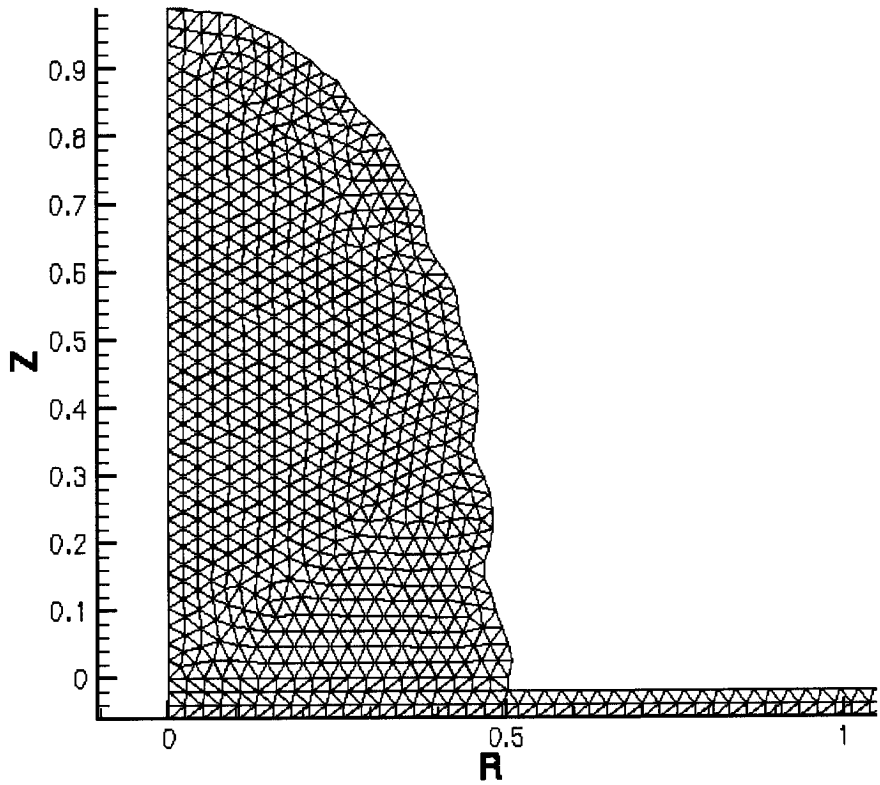

Figure 28: Finite element grid of the test substrate. The full size of the wafer substrate is not shown for better resolution.

A large number of simulations were performed with the same shape and size of the presolidified droplet, or, in other words, the same substrate, in order to shed light on the prevailing physical processes. An identical substrate for all cases was chosen in order not to

make the results dependent on different substrate shapes as was the case in section 2. To this end, Figure 28 shows the test substrate employed for this investigation. It corresponds to the solidified shape of a molten droplet impinged on a flat wafer substrate with the following impact parameters: Re = 363.9, We = 4.17, Fr = 3025.2, Ste = 0.895 (25 [°C]).

It is, for all simulations reported in this thesis, assumed that the thermophysical properties (dynamic viscosity, surface tension, thermal conductivity, specific heat) are not temperature dependent. Changes of the thermophysical properties are only due to phase change (liquid/solid properties). This assumption is reasonable for the narrow temperature range covered by the process considered in this thesis as well as for the small changes in the above mentioned thermophyiscal properties of the employed eutectic solder. However, it must be stressed that the dynamic viscosity changes by orders of magnitude close to the phase change boundary. This transition zone is usually very thin and is neglected in this investigation [71-73].

All simulations reported herein were performed on a conventional PC using a 600 MHz Pentium III processor and 256 MB of internal memory. A typical run required 24 – 48 CPU hours to complete.

4.2 Mesh and Time Step Independence

The numerical solution of mathematical models yields an approximate and never an exact solution of the original mathematical model. In FEM this is easily understandable by, for instance, the fact that the space of trial functions is truncated as well as the finite size of the individual elements. The paramount requirements of a numerical solution are therefore that it converges to the exact mathematical solution as the mesh is refined, the space of trial functions is expanded, and, for time-dependent problems, the time step is decreased. The computational simulation of physical phenomena is subject to four primary types of errors: modelling errors due to lack of knowledge of the inherent physics of the investigated problem, discretization errors interconnected with the FEM approximation, iteration or round-off errors interconnected with finite precision manipulation of numbers in the processor, and postprocessing errors associated to post-manipulation of numbers (i.e. filtering, smoothing). To determine the accuracy of the mathematical modelling of the prevalent physical process of a droplet impacting on a non-flat surface is clearly within the scope of this thesis. This topic will be addressed in the next section featuring comparisons between modelling and

experiments. Postprocessing errors are largely man-made through careless use of visualization and data cleansing tools and can therefore be largely prevented. The discretization errors are affected by a number of factors such as: (1) the order of the interpolation functions as related to the physics under study, (2) the mesh-size and consequently the size of the trial function space, and (3) the distribution of the elements or in other words the mesh quality. The influence of truncation or round-off errors is not trivial to determine. It is however important to carefully code algorithms accessing directly nodal solution variables such as the mesh to mesh interpolation after a remeshing operation as described in section 3.2.6. In general, there is rigorous mathematical foundation for the study of FEM accuracy concerning the discretization scheme. It is however out of the scope of this thesis to go along the purely mathematical path. Verification of numerical solutions can also be achieved in an "engineering manner" by studying solutions upon variation of the relevant parameters as mesh size and thus consequently trial function space size, time step, and mesh distribution. The ability of the presently employed numerical code to yield convergent solutions is examined in terms of the splat thickness at the axis of symmetry $Y_{center}(t)$, the splat radius $R_c(t)$, and the evolution of the solid fraction for varying mesh sizes m_d and time steps $\Delta\tau$. To this end, Figures 29 – 31 show the temporal evolution of the splat thickness $Y_{center}(t)$, the splat radius $R_c(t)$, and the solid fraction for different mesh sizes and time steps for a solder droplet with the following dimensionless impact parameters: Re = 376, We = 4.28, Fr = 2867, Ste = 0.895.

As is visible from inspection of Figures 29 – 31 the solution achieves mesh size - and time step independence for a mesh size m_d of 1.1 – 1.5 [-] and a time step of $\Delta\tau < 2*10^{-3}$ [-]. The time step $\Delta\tau$ is thereby made dimensionless according to Equation 35. The definition of the mesh size m_d is thereby somewhat arbitrary. When automatically generating the mesh with the grid generator, a specific element size has to be defined. In the present simulations this specific size is chosen to be d_{il}, the height of the interfacial layer between the presolidified droplet and the flat wafer substrate. This is so to say the smallest edge length of a triangular element. For all simulations performed in this thesis the height of the interfacial layer is arbitrarily chosen to be 2% of the initial droplet diameter. The mesh size parameter m_d is a scaling factor enabling to control this minimal edge length or in other words proportional to the average element size. It must be stressed, that the height of the interfacial layer features only an influence on the thermal solution in the sense that a change of the height would alter the thermal contact resistance between the wafer substrate and the presolidified droplet. The flow solution is thus not directly affected.

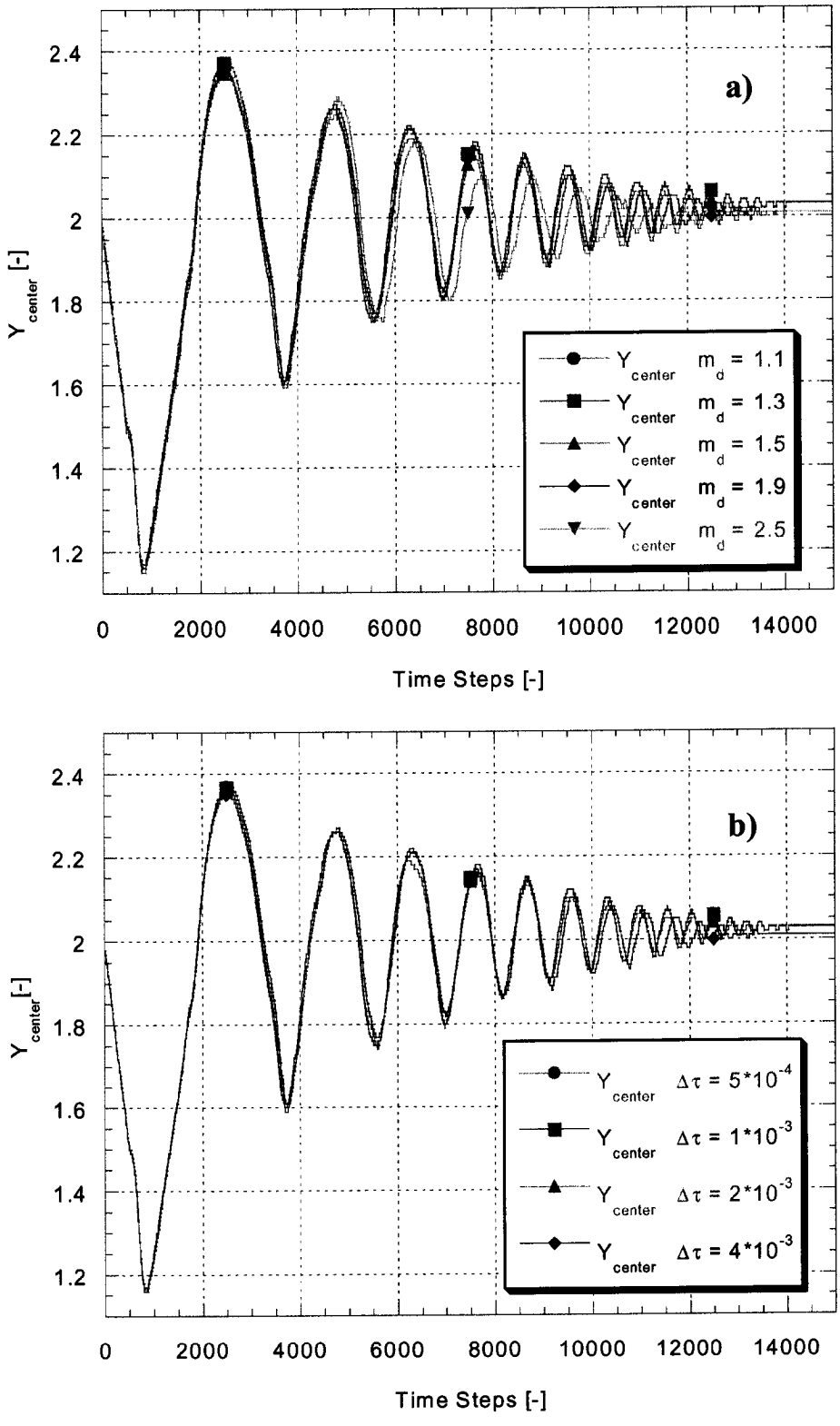

Figure 29: a) Temporal evolution of the splat thickness $Y_{center}(t)$ for different mesh densities m_d. b) Temporal evolution of the splat thickness $Y_{center}(t)$ for different time steps $\Delta\tau$.

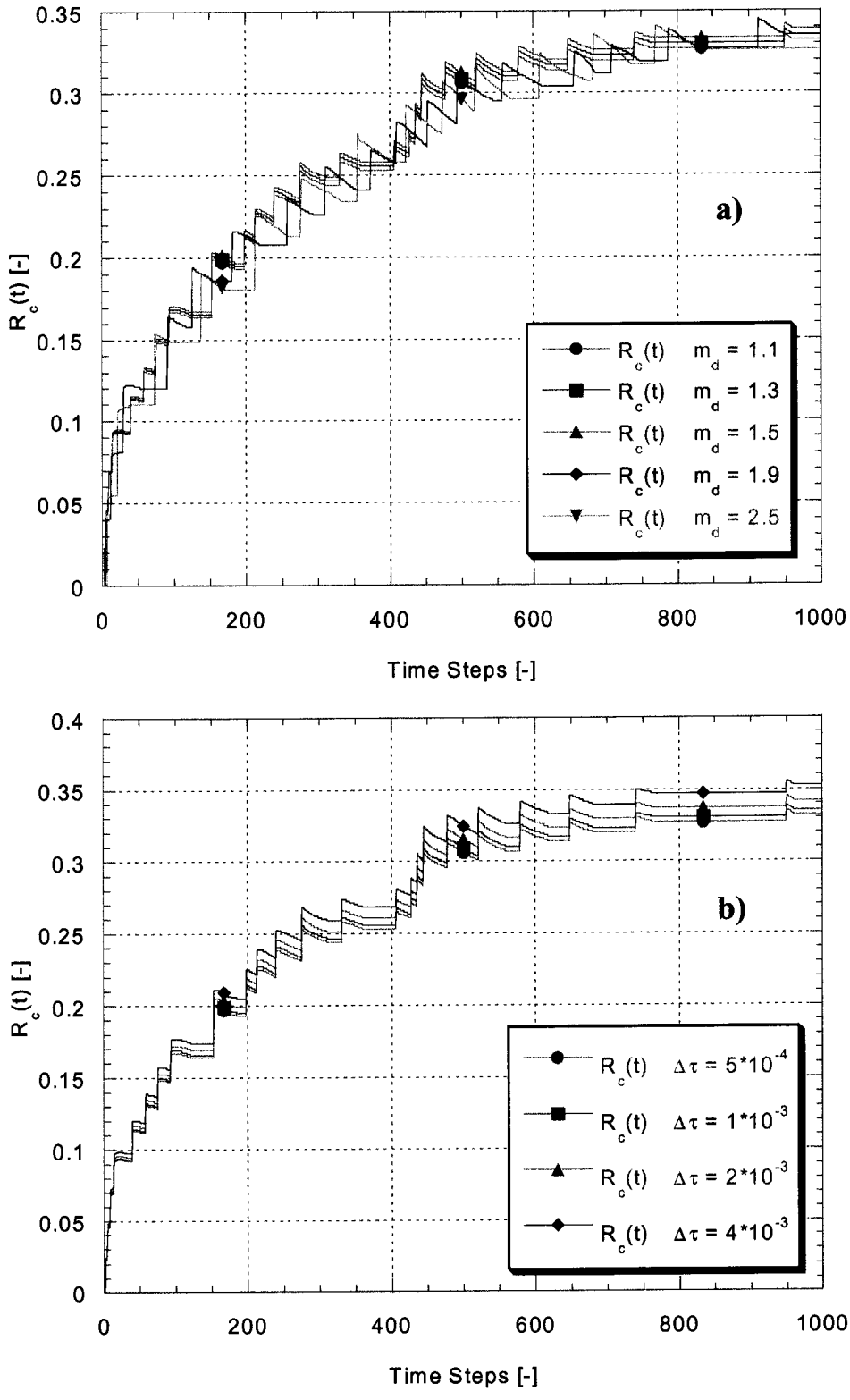

Figure 30: a) Temporal evolution of the contact line radius $R_c(t)$ for different mesh densities m_d. b) Temporal evolution of the contact line radius $R_c(t)$ for different time steps $\Delta\tau$.

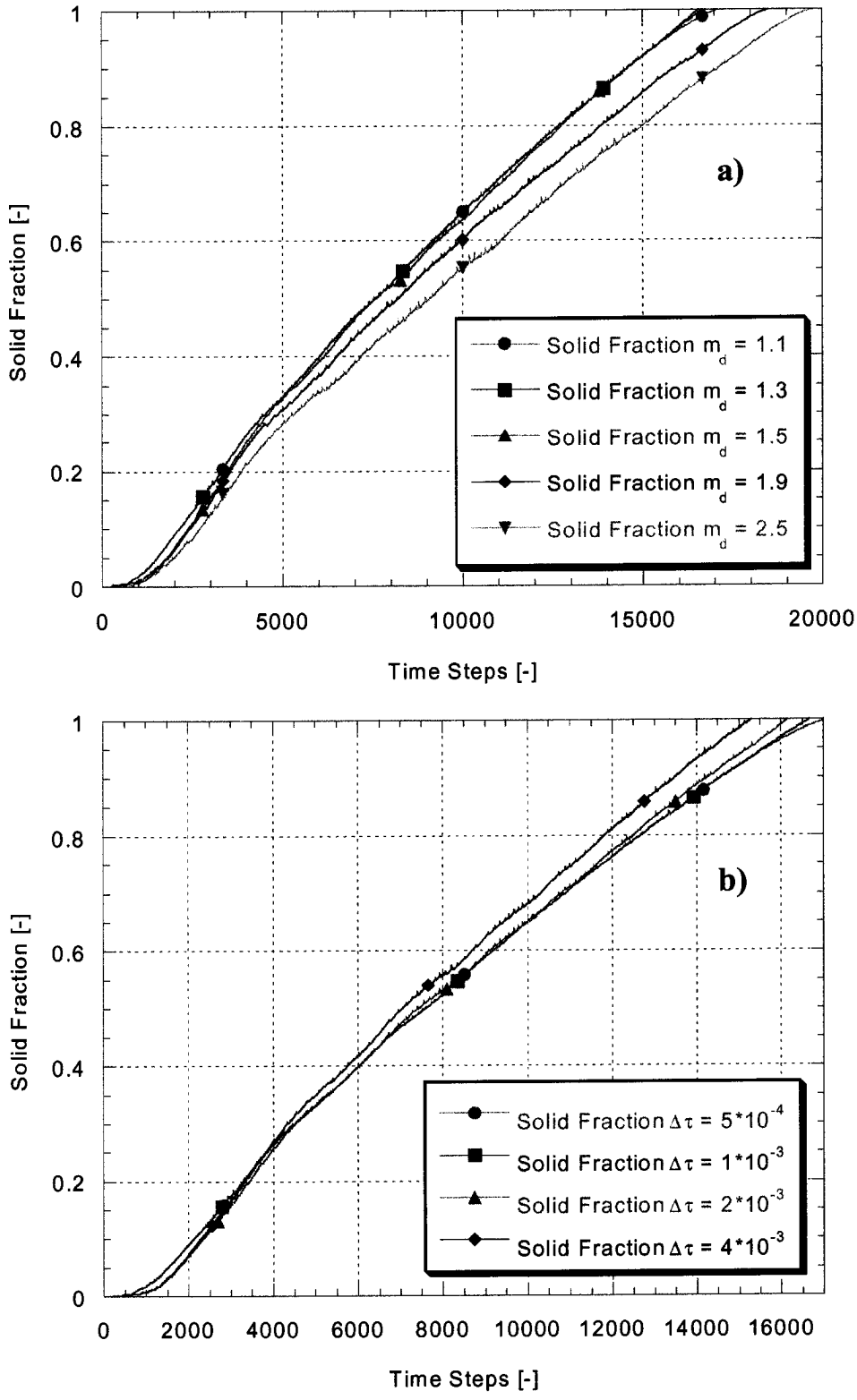

Figure 31: a) Temporal evolution of the solid fraction for different mesh densities m_d. b) Temporal evolution of the solid fraction for different time steps $\Delta\tau$.

It is important to keep in mind that too large a number of elements becomes prohibitively cost intensive with respect to computer memory allocation and processor time. For the present simulations a mesh density $m_d = 1.5$ was used, corresponding to approximately 700 triangular elements in the initially fluid domain and approximately 2000 triangular elements in the substrate, including the presolidified droplet. The dimensionless time step chosen for the simulations after testing was $1*10^{-3}$.

As already mentioned in section 3.2.6 a commercial mesh generator was employed in the current simulations due to its ability to produce highly uniform meshes. This quality prevents the amplification of numerical errors throughout the numerical domain [74,75].

4.3 Energy and Mass Conservation

A matter linked closely to the above outlined issue of numerical errors is the conservation of mass and energy. The governing equations and boundary conditions introduced in section 3 describe a completely closed system, conserving mass and energy. It is therefore important to examine the ability of the numerical code to conserve both energy and mass for a chosen set of mesh size and time step. Potential operations affecting conservation of mass and energy include the remeshing due to the deforming grid in the Lagrangian formulation of the flow equations, the interpolation of the nodal values from the old to the new mesh after each remeshing, the attachment of nodes of the fluid domain to the solid substrate, as well as the calculation of the heat transfer between the impacting droplet and the presolidified splat. More specifically, these operations may affect mass and energy conservation in the following ways: (1) Remeshing operates by first identifying the free surface nodes of the entire computational domain (i.e. liquid domain, and the substrate consisting of the presolidified splat and the wafer substrate). The nodal coordinates of the free surface nodes are handed over to the commercial mesh generator where the boundary of the computational domain is defined by creating a spline through the transferred nodal coordinates of the free surface. Based on the chosen mesh size the so defined boundary of the computational domain is subdivided in a new set of free surface nodes with a better distribution concerning the elemental distortions. This improvement of the nodal distribution on the free surface can lead to a creation or annihilation of mass as shown schematically in Figure 32.

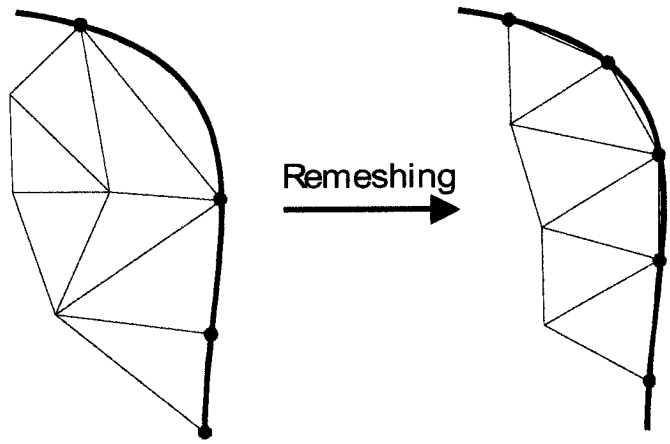

Figure 32: Violation of the mass and the energy conservation during the remeshing operation. The dots represent the free surface nodes. The thick line represents a segment of the free surface.

(2) After each remeshing operation every node has to be assigned the set of nodal variables based on the old mesh as described in section 3.2.6. This involves first for each new node the determination of the element of the old mesh containing the new node. From the so determined element of the old mesh the nodal variables for the new node can be determined by interpolation of the nodal variables of the element of the old mesh. This can only be done with a finite accuracy. In domains with steep gradients this can lead to small but nevertheless cumulative errors. This does not affect mass conservation but energy conservation since minor errors in temperature as well as velocities and pressure occur. (3) The impact of a liquid droplet on a rigid surface involves the creation of a liquid/solid interface replacing a gas/solid interface. This interface change in the system is established through the tendency of the liquid to wet the substrate, but primarily by the fact that the easily deforming, liquid droplet hits the rigid substrate with a certain momentum. Both phenomena determine the amount of liquid/solid interface created. In the numerical code the wetting tendency is modelled approximately using the Navier-Slip condition as described in section 3.2.3. Furthermore, the solution of the Navier-Stokes equations accounts for the creation of liquid/solid interface due to the momentum of the impacting and deforming droplet. The modelling of this issue involves a peculiarity which can create or annihilate mass. The momentum of the impacting droplet forces free surface nodes to move to the substrate surface which they eventually reach after some time. Clearly, the free surface nodes of the liquid domain are prohibited to move into the solid domain due to the no-penetration boundary

condition. However, this boundary condition is enforced for every node having attached to the surface by setting their velocities equal to zero. Thus, after each time step of the flow equations, the free surface nodes have to be inspected on their respective positions relative to the substrate surface. The attachment of nodes is thereby solved by moving those free surface nodes that have been displaced, during a time step, closer to the substrate surface than a prescribed tolerance, in the direction of the velocity vector of the respective node to the substrate surface. Those former free surface nodes are then defined as a new interface nodes. By doing so a tiny amount of mass is created as shown schematically in Figure 33a).

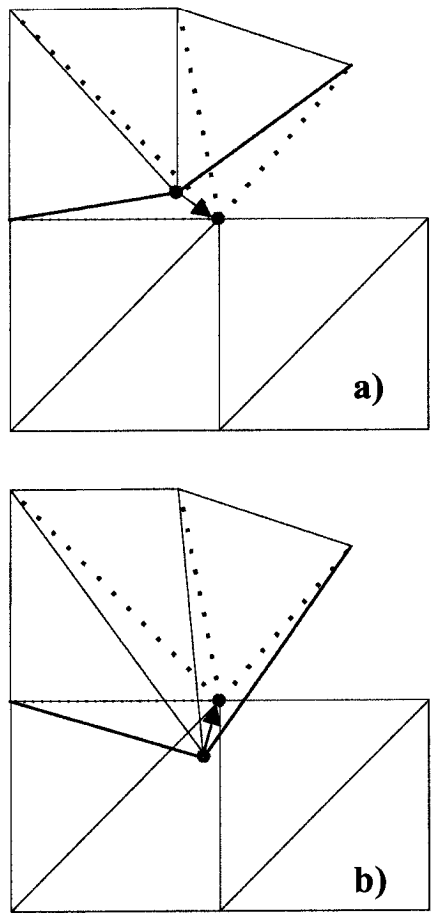

Figure 33: Violations of the mass conservation and the energy conservation due to node attachment to the solid substrate. a) Mass and energy creation. b) Mass and energy destruction.

The opposite case where a tiny amount of mass is annihilated occurs, when a free surface node moves during a time step into the substrate domain. This case is treated identically to the previously described case, as shown schematically in Figure 33b).

(4) The heat transfer between the impacting droplet and the substrate is solved iteratively as described in length in section 3.3.5. The iteration of the temperature field after each time step is truncated based on a convergence criterion. This leads to creation/annihilation of tiny amounts of thermal energy at each time step.

Common to all the non-conservative effects above is the fact that they all act both as source and sink for both mass and energy. Figure 34 shows the time history of mass and thermal energy during a pile up for a sample case with the following dimensionless impact parameters: Re = 376, We = 4.28, Fr = 2867, Ste = 0.895.

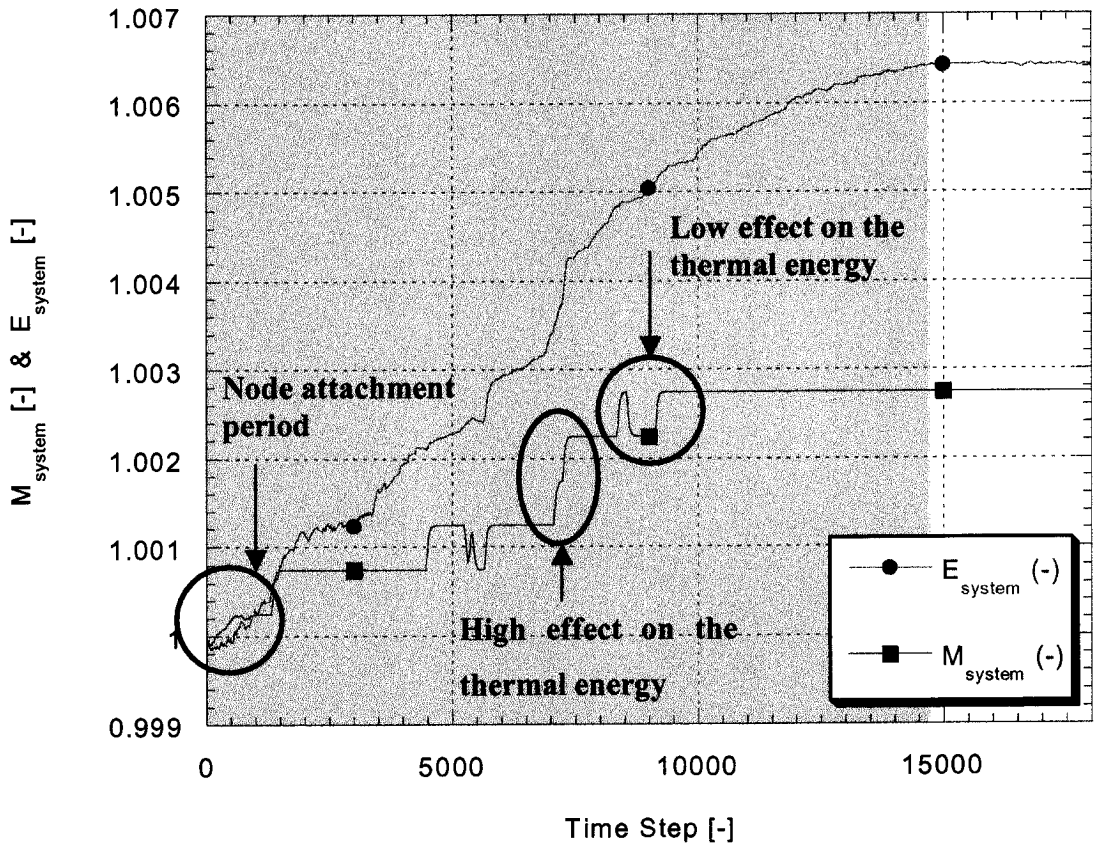

Figure 34: Time history of the mass and energy during a sample case with the following dimensionless impact parameters: Re = 376, We = 4.28, Fr = 2867, Ste = 0.895. The shaded region signifies the solidification period.

The shaded area in Figure 34 represents the solidification period. As can be seen, both mass and energy are conserved below 1% of their initial values during an entire run, clearly a more than satisfactory performance. The discussion in the following paragraphs focuses on the reasons behind this very small error, for the sake of scientific thoroughness.

Both the system mass and energy tend to result in a very small increase of their respective initial values. This means that creation and annihilation of mass and energy do not completely counteract each other. When inspecting the progression of the mass conservation in Figure 34 it is apparent, that upon impact a short period of quasi-continuous change of the mass can be identified. This period pertains to the spreading process, or in other words the period during which node attachment, as described above, occurs. After the spreading process has finished the mass progression features different periods of no change followed by steep changes. These steps can be assigned explicitly to remeshing operations. However, what is not obvious in Figure 34 is that during a typical pile up simulation approximately 150 remeshing operations are performed. This means that the majority of the remeshing operations cause only very small changes in the system mass. The few occurrences of "large" creation or annihilation of mass during remeshing operations can be explicitly associated to large element distortions at the free surface as schematically shown in Figure 33. When inspecting the progression of the thermal energy in Figure 34 it is apparent that the thermal energy is not strongly correlated to the temporal progression of the mass. As shown in Figure 34, the creation or annihilation of mass due to remeshing does not necessarily affect simultaneously the thermal energy. This is due to the fact that, the thermal energy is not uniformly distributed over the mass of the system. Mass created in a region of low thermal energy will of course not contribute much to the system's thermal energy content.

4.4 Thermal Contact Resistance

4.4.1 Brief Background Material on Thermal Contact Resistance

Thermal contact resistance is a key parameter in the deposition of molten droplets as already mentioned in section 3.3.3. In high-precision applications such as electronic packaging or component manufacturing, solder bump height deviations can be detrimental to the success of this technique [3]. Unfortunately, predicting or measuring accurately the contact resistance at the time and length scales of the solder jetting technology (less than 100 microns and 100 microseconds) [13] has proven elusive so far. In recent years a reasonable effort has been expended in enhancing the understanding and estimation of thermal contact resistances, in particular for rapid solidification processes. However, this has still been the case for rather large-scale systems, with respect to both time and space. Numerical and experimental

approaches have been applied in order to get estimates and to study the sensitivity of droplet impact processes on thermal contact resistance. To this end, Pasandideh-Fard et al. [53] and Xiong et al. [3] have reported the sensitivity of the final diameter, the overall shape and the height of a solidified droplet to the contact resistance. Xiong et al. [3] presented numerical results of final shapes of solder microdroplets impinging on a flat, metallic surface, for constant initial conditions but different thermal contact resistance values showing substantial shape differences. By matching experimental and numerical cases corresponding contact heat transfer coefficients in the range of $4 - 350*10^3$ [W/Km^2] were reported.

Detailed experimental investigations of the thermal contact resistance of molten droplets solidifying on a cold substrate have been published by Wang and Matthys [76] recently. They performed experiments on molten copper droplets with a weight of about 0.5 to 0.6 g impinging on inclined copper, aluminum and stainless steel plates with different surface finishes (respectively roughnesses). By matching temperature measurements with strongly simplified model calculations (without fluid dynamics) they were able to estimate interfacial heat transfer coefficients. The major finding was that the interfacial heat transfer coefficient, respectively the thermal contact resistance, is strongly time-dependent. Wang and Matthys [76] were able to assign principally four different stages for the heat transfer coefficient: (1) melt spreading, (2) liquid cooling, (3) solidification and (4) solid cooling. However, as mentioned in [76], it must be noted that for different experimental baselines, i.e. very small droplets impinging on a substrate, still other regimes could be observed, for example when spreading and solidification occur simultaneously. Furthermore, it must be stressed that their matching based on a simple mathematical model. Nevertheless, they were able to give an interesting insight into the prevalent mechanisms. Recently, Pasandideh-Fard et al. [48] also performed experiments somewhat similar to the ones by Wang and Matthys [76] with very similar results. Inada [77] also performed experiments with droplets impacting on a flat substrate. He reported a dependence of the cooling rate and the interfacial heat transfer coefficient on the droplet impact velocity.

Thermal contact resistance has, in spite of its importance, often been neglected in numerical models. Liu et al. [78], Trapaga et al. [79] and Bertagnolli et al. [80] used finite difference models to study the simultaneous spreading and solidification of impacting droplets. They assumed an isothermal substrate, and neglected any thermal contact resistance at the liquid-solid interface. The reason for this simplification seems to be the associated with the uncertainty in determining a proper value for the contact resistance and not any implementation difficulties. Another justification put forward for neglecting the interface heat

transfer resistance has been the assumption that substrate remelting creates a continuous contact between the droplet and the substrate [81]. For droplets impacting on material of its own kind, such as in spray forming, this assumption has been verified by micrographic examinations [81]. In cases where a low melting temperature substance impacts a high melting temperature substrate this phenomenon does not occur.

4.4.2 Influence of the Thermal Contact Resistance (Biot number) on the Numerical Results

The two models for the thermal contact resistance, as introduced in section 3.3.3, allow for an arbitrary choice of an interface heat transfer coefficient or Biot number respectively. As follows from the previous section, the value of the latter is a priori unknown, the influential parameters are unclear as well, and there are no correlations at hand. Nonetheless, the values obtained from matching experiments and numerical simulations, as mentioned above [3], yield an idea on the order of magnitude which has to be expected. Furthermore, as mentioned above [76], experimental evidence shows that the thermal contact resistance features at least four different stages during the impingement of a droplet on a flat substrate. As shown by Wang and Matthys [76] the value of the thermal contact resistance increases considerably while passing through these four stages with the lowest heat transfer coefficient in the last stage when the entire droplet has solidified. The latter is thereby approximately an order of magnitude smaller than the heat transfer coefficient during the first stage, the spreading process of the impinging melt. In the present study the same approach as by Xiong et. al. [3] is employed. The four stages described in the previous section are combined into two regimes: (1) melt spreading and liquid cooling, and (2) solidification and solid cooling. To this end, a Biot number or a thermal contact resistance is attributed to each of these two regimes. The numerical solution/implementation thereby depends on the respective interface (i.e. impinging droplet/presolidified droplet, presolidified droplet/wafer substrate), Figure 27. For the first interface between the impinging and the presolidified droplet this involves monitoring the interfacial node temperatures of the impinging droplet. The conjugate heat transfer from liquid interfacial nodes is treated using the Biot number of the first regime, Bi_l. For solidified interfacial nodes the respective Biot number for the second regime is deployed, Bi_s. The second interface between the presolidified droplet and the wafer substrate features no phase

change and a constant thermal contact resistance is assumed. The value of the latter is estimated as:

$$R_{t,c} = 3*10^{-4}\ [m^2K/W] \tag{71}$$

This value is consistent with experimental measurements [76] and numerical matching [3,19,55]. To this end, a number of simulations with varying values for the two Biot numbers, Bi_l and Bi_s, pertaining to the interface between the impinging and the presolidified droplet were performed. The following two cases with respect to the impact conditions and the Stefan number were investigated, Table V.

Case	Re [-]	We [-]	Fr [-]	Ste [-]
1	250.9	1.91	1274	0.895
2	376.0	4.28	2867	0.895

Table V: Impact regime for the thermal contact resistance cases.

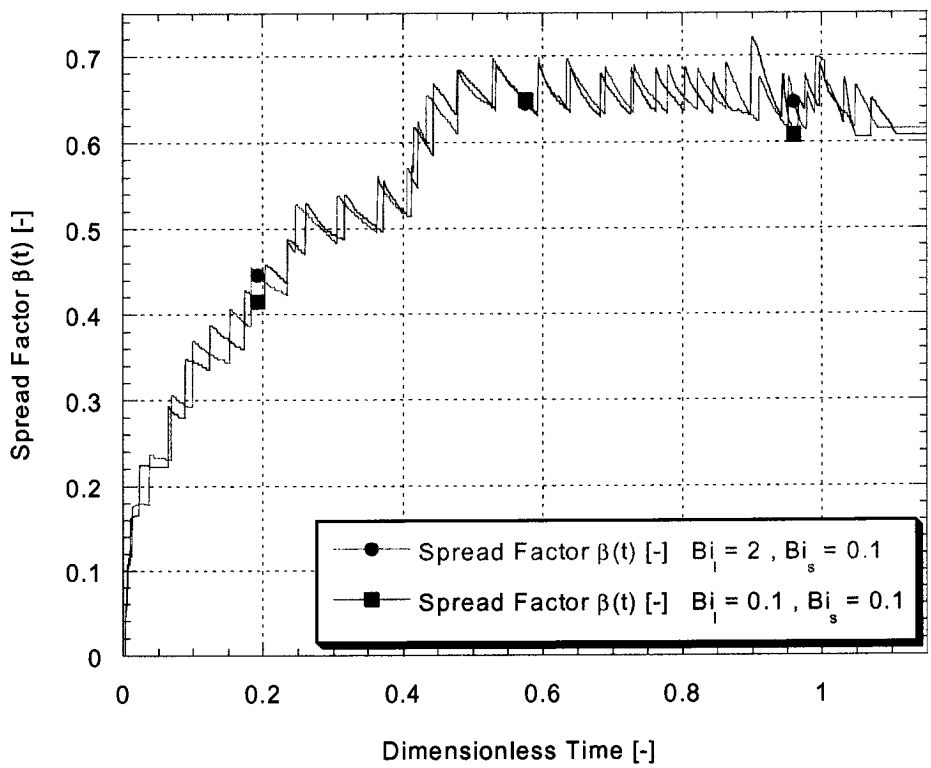

Figure 35: Temporal evolution of the spread factor β(t) for different Biot numbers but identical impact parameters: Re = 376, We = 4.28, Fr = 2867, Ste = 0.895.

The Biot numbers were varied in the following ranges: $Bi_s = 0.01 - 1$; $Bi_l = 0.1 - 2$. This corresponds to the following ranges of the thermal contact resistance: $R_{t,c,s} = 3.2*10^{-4} - 3.2*10^{-6}$; $R_{t,c,l} = 3.2*10^{-5} - 1.6*10^{-6}$. The objective was to investigate the influence of the Biot numbers, as predicted by the numerical model, on the spreading process, the solidification process, the transients of the fluid motion, and the final shape of the pile up.

To this end, Figure 35 shows the progression of the spread factor for two representative cases with the following pairs of Biot numbers: (1) $Bi_l = 2.0$, $Bi_s = 0.1$; (2) $Bi_l = 0.1$, $Bi_s = 0.1$. As illustrated in Figure 35, the evolution of the spread factor is for both cases almost identical yielding approximately the same final spread factor, β_∞. The explanation for the peculiar sawtooth shaped progress of the spread factor will be the scope of section 4.5. The temporal evolution of the solid fraction and thermal energy of the impinging droplet feature a similar behaviour as shown in Figure 36.

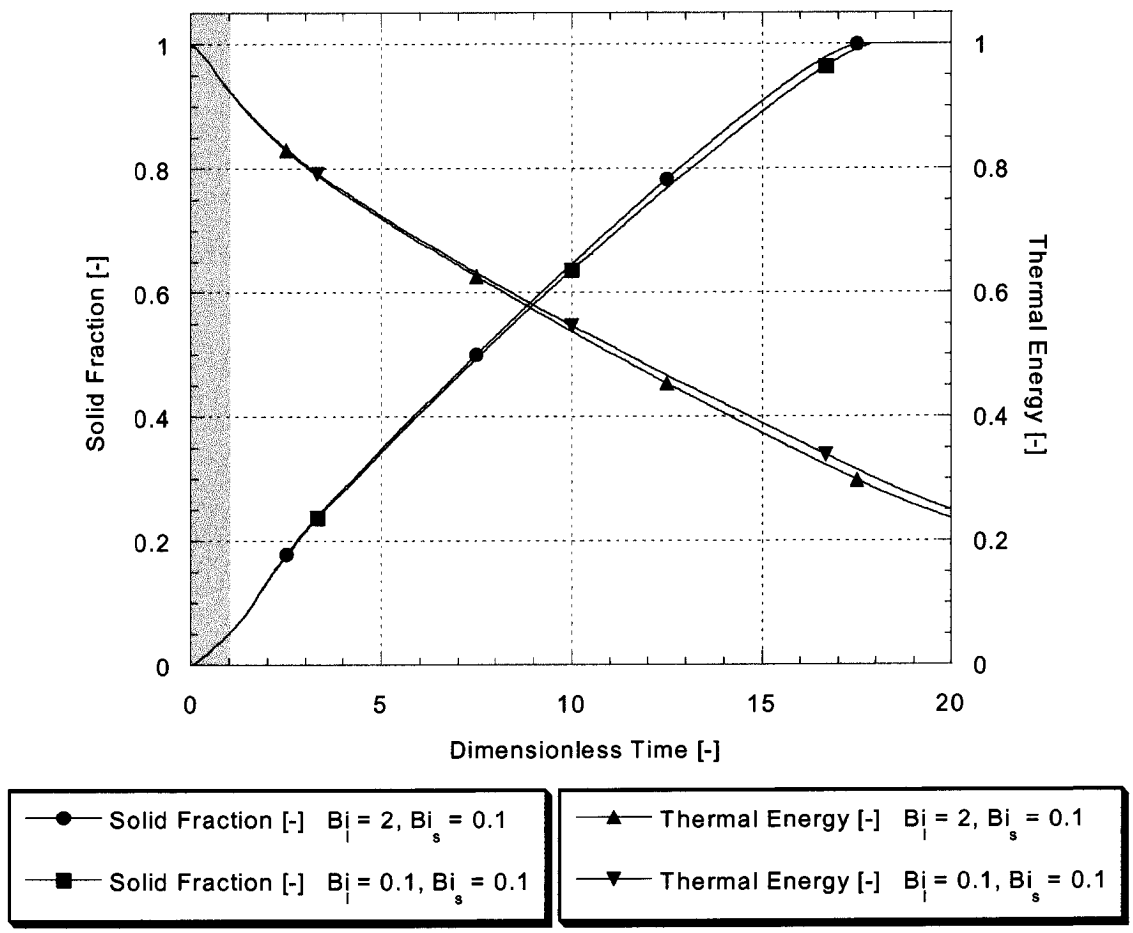

Figure 36: Temporal evolution of the solid fraction and the thermal energy of the impinging droplet for different Biot numbers but identical impact parameters: Re = 376, We = 4.28, Fr = 2867, Ste = 0.895. The shaded area signifies the spreading period.

Although the Biot numbers prior to solidification of the second droplet vary by a factor of 20 for the two representative cases shown, the temporal evolution of the spread factor, the solid fraction and the thermal energy are practically unaffected. As a consequence, the transient behaviour, as illustrated by the oscillatory motion of the dimensionless pile up height, shows for both pairs of the Biot numbers almost identical behaviour, Figure 37.

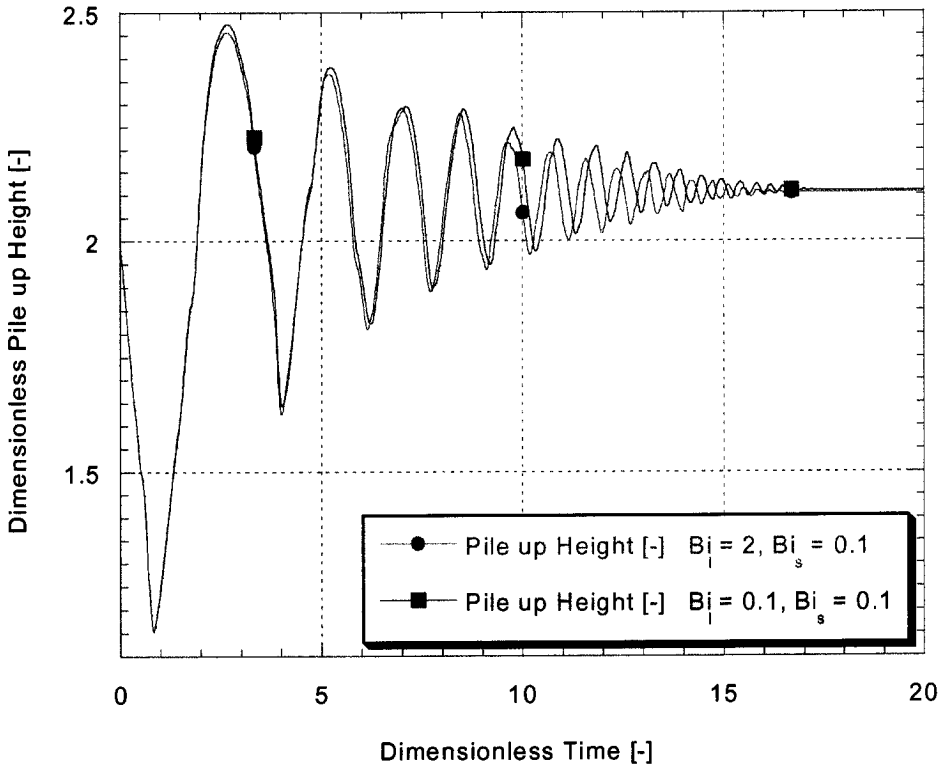

Figure 37: Temporal evolution of the dimensionless height of the pile up structure for different Biot numbers but identical impact parameters: Re = 376, We = 4.28, Fr = 2867, Ste = 0.895.

The weak influence of the Biot number prior to solidification, Bi_l, can be explained as follows. The time period during which a very good thermal contact between the impinging and the presolidified droplet is established is short compared to the entire process of the pile up as shown by the shaded area in Figure 36 (i.e. the spreading stage). Correspondingly, the first of the two combined stages, melt spreading and liquid cooling, is short compared to the second stage including the solidification process. The small differences in the temporal evolution of the solid fraction, the thermal energy and the dimensionless height of the pile up thus have to be attributed to the small difference in the final spread factor shown in Figure 35.

This is corroborated by Figure 38 showing the decrease of thermal energy of the impinging droplet due to cooling for both pairs of Biot numbers during the spreading process.

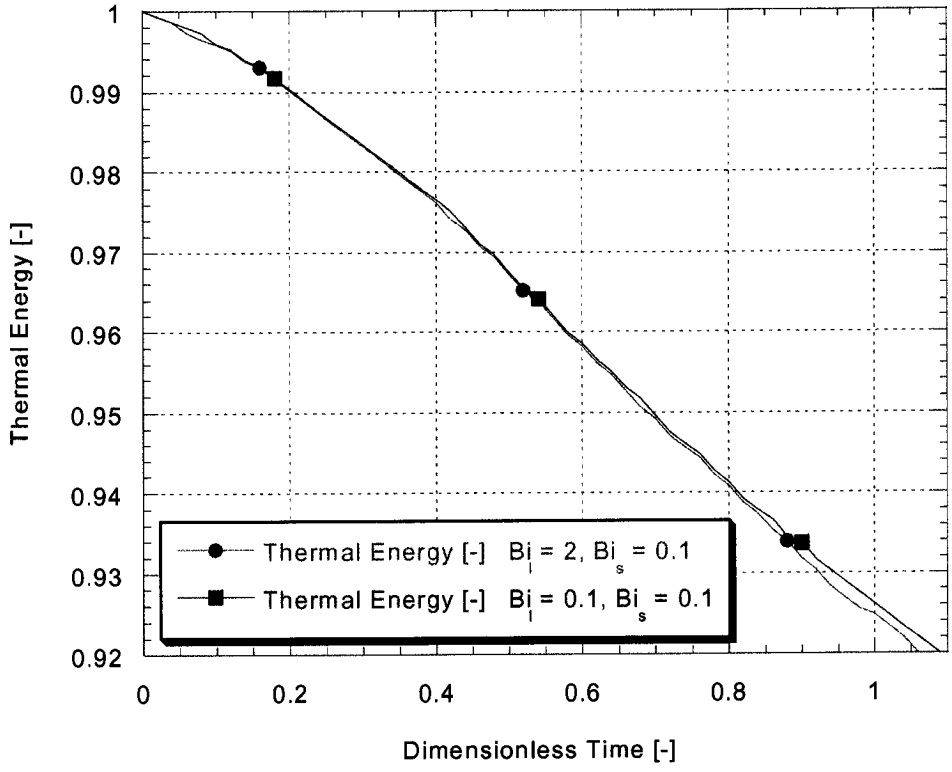

Figure 38: Decrease of the thermal energy during the spreading process for different Biot numbers but identical impact parameters: Re = 376, We = 4.28, Fr = 2867, Ste = 0.895.

Both cases show approximately the same cooling behaviour making the above mentioned differences in the temporal evolution of the pile up only dependent on the final spread factor. The reason for the similar decrease in thermal energy is that melt spreading, cooling, and solidification at the interface, for both pairs of Biot numbers, occur simultaneously and very fast. Thus, the conjugate heat transfer is dominated by the Biot number pertaining to the solidified interface, Bi_s. A marked influence of Bi_l can only occur when the heat transfer during the first stage has a strong impact on the final spread factor. The spread factor defines the contact area controlling, along with Bi_s, the cooling of the droplet by the underlying substrate.

In cases where the spreading process is short compared to the entire pile up process, and most of all when solidification is likely to occur very fast upon contact of the melt with the presolidified droplet, leading to a final spread factor controlled only by the initial momentum

of the impinging droplet, then the Biot number pertaining to the liquid contact has an almost negligible influence on the progression of the pile up.

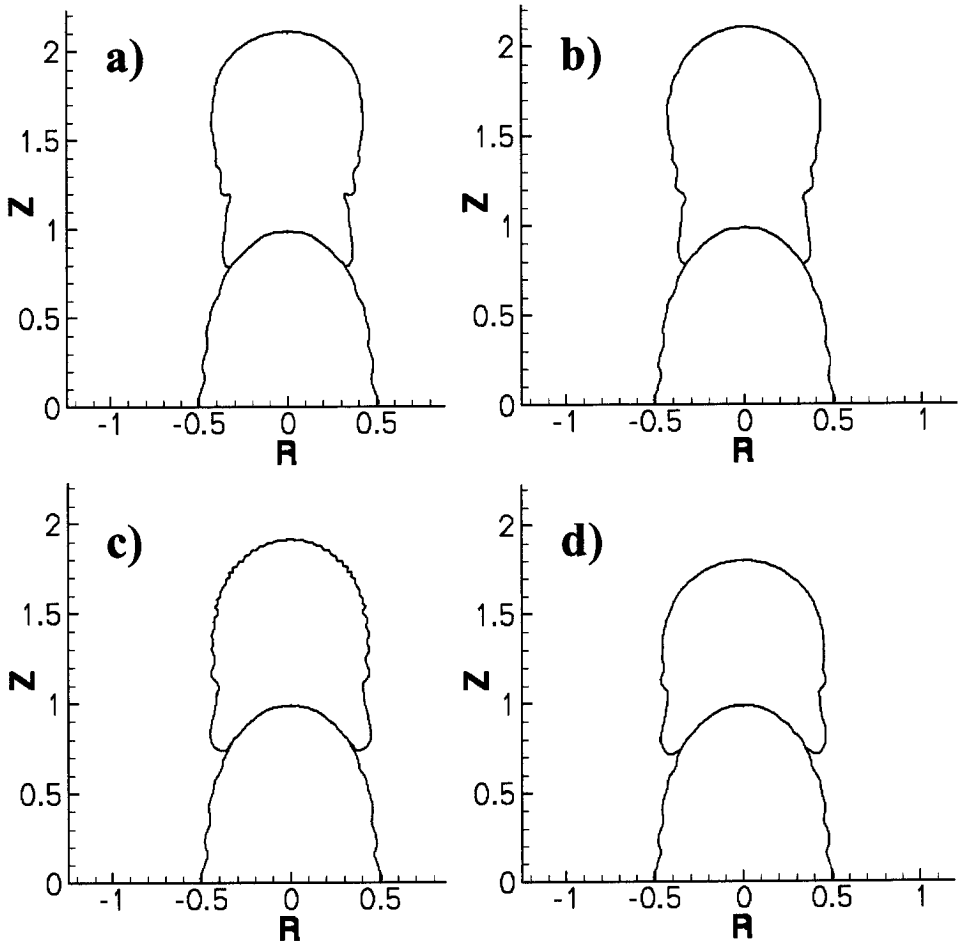

Figure 39: Pile up endshapes for the following impact parameters: Re = 376, We = 4.28, Fr = 2867, Ste = 0.895. (a) $Bi_s = 0.1$, $Bi_l = 2.0$; (b) $Bi_s = 0.1$, $Bi_l = 0.1$; (c) $Bi_s = 1.0$, $Bi_l = 1.0$; (d) $Bi_s = 0.9$, $Bi_l = 1.0$;

To further add complexity to this issue, it has to be emphasized that the Stefan number was kept constant for this investigation as can be seen in Table V. A further illustration of the effect of the Biot number, is presented in Figure 39 which shows endshapes of different pile ups for different pairs of Biot numbers. For identical impact conditions, varying Biot numbers pertaining to solid – solid interface contact have a decisive influence on the endshape of a pile up.

4.5 Spreading and the Influence of the Slip Model on the Numerical Solution

The numerical investigation of the pile up process involves employing a slip boundary condition in the contact line region. This is achieved by imposing the Navier-Slip model at the contact line as described in section 3.2.3, Equation 34. This purely mathematical model allows for slippage of the contact line and thereby alleviates the stress singularity arising through a no-slip boundary condition. The Navier-Slip model allows the contact line to attain a velocity which is proportional to the strain rate in the vicinity of the contact-line as mentioned in section 3.2.3. The proportionality is thereby influenced by the so called slip parameter ε. The latter serves as a control and possible matching factor and has to be chosen ad hoc. In order to study the respective influence of the latter on the spreading and thus on the pile up process, a parametric study on the slip parameter was conducted. To this end, the slip parameter was varied in the following range: $\varepsilon = 0.001 - 100$. The sample case studied is defined by the following dimensionless impact parameters: Re = 376, We = 4.28, Fr = 2867, Ste = 0.895.

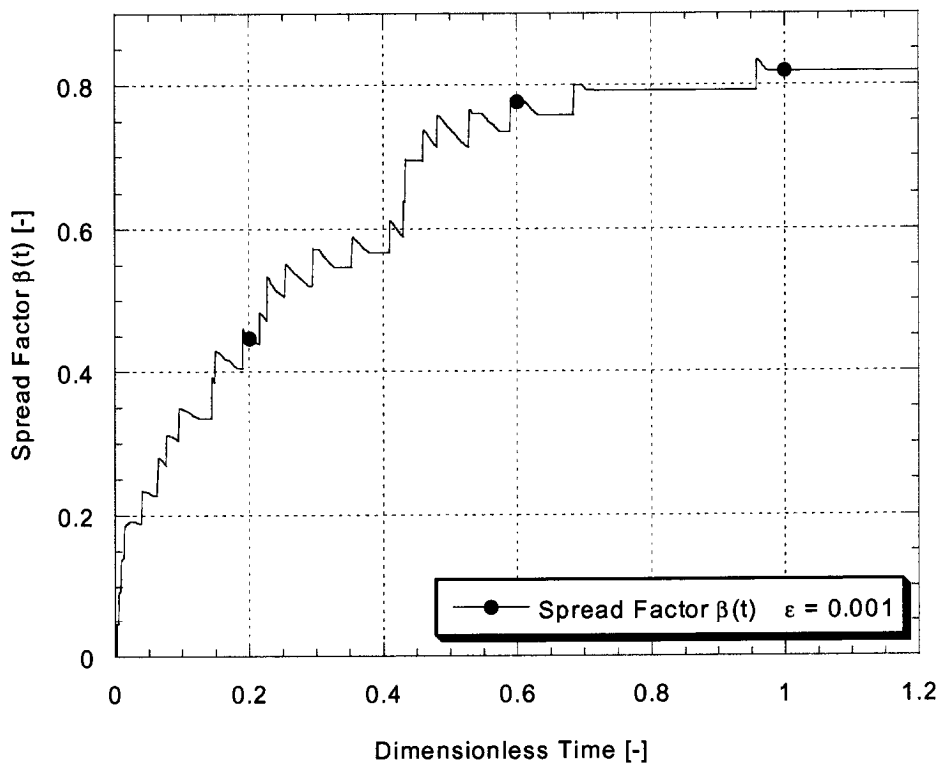

Figure 40: Numerically obtained evolution of the spread factor β(t). The dimensionless impact parameters are: Re = 376, We = 4.28, Fr = 2867, Ste = 0.895. The slip parameter is ε = 0.001.

As follows from inspection of Figure 40, the numerically calculated spreading process exhibits a sawtooth behaviour in the temporal evolution of the spread factor, or the contact line position, respectively. This behaviour is a direct consequence of the employed finite element approach. As mentioned in section 4.3, changes of the interface area are established through the tendency of the liquid to wet the substrate as well as the fact that the easily deforming, liquid droplet meets the rigid substrate with a certain momentum. In the numerical code the wetting tendency is not really modelled. At the contact line the Navier-Slip condition is employed as described in section 3.2.3.

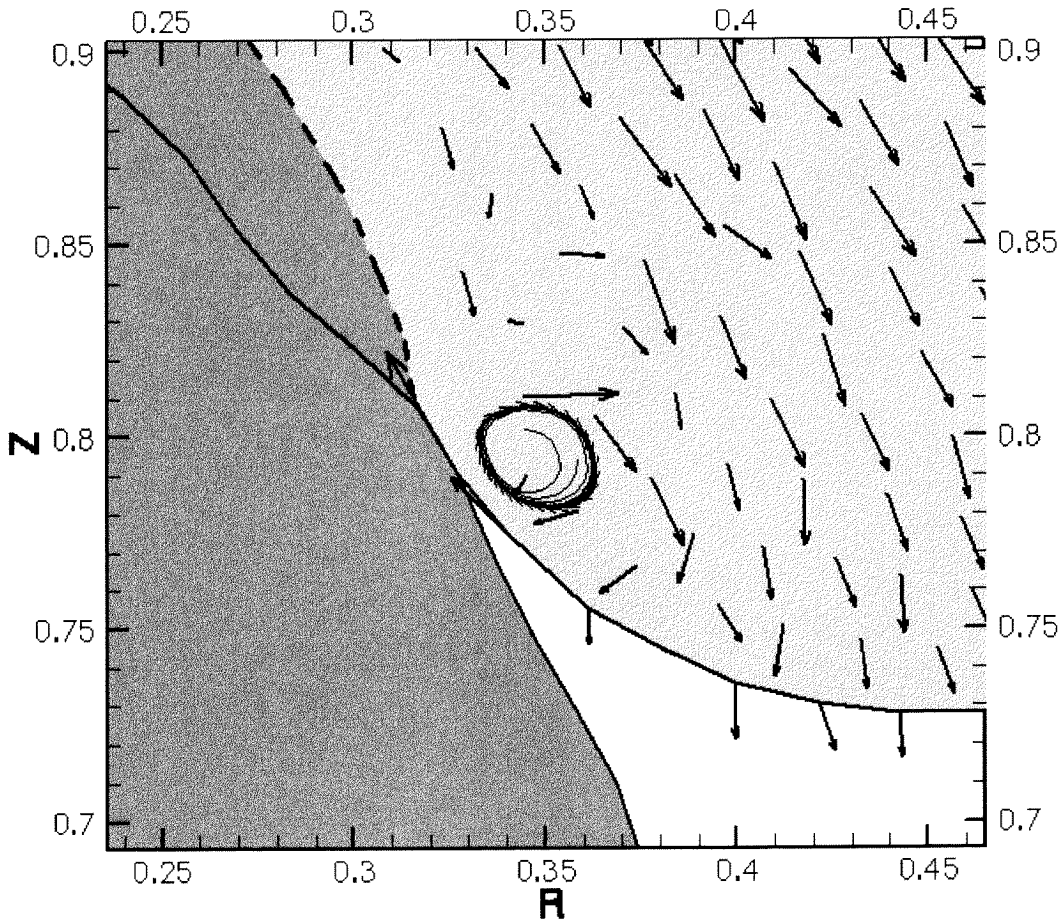

Figure 41: Rolling motion in the vicinity of the contact line. The dark region signifies solid material, the light region signifies still liquid material. The thin, black lines correspond to streamlines

Furthermore, and more importantly, the solution of the Navier-Stokes equations accounts for the creation of liquid/solid interface due to the momentum of the impacting and deforming droplet. Since the fluid domain is triangulated into small, linear elements with a finite edge

length, every attachment of a free surface node of the impinging droplet to the free surface of the predeposited droplet causes such a step-like increase of the spread factor. Between these step increases, Figure 40, a slight receding motion of the contact line can be identified causing the saw tooth shape. This receding motion of the contact line during the spreading phase can be explained. The character of the Navier-Slip model, as applied to the impact of a droplet, causes a rolling motion at the contact line. This means that fluid elements at and near to the free surface of the impinging droplet, very close to the contact line, are moving into the direction of the contact line, Figure 41. At the contact line, the free surface is consumed in favour of the creation of new liquid – solid interface between the impinging and the presolidified droplet. This rolling motion is not an artifact of the Navier-Slip model. It has also been observed experimentally by, for example, Dussan et. al. [63,82-84]. The velocity vector at the contact line, Figure 41, is directed to the interior of the impinging droplet. Also shown is a recirculation zone, an instantaneous vortex in the vicinity of the contact line, further illustrating the rolling motion which takes place.

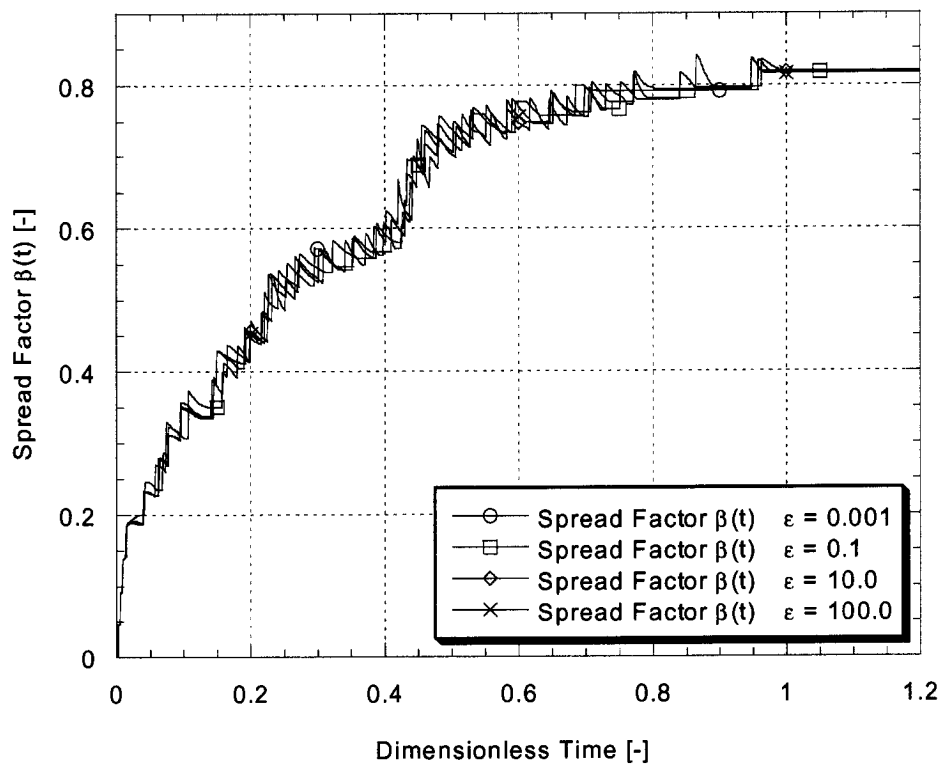

Figure 42: Numerically obtained evolution of the spread factor β(t). The dimensionless impact parameters for this case are: Re 376, We = 4.28, Fr = 2867, Ste = 0.895. The slip parameter are ε = 0.001, ε = 0.1, ε = 10.0, ε = 100.0

Regarding the dependence of the spreading process on the slip parameter ε, Figure 42 shows the temporal evolution of the spread factor for a host of values of ε. Although the slip parameter spans a range of 10^5, only slight differences in the spreading behaviour can be observed. The general behaviour of the spreading process remains the same yielding approximately the same final spread factors irrespective of the chosen value of the slip parameter. Hence, the local character of the flow in the very small contact line region, represented by the slip parameter, has practically no effect on the overall pile up process.

It has to be emphasized that the Navier-Slip model only allows for the movement of the contact line. It does not account for interfacial wetting phenomena. This means that uncompensated interfacial forces at the contact line, of the kind for instance modelled by the well known Young-DuPré equation [85], Equation 72 / Figure 43, are not balanced in the numerical solution.

$$\gamma_{LG}\cos\psi + \gamma_{LS} = \gamma_{GS} \tag{72}$$

where the indices LG, LS, and GS pertain to the liquid-gas, the liquid-solid, and the gas-solid interface, respectively.

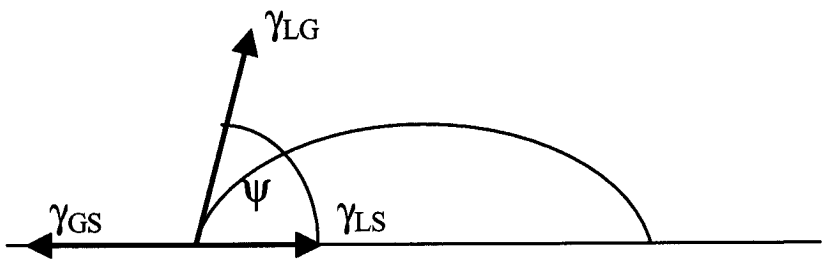

Figure 43: A liquid droplet on a solid substrate. Surface tensions at the contact line and the contact angle.

As an example, Figure 44 shows the maximum spreading stage of a droplet impinging at a velocity of 0.01 [m/s]. In terms of dimensionless numbers this case is defined by the following set of Reynolds, Weber, and Froude number: Re = 2.51, We = 0.019, Fr = 0.13. This is equivalent to gently placing a droplet on top of another. As can be seen, the droplet behaves like a rubber ball with an elasticity defined by the surface tension of the fluid. No wetting in the sense of equilibration of the contact angle occurs. Thus, the Navier-Slip model only accounts for contact line movement induced and dominated by inertia.

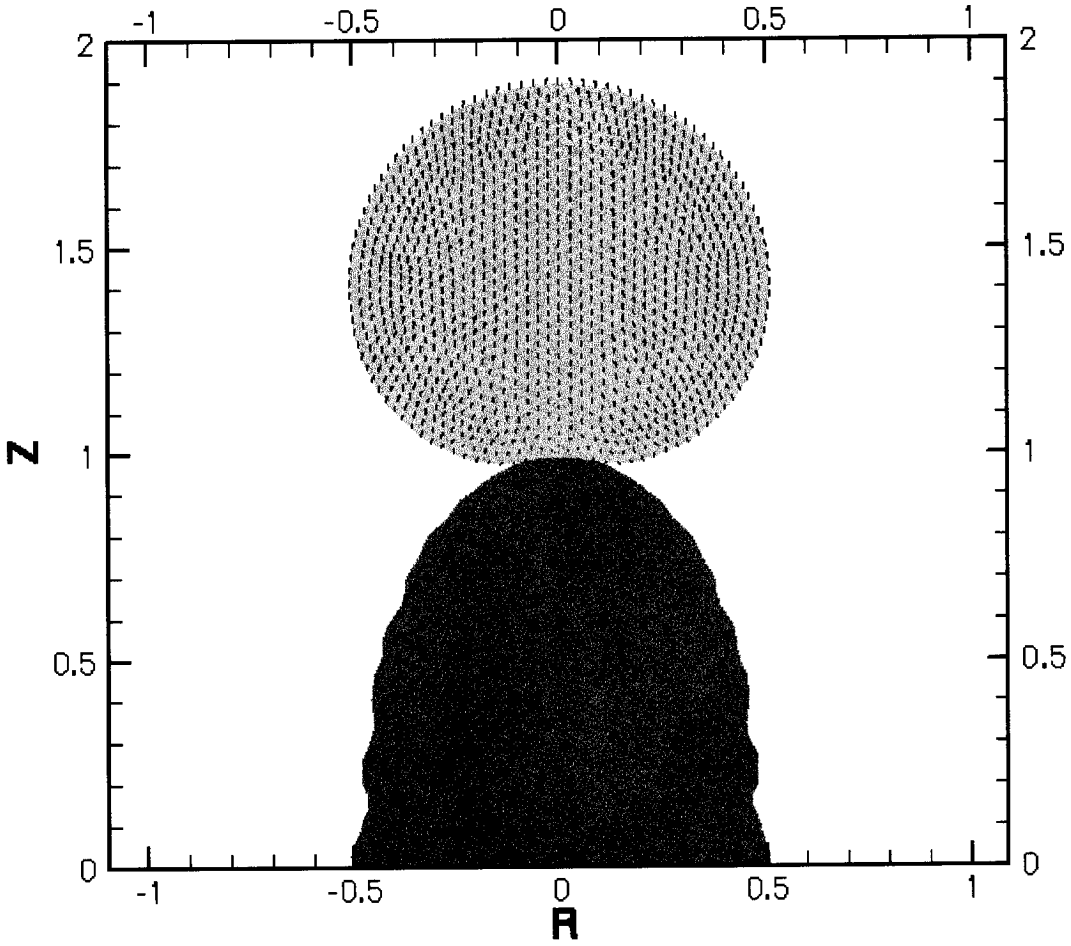

Figure 44: Maximum spreading and deformation of a droplet impinging with the following dimensionless impact numbers: Re = 2.51, We = 0.019, Fr = 0.1274. The slip parameter is ε = 0.001. The simulation does not account for conjugate heat transfer.

This is the case for the impact conditions of all the pile ups investigated in this study, Table II, due to the contact line velocities which are approximately on the same order of magnitude as the impact velocity. This situation holds at least for the initial stages of the spreading. At later stages, shortly before the contact line is arrested and the final spread factor is obtained, the contact line velocity tends to zero and the influence of inertia at the contact line becomes negligible. During this stage the contact line behaviour should be controlled by capillarity. This means that, in the absence of inertia, interfacial forces should dominate and cause a flow pattern aiming at equilibrating interfacial energies. This is equivalent to balancing the Young-DuPré equation [85] which means that the system is forced to attain equilibrium contact

angles. A representative situation of this last stage of the spreading process is shown in Figure

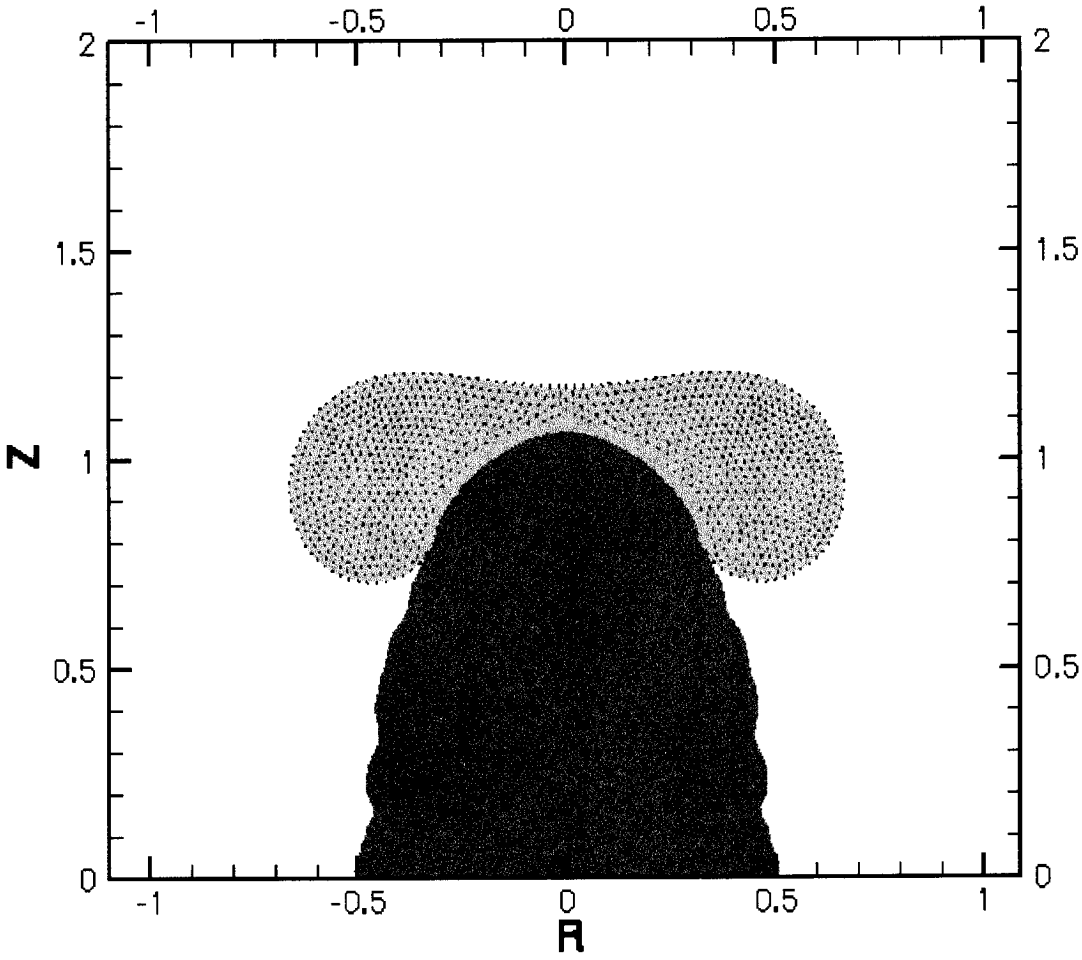

Figure 45: Maximum spreading and deformation of a droplet impinging with the following dimensionless impact numbers: Re = 376, We = 4.28, Fr = 2867, Ste = 0.895. The slip parameter is $\varepsilon = 0.001$. No capillarity effects occur at the contact line.

As can be seen, the contact line is not solidified yet and has stopped moving. The impinging droplet has just changed from the spreading to the recoiling regime. This means that the initial momentum of the droplet is currently stored, to a large part, as potential energy of the deformed surface. The contact angle thereby features a value of approximately 175°. This corresponds to a non-wetting situation. As is known from the literature [85,86] most substances feature a good wettability on substrates of their own kind. It has to be expected that the equilibrium contact angle between liquid and solid solder should gradually adjust to a value much smaller than the above value. Thus, based on the Young-DuPré equation, Equation 72, a

wetting motion at the contact line should take place during the last stage of the spreading process. However, it has to be emphasized that this period with low inertia effects during which the non-solidified contact line has stopped moving is short. Numerical simulations, for the sample case mentioned above, predict this time period to be on the order of approximately 15 [μs]. This is reasonable following inspection of Figures 16, 19, and 22, showing the experimentally determined spreading and oscillation process. The first minimum in the oscillation of the impacting droplet lies in the last stage of the spreading process and covers a time period which is approximately the same as predicted by the numerics. Thus, it is not expected that in this short time period an equilibration of the interfacial energies, respectively the contact angles, occurs. However, it is expected that the spreading behaviour in the last stage could be influenced by capillarity. If the details of the contact line region are of importance capillary phenomena in this region need to be carefully considered and this can only be done with experimental input to numerical simulations. The Navier-Slip model is an appropriate approach to circumvent the moving contact line problem. However, it is not capable to account for the above described wetting phenomena.

4.6 Influence of the Artificial Compressibility Method on the Numerical Solution

In an incompressible flow, a disturbance in the pressure causes waves that travel with practically infinite speed. With the introduction of an artificial compressibility, as described in section 3.2.1, these waves travel with finite but large speed. The magnitude of this speed thereby depends on the artificial compressibility parameter [87]. The latter is, as follows from inspection of Equation 36, equal to the inverse square of the Mach number. As stated by Ferziger et. al. [57], by adding a time derivative of the pressure to the continuity equation, Equation 28, the true incompressible equations are no longer solved. As a result, the time history generated cannot be accurate and the applicability of artificial compressibility methods to unsteady incompressible flows can be questioned and needs to be justified. Among others Chang et. al. [88] published a thorough study on the accuracy of the artificial compressibility method. They derived an upper and lower bound within which they showed both sufficient accuracy as well as stability of the method. Transferring their expressions for these bounds, which were derived for a channel flow, to the case of an impinging droplet leads to the following two requirements on the choice of the Mach number:

$$\frac{1}{Ma^2} >> \frac{1}{\rho u_{z0}^2}\left[\left(u_{z0} + \frac{4d_0}{Re}\right)^2 - u_{z0}^2\right] \tag{73}$$

$$O\left(\frac{\Delta\tau}{Ma^2}\right) < 1 \tag{74}$$

The control variable in the artificial compressibility parameter, or the Mach number, is thereby the speed of sound which follows from inspection of the definition of the Mach number, Equation 4. Employing again the same sample case as in the previous section, Re = 376, We = 4.28, Fr = 2867, and using the dimensionless time step $\Delta\tau = 10^{-3}$, the Mach number can thus lie in the range Ma = $2.3*10^{-4}$ – $3.1*10^{-2}$, in order to satisfy the above accuracy and stability criterion. To this end, a study on the influence of the Mach number on the pile up process is shown in Figure 46.

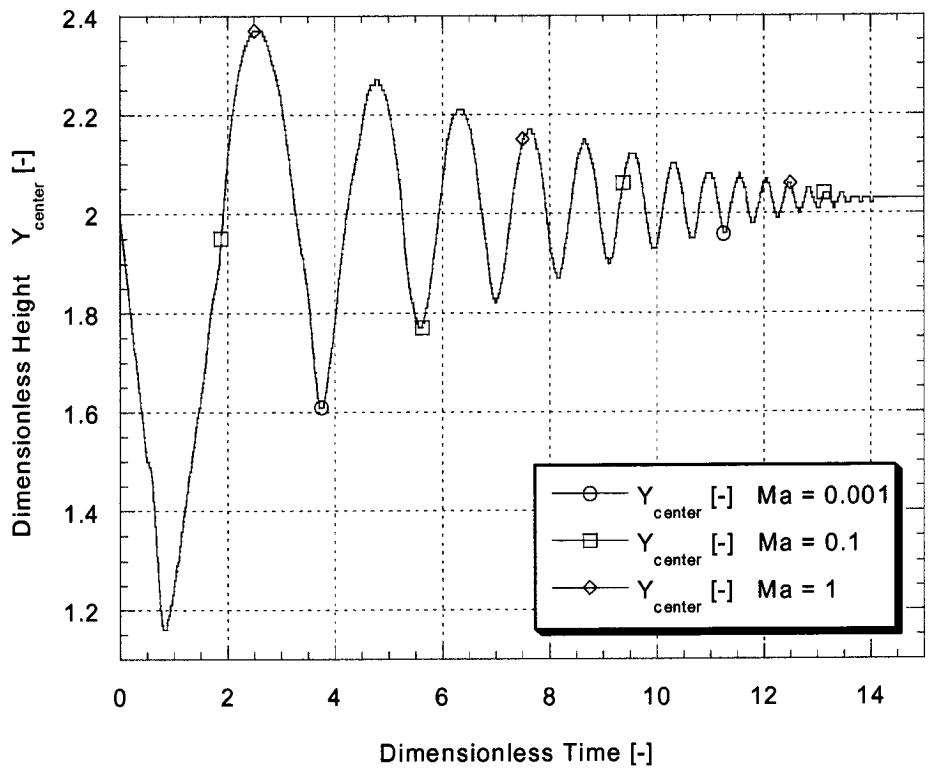

Figure 46: Oscillatory motion of the dimensionless pile up height for different values of the Mach number. The dimensionless impact parameters are thereby: Re = 376, We = 4.28, Fr = 2867.

The oscillatory motion of the dimensionless pile up height shows no influence on a representative range of Mach numbers.

The analysis of the artificial compressibility method shows that within the stability criterion given by Chang et. al. [88] the artificial compressibility parameter, or the Mach number, has negligible influence on the numerical solution of the pile up process. In the investigated range of the Mach number (Ma = 0.001 – 1) no difficulties pertaining to the stability of the numerical solution could be obtained. The reason why for Mach numbers outside the limiting range as given above, no difficulties pertaining to accuracy and stability could be observed, has to be attributed to the difference in geometry and flow physics between the present case and the case investigated by Chang et. al. [88].

4.7 Impact Parameters

The most relevant parameters affecting the flow of the impinging droplet in this study are the impact velocity (represented through the Reynolds number since it is assumed that the effect of viscosity is not important in the overall system) and the Weber number representing the relative importance of inertial to surface tension forces. These dimensionless groups contain the information on the impact velocity, the initial diameter of the droplet, the density, the viscosity and the surface tension of the impinging fluid. In addition to the Reynolds and Weber numbers, the nondimensionalization of the Navier-Stokes equations yields also the Froude and the Mach numbers, as described in section 3.2.4. As follows from the previous section the influence of the Mach number is negligible. The Froude number, as the fourth dimensionless parameter in the flow equations, has a negligible influence as well. This follows immediately from inspection of the definition of the Froude number, Equation 3, and the range of diameters and velocities in this study, Table II. Gravity plays, as compared to the initial inertia of the impinging droplets, a negligible role since the droplets are so small (featuring a low mass) and their surface tension is large. The Reynolds and Weber numbers are the dimensionless parameters which control the fate of the droplet [41,89] in most isothermal cases. On flat substrates, both the amount of spreading and the deformation of the droplet increase with increasing impact velocity or Reynolds and Weber number, as for instance shown by [28,29,41,89,90]. The same has to be expected for the impact on non-flat substrates. To this end, Figure 47 shows the temporal evolution of the spread factor for

identical droplets impacting with the sets of dimensionless numbers given in Table VI, on identical, presolidified droplets.

Case	Reynolds [-]	Weber [-]	Froude [-]	Stefan [-]
1	251	1.90	1274	0.895
2	345	3.60	2409	0.895
3	407	5.03	3364	0.895

Table VI: Dimensionless parameters regime for the impact cases.

As can be seen in Figure 47, the numerical simulation predicts the same qualitative behaviour as occurs for droplet impacts on flat substrates. With increasing impact velocity, respectively Reynolds number, the maximum as well as the final spread factor for the cases 1 – 3, Table VI, increase.

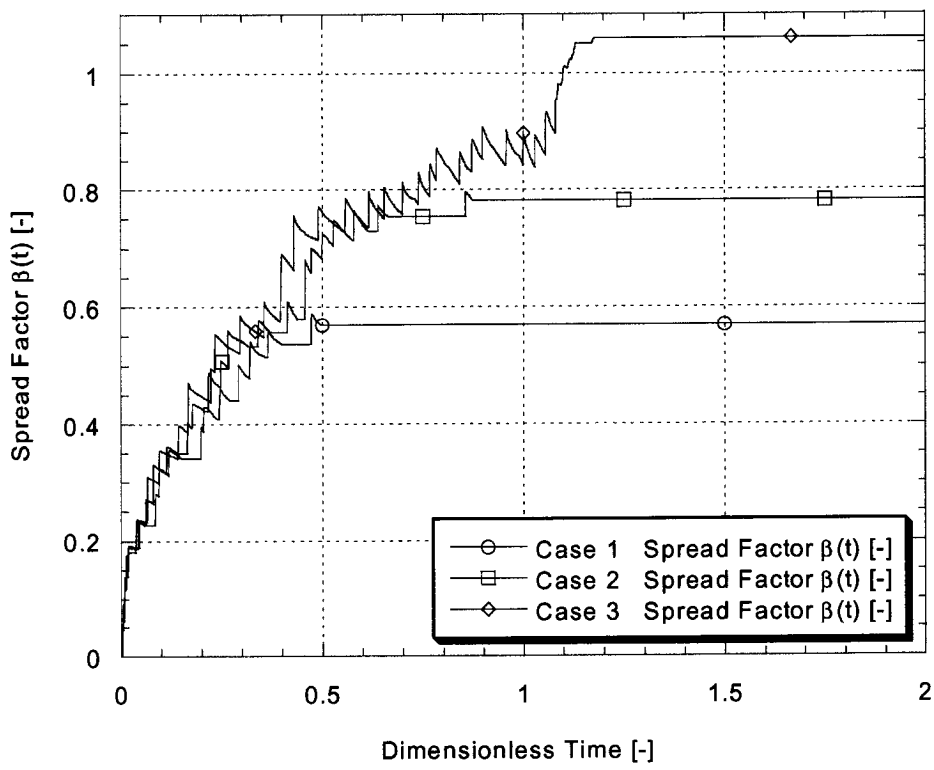

Figure 47: Temporal evolution of the spread factor for different impact regimes. Case 1: Re = 251, We = 1.90, Fr = 1274; Case 2: Re = 345, We = 3.60, Fr = 2409; Case 3: Re = 407, We = 5.03, Fr = 3364. The Stefan number is for all cases the same Ste = 0.895.

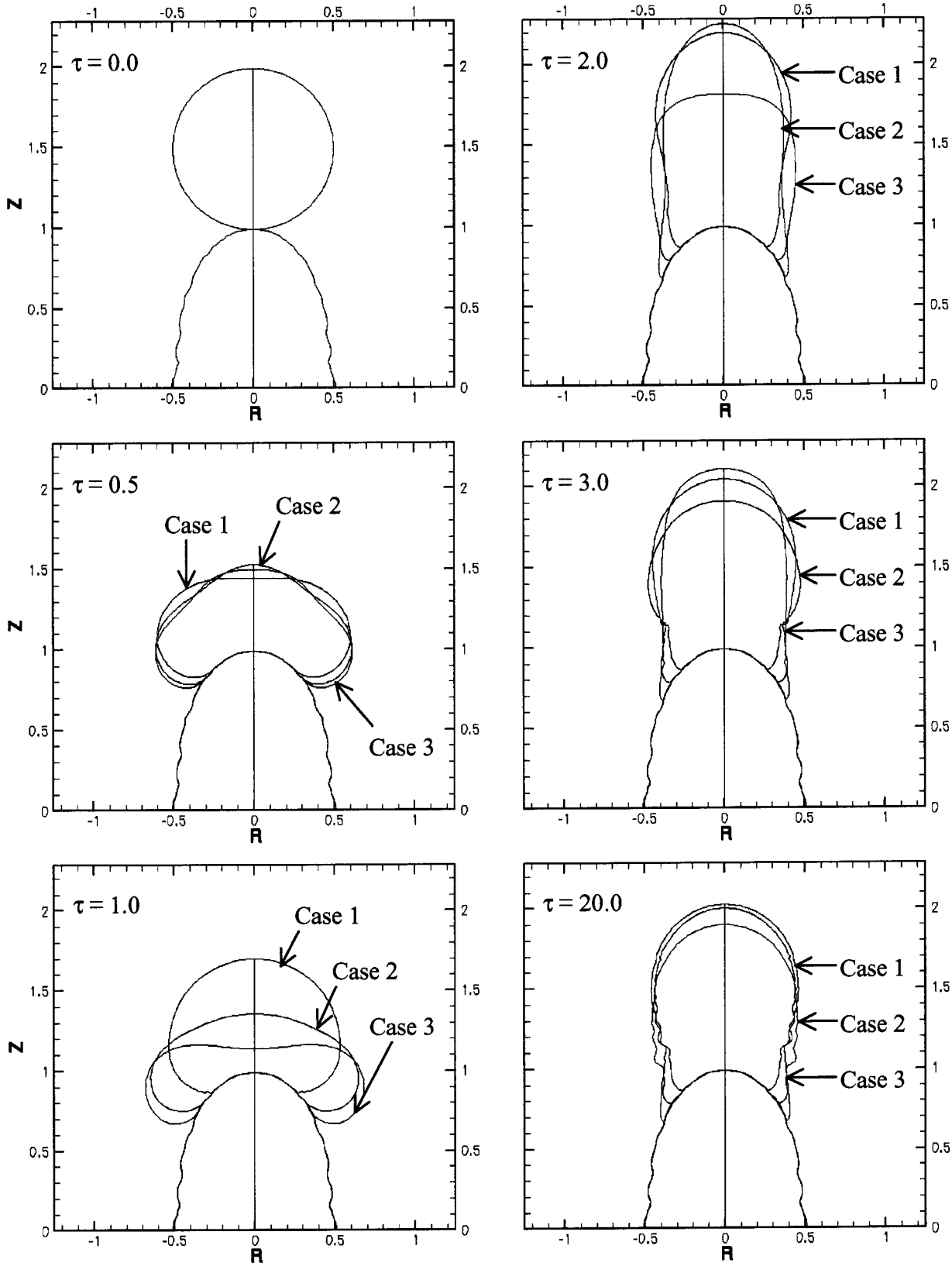

Figure 48: Impact stages and final solidified shape for different impact regimes. Case 1: Re = 251, We = 1.90, Fr = 1274; Case 2: Re = 345, We = 3.60, Fr = 2409; Case 3: Re = 407, We = 5.03, Fr = 3364. The Stefan number is for all cases the same Ste = 0.895.

The deformation of the corresponding droplets increases also with increasing Reynolds number (impact velocity) as shown by the successive impact stages in Figure 48. This affects, of course, the final shapes of the pile up (τ = 20) as well, as also shown in Figure 48. Nonetheless, the variation of the impact parameters is limited by an upper as well as by a lower bound depending on the capabilities of the numerical code as well as the model. As discussed in section 4.5 the numerical model does not include capillary effects which become increasingly important for droplets impinging at very low impact velocities. On the other hand, the impingement of droplets at higher impact velocities can lead to other difficulties that can be attributed to algorithmic limits of the numerical code. One such difficulty occurs when an impinging droplet impacts at high Reynolds number (still without splashing) leading to a strong deformation at the droplet center. The concurrently progressing solidification front can thereby solidify the free surface of the impinging droplet in the center region as shown in Figure 49.

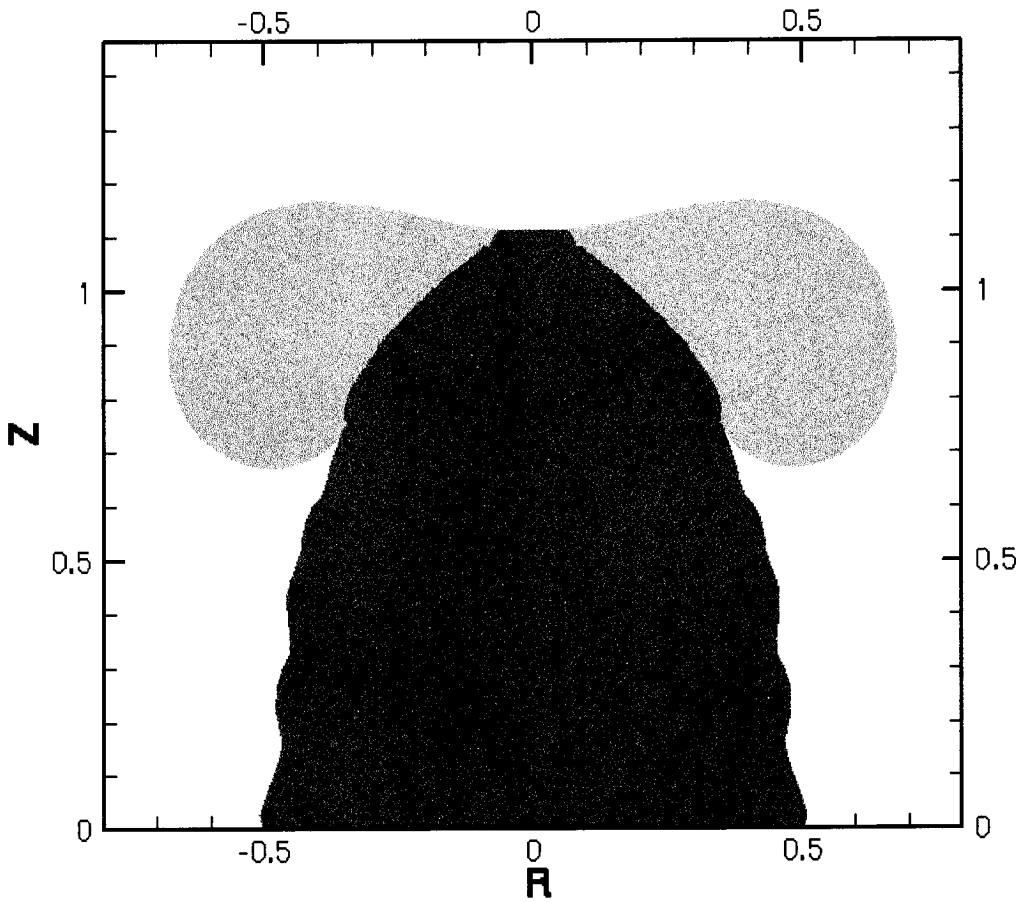

Figure 49: Solidification of the free surface of the impinging droplet at the line of symmetry due to large deformation. The dimensionless impact parameters are: Re = 407, We = 5.03, Fr = 3364, Ste = 0.895, Bi_s = 0.05, Bi_l = 0.5. The dark shaded region signifies solid material, the light shaded region signifies liquid material.

The still liquid domain of the impinging droplet thereby forms a torodial shape. The difficulty with this event is the separation of the still liquid domain from the line of symmetry. When the toroidal fluid domain recoils the free surfaces will connect again at the line of symmetry. This coalescence is at least locally a complex phenomenon where capillary forces reduce the large curvatures at the rapidly growing area of contact. This happens at very short time scales probably on the order of magnitude of the computational time step employed in the present study [91]. Furthermore, coalescence can lead to an inclusion of an air bubble in the liquid domain. This would require the numerical solution of the compressible air domain as well as accounting for an internal free surface boundary inside the fluid domain. The treatment of such a situation is well outside the scope of this thesis. In addition, the domain of its occurrence is outside the parametric range of the technology of interest.

A further modeling difficulty is the possible break up of an impinging droplet as shown in Figure 50. Such a situation can occur depending on the impact numbers as well as on the rate of solidification. Hence, this is also depending on the Biot number or the Stefan number. Solidification at the contact area between the impinging and the presolidified droplets control to a very large extent the shape and the transients of the pile up process, as described in sections 2, and 4.4. Furthermore, solidification annihilates kinetic energy [48]. Thus, when the contact line is not arrested by solidification or capillarity, leading to a bonding between the impinging and the presolidified droplet, the droplet can bounce off (i.e. detach from the substrate) when the initial kinetic energy is not dissipated by viscosity. On the other hand, as is the case shown in Figure 50, when the final spread factor and the solid fraction are small at late stages of the recoiling process but solidification has already connected the droplet to the substrate, recoiling-break up can occur. This means, that the droplet can form a bottle neck at the location of smallest cross-sectional radius, driven by capillarity as well as the upward momentum of the bulk of the droplet. The associated difficulty is not the lack of knowledge concerning the prediction when the liquid structure becomes unstable and breaks up. This can be modeled based on Rayleigh's theory on the instability of liquid filaments [42]. It is the difficulty arising through the lack of knowledge on the time scales of the break up, the small curvatures which cannot be properly represented by the finite sized elements of the numerical method, and the local momentum created by the break up in the emerged liquid cusps [42]. All these items can of course be handled numerically with empirical laws that circumvent the above mentioned difficulties without proper consideration of the underlying physics. In this dissertation, break up of the impinging droplet is not considered for it is little relevant to the technology of interest.

The above mentioned upper and lower bounds for the variation of the impact parameters are only partially reached in the experimental impact regime considered in section 2, Table II. Concerning the lower bound, the lack of modeling of capillary effects only occurs in the final stages of the spreading process. Such effects occur and influence the results as will be discussed in section 5. Concerning the upper bound, recoiling-break up of the impinging droplets could not be observed in the experimental cases studied for impact velocities up to 2 [m/s].

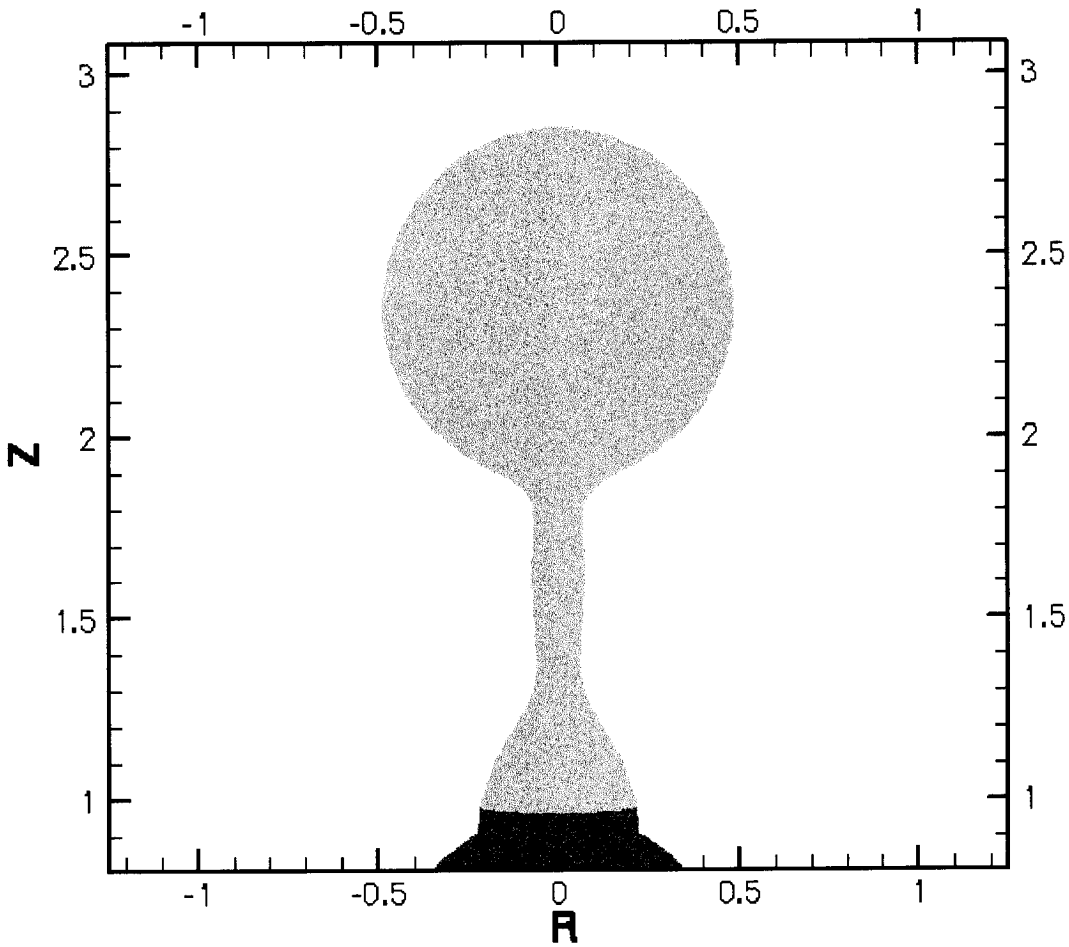

Figure 50: Bounce off scenario during the recoiling stage of an impinged droplet. The dimensionless impact numbers are: Re = 407, We = 5.03, Fr = 3364, Ste = 0.895, $Bi_s = 0.01$, $Bi_l = 0.1$. The dark shaded region signifies solid material, the light shaded region signifies liquid material.

4.8 Summary

The numerical simulations perform very well concerning the conservation of mass and energy. The pressure solution method employed in order to impose a divergence free velocity field shows no stability or accuracy problems. The latter is assumed on the basis that the Mach number, as the parameter controlling the artificial compressibility method, features no influence on the numerical results, as follows from section 4.6. The choice of the Navier-Slip model and the slip parameter showed negligible influence on the numerical solution, as follows from section 4.5. It can be speculated that imposing, in addition to the Navier-Slip model, a contact angle boundary condition [21] would increase the influence of the slip parameter by reducing or even circumventing the attachment of free-surface nodes of the impinging to the presolidified droplet. As follows from sections 4.4 and 4.7 the impact velocity (Reynolds number) and the Weber number for the fluid mechanics, coupled with the Biot numbers and the Stefan number for the heat transfer constitute the predominant dimensionless numbers controlling the numerical model. All these groups are known from the design parameters of the process except for the Biot numbers the determination of which relies on estimated values and/or experimental data on the transient contact resistance, where only a very limited data base exists currently in the open literature.

5. Comparison between Experimental and Numerical Results

5.1 Objectives

The previous section showed that, given a specific substrate shape, the numerical model can be employed to investigate the effect of a host of parameters represented by a number of dimensionless groups. These are the Reynolds, Weber, the two Biot numbers (solid/solid interface, Bi_s, and liquid/solid interface, Bi_l), as well as the Stefan number. The objective of this section is to simulate the experimentally visualized cases of the pile up numerically, for characteristic ranges of the above mentioned dimensionless numbers. A compilation of the experimental cases is given in Table II. The intention is to determine to which extent the versatile numerical model is able to predict the physical phenomena occurring during a pile up, to identify the prevailing mechanisms and to explain why the model does not perform satisfactorily in cases where this is true. Based on the previous section it is assumed that the influence of the Mach number and the slip parameter is negligible. Thus, these parameters are kept constant throughout the simulations (Ma = 0.001, ε = 0.005) in this section. Furthermore, the thermal contact resistance between the presolidified droplet and the wafer substrate (Region 3, Figure 27) is assumed constant with the value given in Equation 71.

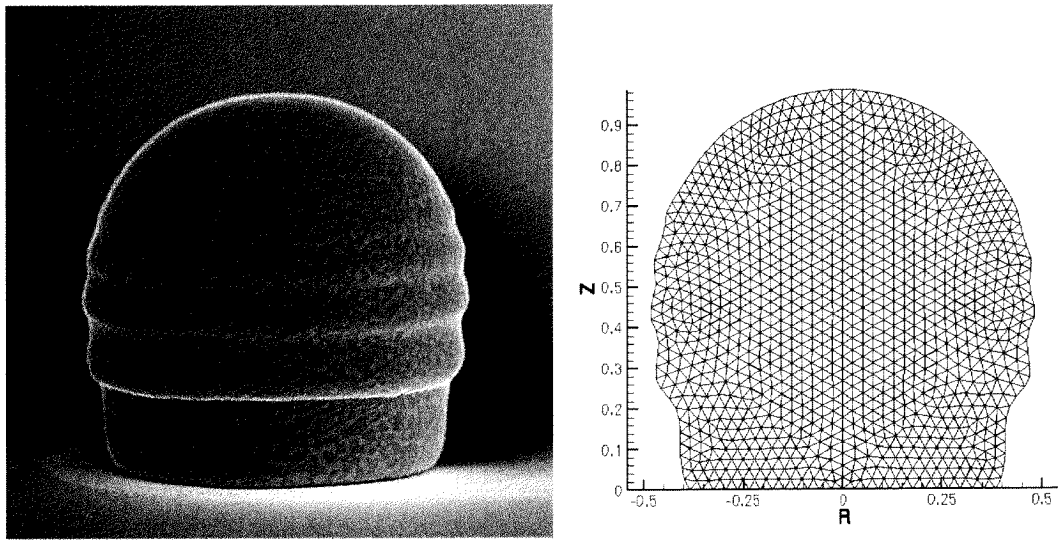

Figure 51: SEM micrograph of a presolidified droplet and the corresponding digitised FEM grid.

Given the values of the dimensionless numbers (Reynolds, Weber, Froude, Stefan) in Table II, and the thermophysical properties of the investigated materials in Appendix A, only the two Biot numbers are the unknown (no data for the thermal contact resistance exist in the literature) and need to be determined by matching numerical and experimental end shapes of the solidified microdroplet.

The initial substrate shapes (i.e. the presolidified droplet on the wafer substrate) were obtained by digitising SEM micrographs of single, solidified droplets. A representative example of such a SEM micrograph with the corresponding FEM grid of the presolidified droplet is shown in Figure 51. The initial substrate shape could have also been obtained numerically by solving the impact of a single droplet on a flat substrate as has been done previously by a number of authors [4,14,55]. However, by directly digitising SEM micrographs of the presolidified droplet all the microscopic surface features are correctly taken into account.

5.2 Comparison in the Impact Regime

The matching of the numerical simulations with the experimental cases 7 – 12, Table II, is based, as mentioned above, on solely varying the two Biot numbers Bi_s, and Bi_l. This was done extensively for all cases pertaining to the impact regime. The Biot numbers were thereby varied in the same range as described in section 4.4.2 (e.g. $Bi_s = 0.01 - 1$, $Bi_l = 0.01 - 1$).

Numerical Case	Reynolds [-]	Weber [-]	Stefan [-]	Biot Bi_s [-]	Biot Bi_l [-]
7	281.39	2.39	0.895	0.2	0.9
8	303.65	2.91	0.895	0.2	0.9
9	344.51	3.61	0.895	0.2	0.9
10	363.89	4.17	0.895	0.2	0.9
11	396.29	4.91	0.895	0.2	0.9
12	453.16	5.99	0.895	0.2	0.9

Table VII: The relevant dimensionless numbers and optimal values of the Biot numbers for the numerical cases for the impact regime.

In general, the same results concerning the strong influence of the Biot number pertaining to the solid/solid interface compared to the weak influence of the Biot number pertaining to the liquid/solid interface was observed. For the sake of brevity, only the results corresponding to the optimal values of the Biot numbers, giving the best conformity between the experimental and numerical cases, are shown and discussed herein. Table VII presents the relevant dimensionless numbers corresponding to the numerically simulated cases (the numerical cases are numbered in the same fashion as the experimental cases). The values of the Reynolds, the Weber and the Stefan number are taken from Table II. The Biot numbers in Table VII represent the optimal values of the latter. As follows from Table VII the Biot numbers leading to the best conformity between the experimental and numerical cases are practically equal for all cases.

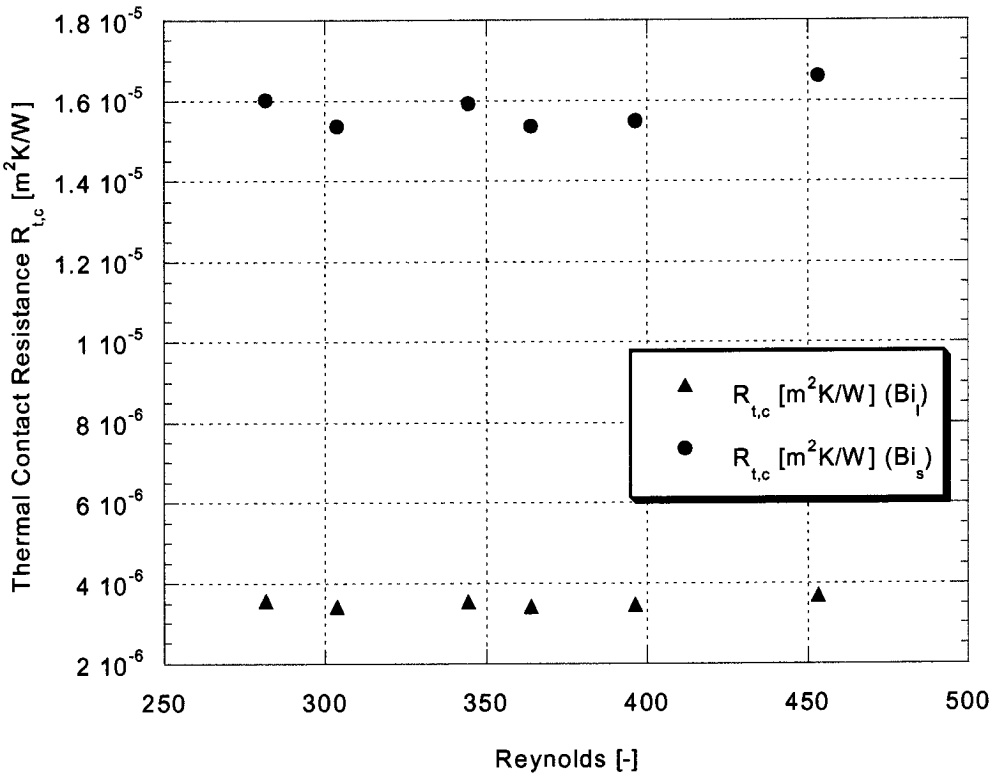

Figure 52: Optimal thermal contact resistances for the impact regime in function of the Reynolds number.

A compilation of the actual thermal contact resistances as a function of the Reynolds number is shown in Figure 52. No dependence between the impact velocity and the corresponding thermal contact resistance exists for the impact regime investigated herein. This result points

to an independence (for all practical purposes) of the Biot numbers employed in the thermal contact resistance model, described in section 3.3.3, on the impact velocities, for the narrow impact velocity range investigated in this study.

In general, a very good agreement between the experimental and the numerical cases was observed for the impact regime using the above values of the Biot numbers. Figures 53 and 54 show, representatively, the oscillatory motion of the center of the impinging droplet, Y_{center} [-] for two experimental and numerical cases (Case 7 and Case 12).

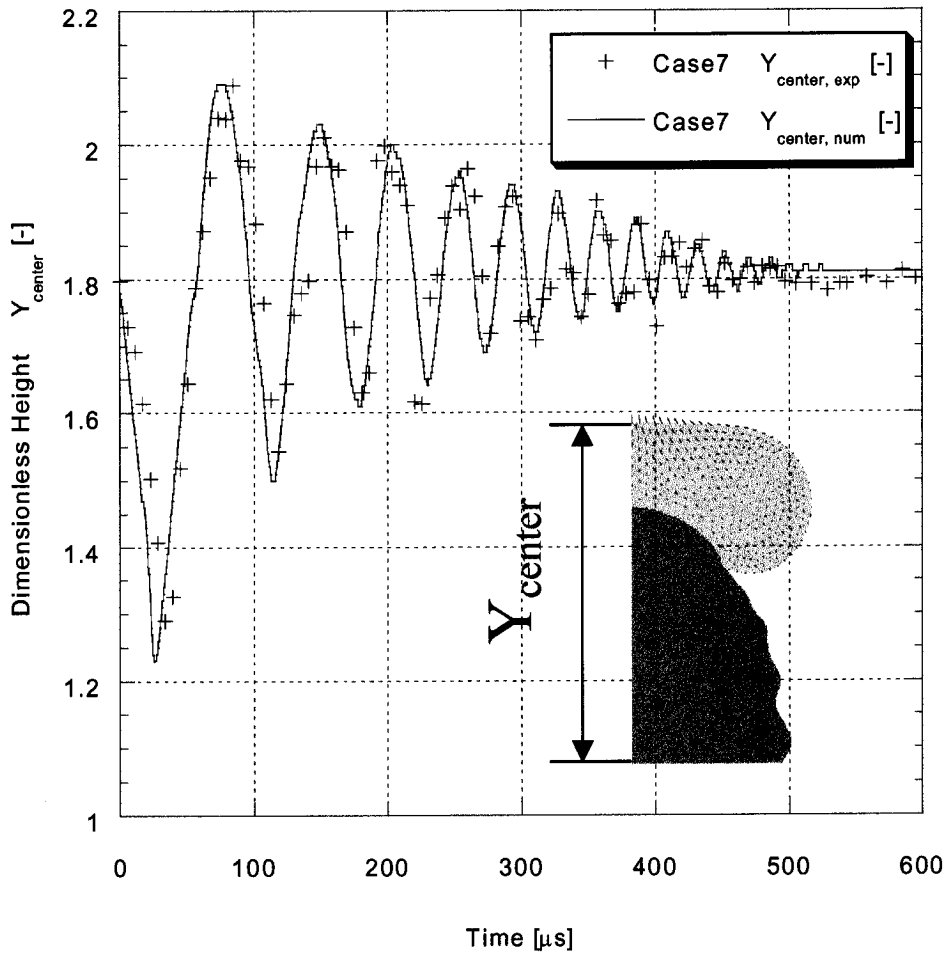

Figure 53: Temporal evolution of the dimensionless pile up height for Case7.

As can be seen, a very good matching in the transient behaviour as well as the actual pile up height of the experimental and the numerically simulated pile up process is achieved. The insets in the bottom corners of Figures 53 and 54 clarify the definition of Y_{center} for the numerical simulations. It is worth stressing at this point that the corresponding experimental values of the dimensionless pile up height, for cases of large deformations, actually

correspond to the rim height as viewed from the side and not to the center height of the droplet. Nevertheless, such large deformations occur primarily during the first oscillation cycle as shown in Figures 53 and 54. The experimentally measured dimensionless pile up heights are thus as a result larger than the numerical values, as can also be seen in Figures 53 and 54.

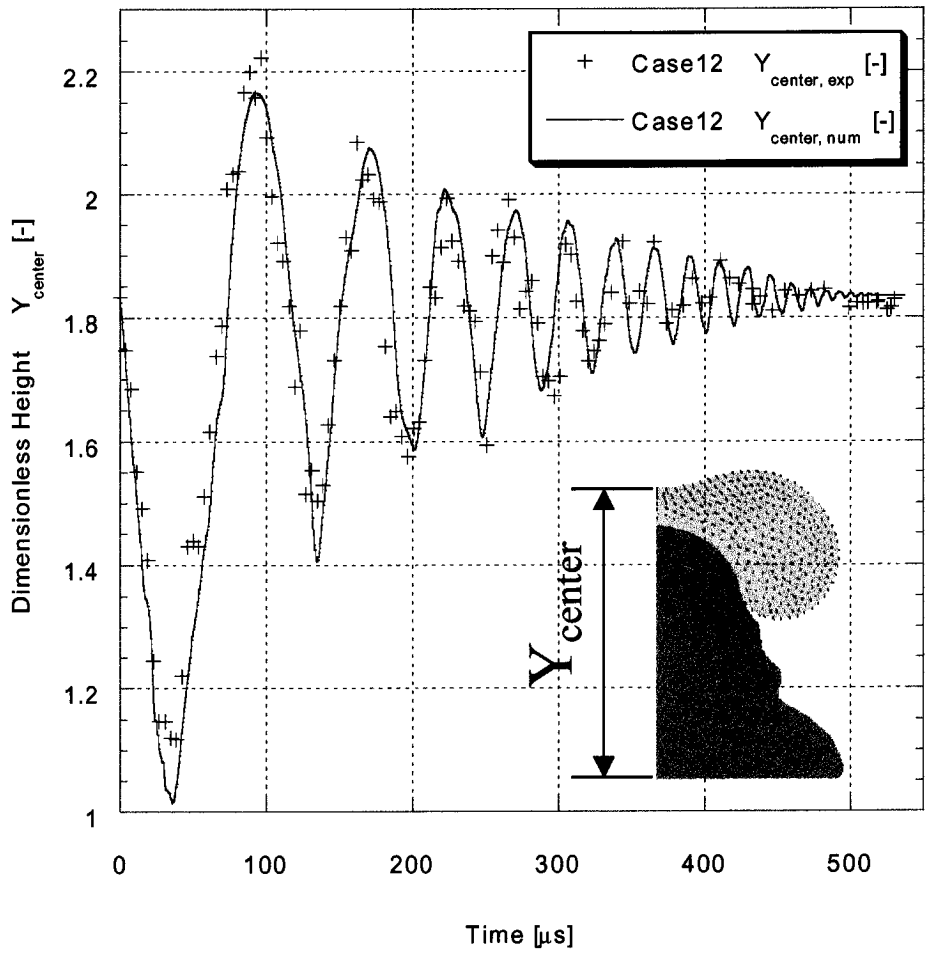

Figure 54: Temporal evolution of the dimensionless pile up height for Case12.

The final, solidified dimensionless pile up heights, $Y_{center,\infty}$, for both the experiments and the simulated cases are shown in Figure 55. As can be seen a good agreement is achieved.

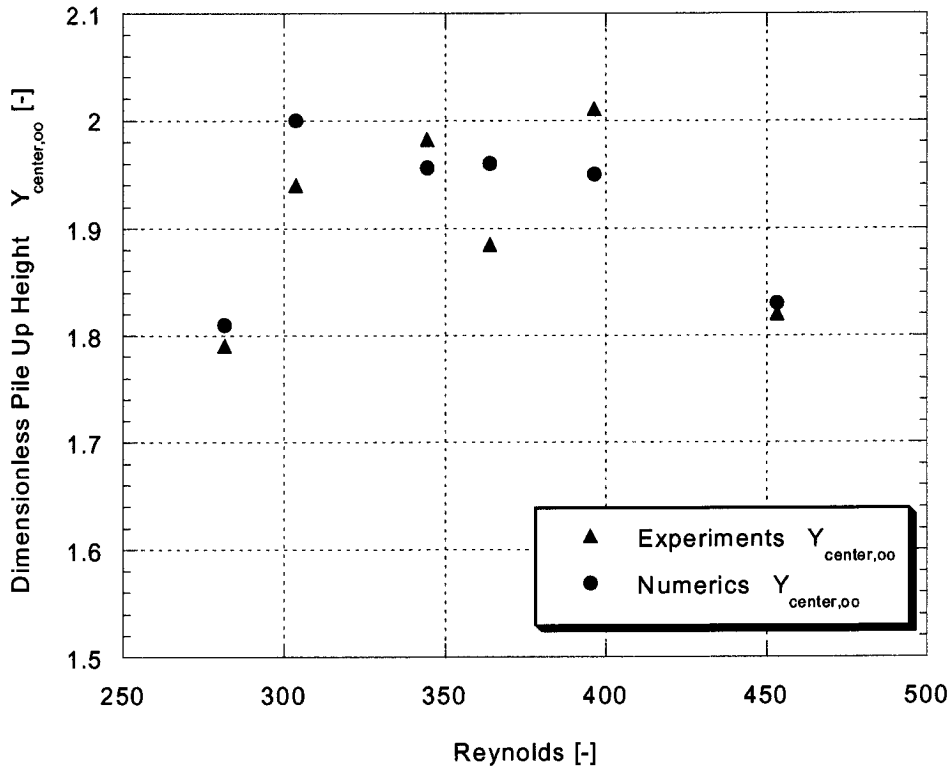

Figure 55: Experimentally measured and numerically calculated values of the final dimensionless pile up height for the impact regime.

The difference between the numerically calculated and experimentally measured heights is given in Table VIII.

Cases	7	8	9	10	11	12
$Y_{center,\infty}$[-] numerical	1.81	2.00	1.956	1.96	1.95	1.83
$Y_{center,\infty}$[-] experimental	1.79±0.03	1.94±0.02	1.98±0.03	1.885±0.02	2.01±0.03	1.82±0.04
Difference in %	1.1	3	1.2	3.8	2.98	0.5

Table VIII: Numerically calculated and experimentally measured dimensionless heights of the solidified pile up for the impact regime.

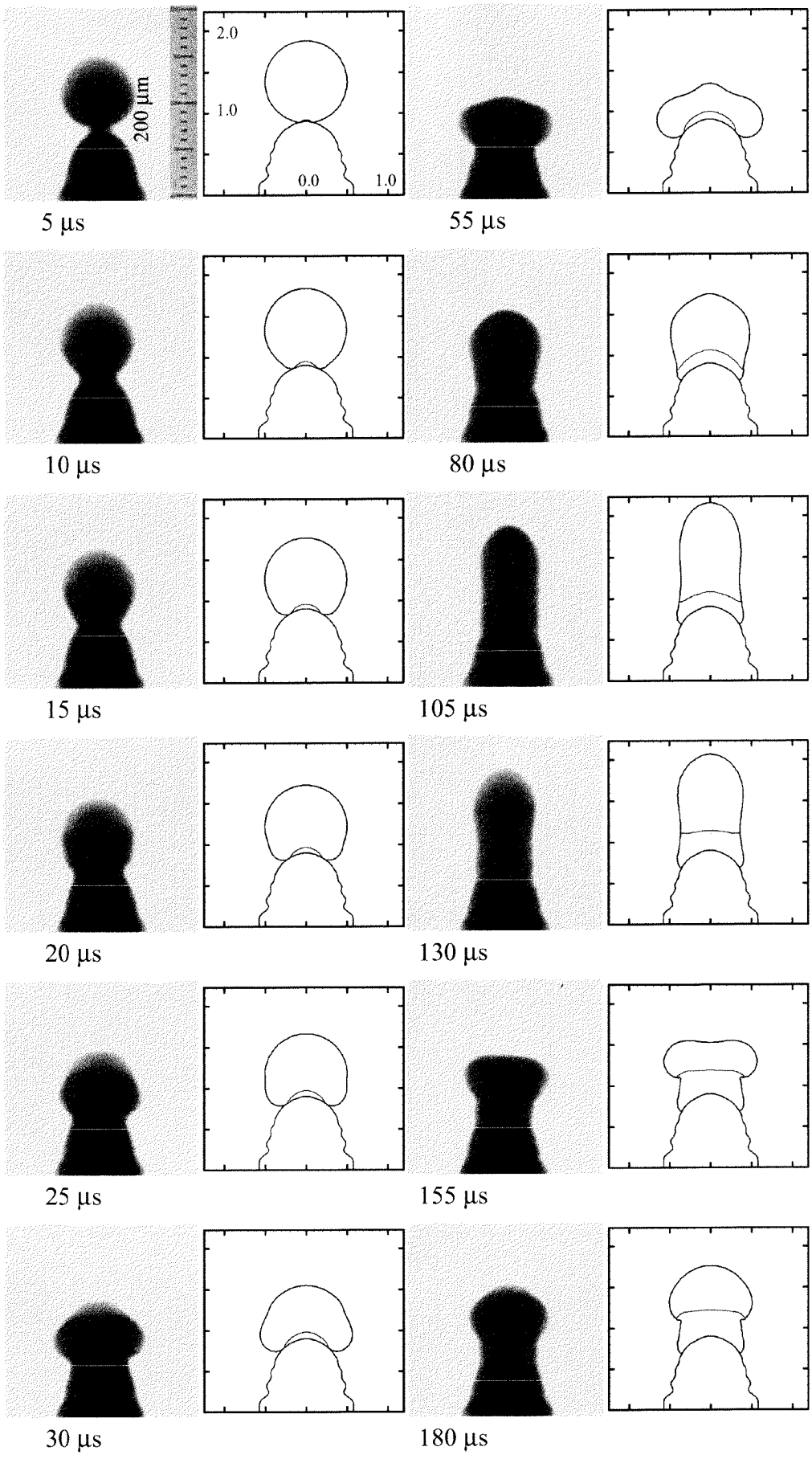

Figure 56 (continued)

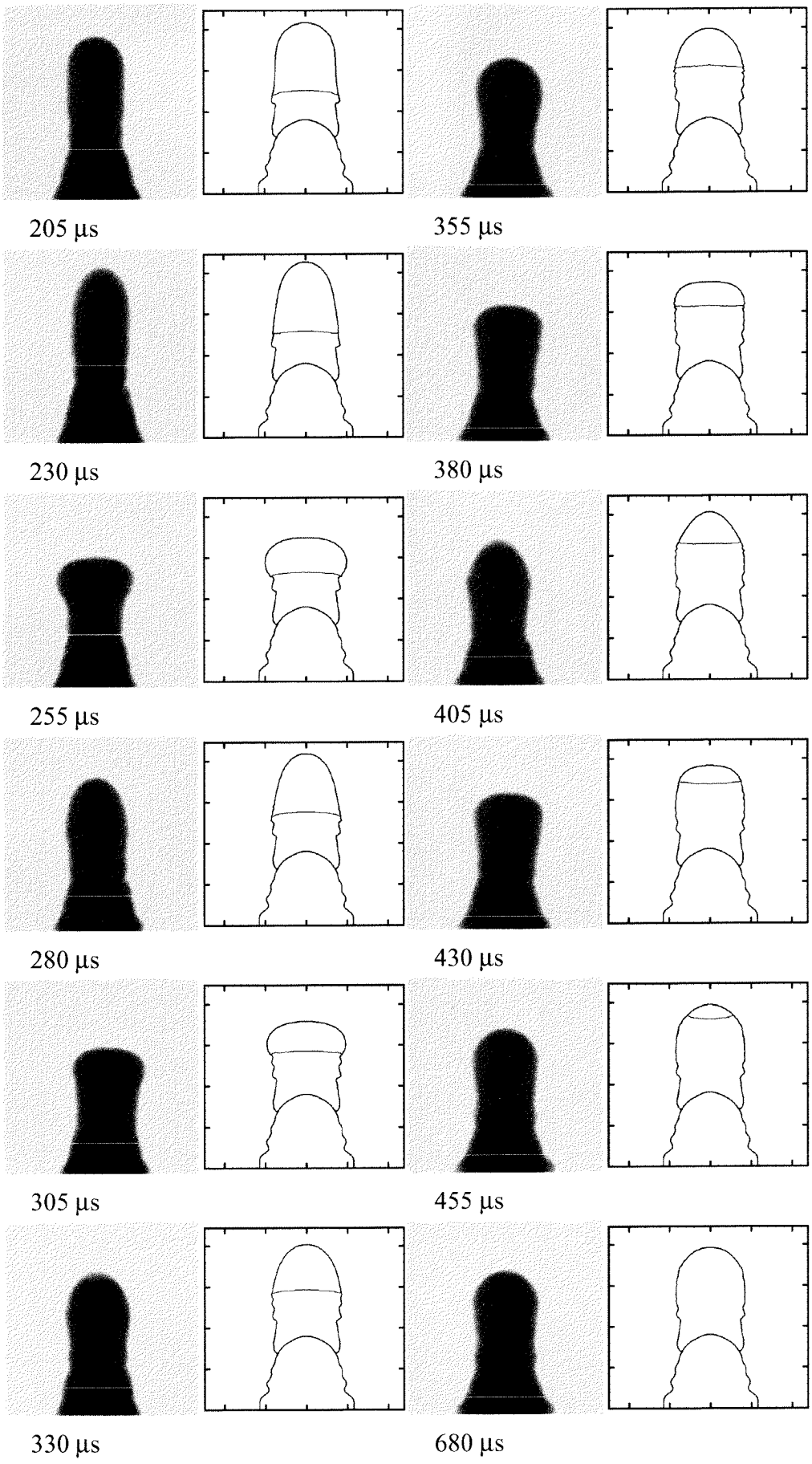

Figure 56: Experimentally visualized and numerically simulated sequence of Case10.

The experimental values given in Table VIII are averages of 20 measurements on different pile up structures of the same case. The variations of the latter, given in Table VIII, stem from the intertwined variations of the impact velocity and the initial diameter as described in section 2.5. In addition to the variation in the pile up height the estimated error of 5% of the initial diameter of the impinging droplet has to be accounted for. Nevertheless, a difference in the final pile up height of only a few percent has to be deemed as very good.

A sequence comparing the experimentally visualized and the numerically simulated pile up process of Case 10 is shown in Figure 56. Again, agreement between the experimental and the numerical results is demonstrated. However, during the initial stages of the impact (i.e. the first 55 microseconds of the impact), slight differences in the shape of the impinging droplet are visible. During this spreading period the largest part of the droplet is still liquid (including the advancing contact line). At later stages of the impact process, the temporal evolution of the shape of the impinging droplet shows very good agreement between the experimental result and the numerical simulation, Figure 56. The above mentioned shape differences are most of all visible in the contact line region respectively the dynamic contact angle of the impinging droplet. At this point it is worth discussing the limitations of the numerical treatment of the contact line because it is very relevant to forthcoming results when wetting effects are of importance. As discussed in section 4.5, the numerical model merely allows for a movement (slip) of the contact line in order to remove the stress singularity at this location. The Navier-Slip model does not permit the definition of a specific contact angle behaviour. This means the latter is defined based on the movement of the contact line as well as the hydrodynamic bending of the free surface of the impinging droplet due to the deformation of the fluid domain. No capillary/wetting effects or considerations of gradients in the interfacial energies of the system are taken into account in the numerical model as already mentioned in section 4.5. It has to be expected that the enforcement of a specific contact angle could influence the shape of the impinging droplet in particular in the contact line region. Dussan et. al. [63] reported studies on the influence of different slip boundary conditions on the overall flow field. They reported that different slip boundary conditions lead locally to differences in the flow field in the vicinity of the contact line. However, the overall flow field was not affected. This is analogous to the findings reported in section 4.5 on the influence of the slip parameter on the spreading behaviour. Two characteristic length scales were introduced by Dussan et. al. [63]: the slip length which is the microscopic region including the contact line, and the meniscus length scale which is the length scale at which most fluid mechanical measurements are made. According to the purely analytical study by Dussan et. al. [63] no

influence of the slip boundary condition on the meniscus length scale could be observed. The general conformity between the experimental and the numerical results, as exemplified by Figures 53, 54, and 56, lead to the conclusion that the numerical model accounts to a large extent for the prevailing mechanisms occurring during a pile up in the impact regime. The exception is the above mentioned discrepancy in the droplet shape during the spreading process. Thus, the latter is certainly influenced by the interfacial, respectively capillary, effects not accounted for by the numerical model due to the lack of the needed experimental data (for example on the dynamic contact angle) for the materials and geometries of interest. Such data if available could be easily incorporated in the numerical model. Therefore, by employing an appropriate boundary condition at the dynamic contact line these discrepancies at the meniscus length scale should be alleviated in contrast to the analytical predictions by Dussan et. al. [63].

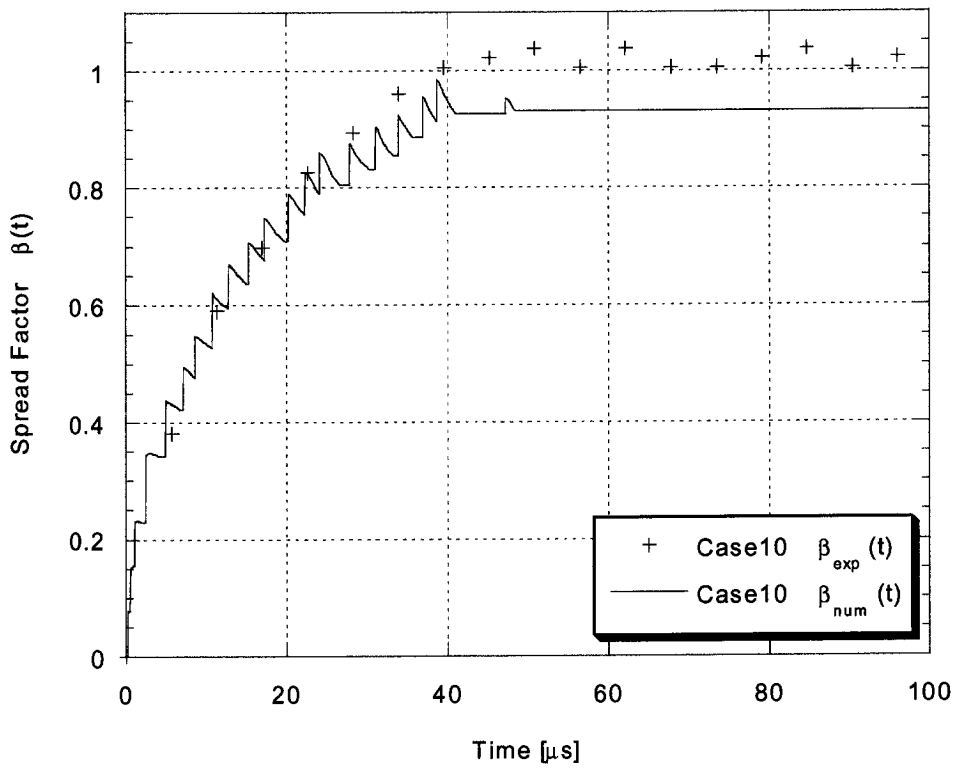

Figure 57: Experimentally measured and numerically calculated spread factor for Case10.

The influence of the above discussed dynamic contact angle/contact line phenomena on the spreading behaviour is shown, as an example, in Figure 57 for Case 10. Except for the saw tooth progression of the contact line, the numerical and experimental results agree very well during the initial stages of the spreading process. Thus, during the inertia driven part of the

spreading (see section 4.5), the numerical simulation predicts the spreading process very well, irrespective of discrepancies in the droplet shape at the meniscus length scale. The final stage of the spreading process, which is, as mentioned in section 4.5, critical due to possible capillary effects, shows some (but not large) discrepancy between the experimental and the numerical results. This leads to the conclusion that capillary effects indeed have, at the late stages of the spreading process and if freezing has not started until that point, an impact on the spreading. A compilation of the final spread factors for the experimentally visualized and numerically simulated cases of the impact regime is given in Figure 58 and Table IX. The numerical simulations follow very well the trend observed in the experiments. However, the experimentally measured final spread factors are a bit underpredicted by the numerical solution in all cases. This further points to the existence of a wetting mechanism during the late stages of the spreading process not accounted for by the numerical model as explained earlier.

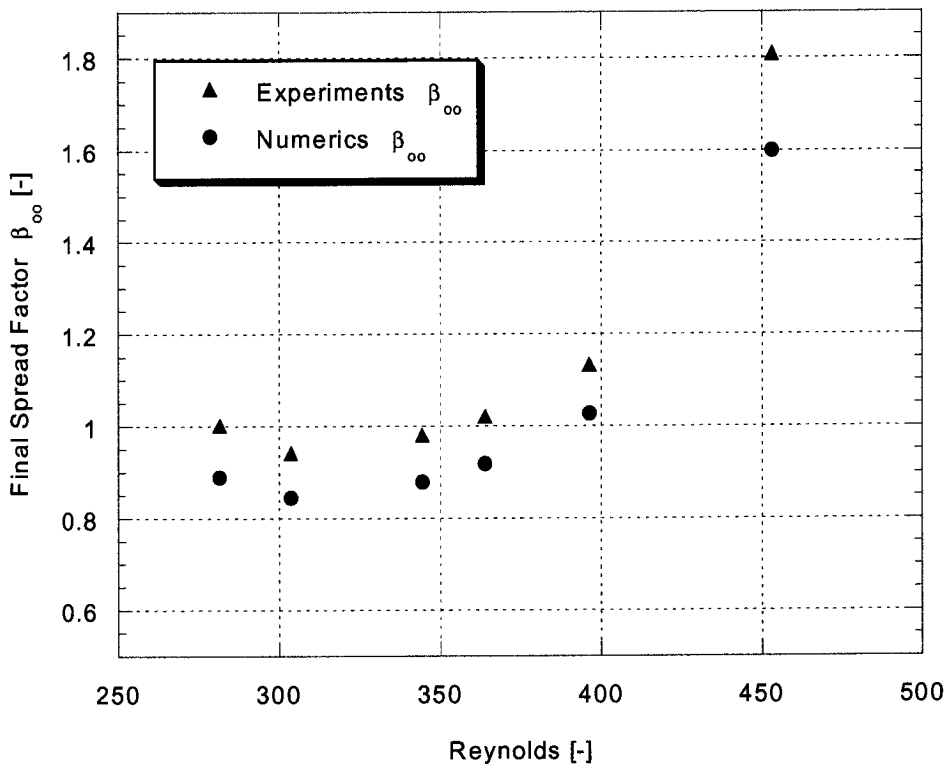

Figure 58: Experimentally measured and numerically calculated final spread factors for the impact regime.

The experimental values of the final spread factor shown in Figure 58 are averages of 20 measurements on different pile up structures of the same case. The variations of the latter,

given in Table IX, stem again from the intertwined variations of the impact velocity and the initial diameter as described in section 2.5. In addition to the variation in the final spread factor an estimated error of 1% of the initial diameter of the impinging droplet has to be accounted for as described in section 2.5.

Cases	7	8	9	10	11	12
β_∞ [-] numerical	0.89	0.845	0.879	0.92	1.028	1.599
β_∞ [-] experimental	1.0±0.02	0.94+0.02	0.98+0.02	1.02+0.02	1.13+0.02	1.80+0.02
Difference in %	11.2	10.2	10.3	9.8	9.2	11.5

Table IX: Numerically calculated and experimentally measured final spread factors β_∞ for the impact regime.

The differences in the final spread factor between the experimental and the numerical results, as given in Table IX, are with approximately 10% small but not negligible. The fact, that the final spread factors are underpredicted should, following the discussion on the thermal contact resistance in section 4.4 and the solidification behaviour in section 2.6.3, lead to a somewhat reduced agreement between the experimental and the numerical results because of the differences in the contact area relevant for the heat transfer. However, using optimised Biot numbers for the thermal contact resistance the disagreement can be reduced.

The comparison of the experimental and numerical solidification times are shown in Figure 59 and Table X. As can be seen the numerically calculated solidification times are larger than the experimentally measured times.

Cases	7	8	9	10	11	12
t_s [µs] numerical	526	529	588	574	611	532
t_s [µs] experimental	450 −10/+30	425 −10/+30	480 −10/+30	440 −10/+30	500 −10/+30	435 −10/+30
Difference in %	14.4	19.7	18.4	23.3	18.2	18.2

Table X: Numerically calculated and experimentally measured solidification times t_s [µs] for the impact regime.

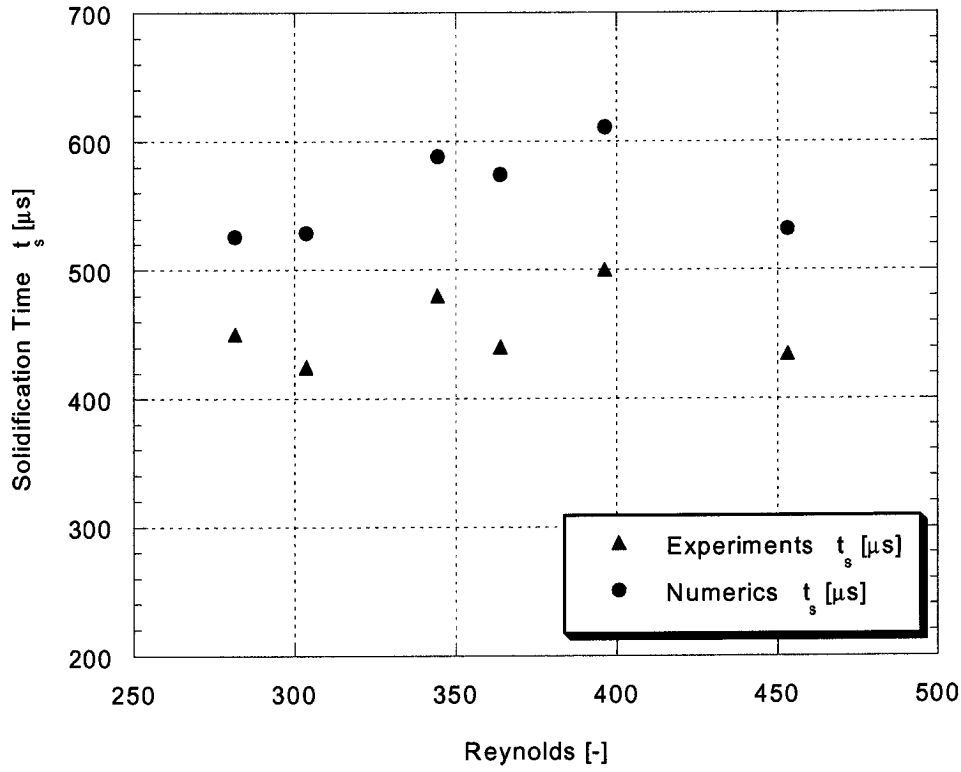

Figure 59: Experimentally measured and numerically calculated solidification times for the impact regime.

In a first attempt to interpret the differences in the solidification time between the experimental and the numerical results one may attribute them to the smaller final spread factors attained in the numerical simulations. However, when inspecting the last stages of the oscillatory motions of the impinging droplets, representatively shown for Cases 7 and 12, Figures 53 and 54, it can be seen that the numerical solution predicts a lengthy period during the last stages of the impact process with small oscillations at increasing frequencies of the latter. A magnification of this late period for Case 12 is shown in Figure 60. The time period displayed, covers the time between the experimentally determined and the numerically calculated solidification times for Case 12.

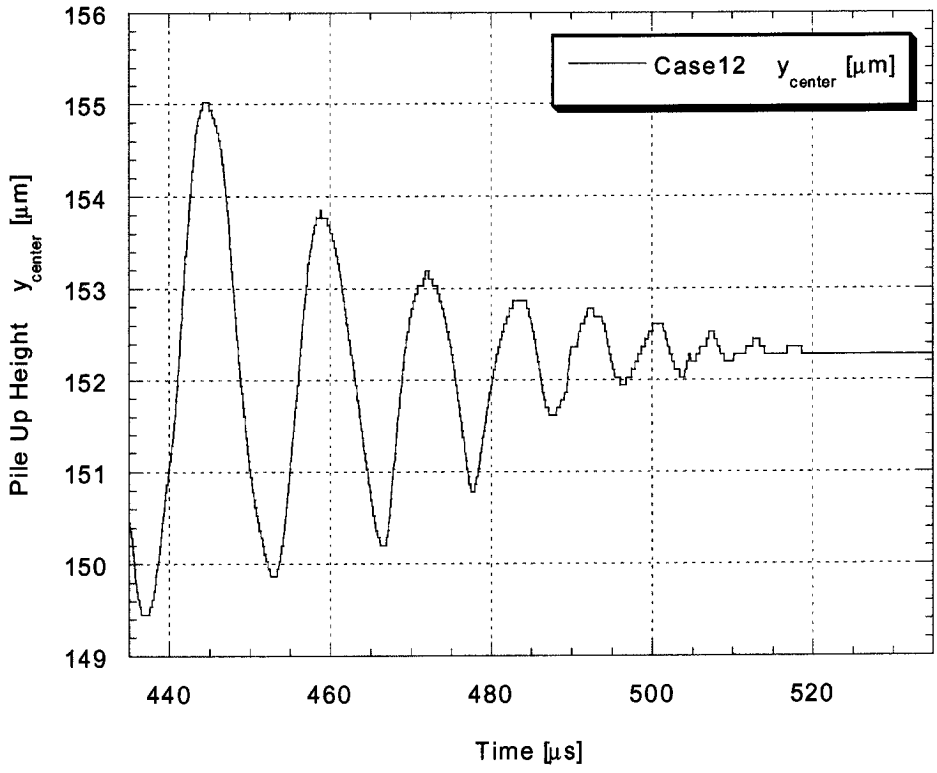

Figure 60: Final stages of the oscillation process for Case12 as obtained by the numerical simulation.

As mentioned in section 2.6.3, the experimental solidification time t_s is defined as the instance where the height $y_{center}(t)$ of the pile up structure remains constant (within ± 2% of the initial droplet diameter) for a time length more than half a period of its oscillations. For the considered case in Figure 60, Case 12, this corresponds to a change in the pile up height of 3.3 [μm]. On the other hand, the first oscillation cycle shown in Figure 60 covers a change in the pile up height of approximately 5.5 [μm] already very close to what was experimentally considered a negligible movement, thus signalling complete solidification based on the definition of the experimentally determined solidification time. Furthermore, the sampling period in the experimental visualization is equal to the experimental time resolution of 5 [μs], as defined in section 2, which corresponds to an experimental sampling rate of the pile up height of 200 [kHz]. The numerically calculated oscillation periods shown in Figure 60 correspond to frequencies in the range of 62.5 – 500 [kHz]. Based on the Nyquist theorem [92], the sampling rate must be equal to or greater, than twice the highest frequency component in the analog signal in order to avoid aliasing of the latter. The analog signal

thereby pertains to the temporal evolution of the pile up height $y_{center}(t)$. Assuming that the numerically calculated variation of the pile up height $y_{center}(t)$ represents its real variation in the experiments, it is clear that based on both the definition of the experimental solidification time above and the sampling theorem, an underprediction of the experimental solidification time has to be expected. The error estimate for the experimental solidification time of –10/+30 [μs], as given in Table X, has to be considered as very conservative. It has to be expected that the real solidification times are larger than the measured ones and thus closer to the numerically calculated ones. This discussion explains the differences between the experimentally observed and numerically calculated solidifications times, Table X, and points to the direction that the numerical solution yields results closer to the real times, since the experimentally determined times, for the reasons explained above, will tend to underpredict the end of the freezing process.

As a general overview of all experimentally and numerically obtained pile up cases pertaining to the impact regime (Cases 7 – 12), Figures 61 and 62 show the attained endshapes. A very good agreement between the numerically calculated and the experimentally obtained endshapes is observed.

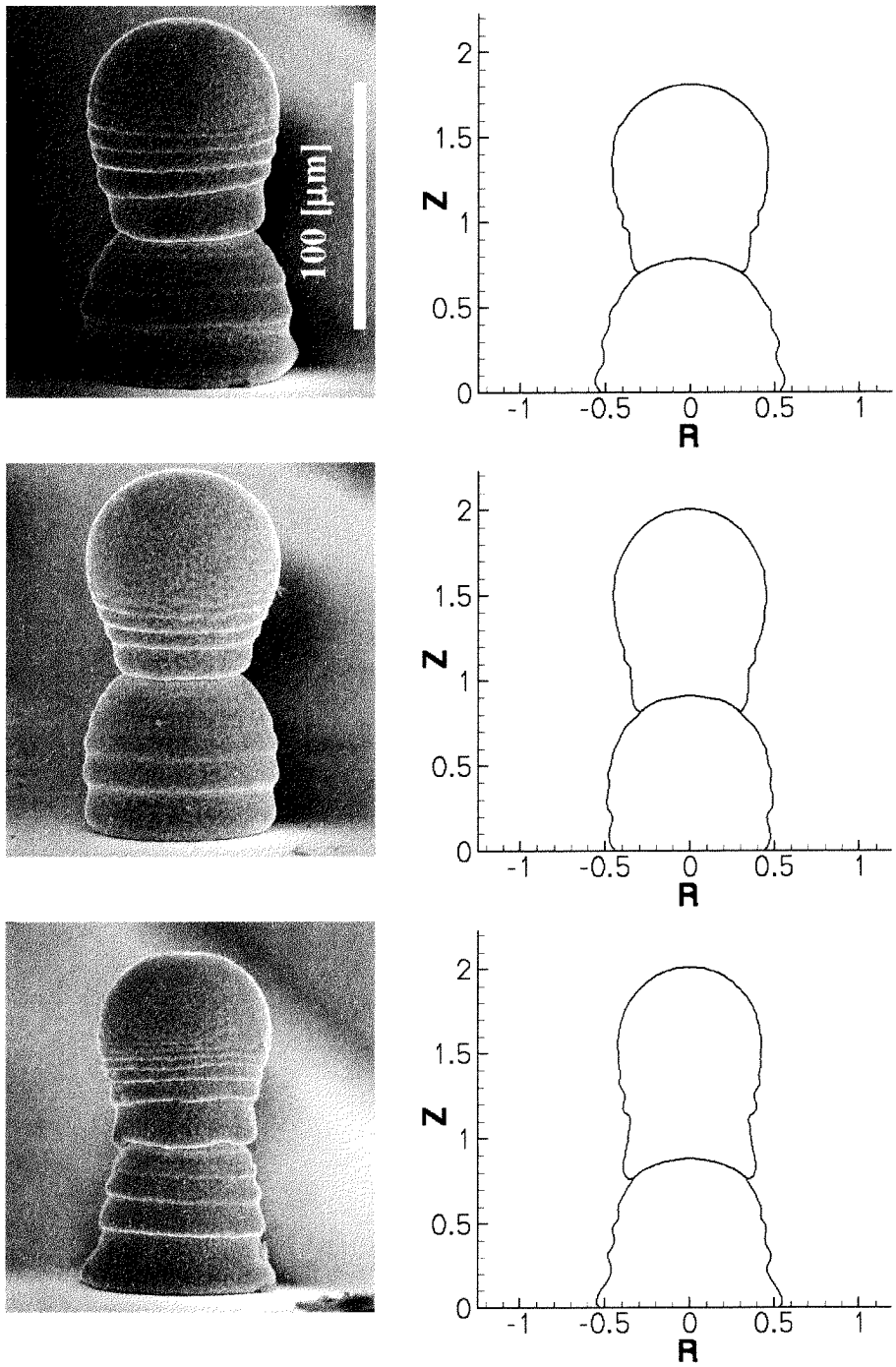

Figure 61: Experimental and numerical endshapes of the cases 7 –9 (from top to bottom).

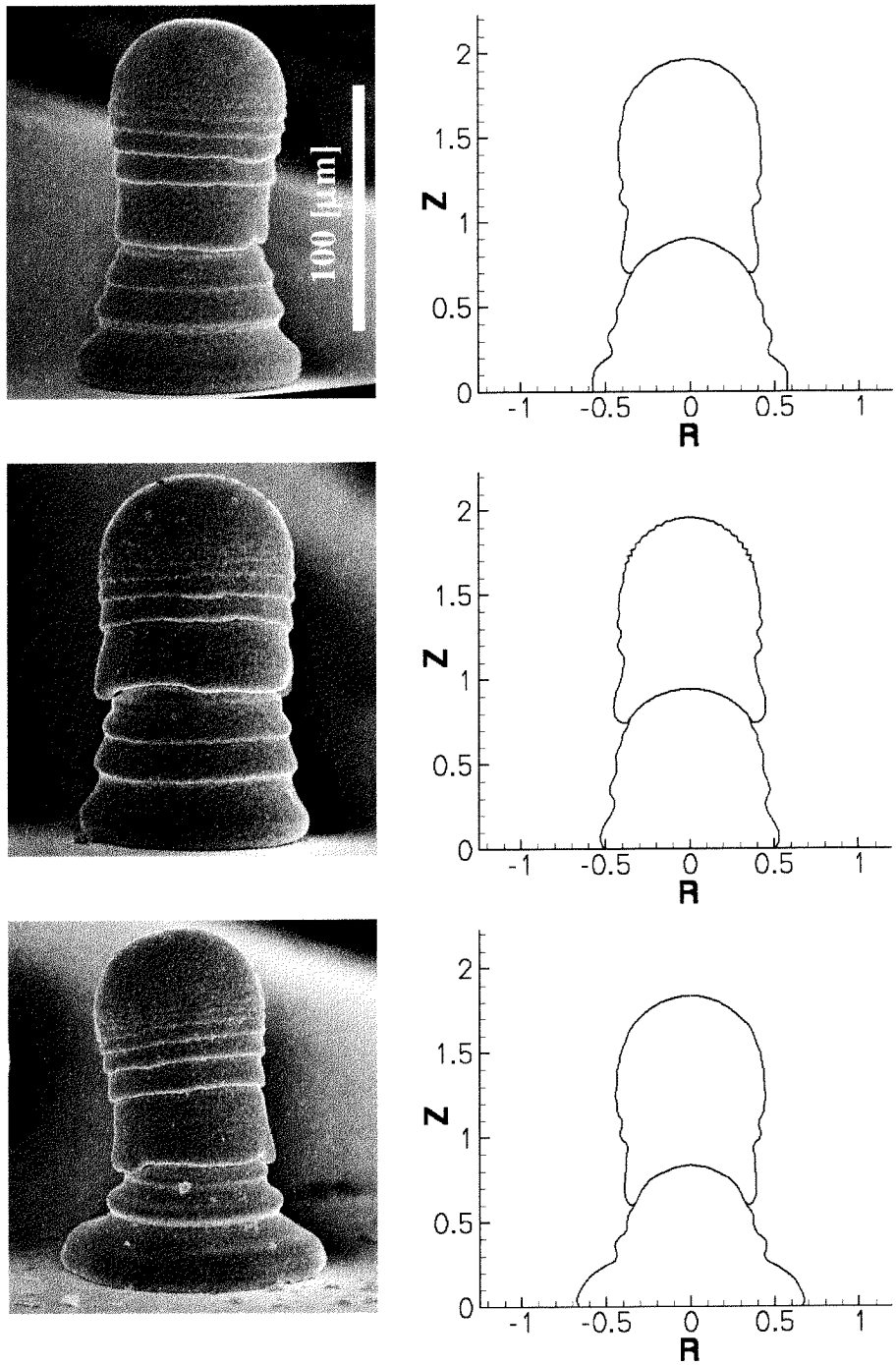

Figure 62: Experimental and numerical endshapes of the cases 10 –12 (from top to bottom).

5.3 Comparisons in the Thermal Regime

The matching of the numerical simulations with the experimental cases 1 – 6, Table II, is accomplished in the same manner as in the previous section discussing the impact regime. It has to be emphasized that Case 1 in the thermal regime is essentially identical to Case 10 in the impact regime. As was shown for Case 10 in the previous section, a good agreement

between the numerical simulation and the experimental visualization was obtained. The focus in this section will therefore be on the cases 2 – 6 of the thermal regime.

Whereas in the impact regime the Stefan number is the only relevant dimensionless number kept constant, in the thermal regime the latter is the only influential parameter being varied significantly, except for the Biot numbers. The Stefan number has, in an implicit manner, a very strong impact on the numerical results and the predictive capabilities of the numerical model, and its significance will be the scope of this entire subsection. It has to be emphasized from the outset that there is no actual set of optimal Biot numbers in contrast to the previous section. If not stated otherwise, the results for the corresponding cases presented herein always pertain to the Biot numbers given in Table XI. The relevant dimensionless numbers for the numerically solved cases of the thermal regime presented herein are shown in Table XI.

Numerical Case	Reynolds [-]	Weber [-]	Stefan [-]	Biot Bi_s [-]	Biot Bi_l [-]
1	363.89	4.17	0.895	0.2	0.9
2	363.31	4.14	0.754	0.2	0.9
3	362.42	4.13	0.612	0.3	1.0
4	360.77	4.14	0.470	0.5	1.5
5	357.67	4.13	0.329	2.0	3.0
6	359.07	4.06	0.187	5.0	10.0

Table XI: The relevant dimensionless numbers and corresponding values of the Biot numbers for the numerical cases of the thermal regime.

The most important finding is that with decreasing Stefan number the agreement of the experimental and numerical results deteriorates strongly. This deterioration of agreement for the oscillatory motion of the center of the impinging droplet, Y_{center} [-] for two representative experimental and numerical cases (Case 2 and Case 5), is shown in Figures 63 and 64.

Figure 56, Case 10, respectively Case 1 of the thermal regime discussed earlier, features a very good matching between the experimental visualization and the numerical simulation. The oscillatory motion of the center of the impinging droplet, Y_{center} [-] for Case 2, Figure 63, still shows an acceptable conformity between the experimental and the numerical results.

However, the agreement in Case 5, Figure 64, is limited to the first half-cycle of the deformation process.

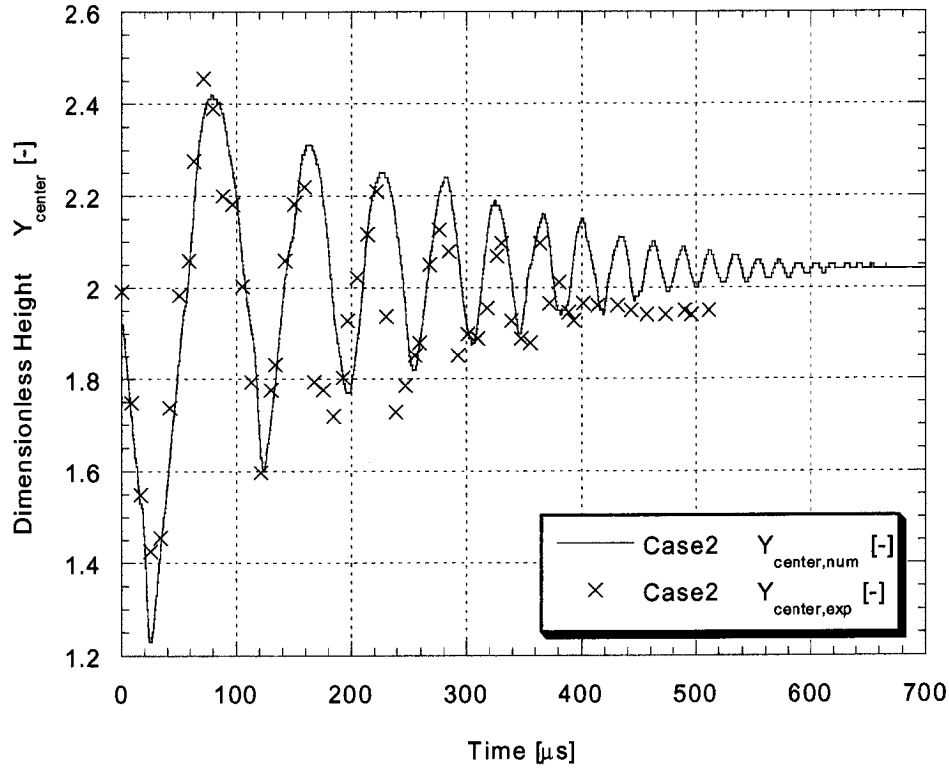

Figure 63: Temporal evolution of the dimensionless pile up height for Case2.

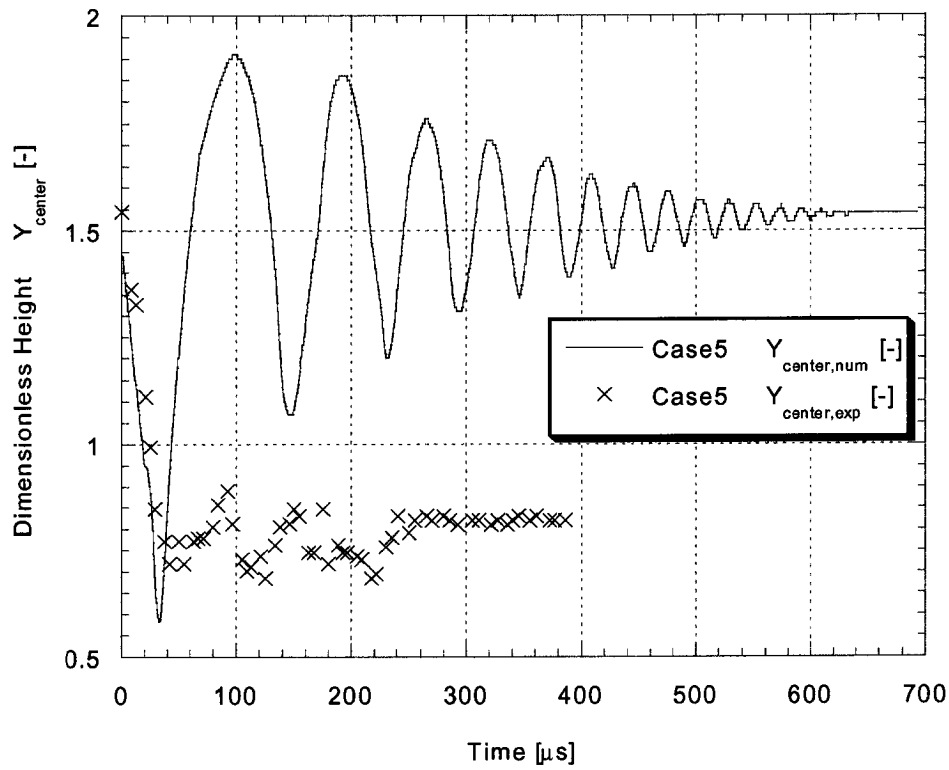

Figure 64: Temporal evolution of the dimensionless pile up height for Case5.

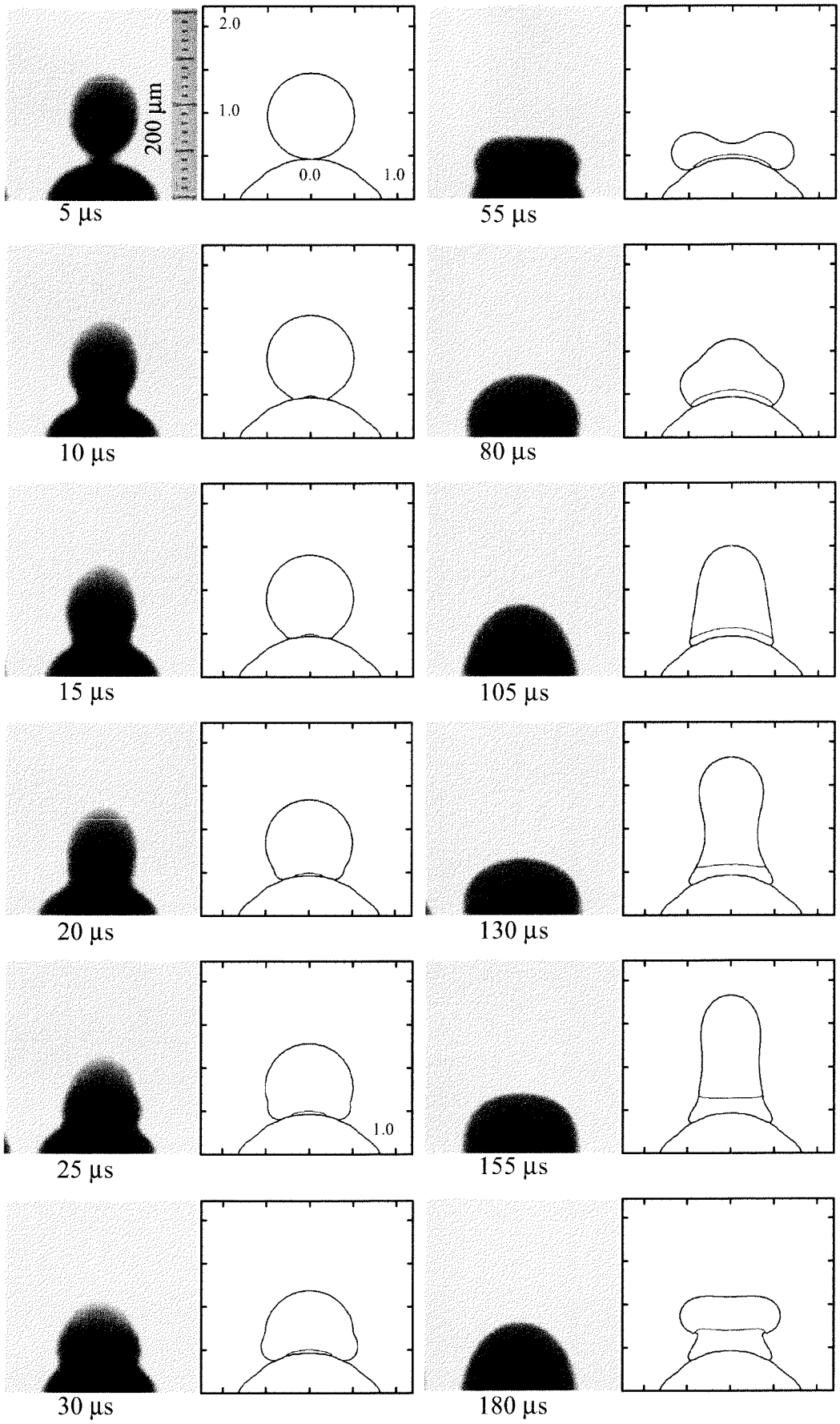

Figure 65 (continued)

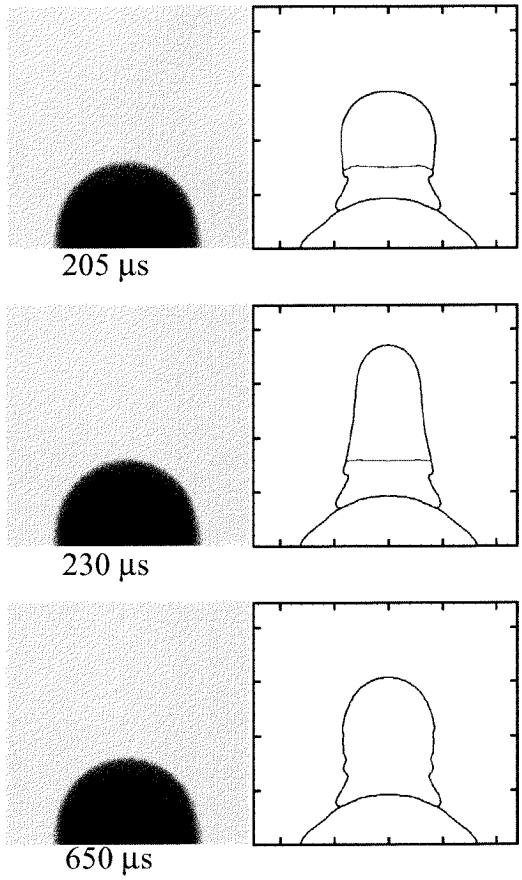

Figure 65: Experimentally visualized and numerically simulated sequence of Case5.

Thereafter, a completely different transient behaviour of the numerical and experimental results can be observed. This is further exemplified by the numerically simulated and experimentally visualized impact sequence of Case 5, Figure 65.

A compilation of the measured and calculated final pile up heights, $Y_{center,\infty}$ [-], is given in Figure 66 and Table XII.

Cases	1	2	3	4	5	6
$Y_{center,\infty}$[-] numerical	1.96	2.04	2.05	1.72	1.54	1.59
$Y_{center,\infty}$[-] experimental	1.885±0.02	1.93±0.02	1.70±0.03	1.20±0.03	0.82±0.04	0.85±0.04
Difference in %	3.8	5.3	17.0	30.2	46.7	46.5

Table XII: Numerically calculated and experimentally measured dimensionless heights of the solidified pile up for the thermal regime.

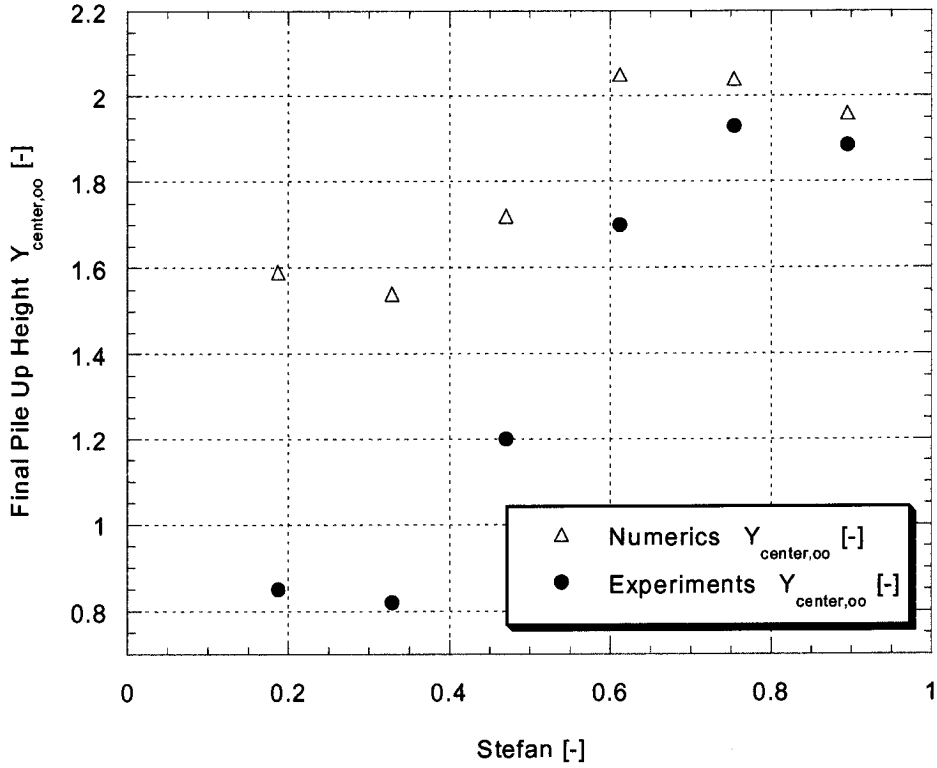

Figure 66: Final pile up heights in function of the Stefan number for the thermal regime.

The experimental values shown in Figure 66 are averages of 20 measurements on different pile up structures of the same case. The predicted final pile up heights are within a tolerable range for Cases 1 and 2. Thereafter, the differences become larger and show substantial disagreement.

A similar decrease in the conformity between the experimental and numerical results with decreasing Stefan number can also be observed in the spreading behaviour for the cases of the thermal regime. A compilation of the experimentally measured and the numerically calculated final spread factors is shown in Figure 67 and Table XIII.

Cases	1	2	3	4	5	6
β_∞ [-] numerical	0.92	0.855	0.76	0.953	1.07	0.916
β_∞ [-] experimental	1.02±0.02	1.09+0.02	1.08+0.02	1.42+0.02	1.83+0.04	1.82+0.04
Difference in %	9.8	21.5	29.6	32.8	41.5	49.6

Table XIII: Numerically calculated and experimentally measured final spread factors β_∞ for the thermal regime.

As is clearly visible, for decreasing Stefan numbers the differences between the experimentally measured and the final spread factors obtained from the numerical simulations increase distinctly. The strong underprediction of the final spread factor for decreasing Stefan number corresponds to the large difference in the final pile up heights, Table XII and Figure 66. Since less mass or volume covers the free surface of the presolidified droplet, more volume remains directly above the presolidified droplet leading to a larger final pile up height in the numerical simulations as compared to the experimental observations.

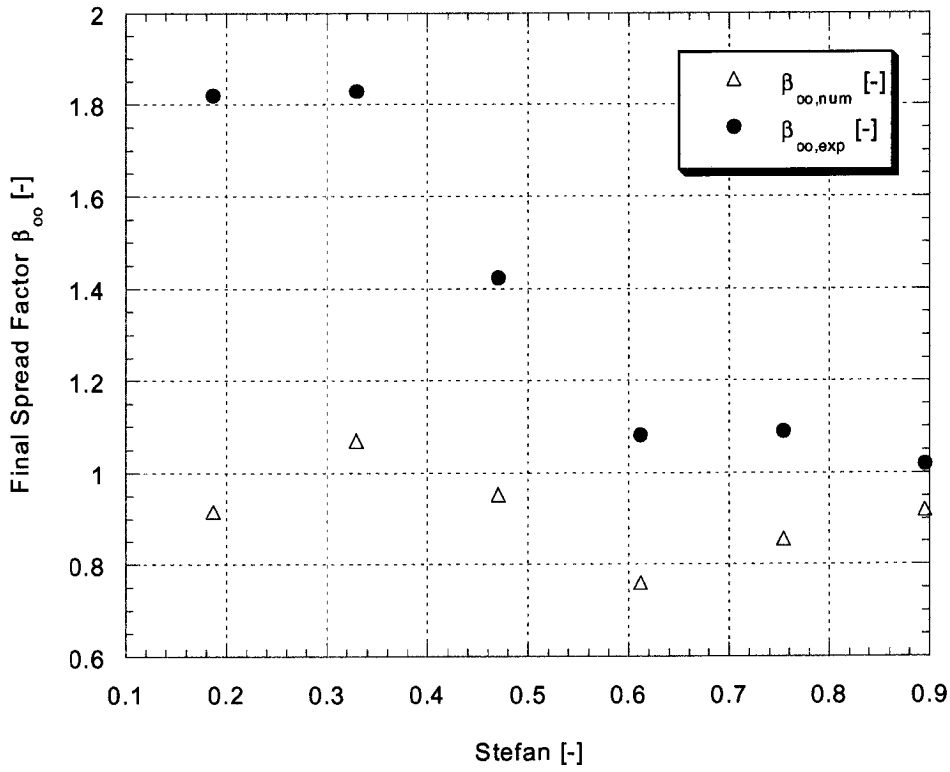

Figure 67: Final spread factor in function of the Stefan number for the thermal regime.

A closer inspection of the temporal evolution of the spread factor, as representatively shown for Case 2 and Case 5 in Figure 68 and Figure 69 respectively, reveals a similar tendency as observed for the impact regime. During the first, inertia driven stage of the spreading process a good agreement between the experimentally measured and the numerically calculated spread factors can be observed. During the later stages of the spreading process, where capillary effects become more important, clear differences between the numerical and experimental results are apparent.

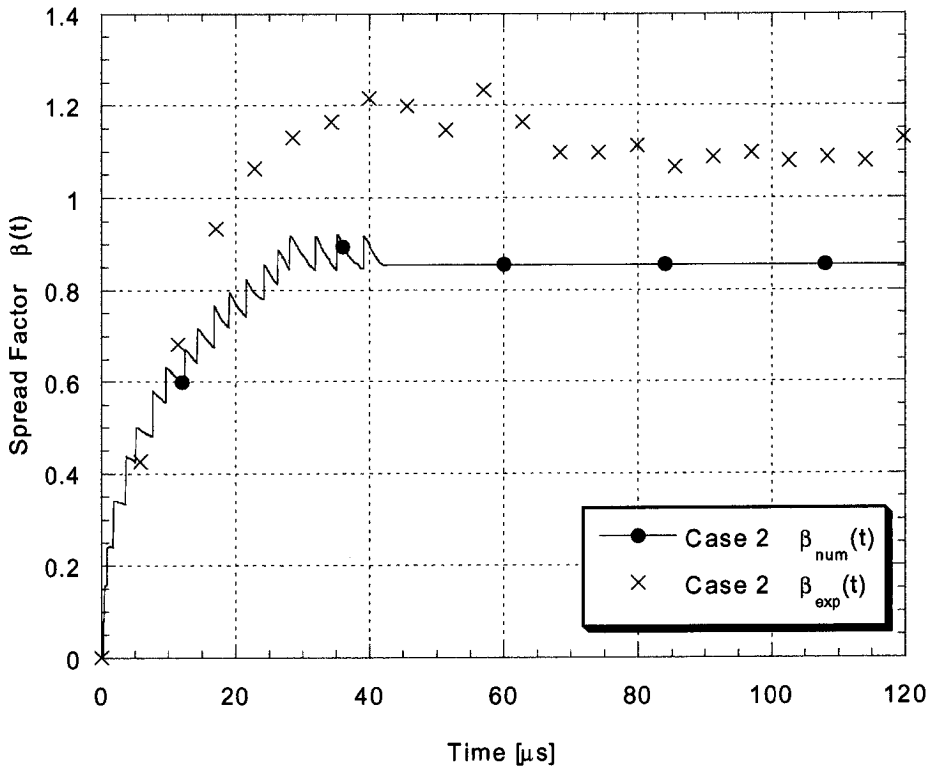

Figure 68: Temporal evolution of the experimentally measured and numerically simulated spread factor for Case 2.

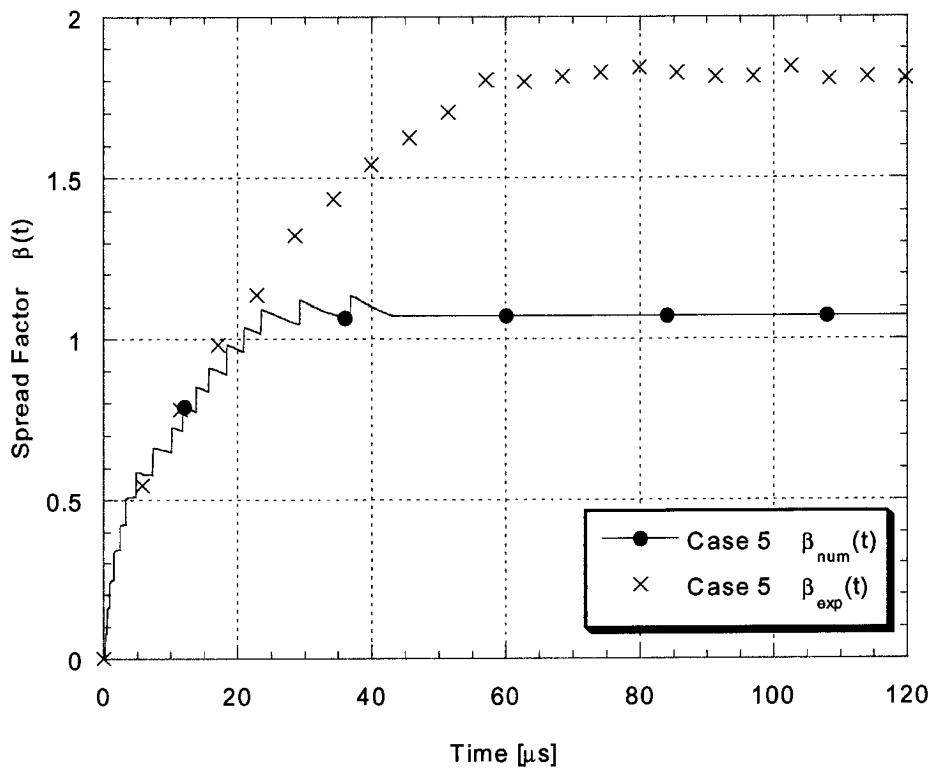

Figure 69: Temporal evolution of the experimentally measured and numerically simulated spread factor for Case 5.

This leads again to the same conclusion as stated for the impact regime. The lack of modelling of capillary effects lead to a numerical underprediction of the spread factor. The disagreement clearly increases with decreasing Stefan number. This means that the importance of capillary or interfacial effects become, even in an impact-inertia dominated impact regime, increasingly important with increasing substrate temperatures (decreasing Stefan numbers). Wetting experiments using metal droplets on metal surfaces (not of the same material) have shown that an increase of the substrate temperature usually leads to an increased wettability [93]. Furthermore, it has been observed that the spreading time of a droplet depends logarithmically on temperature and that the time decreases with increasing temperature [93]. Similar results were obtained for 60Sn40Pb solder droplets on gold-platinum metal films [94]. The above referenced experiments relied basically on gently placing macroscopic metal droplets on respective metal substrates. Thus, spreading of the droplets was controlled by capillarity. No experiments covering the material system of the present study could be found in the scientific literature. Nonetheless, the above referenced experimental observations point to a possible explanation for this increasing disagreement of the experimentally obtained and numerically calculated final spread factors for decreasing Stefan numbers. An additional perhaps more plausible explanation of the disagreement is remelting of the bottom droplet due to the heat input from the top droplet, a phenomenon not included in the numerical model. This is clearly possible as the substrate temperature (bottom droplet) approaches the melting temperature (the Stefan number approaches zero).

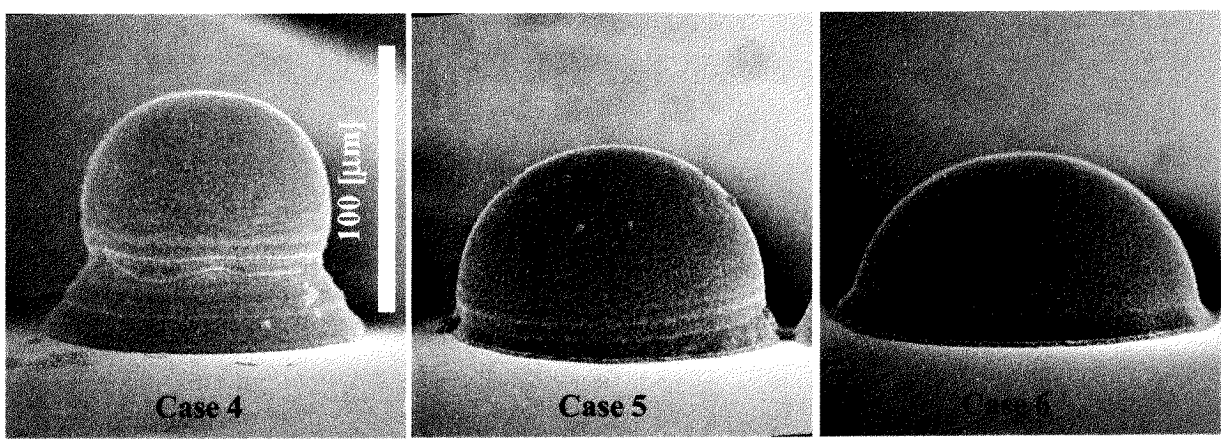

Figure 70: Experimental endshapes of the cases 4 – 6.

However, remelting studies with flat substrates indicate [95] that for the temperature regime of the present study substrate melting is unlikely to occur except perhaps at a thin region at the interface. Hence, it is the wetting mechanism that governs the spreading in Figure 70, showing the completely solidified cases corresponding to the smallest Stefan numbers of the study (Case 4, 5, and 6). In particular cases 5 and 6 feature hemispherical shapes which could be the result of the second droplet travelling all the way to the wafer and completely coating the first droplet.

5.4 Exemplary Result for a Multiple Droplet Pile Up

As postulated in the introduction, section 1.2, the investigation of a pile up consisting of two droplets only can easily be enhanced to the case of multiple droplets. This was done numerically for Case 11. Thus, Figure 71 shows representatively the attained endshapes for the numerically calculated and experimentally visualized pile up. The simulated pile up was thereby manufactured in the following manner: First, a single droplet impinged on the bare, flat wafer substrate. Next, a two-droplet pile up was simulated followed by the third and last droplet. Thus, the shapes of the presolidified structures (i.e. single droplet, and two-droplet pile up) were entirely fabricated numerically and not by digitising SEM micrographs of final structures. Table XIV shows the relevant dimensionless parameters for every impinged droplet.

# Droplet	Reynolds [-]	Weber [-]	Froude [-]	Stefan [-]	Biot Bi_s [-]	Biot Bi_l [-]
1.	396.29	4.91	3494.2	0.895	0.2	0.9
2.	396.29	4.91	3494.2	0.895	0.2	0.9
3.	396.29	4.91	3494.2	0.895	0.2	0.9

Table XIV: Relevant impact parameters for a multiple droplet pile up.

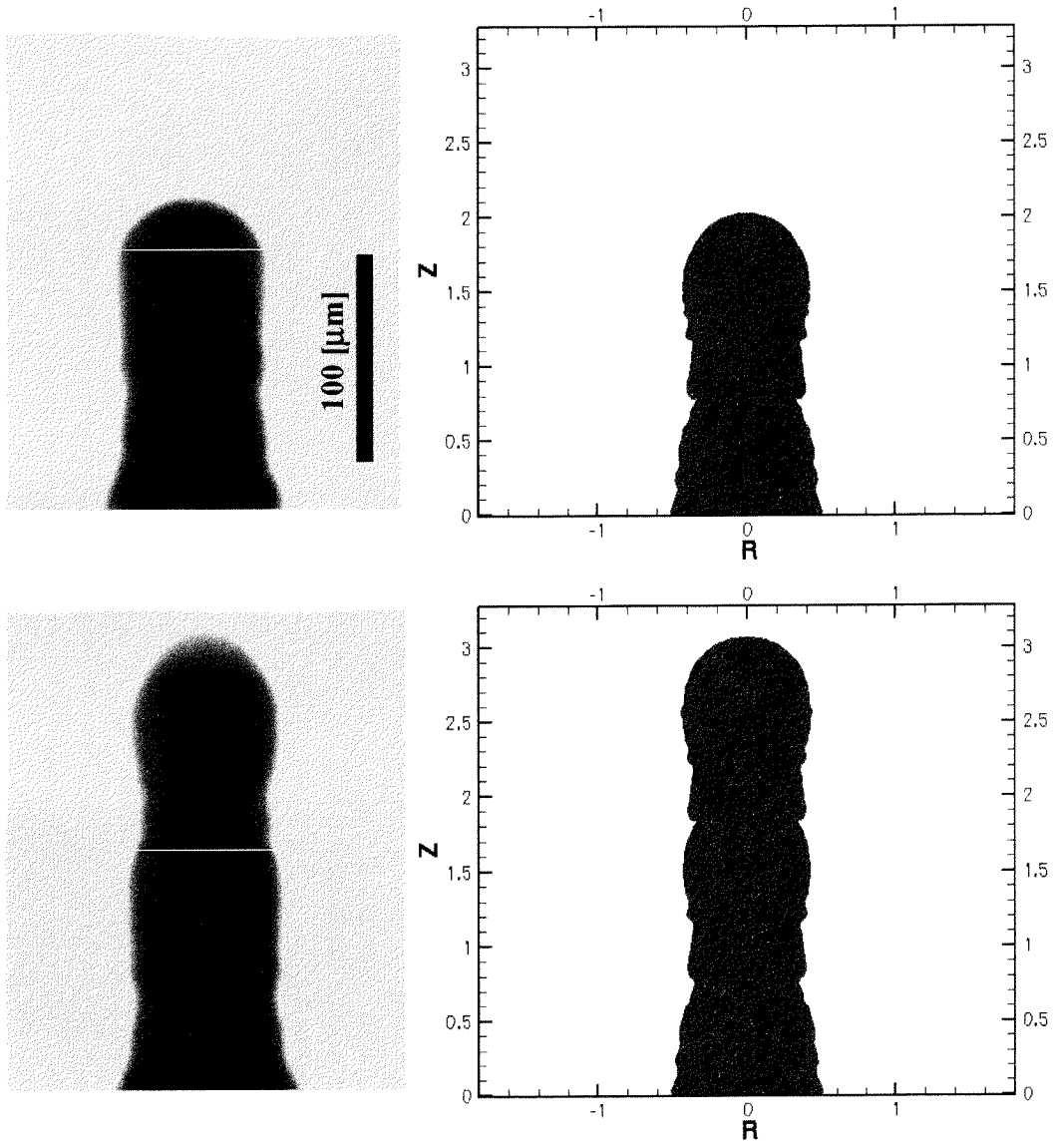

Figure 71: Experimentally visualized and numerically simulated two- and three-droplet pile up for Case 11.

The Biot numbers chosen, were taken from section 5.2. All impacts were simulated with the same pair of Biot numbers. As has to be expected from the results presented in section 5.2, the simple pile up consisting of two droplets only matches well with the experimental result. In addition to that, the three-droplet pile up shows also a very good agreement with the experimental result. This makes sense since the free surface shapes of the first and second droplet are similar.

Although no transient visualizations of the multiple pile up structure was presented, it can be argued that the extension of a two-droplet pile up to columns of multiple droplets, as representatively shown for Case 11 in Figure 71, is indeed straightforward.

5.5 Summary

The fact that the numerical model does not account for wetting phenomena in a sufficient manner manifests itself in an increasing disagreement between the experimental and numerical results with decreasing Stefan number. For moderate values of the latter (i.e. low substrate temperatures) capillarity effects appear in the experiments but their effect on the final spread factor is not dominant. As shown in section 5.4, the solution of the two-droplet pile up problem contains all the physics of the general case of axisymmetric multiple droplet pile up structures.

6. On an Approach to a Refined Contact Line Modeling

6.1 Objectives

The modeling of an impacting droplet on a substrate can be achieved rather successfully using the approaches described in section 3. However, there are some critical issues as described in section 4 and 5 (i.e. thermal contact resistance and dynamic wetting). Probably the most prominent issue is the modeling or understanding of the dynamic contact line. Not only are the parameters of the few ad-hoc mathematical models a priori unknown but more importantly the physical background of the wetting process is not well understood. Dynamic wetting is therefore receiving a great deal of attention. Despite this fact, no theory is as yet experimentally verified, generally accepted, or complete enough to warrant its general application. The major problem is that most experiments probe the meniscus/interface profile of a dynamic wetting line at distances of several tens of microns (or even greater) from the solid. This is not accurate enough since it has to be expected that wetting is controlled at the molecular level. Therefore, any agreement between theoretical predictions and experimental observations, such as apparent contact angles, rates of spontaneous spreading, or forces needed to advance a liquid front over a solid, does not necessarily validate the assumptions made, hence cannot be invoked to identify the mechanisms based on which a liquid advances over a solid [23]. New experimental techniques resolving the submicron domain and further advances in molecular dynamics numerical techniques might yield some more insight to wetting physics. Hence, a marked part of this thesis focused on experimentally approaching the molecular processes of an advancing contact line using scanning force microscopy. We set to find out if scanning force microscopy is suitable when investigating interfacial and wetting phenomena of liquid microstructures such as the shape of the liquid interface and the movement of the dynamic contact line.

6.2 Literature Review

Experiments at the sub-microscopic scale on the spreading behaviour of completely wetting liquid microstructures on smooth surfaces using such techniques as ellipsometry have been reported in the literature recently [96-102]. These experiments have recently revealed for some

liquids the formation of precursor films, which in some cases exhibited staircase-like structures underlining the molecular nature of the wetting process and therefore pointing toward the need of an in-depth analysis of the relevant phenomena. It is worth noting that the lateral resolution of the aforementioned experiments is of the order of ten micrometers, which when compared to their vertical resolution (of the order of Angstrøms) is deemed poor.

Scanning force microscopy has demonstrated success in characterizing solid surfaces having the ability to achieve atomic level resolution. Recently, scanning force microscopy (SFM) and scanning polarization force microscopy (SPFM) operating at low interaction force modes have been applied to study liquid structures [103-109]. However, these studies have been either focused on static wetting behaviour [103,104,108], or in the case of long-term studies, on very viscous or particle-like liquids [105-107,109]. Scanning force microscopy has so far not been applied to dynamic contact lines.

6.3 Scanning Force Microscopy of Liquid Microstructures

6.3.1 Experimental Procedure

A Topometrix Explorer™ scanning force microscope with a phase contrast extension operating in tapping mode was utilized to investigate the wetting behaviour of droplets of different liquids on a host of substrates. Non-contact tips (NT-MDT, Russia) with resonant frequencies in the range of 60-150 [kHz] were utilized for the experiments. In the tapping mode operation, the cantilever system vibrates at frequencies of the order of 100 [kHz] near its resonance. The damping of the oscillation amplitude, at constant excitation frequency, due to the interaction of the tip with the sample serves as a feedback signal. The equilibrium separation between the tip and the sample is smaller than the relatively large oscillation amplitude, which lies approximately in the range of 10 - 150 [nm]. Therefore the tip strikes the sample once each cycle. The contact times are, due to the high oscillation frequencies used, very short (of the order of 1 [μs]) and can be controlled by either altering the tip-sample proximity or the oscillation amplitude [110]. The relatively large oscillation amplitude in tapping-mode operation usually provides the cantilever with enough kinetic/potential energy to overcome adhesion or capillary forces which may lead to meaningless results.

Liquids employed for the experiments were glycerin (87%), pentadecane (>98%), hexadecane (>98%), heptadecane (~99%), polydimethysiloxane (PDMS), 1-2 butanediol (>98%), 1-5

pentanediol (~97%), 1-2 pentanediol (>95%), 1-2 hexanediol (>97%), and squalane (>99%). Two different fractions of PDMS were utilized with viscosities at 25 [°C] of : ~20 [mPas] (PDMS I), and ~500 [mPas] (PDMS II). All fluids were purchased from FLUKA Chemie AG, Switzerland. Substrates employed for the experiments were muscovite ruby mica, glass, and polished wafers (orientation 111, purity 99.999%, phosphorus dopant), purchased from Goodfellow Cambridge Ltd., England. Criteria for the selection of a specific fluid were primarily a low volatility and a sufficient wettability of the chosen substrates. The reason for this is obvious. A highly volatile liquid prevents a stationary formation of micro- or even nanodroplets on a solid substrate. Such a liquid either evaporates before an experiment can be initiated, or spreading and evaporation occur simultaneously during the imaging procedure. Evaporation and condensation processes may indeed have an important influence on the mechanism of wetting [111]. However, controlling and reducing the number of competing processes involved, facilitates the interpretation of results. Furthermore, a sufficient wettability is a necessary condition. If a liquid microstructure forms a large contact angle in partial or non-wetting situations, the microscope tip cannot image the profile of the probed liquid microstructure, or it creates a convolution of its geometry and the profile of the latter.
In order to investigate the dynamic wetting behaviour of the above mentioned fluids, two different approaches, depending on the wetting characteristics (completely or partially wetting) were applied in the present studies. The first approach, employed for partially wetting fluids, was to externally induce a spreading motion by changing in situ the physical properties of the observed solid/liquid system. The latter was accomplished by slightly heating both the substrate and the droplets situated upon it with a temperature-controlled microheater, thus changing the equilibrium configuration of the investigated system. The second approach was to use spontaneously spreading liquids which spread from an initial droplet shape after deposition on the substrate to a pancake-like film at equilibrium.

6.3.2 Sample Preparation

The liquids were deposited randomly on substrates with a size of the order of 1 [cm^2] in the form of nano- and microdroplets or single macrodroplets. To this end, the sample liquid was either atomized with a commercially available spray and deposited on the substrates out of the aerosol phase forming a large number of nano- and microdroplets, or single macrodroplets were deposited on the substrates by means of a microsyringe (drop volume on the order of 5

[µl]). By blowing off these macrodroplets from the substrate with dry nitrogen gas, liquid filaments are created on the surface. These ligaments subsequently undergo a Rayleigh-Plateau-like instability forming a large number of small droplets [103]. This method can, however, only be employed in connection with partially wetting liquids. Completely wetting liquids would, of course, immediately form a film. Before depositing liquid droplets, the substrates (except mica) were cleaned in an ultrasonic bath, rinsed with ethanol and blown dry with dry nitrogen gas. Mica substrates were prepared by peeling off a few layers with an adhesive tape making further cleaning operations unnecessary.

6.3.3 Experimental Setup

The experiments were performed in a dust-free glovebox under a constant flow of dry nitrogen. The samples were also prepared in a dust-free environment in ambient atmosphere. The experiments were performed at ambient pressure and ambient temperature (20 [°C]) The relative humidity in the glovebox was set to 20 %. Figure 72 shows a schematic of the experimental setup.

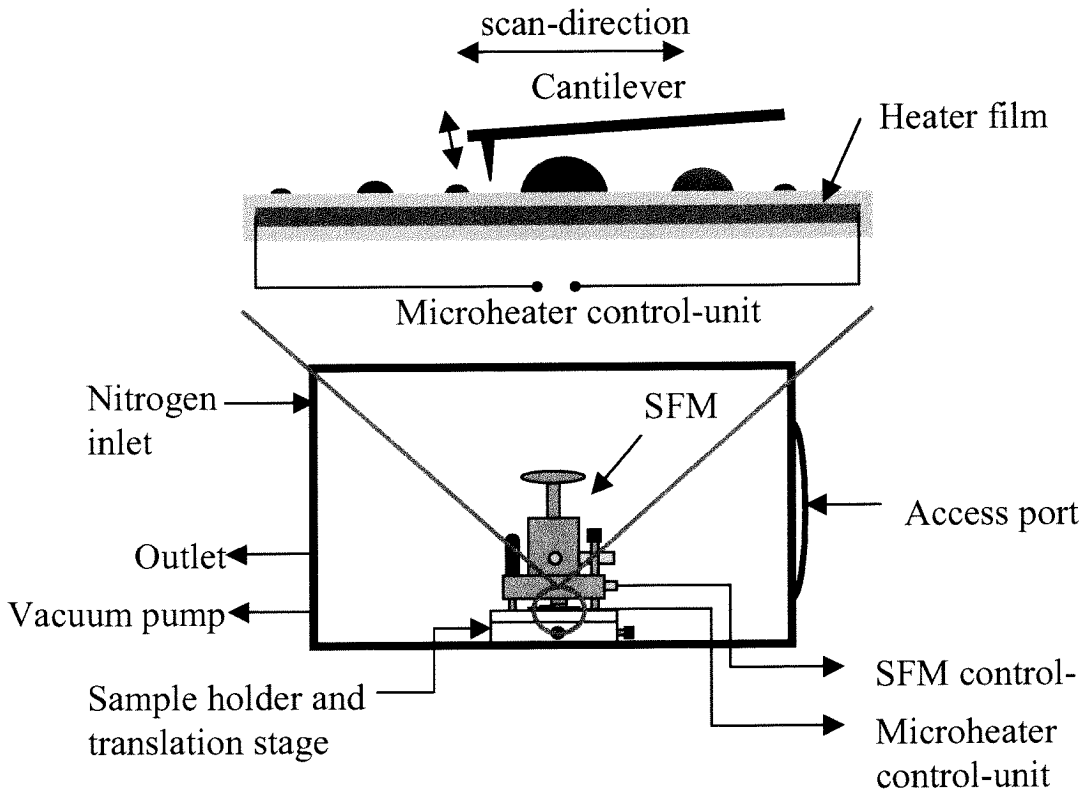

Figure 72: Schematic of the experimental setup. Enlargement: Schematic of the microheater setup.

The heating system with which the substrate and drop temperature were controlled when so desired, consisted of commercially available thin film platinum microheaters purchased from Hereaus Sensor Nite GmbH, Germany. These microheaters can be used simultaneously as heating and as temperature measurement devices. To this end, the temperature-resistance calibration curves of the microheaters were measured in a muffle furnace. The microheaters are built in a sandwich structure with the platinum film placed between two sheets of glass and aluminum oxide. Each of these sheets possess a thickness of approximately 150 [μm].
The heating device was only utilized for experiments in connection with mica substrates. For these experiments the glass layer was stripped off the heater with hydrofluoric acid and replaced by a thin sheet of mica with a thickness of approximately 200 [μm] which was then employed as substrate. Temperatures measured with the heater correspond to the temperature of the platinum film in the middle of the heater. Nevertheless, this temperature is very close to the surface and liquid temperature on top of the substrate since the mica sheet is very thin (~200 [μm]). A small amount of conductive heat compound is used to fix this sheet on the heater and, at the same time, to reduce the thermal contact resistance between the platinum film and the mica substrate. Our numerical calculations further corroborate this assumption [112]. The estimated, and calculated temperature differences between the platinum film and the substrate surface are of the order of 1 [°C]. Temperature gradients along the surface, which could influence spreading behaviour, are not measurable in a range of 100 [μm] as observed by means of a scanning thermal microscope and as also corroborated by the numerical calculation.

6.3.4 Tip/Cantilever Preparation

In order to reduce difficulties possibly arising through wetting phenomena between the tip and the liquid structures on the sample, some of the silicon tips utilized in the experiments were coated. The aim was to reduce the high interfacial energy associated with silicon/siliconoxide surfaces. Coatings with lowered surface energies were accomplished in two different ways: (i) By means of chemical vapour deposition, a thin Teflon-like layer consisting of a mesh of carbon and fluorine was deposited on the cantilever/tip ensemble [113,114]. To this end, a plasma coating unit assembled by the nanotechnology group of ETH Zurich [115] was employed first to clean the surfaces of the SFM cantilevers in an air plasma

for 15 seconds from possible hydrocarbonic contaminants and subsequently to expose the surfaces to a hexafluorpropene (HFP) plasma for another 15 seconds. The resulting Teflon-layer is approximately 7 [nm] thick increasing the total tip radius to approximately 17 [nm]. (ii) By means of self-assembling monolayers (SAM) a monolayer of 1-dodecanethiol (>97%), purchased from FLUKA AG, Switzerland, is adsorbed spontaneously from solution on the surface of the cantilever/tip ensemble. More specifically, first a sputter source (Balzers MED010) with a film thickness monitor (Balzers QSG301) was used to coat the silicon SFM cantilevers with 3 [nm] of chromium and then subsequently with a layer of gold with a thickness of approximately 14 [nm] increasing the total tip radius to approximately 27 [nm]. The coated cantilevers/tips were subsequently immersed in a bath of 1-dodecanethiol for several hours. 1-dodecanethiol forms a densely packed, crystalline or liquid-crystalline monolayer on gold [116]. Before use, the tips were taken out of the immersion bath and blown dry with a stream of dry nitrogen gas.

The change in the wetting behaviour of the surface treated tips can be visualized by a qualitative sessile drop experiment. For both SAM and HFP coated tips small changes in the wetting behaviour could be observed [117]

6.4 Results and Discussion

6.4.1 Static Behaviour Measurements

The experimental procedure and the imaging process were tested in a series of long-term stability test runs on static droplets. Optimal scan frequencies, settings for the oscillation amplitude and the set-point (degree to which the amplitude of the free oscillating cantilever is damped by the force interaction of the sample), as well as agreement with theoretical predictions were investigated. The aim of these preliminary experiments was to ensure that the microscope performance does not change with time, since a study of dynamic behaviour requires that a sample is scanned fast and repetitively over a long period in order to receive a good time discretization of the investigated wetting process. To this end, glycerin droplets of different sizes were imaged on mica substrates. Glycerin as a test liquid was chosen because it exhibits a low wettability of the tips. Figure 73 shows a representative result for a glycerin droplet with an approximate initial diameter prior to deposition of 10 [μm].

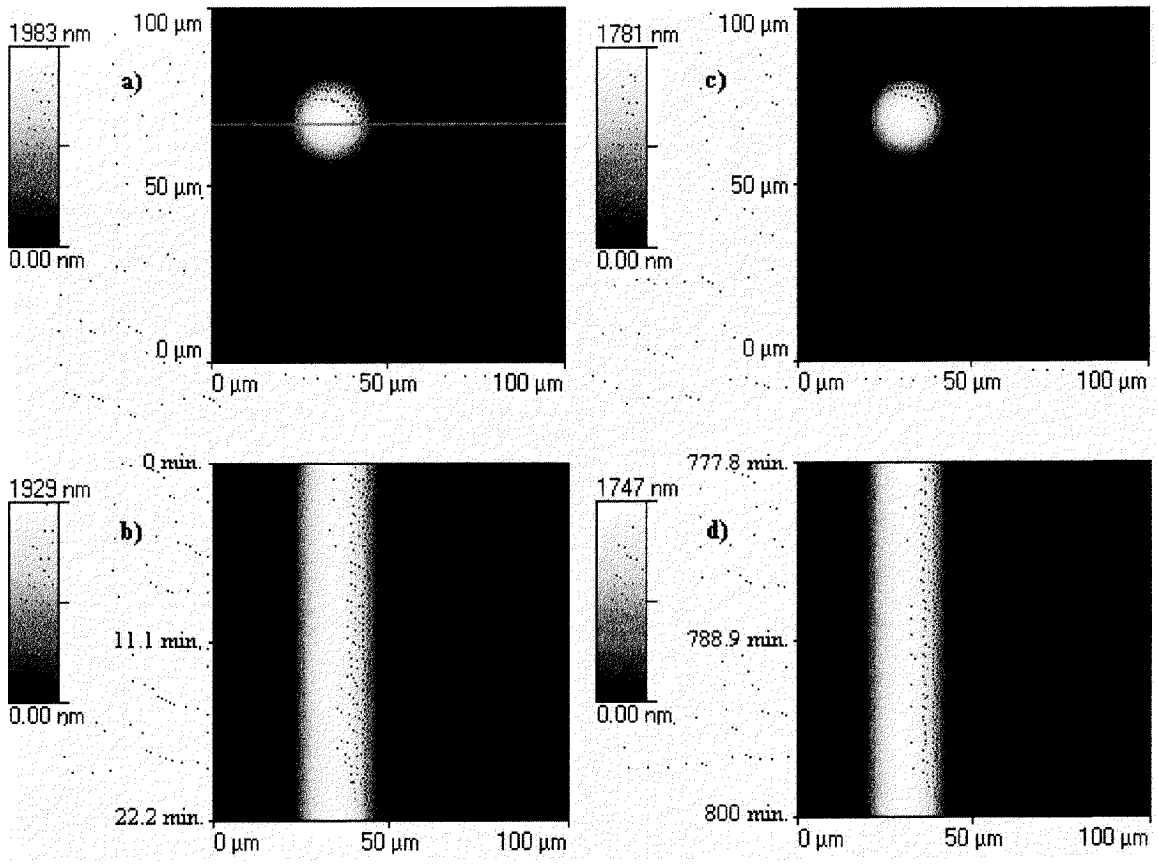

Figure 73: (a) Scanning force micrograph of a glycerin droplet on mica directly after deposition on the substrate. The line marks the profile which is being scanned continuously in the line-scanning process. (b) First 22 min of the line scanning process. (c) Scanning force micrograph of the investigated glycerin droplet after 800 min of continuous scanning. (d) Last 22 min of the line-scanning process. (The dots in Figure 73 have no physical meaning and are due to the visualization tool).

Figure 73a) shows the scanning force micrograph of the glycerin droplet immediately after deposition on the mica substrate. Figure 73b) shows the first 22 minutes of the line-scanning process. Figure 73c) shows the entire droplet after 800 minutes of continuous scanning. Figure 73d) shows the last 22 minutes of the line-scanning process. The performance of the microscope remains, as desired, stable from the initiation of the experiment until the end after 800 minutes. A calculation of the drop volume from the SFM data by numerical integration reveals, as expected, a loss in volume of the glycerin droplet of 18 % from the initiation to the end of the imaging process. The scanning micrograph in Figure 73c) does not reveal different patches of glycerin on the scan area, besides the droplet itself. This leads to the conclusion

that the loss in volume of the glycerin droplet occurs through evaporation only. Using tips with HFP or 1-dodecanethiol coatings led to similar results.

Another avenue to investigate the performance of the microscope, is to compare experimental results with theoretical predictions. For partially wetting droplets with sizes that are small compared to the capillary length of the droplets and for drop heights larger than the range of the van der Waals interaction of the substrate (< ~10 - 100 [nm]), theory predicts a spherical cap shape of the droplets in equilibrium. Figure 74a-c) show: (a) a glycerin droplet on mica with an initial diameter before deposition of 10 [μm], (b) a spherical cap fit to the data obtained from the microscope, and (c) the local deviation of the experimental data from the best fit. It is clearly seen that the experimental data fit the theoretical prediction well. However, as shown in the detailed local information of Figure 74c, the experimental data fluctuate randomly in the range ± 50 [nm] around the theoretically predicted spherical cap shape. This can be due both to a decrease in resolution of the microscope performance when applied to liquid structures (compared to solid surfaces), as well as to interactions between the liquid structure and the microscope tip.

Regarding optimal settings for the oscillation amplitude and the set-point, the experiments with the glycerin droplets revealed that a stable operation is only possible in a narrow bandwidth of both the oscillation amplitude and the set-point. These parameters have to be determined by a trial and error process rather than a heuristic rule, which would be preferable. Furthermore, very low interaction between the tip and the sample, corresponding to almost undamped cantilever oscillations, would not lead in most cases to a stable microscope operation. Scan frequencies with reasonable imaging results could go up to 2.0 [Hz]. Higher frequencies result in distortions of the droplet profile.

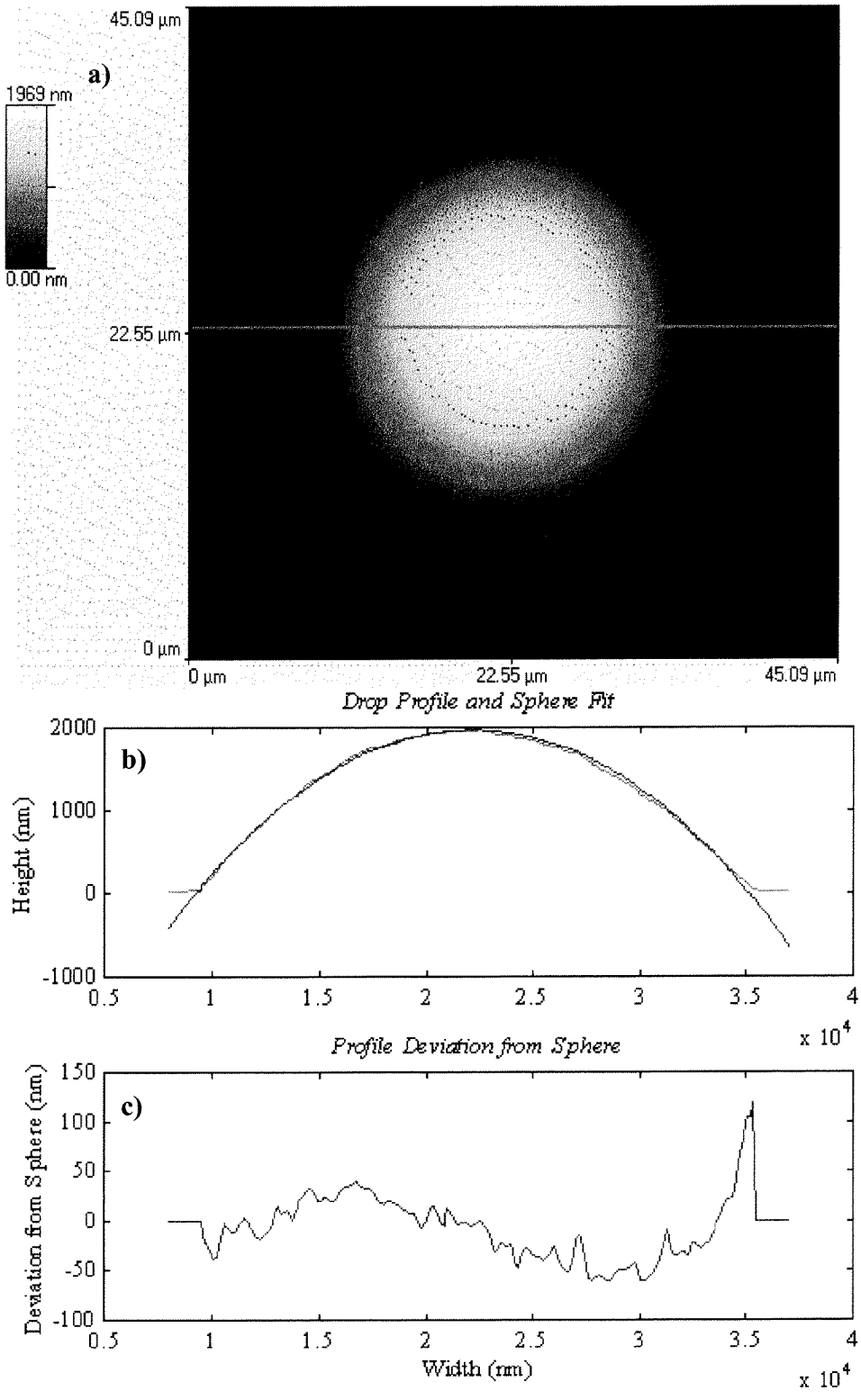

Figure 74: (a) Glycerin droplet on mica; the indicated line represents the profile visualized in Figure 74b; (b) Experimental profile vs. circle segment fitted to the topography data. (c) Vertical deviation of the experimental data and the fitted circle.

6.4.2 Dynamic Behaviour Measurements

6.4.2.1 Requirements for Dynamic Measurements

The most important condition for the measurement of dynamic wetting behaviour is to perform the experiments while the liquid structures are not in a wetting equilibrium with the substrate. The chosen methods to achieve such conditions are already described in section 6.3.1. Furthermore, it is important that the microscope performs the scans within time-scales which are orders of magnitude smaller than the investigated wetting time-scales in order to achieve a good time discretization of the observed process. Since it takes approximately 5 – 10 min from sample preparation to the initiation of the imaging process, it is not possible to capture the initial stages of the spreading process and the possible faster spreading time scales immediately following the deposition. Scanning times for a complete area scan, with respect to the above mentioned largest stable scan frequency of 2 [Hz], are in the range of 5 – 30 min. On the other hand, Fraysse et al. [98] show in their ellipsometric study on completely wetting fluids, that for example PDMS[1] and squalane droplets on silicon wafers have not reached equilibrium after over 100 h following the deposition on the substrate. Thus, the spreading time-scales of these liquids on silicon wafers are at least two orders of magnitude larger than the time required for the completion of an area scan and five orders of magnitude larger than the time required for a line-scan. It is therefore expected that the time discretization of the scanning process is sufficient.

Another requirement is that the interaction of the probing tip with the sample is minimal such that the scanning process does not alter or even destroy the sample topography. Possible interactions which may affect the results are: (i) strong repulsive or attractive interaction between the tip and the sample; (ii) formation of a liquid bridge between the tip and the sample; (iii) possible enhancement or initiation of evaporation due to intermittent contact of the tip and the liquid surface. All these requirements serve as additional challenges to the general care that has to be taken in the preparation of clean and homogeneous samples and the experimental setup.

[1] The viscosity of the PDMS employed in their study is not clear. Supposedly it is 3 [Pa s], [98].

6.4.2.2 Use of an External Wetting Promoter

The fluids employed for the experiments using an external wetting promoter were glycerin, pentadecane, hexadecane, heptadecane, 1-2 butanediol, 1-5 pentanediol, 1-2 pentanediol, 1-2 hexanediol, and squalane. The substrates were, as already described in detail in section 6.3.2, thin sheets of mica (~200 [μm]), fixed on top the microheaters.

Four different kinds of temperature changes were induced by means of the microheater: (i) temperature jumps from ambient temperature to higher temperatures; (ii) temperature jumps in the opposite direction; (iii) linear ramping up of the temperature from ambient to a higher temperature; (iv) linear ramping down from a higher temperature to ambient temperature.

Great challenges concerning the stability of the microscope performance were observed employing any of the above mentioned four procedures to change the temperature of both the substrate and the liquid structures. Already small changes in the temperature of the substrate lead to distortive and destabilizing effects on the microscope interaction with a liquid interface. Furthermore, once the microscope tip starts to distort the drop profile it will not return to a stable operation (self-stabilize). This observation illustrates the sensitivity of such experiments and the importance of operating the microscope with a set of stable feedback parameters and microscope settings (set-point, drive amplitude). A possible explanation is the fact that the bandwidth of the microscope settings is too narrow. By changing the wetting behaviour of the investigated solid/liquid system, one also alters the wetting behaviour of the liquid and the tip. This change may lead to a departure of the microscope settings from the narrow, optimal setting range, resulting in an unstable imaging process. One can conclude that temperature changes in the microscope environment, during the scanning of liquid interfaces, can lead to stability problems difficult to control and should be avoided.

A representative example of these type of experiments is given in Figure 75a) showing an area scan of a glycerin droplet before initiation of a temperature ramp. The experiment starts at ambient temperature (20 [°C]). The power input increases linearly over 6 min. changing the temperature with a rate of 0.016 [°C/sec.] up to a constant temperature of 26 [°C]. Figure 75b,c) shows the obtained profile line-scans, whereas Figure 75d,e) shows the associated phase contrast signals. The profile data in Figure 75b,c) indicate a strong evaporative behaviour of the droplet which is not expected due to this small temperature change and also not expected when compared with the results in Figure 73 where an experiment with glycerin at constant ambient temperature only shows a fraction of the evaporative behaviour of this experiment. However, the phase contrast data point to an explanation for this behaviour.

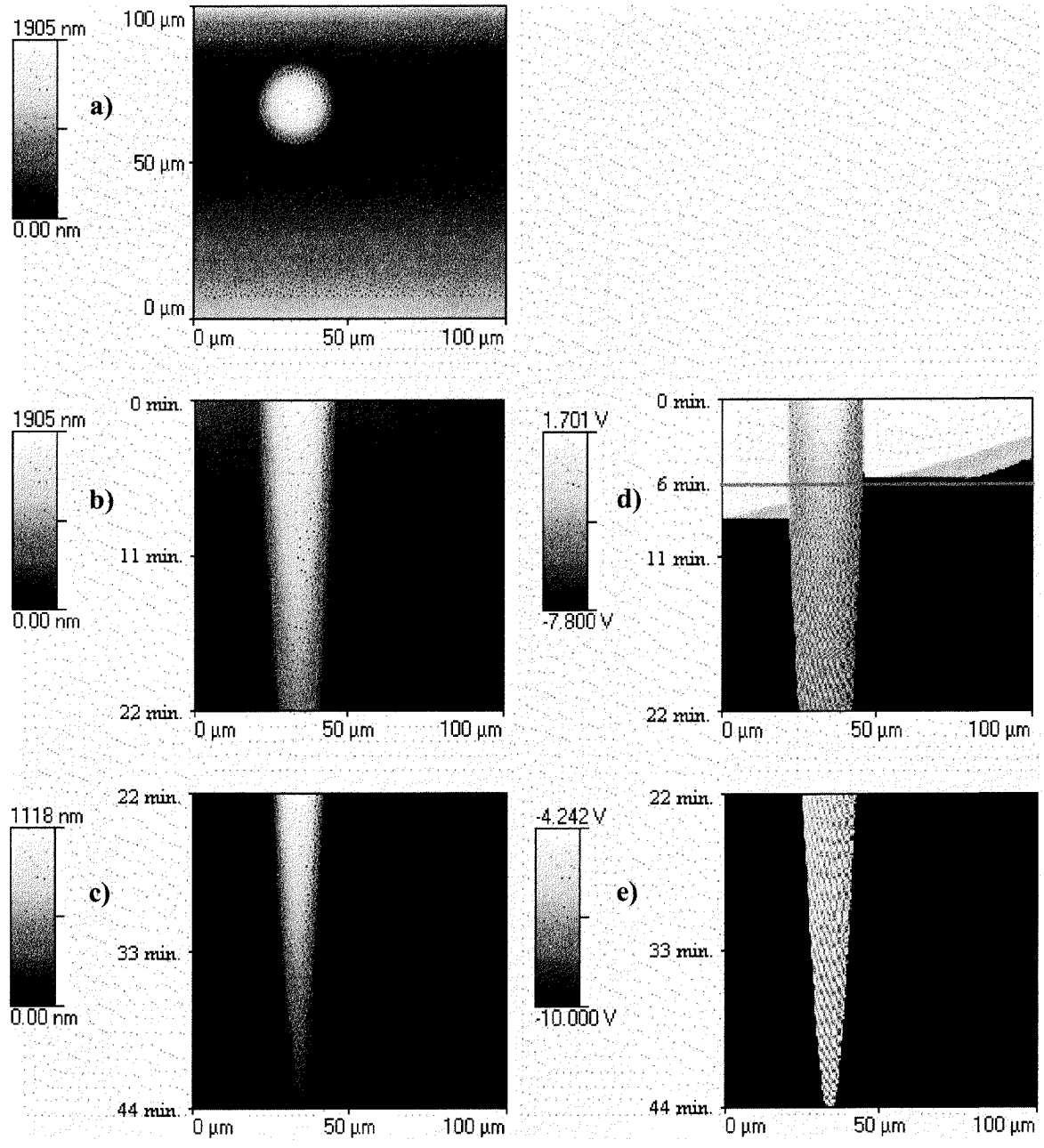

Figure 75: (a) Area scan of a glycerin droplet on mica situated on a microheater at ambient temperature (20 °C); (b,c) Line scans of the glycerin droplet. (d,e) Phase-contrast signal of the line scans.

As shown in Figure 75d,e) the phase contrast data exhibit a patterned structure on the liquid, which cannot be seen in Figure 75b) but is slightly visible on Figure 75c) bottom, at the end of the scan. An investigation of the corresponding profiles is given in Figure 76a-c),

illustrating (a) a profile of the phase contrast of Figure 75e), (b) a profile of the drop topography of Figure 75c), and (c) a profile of the center-line of the droplet of Figure 75a). These results reveal strong oscillations.

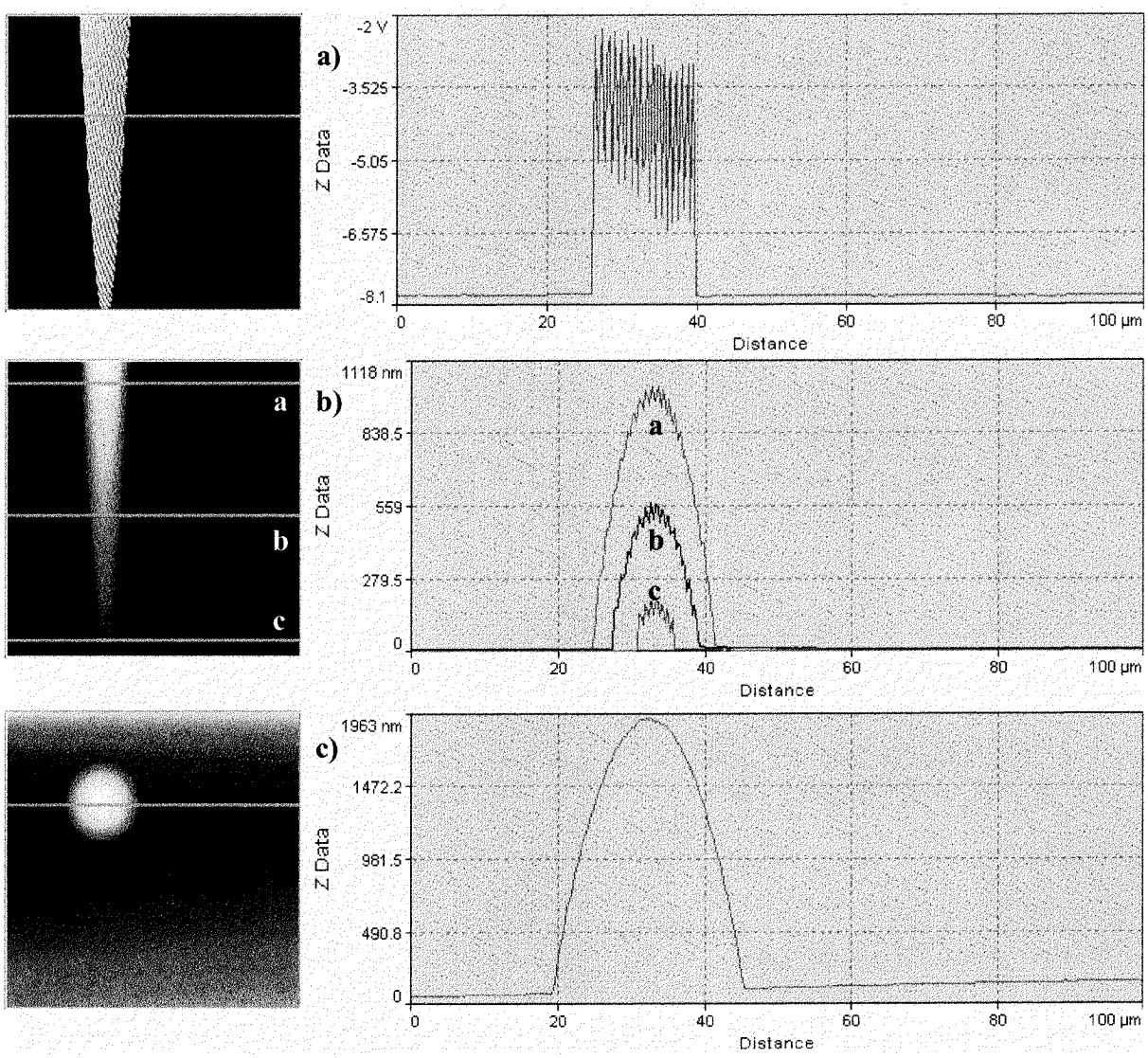

Figure 76: (a) Phase-contrast profile of the line scan in Figure 75c, showing strong oscillations. (b) Corresponding topography profiles showing oscillatory behaviour. (c) Topography profile of the glycerin droplet before initiation of the heating process, showing no visible signs of oscillations or distortions.

The drop profile in Figure 76b) shows a severely perturbed surface possibly by repetitive indentation of the microscope tip into the droplet, whereas the drop profile in Figure 76c), before initiation of the heating process, reveals an unperturbed drop. The repetitive

indentation of the microscope tip can well be the reason for this strongly enhanced evaporative behaviour. The increase of the substrate temperature of 6 [°C] above the ambient temperature will certainly also contribute to an enhanced evaporation. However, the main contribution to evaporation in the experiment illustrated by Figure 75 appears to be the interaction of the microscope tip with the liquid microstructure.

6.4.2.3 Spontaneously Spreading Liquids

The experiments in the following section are based on the use of spontaneously spreading liquids to study the dynamic wetting behaviour. All microscope parameters were kept constant for the entire duration of the experiments (e.g. temperature, feedback parameters etc.). To this end, polished silicon wafers and mica were used as substrates. Liquids employed spreading spontaneously on both substrates were PDMS I and PDMS II. Squalane was employed on silicon substrates only. Preliminary experiments revealed that uncoated silicon tips could not be used for these experiments. No stable operation of the microscope could be achieved, due to interfacial processes between the tip and the liquids which wet the silicon tips completely. Therefore, HFP and 1-dodecanethiol coated tips were used. Experimental results using the latter tips with PDMS I and II on either mica or polished wafers as well as squalane on polished wafers all exhibit the form represented by Figure 77a-d), showing a droplet (or rather a film) of PDMS II on mica. Figure 77a) shows the PDMS II droplet after deposition on the mica substrate. Figure 77c) represents the corresponding phase contrast signal. Figure 77b,d) show the same drop after 334 min. The phase contrast of the initial scan, Figure 77c), reveals that the drop has already spread beyond the scan range of the microscope, which is 100x100 [μm], since no phase difference indicating a change from liquid to solid substrate is observable. The phase contrast is constant except for the center region of the drop. After 334 min. the same drop takes the form given by Figure 77b,d). The phase contrast signal is still constant except for the center region of the drop. Two differences are identified between Figure 77a) and b): (i) the height of the drop has decreased as expected due to the spreading of the PDMS II droplet on the mica surface; (ii) interestingly the center of the drop has moved.

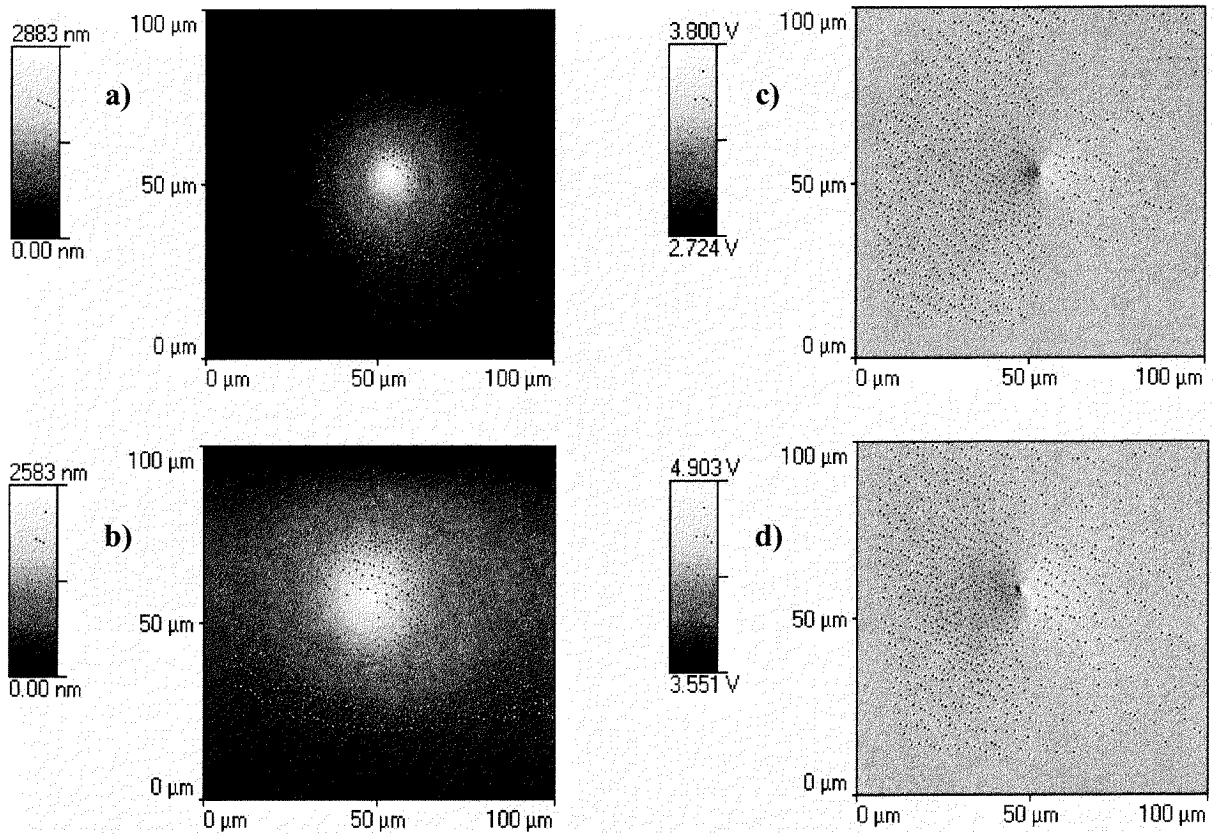

Figure 77: (a) PDMS II drop on mica right after deposition. (b) The same droplet after 334 min of continuous scanning. (c) Phase-contrast of the droplet right after deposition. (d) Phase-contrast after 334 min of continuous scanning. The center of the droplet in (b) has moved relative to the droplet center in (a).

The corresponding profile plots of Figure 77a,b) are shown in Figure 78a,b). Three profiles at different cross-sections of the droplet are shown. The center cross-sections, Figure 78a,b) show, a peak-like topography at the corresponding centers of the droplets. Scans of the same droplet at even later times do not change significantly. The drop height stays approximately the same and shows the same peak-like behaviour whereas a further spreading and decrease of the drop height was expected. The conclusion is therefore that the liquid has possibly aggregated on a particle left back on the substrate after the cleaning procedure.

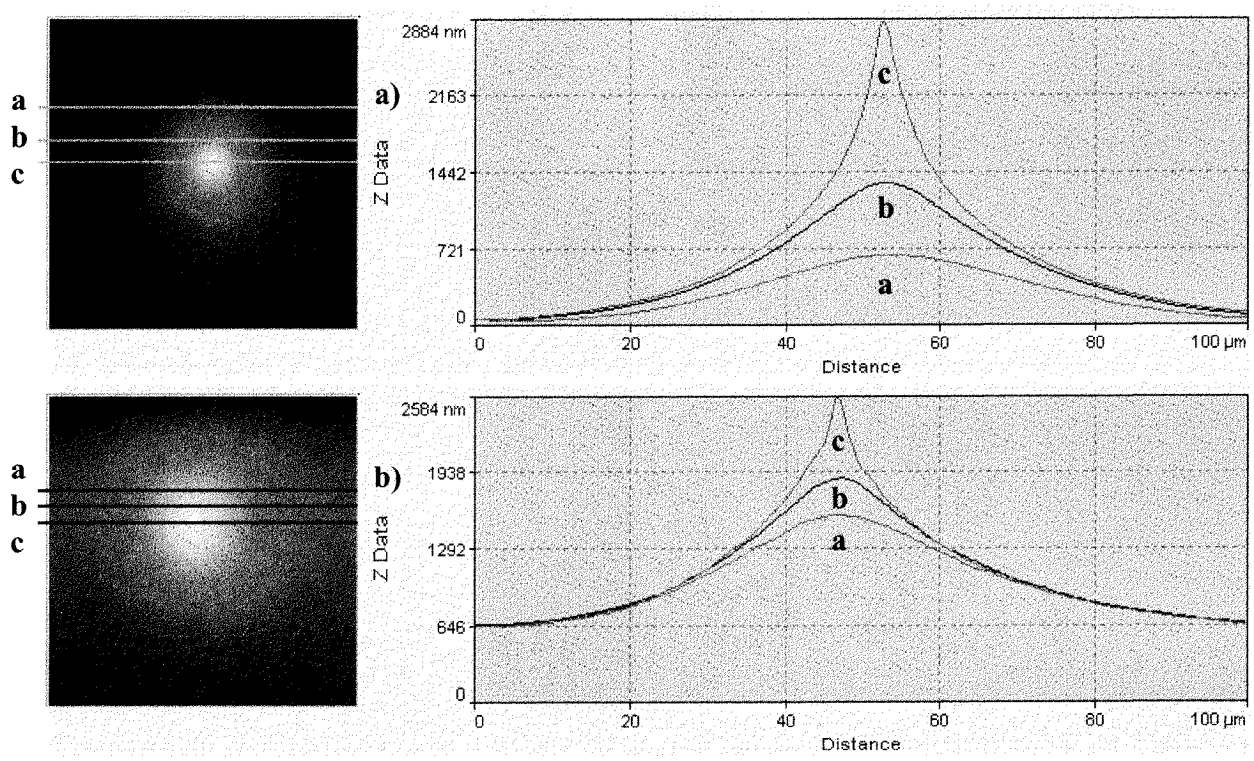

Figure 78: (a) Topography profiles of the droplet shown in Figure 77a. (b) Topography profiles of the drop shown in Figure 77b.

Results of different nature, without the possible presence of particles on the substrate, could not be obtained from this experimental procedure. A reason for this is that droplets deposited on particle-free regions of the substrates form a very thin film-like state prior to scan initiation, possibly already exceeding the maximum scanning range of the microscope and therefore rendering the detection of a droplet very difficult.

To gain more insight into these observations, experiments with PDMS I and II as well as squalane were conducted on gold-coated wafers with a SAM of 1-dodecanethiol to prevent complete wetting of the liquids. These experiments revealed interesting details of the imaging process.

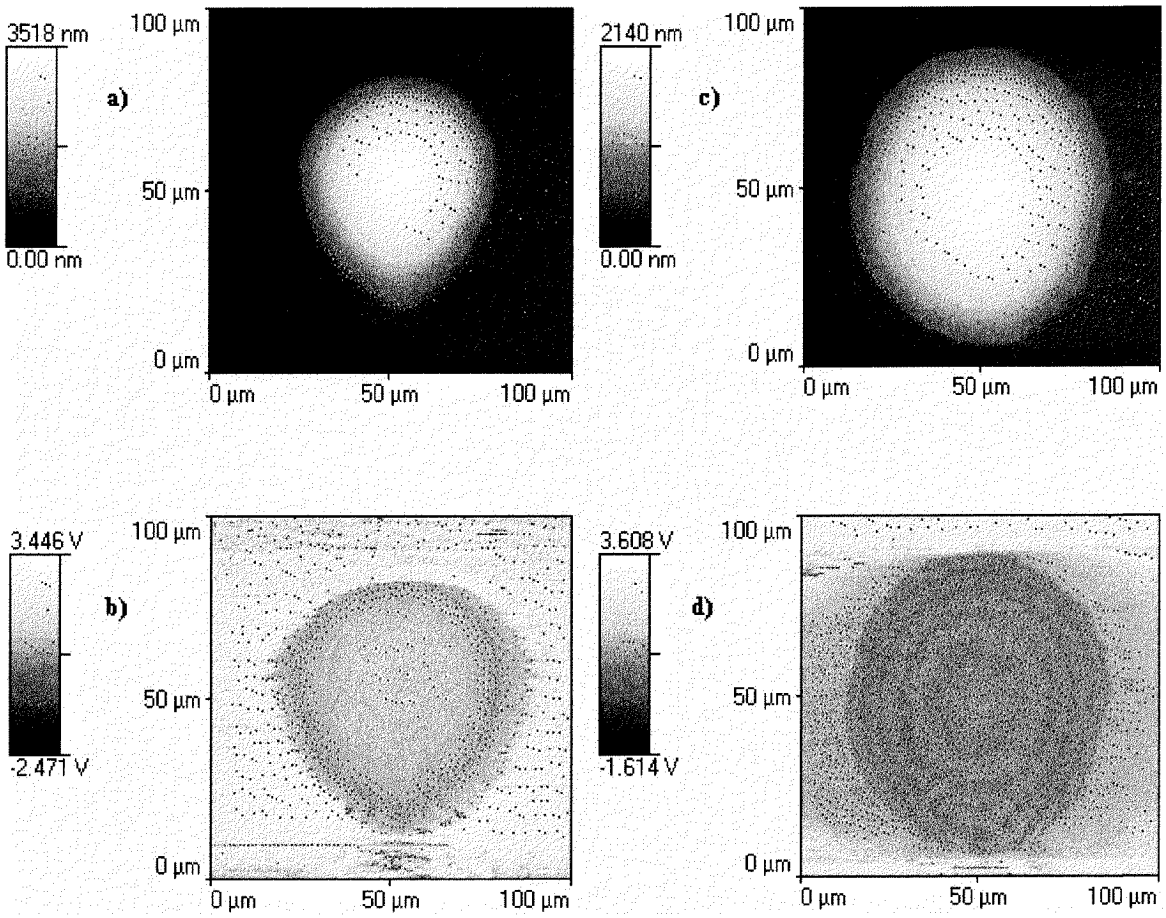

Figure 79: (a) Area scan of a PDMS II droplet on a gold-coated wafer with a SAM of 1-dodecanethiol after deposition on the substrate. (b) Phase-contrast of (a). (c) Area scan after 667 min of repetitive scanning. (d) Phase contrast of (c).

Figure 79a-d) show a PDMS II droplet on a SAM of 1-dodecanethiol illustrating the topographies of the trace and the retrace of the same droplet. There is a clear difference visible in the droplet perimeters. The phase contrast signals in Figure 79b,d) show that depending on the scan direction (the direction of tip movement and data collection) the tip of the microscope drags parts of the droplet over the substrate. Although PDMS II on a SAM of 1-dodecanethiol exhibits a partial wetting behaviour, the droplet starts to spread after initiation of the scanning process. The PDMS II droplet is literally aided to spread on the substrate by the interaction of the moving microscope tip with the liquid droplet. A similar experiment with squalane, Figure 80a,b), shows an even more serious interaction of the microscope tip with the liquid structure.

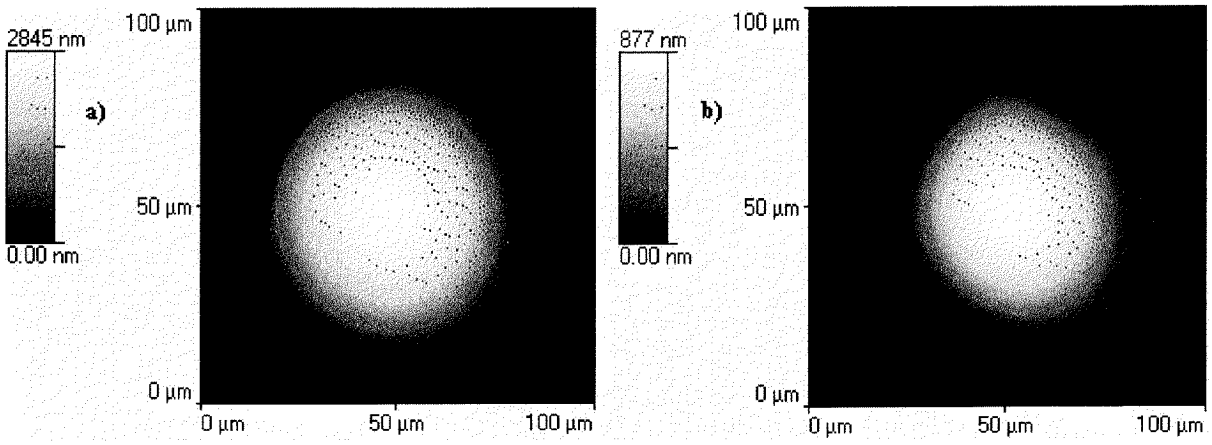

Figure 80: (a) Area scan of a squalane droplet on a gold-coated wafer with a SAM of 1-dodecanethiol right after deposition. (b) Droplet after 1853 min of repetitive scanning.

As can be seen in Figure 80b) the droplet has started disintegrating by the interaction of the microscope tip after 1853 min. of repetitive scanning. The profile plot of Figure 80b) shown in Figure 81 further illustrates this observation. In addition to the remaining core part of the squalane droplet, a number of liquid patches has formed around the droplet. However, none of the instabilities encountered in the experiments employing microheaters as wetting promoters are observed, although doubtlessly the microscope tip interacts with the liquid structures dragging outwards some of the liquid for each scanned line. The profile of the remaining core of the squalane droplet shows no distortions or oscillations. These results exhibit different phenomena of the imaging process than in the microheater experiments.

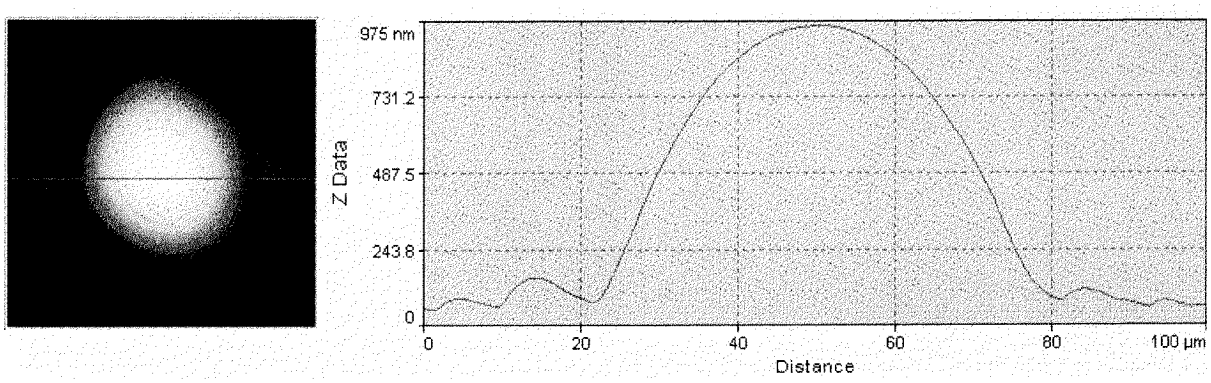

Figure 81: Profile of the squalane droplet shown in Figure 80b.

A possible interpretation of the overall results is that oscillatory behaviour occurs, as shown for instance in Figure 76b), when the tip indents the liquid structure but the tip/cantilever assembly has enough kinetic/potential energy to overcome a possible formation of a permanent liquid bridge between the drop and the tip. This emerges in experiments employing glycerin, which only wets the microscope tips partially (uncoated and coated), when a departure from the optimal setting occurs. A departure from the optimal setting range can lead to an intensified indentation and therefore to visible perturbations of the liquid interface. On the other hand, when using fluids as PDMS I and II as well as squalane that wet the tip completely or in a transitional regime between complete and partial wetting, there might occur a formation of a permanent liquid bridge between the tip and the liquid structure. This may cause a large decrease of the tip oscillation amplitude, resulting in unperturbed, but physically untrue profiles as shown in Figure 81. This interpretation might also give an explanation as to why the drop center in Figure 77a,b) moves. A strong interaction of the tip with the liquid structure aggregating on a possible particle might lead to a dragging of the latter on the substrate leading to a movement of the particle and thus the center of the droplet.

6.5 Discussion and Conclusion

In general significant challenges are encountered in employing scanning force microscopy on liquid interfaces. The reasons for this are first that all liquids are prone to possible manipulations or distortions when a moving object interacts with their surface, and second that interfacial processes between the sample and the probing tips can only be reduced but not completely avoided altering the result to some extent which is important but also difficult to determine a-priori. The use of surface modified tip/cantilever assemblies with reduced surface energies yielded clear improvements of the imaging process. Nevertheless, when departing slightly from the optimal setting range, distortions or oscillatory indentation of the tips into the liquid surface, as exemplified by Figure 76, emerge. Using fluids exhibiting a wetting behaviour with the tip (uncoated or coated,) can lead to dragging of liquid parts out of the perimeter of the investigated droplet, as shown in Figure 80. This interaction may be minimized and controlled but not completely eliminated.

It appears that a weak wetting behaviour of the investigated liquid structure on the tip yields better results. Glycerin, though evaporative and therefore not ideally suited for these experiments, showed the most stable and reliable results. PDMS, squalane and all the other

employed fluids, except for glycerin, showed a good wetting behaviour on the employed tips (coated or uncoated). Images of these liquids obtained from SFM were all distorted.

Concerning the resolution of the microscope when applied to liquid structures, the comparison of a drop profile with theoretical predictions, Figure 74b), illustrates that the microscope data agree with the theoretical prediction well. Local deviations of only 50-100 [nm] are present.

The experiences gathered so far have shown a marked interaction of the tip and the liquid, which would support the assumption that a part of the distortions are caused by manipulations of the microscope tip due to interfacial and also mechanical effects. As is common to all scanning force microscope applications, it is difficult to decide whether a parameter setting of the microscope is optimal or not. Without some information of the topography of the investigated sample this is hardly possible. Pompe et al. [108] showed that changing the microscope set-point within the narrow bandwidth of stable operation can change the topography of an observed droplet considerably. Our study corroborates these observations.

Scanning force microscopy may not yet be a reliable, general method for the investigation of liquid microstructures and wetting. However the prospects can be formidable. If interfacial phenomena between the probing tip and the probed liquid structure can be minimized and controlled, scanning force microscopy can give insights to wetting and possibly other interfacial phenomena. A reduced overall resolution compared to the operation of the SFM on more rigid samples may have to be taken into account. On the other hand higher resolutions in both vertical and lateral direction than those achievable presently with conventional optical microscopes are possible.

7. Summary

The objectives of this thesis were to investigate the fundamental thermofluidic transport phenomena occurring during the deposition of a droplet pile up, a building block for the manufacturing of droplet-based microstructures, or simply for the deposition of precise amounts of a molten material on a substrate.

The axisymmetric impact of a solder microdroplet on top of an already deposited and solidified droplet was studied both experimentally as well as numerically. The length, velocity and time scales of the investigated pile up process were O(100 μm), O(1 m/s), and O(100 μs) respectively. The substrate temperatures were varied in a range of 25 – 150 [°C].

To the best of our knowledge, this thesis presents the first experimental as well as verified numerical results on the transient fluid dynamics, wetting and solidification of molten microdroplets impinging on presolidified droplets or in more general terms on non-flat substrates. The experimental findings point to a considerable influence of the substrate shape (i.e. the shape of the presolidified droplet) on the spreading behaviour of the impacting droplets. The cooling and subsequent solidification of the impinging droplets is strongly influenced by the fin-type structure of the substrates employed. The solidification time therefore depends, in addition to the thermal contact resistances at the interfaces, on the transport of heat through the solid structures above the flat wafer substrate. The impact velocities affect strongly the final shapes of the observed pile up structures but not the solidification time due to possible better thermal contact and/or higher convection in the impinging droplets. This means that the above mentioned fin-type cooling of the impinging droplet, or the geometry of the presolidified droplet, controls the solidification time. The freezing coupled with the all important fluid mechanics determines the transient behaviour of the impinging droplet. For decreasing Stefan number (i.e. higher substrate temperatures) an increasing importance of capillary phenomena, or wettability, is observed. This is manifested by larger spread factors. The latter are again coupled through the larger thermal contact area to the solidification time and thus the transient behaviour as well as the endshapes of the pile up process.

A versatile numerical model accounting for the incompressible and axisymmetric Navier-Stokes equations, conjugate heat transfer, as well as solidification in a severely deforming domain containing a free surface and three interfaces, including the freezing front, was developed in order to shed light on the prevailing physical phenomena and to test predictive capabilities. The numerical implementation of the developed mathematical model showed

desirable stability, accuracy, and mass as well as energy conserving properties. It was shown that, in addition to the complex shape of the presolidified droplet, respectively the substrate shape, the mathematical model features five relevant dimensionless groups. These are the Reynolds number, the Weber number, the two Biot numbers, and the Stefan number. It was shown that the Reynolds and Weber number predominantly affect the amount of spreading and deformation of the impinging droplet. The two Biot numbers control the conjugate heat transfer. Because of the coupling of the latter with the fluid mechanics, the Biot numbers also affect the transient behaviour of the pile up process in an implicit manner. Likewise, the Stefan number affects the thermal solution and therefore in an implict manner the transients of the pile up process. As observed in the experiments, the Stefan number (substrate temperature) affects the wetting process and consequently the shape of the generated microstructure strongly.

Given an optimal choice of the Biot numbers for the conjugate heat transfer, a very good matching between numerical and experimental results is achieved. However, this is strongly dependent on the Stefan number. The latter controls in an implicit manner the wettability. Capillary effects have to be accounted for with the help of experimental data (currently unavailable in the literature) in order to achieve good numerical agreement with the experiments in the low Stefan number regime.

The employed model at the dynamic contact line is the well known Navier-Slip model. As long as capillary effects are not dominant (high Stefan number), this model predicts the spreading process well. At lower Stefan numbers the agreement of the spread factor predicted by the Navier-Slip model and the experimentally observed spread factor deteriorates due to increasing capillary effects. Presently, no integral models are available in the literature accounting for slip of the contact line, specific dynamic contact angle regimes as well as capillary forces due to the lack of knowledge of the physics of the contact line, in particular in the presence of temperature gradients and phase change. A possible promising but very challenging approach to access the molecular level of wetting using scanning force microscopy was presented in section 6 of this thesis.

Regarding the implementation in industrial applications and processes, good predictive capabilities of numerical models are of central importance because this helps to avoid extensive and difficult experimental testing. To this end, the microscale physics represented by the thermal contact resistance as well as the wetting have to be clearly re-emphasised and imputed to state of the art models like the one presented in this thesis. Further work has to be directed towards a clear definition of cause and effect of capillary phenomena in the observed

surface wetting of the impinging droplet. This can be done concurrently experimentally and (with the ever increasing computational power) based on rigorous molecular dynamics simulations. Since wetting phenomena have to be described at the molecular level to circumvent ad-hoc assumptions that are necessary in continuous treatments, a need also arises to couple molecular physics with continuum approaches, certainly a viable concept and a recommendation for future research.

Appendix

Appendix A: Relevant Thermophysical Properties [118]

Material	k [W/mK]	μ [Pas]	ρc_p [kJ/m^{3}K]	ρ [kg/m^3]	γ [N/m]	T_m [°C]	L [J/kg]	c_p [J/kgK]
Solder (liquid)	25	0.00262	1750	8218	0.345	183	42000	238
Solder (solid)	48	-	1450.2	8240	-	183	42000	176
Gold	317	-	2489.7	19300	-	1064.4	-	129
Silicon	148 (25°C) 98.9 (125°C) 94 (180°C)	-	1658.96	2330	-	1410	-	712
Silicon Nitride 1)	27	-	2260.98	3180	-	1800	-	711
Ti90W 2)	159	-	2630.7	14730	-	-	-	178.6
Thermal Paste (HTC)	0.84	-	-	-	-	-	-	-

1) Source: www.accuratus.com

2) Source: www.puretechnic.com

References

[1] D. J. Hayes, D. B. Wallace, and M. T. Boldman, Solder Jet for Low Cost Wafer Bumping, Proceedings ISHM, 1996.

[2] D. J. Hayes and D. B. Wallace, Solder Jet Printing: Wafer Bumping and CSP Applications, Chip Scale Review, Vol. 2, pp. 75-80, 1998.

[3] B. Xiong, C. M. Megaridis, D. Poulikakos, and H. Hoang, An Investigation of Key Factors Affecting Solder Microdroplet Deposition, J. Heat Transfer, Vol. 120, pp. 259-270, 1998.

[4] D. Attinger, Z. Zhao, and D. Poulikakos, An Experimental Study of Molten Microdroplet Surface Deposition and Solidification: Transient Behaviour and Wetting Angle Dynamics, ASME Journal of Heat Transfer, Vol. 122, pp. 544-556, 2000.

[5] F. Gao and A. Sonin, Precise Deposition of Molten Microdrops: The Physics of Digital Microfabrication, Proc. R. Soc. Lond. A, Vol. 444, pp. 533-554, 1994.

[6] L. J. Zarzalejo, K. S. Schmaltz, and C. H. Amon, Molten Droplet Solidification and Substrate Remelting in Microcasting. Part I: Numerical Modeling and Experimental Verification, Heat and Mass Transfer, Vol. 34, pp. 477-485, 1999.

[7] J. P. Kruth, Material Incress Manufacturing by Rapid Prototyping Techniques, Annals of the CIRP, Vol. 40/2, pp. 603-614, 1991.

[8] M. Orme, A Novel Technique of Rapid Solidification Net-Form Materials Synthesis, J. Materials Engineering and Performance, Vol. 2, pp. 399-405, 1993.

[9] M. Orme, C. Huang, and J. Courter, Deposition Strategies for Control of Microstructures Microporosity and Surface Roughness in Droplet-Based Solid Freeform Fabrication of Structural Materials, in E. F. Matthys and W. G. Truckner

(ed.), Melt Spinning, Strip Casting and Slab Casting, pp. 125-143,, The Minerals, Metals and Materials Society, Warrendale Pennsylvania, 1996.

[10] M. E. Orme, C. Huang, and J. Courter, Precision Droplet-Based Manufacturing and Material Synthesis, Atomization and Sprays, Vol. 6, pp. 305-329, 1996.

[11] M. Orme and R. Smith, Enhanced Aluminum Properties with Precise Droplet Deposition, ASME J. Manufacturing Science and Engineering, Vol. 122, pp. 484-493, 2000.

[12] J. M. Waldvogel, Transport Phenomena and Solidification in Picoliter Solder Droplet Deposition, Ph.D. Thesis, University of Illinois at Chicago, Chicago, 1995.

[13] J. M. Waldvogel, D. Poulikakos, D. B. Wallace, and R. Marusak, Transport Phenomena in Picoliter Size Solder Droplet Dispension on Composite Substrate, J. Heat Transfer, Vol. 118, pp. 148-156, 1996.

[14] J. M. Waldvogel and D. Poulikakos, Solidification Phenomena in Picoliter Size Solder Droplet Deposition on a Composite Substrate, Int. J. Heat Mass Transfer, Vol. 40, pp. 295-309, 1997.

[15] A. M. Worthington, A Second Paper on the Forms Assumed by Drops of Liquids Falling Vertically on a Horizontal Plate, Proc. Roy. Soc. London, Vol. 25, pp. 498-503, 1877.

[16] A. M. Worthington, On the Forms Assumed by Drops of Liquids Falling Vertically on a Horizontal Plate, Proc. Roy. Soc. London, Vol. 25, pp. 261-271, 1877.

[17] J. Che, S. Ceccio, and G. Tryggvason, in *1999 TMS Annual Meeting* (San Diego, California, February 1999).

[18] H. Liu, E. J. Lavernia, and R. H. Rangel, Modeling of Molten Droplet Impingement on a Non-Flat Surface, 1994 International Mechanical Engineering Congress and ExpositionChicago, Ill., 1994.

[19] J. M. Waldvogel and D. Poulikakos, Solidification Phenomena in Picoliter Size Droplet Deposition on a Composite Substrate, Int. J. Heat Mass Transfer, Vol. 40, pp. 295-309, 1997.

[20] D. B. Kothe, R.C. Mjolsness, and M. D. Torrey, RIPPLE: A computer Program for Incompressible Flows with Free Surfaces, LA-12007-MS, UC-000, Los Alamos National Laboratory, New Mexico, 1991.

[21] S. Haferl, Z. Zhao, J. Giannakouros, D. Attinger, and D. Poulikakos, Transport Phenomena in the Impact of a Molten Droplet on a Surface: Macroscopic Phenomenology and Microscopic Considerations Part I: Fluid Dynamics, in C.-L. Tien (ed.), Annual Reviews in Heat Transfer, Vol. XI, pp. 65-143, Begell House, New York, 2000.

[22] D. Attinger, S. Haferl, Z. Zhao, and D. Poulikakos, Transport Phenomena in the Impact of a Molten Droplet on a Surface: Macroscopic Phenomenology and Microscopic Considerations. Part II Heat Transfer and Solidification, in C.-L. Tien (ed.), Annual Reviews in Heat Transfer, Vol. XI, pp. 145-205, Begell House, New York, 2000.

[23] S. F. Kistler, Hydrodynamics of Wetting, in J. C. Berg (ed.), Wettability1 ed., Dekker, New York, 1993.

[24] J. Koplik, J. R. Banavar, and J. F. Willemsen, Molecular Dynamics of Poiseuille Flow and Moving Contact Lines, Phys. Rev. Lett., Vol. 60, pp. 1282-1285, 1988.

[25] J. Koplik, J. R. Banavar, and J. F. Willemsen, Molecular Dynamics of Fluid Flow at Solid Surfaces, Phys. Fluids A, Vol. 1, pp. 781-794, 1989.

[26] P. A. Thompson and M. O. Robbins, Simulations of Contact-Line Motion: Slip and the Dynamic Contact Angle, Phys. Rev. lett., Vol. 63, pp. 766-769, 1989.

[27] P. A. Thompson and S. M. Troian, A General Boundary Condition for Liquid Flow at Solid Surfaces, Nature, Vol. 389, pp. 360-362, 1997.

[28] Z. Zhao, D. Poulikakos, and J. Fukai, Heat Transfer and Fluid Dynamics during the Collision of a Liquid Droplet on a Substrate : I-Modeling, Int. J. Heat Mass Transfer, Vol. 39, pp. 2771-2789, 1996.

[29] Z. Zhao, D. Poulikakos, and J. Fukai, Heat Transfer and Fluid Dynamics during the Collision of a Liquid Droplet on a Substrate I. Experiments, Int. J. Heat Mass Transfer, Vol. 39, pp. 2791-2802, 1996.

[30] D. B. Wallace, Automated Electronic Circuit Manufacturing Using Ink-Jet Technology, J. Electronic Packaging, Vol. 36, 1989.

[31] D. J. Hayes, D. B. Wallace, and M. T. Boldman, Picoliter Solder Droplet Dispension, ISHM Symposium 92 Proceedings, pp. 316-321,1992.

[32] J. F. Dijksman, Hydrodynamics of Small Tubular Pumps, J. Fluid Mech., Vol. 139, pp. 173-191, 1984.

[33] C. D. Ohl, A. Philipp, and W. Lauterborn, Cavitation Bubble Collapse Studied at 20 Million Frames per Second, Annalen der Physik, Vol. 4, pp. 26-34, 1995.

[34] S. Chandra and C. T. Avedisian, On the Collision of a Droplet with a Solid Surface, Proc. R. Soc. Lond. A, Vol. 432, pp. 13-41, 1991.

[35] C. D. Stow and M. G. Hadfield, An Experimental Investigation of Fluid Flow Resulting from the Impact of a Water Drop with an Unyielding Dry Surface, Proc. Roy. Soc. London A, Vol. 373, pp. 419-441, 1981.

[36] L. H. Wachters and N. A. J. Westerling, The Heat Transfer from a Hot Wall to Impinging Water Drops in the Spherical State, Chem. Eng. Sci., Vol. 21, pp. 1047-1056, 1966.

[37] A. L. Yarin and D. A. Weiss, Impact of Drops on Solid Surfaces: Self-Similar Capillary Waves, and Splashing as a New Type of Kinematic Discontinuity, J. Fluid Mech., Vol. 283, pp. 141-173, 1995.

[38] C. Mundo, M. Sommerfeld, and C. Tropea, Droplet-Wall Collisions: Experimental Studies of the Deformation and Breakup Process, Int. J. Multiphase Flow, Vol. 21, pp. 151-173, 1995.

[39] S. Toda, A Study of Mist Cooling, Heat Transfer Japanese Research, Vol. 1, pp. 1-44, 1974.

[40] A. F. J. Baggerman and D. Schwarzbach, Solder-Jetted Eutectic PbSn Bumps for Flip-Chip, IEEE Trans. Comp., Pack. and Manuf. Tech. B, Vol. 21, pp. 371-381, 1998.

[41] M. Rein, Phenomena of Liquid Drop Impact on Solid and Liquid Surfaces, Fluid Dynamics Research, Vol. 12, pp. 61-93, 1993.

[42] Z. Zapryanov and S. Tabakova, Dynamics of Bubbles, Drops and Rigid Particles,, vol. 50, Kluwer Academic, Dordrecht, Boston, London, 1999.

[43] B. Kang, J. Waldvogel, and D. Poulikakos, Remelting Phenomena in the Process of Splat Solidification, J. Mat. Science, Vol. 30, pp. 4912-4925, 1995.

[44] T. Bennett and D. Poulikakos, Heat Transfer Aspects of Splat-Quench Solidification: Modeling and Experiment, J. Mat. Sci., Vol. 29, pp. 2025-2039, 1994.

[45] W. E. Ranz and W. R. Marshall, Evaporation from Drops I & II, Chem. Eng. Prog., Vol. 48, pp. 173-180, 1952.

[46] S. Schiaffino and A. A. Sonin, On the Theory for the Arrest of an Advancing Molten Contact Line on a Cold Solid of the Same Material, Phys. Fluids, Vol. 9, pp. 2227-2233, 1997.

[47] S. Schiaffino and A. A. Sonin, Motion and Arrest of a Molten Contact Line on a Cold Surface: An Experimental Study, Phys. Fluids, Vol. 9, pp. 2217-2226, 1997.

[48] M. Pasandideh-Fard, R. Bhola, S. Chandra, and J. Mostaghimi, Deposition of Tin Droplets on a Steel Plate: Simulations and Experiments, Int. J. Heat Mass Transfer, Vol. 41, pp. 2929-2945, 1998.

[49] T. Bennett and D. Poulikakos, Splat-Quench Solidification: Estimating the Maximum Spreading of a Droplet Impacting a Solid Surface, J. Mat. Sci., Vol. 28, pp. 963-970, 1993.

[50] S. Schiaffino and A. A. Sonin, Molten Droplet Deposition and Solidification at Low Weber Numbers, Phys. Fluids, Vol. 9, pp. 3172-3187, 1997.

[51] D. Poulikakos and J. M. Waldvogel, Heat Transfer and Fluid Dynamics in the Process of Spray Deposition, Advances in Heat Transfer, Vol. 28, Academic Press, 1996.

[52] J. Fukai, Z. Zhao, D. Poulikakos, C. M. Megaridis, and O. Miyatake, Modeling of the Deformation of a Liquid Droplet Impinging upon a Flat Surface, Phys. Fluids A, Vol. 5, pp. 2588-2599, 1993.

[53] M. Pasandideh-Fard and J. Mostaghimi, On the Spreading and Solidification of Molten Particles in a Plasma Spray Process: Effect of Thermal Contact Resistance, Plasma Chemistry and Plasma Processing, Vol. 16, pp. 83-98, 1996.

[54] M. Pasandideh-Fard, Y. M. Qiao, S. Chandra, and J. Mostaghimi, Capillary Effects during Droplet Impact on a Solid Surface, Phys. Fluids, Vol. 8, pp. 650-659, 1996.

[55] S. Haferl, V. Butty, D. Poulikakos, J. Giannakouros, K. Boomsma, C. M. Megaridis, and V. Nayagam, Freezing Dynamics of Molten Solder Droplets Impacting onto Flat Substrates in Reduced Gravity, Int. J. Heat Mass Transfer, Vol. 44, pp. 3513-3528, 2001.

[56] L. D. Landau and E. M. Lifshitz, Fluid Mechanics, Course of Theoretical Physics, 1 ed., vol. 6, pp. 230-235, Pergamon, Oxford, 1959.

[57] J. H. Ferziger and M. Peric, Computational Methods for Fluid Dynamics, 2 ed., Springer Verlag, Berlin, Heidelberg, New York, 1999.

[58] A. J. Chorin, A Numerical Method for Solving Incompressible Viscous Flow Problems, J. Computational Physics, Vol. 2, pp. 12-26, 1967.

[59] F. Bosnjakovic, Technische Thermodynamik, 7 ed., Steinkopff Verlag, Darmstadt, 1988.

[60] J. U. Brackbill, D. B. Kothe, and C. Zemach, A Continuum Method for Modeling Surface Tension, J. Compt. Phys., Vol. 100, pp. 335-354, 1992.

[61] G. Grosche, V. Ziegler, and D. Ziegler, Teubner-Taschenbuch der Mathematik,, vol.,, B.G. Teubner Verlagsgesellschaft, Stuttgart, 1996.

[62] C. Huh and L. E. Scriven, Hydrodynamic Model of Steady Movement of a Solid/Liquid/Fluid Contact Line, J. Coll. Inter. Sci., Vol. 35, pp. 85-101, 1971.

[63] E. B. Dussan, The Moving Contact Line: The Slip Boundary Condition, J. Fluid Mech., Vol. 77, pp. 665-684, 1976.

[64] S. H. Davis, Contact Line Problems in Fluid Mechanics, J. Appl. Mech., Vol. 50, pp. 977-982, 1983.

[65] M. D. Gunzburger, Finite Element Methods for Viscous Incompressible Flows, 1 ed., Academic Press Inc., Boston, San Diego, 1989.

[66] C. Schwab, Einführung in die Numerik Partieller Differentialgleichungen Teil 1 & 2, ETH Zürich, Zürich, 1997.

[67] L. Piegl and W. Tiller, The Nurbs Book, 2 ed., Springer, Berlin, Heidelberg, 1997.

[68] P. Bach and O. Hassager, An Algorithm for the Use of the Lagrangian Specification in Newtonian Fluid Mechanics and Applications to Free-Surface Flow, J. Fluid Mech., Vol. 152, pp. 173-190, 1985.

[69] W. Bushko and I. R. Grosse, New Finite Element Method for Multidimensional Phase Change Heat Transfer Problems, Numerical Heat Transfer B, Vol. 19, pp. 31-48, 1991.

[70] W. Liu, G. X. Wang, and E. F. Matthys, Determination of the Thermal Contact Coefficient for a Molten Droplet Impinging on a Substrate, Transport Phenomena in Materials Processing and Manufacturing ASME, Vol. HTD 196, 1992.

[71] H. A. Barnes, J. F. Hutton, and K. Walters, An introduction to Rheology, 3 ed., vol. 3, Elsevier, Amsterdam, 1993.

[72] D. B. Spencer, R. Mehrabien, and M. C. Flemings, Rheological Behaviour of Sn-15%Pb in the Crysallization Range, Metallurgical Transactions, Vol. 3, p. 1925, 1972.

[73] J. Koke, Rheologie teilerstarrter Metalllegierungen, Vol. 620, VDI Verlag, Düsseldorf, 2001.

[74] D. S. Burnett, Finite Element Analysis, 1 ed., Addison-Wesley, Reading, Massachusetts, 1987.

[75] D. Braess, Finite Elemente, 2 ed., Springer, Berlin, Heidelberg, 1997.

[76] G. X. Wang and E. F. Matthys, Experimental Investigation of Interfacial Thermal Conductance for Molten Metal Solidification on a Substrate, J. Heat Transfer, Vol. 118, pp. 157-163, 1996.

[77] S. Inada, Transient Heat Transfer from a Free-Falling Molten Drop of Lead to a Cold Plate, J. Chem. Eng. Japan, Vol. 21, pp. 582-588, 1988.

[78] H. Liu, E. J. Lavernia, and R. H. Rangel, Numerical Simulation of Substrate Impact and Freezing of Droplets in Plasma Spray Processes, J. Phys. D : Appl. Phys., Vol. 26, pp. 1900-1908, 1993.

[79] G. Trapaga, E. F. Matthys, J. J. Valencia, and J. Szekely, Fluid Flow, Heat Transfer and Solidification of Molten Metal Droplets Impinging on Substrates: Comparison of Numerical and Experimental Results, Metall. Trans. B, Vol. 23, pp. 700-718, 1992.

[80] M. Bertagnolli, M. Marchese, and G. Jacucci, Modeling of Particles Impacting on a Rigid Substrate under Plasma Spraying Conditions, J. Therm. Spray Tech., Vol. 4, pp. 41-49, 1995.

[81] K. S. Schmaltz and C. H. Amon (ed.), Thermal Issues in Microcasting Shape Deposition Manufacturing, The Minerals, Metals and Materials Society, Warrendale Pennsylvania, 1996.

[82] E. B. Dussan and S. H. Davis, On the Motion of a Fluid-Fluid Interface along a Solid Surface, J. Fluid Mech., Vol. 65, pp. 71-95, 1974.

[83] E. B. Dussan, On the Spreading of Liquids on Solid Surfaces: Static and Dynamic Contact Lines, Ann. Rev. Fluid Mech., Vol. 11, pp. 371-400, 1979.

[84] E. B. Dussan, E. Rame, and S. Garoff, On Identifying the Appropriate Boundary Condirtion at a Moving Contact Line, J. Fluid Mech., Vol. 230, pp. 97-116, 1991.

[85] A. W. Adamson, Physical Chemistry of Surfaces, 5 ed., John Wiley & Sons Inc., New York, 1990.

[86] J. C. Berg (ed.), Wettability, 1 ed.,Dekker, New York, 1993.

[87] S. E. Rogers, D. Kwak, and U. Kaul, On the Accuracy of the Pseudocompressibility Method in Solving the Incompressible Navier-Stokes Equations, Appl. Math. Modelling, Vol. 11, pp. 35-44, 1987.

[88] J. L. C. Chang and D. Kwak, On the Method of Pseudocompressibility for Numerically Solving Incompressible Flows, AIAA Pap. 84-0252, Reno, NV, 1984.

[89] M. Rein, The Transitional Regime between Coalescing and Splashing Drops, in S. Morioka and L. v. Wijngaarden (ed.), IUTAM Symp. On Waves in Liquid/Gas and Liquid/Vapor Two Phase Systems, pp. 171-190,, Kluwer, 1996.

[90] M. B. Lesser, Thirty Years of Liquid Impact Research : A Tutorial Review, Wear, Vol. 186-187, pp. 28-34, 1995.

[91] J. Koplik and J. R. Banavar, Continuum Deductions from Molecular Hydrodynamics, Ann. Rev. Fluid Mech., Vol. 27, pp. 257-292, 1995.

[92] H. P. Geering, Regelungstechnik, 5 ed., Springer Verlag, Berlin, 2001.

[93] J. V. Naidich, Wettability of Solids by Liquid Metals, Progress in Surface and Membrane Science, Vol. 14, pp. 353-484, 1981.

[94] J. Campbell and H. Conrad, Wetting Kinetics of Molten 60Sn40Pb on a Ag-0.33 wt.% Pt Thick Film Conductor, Journal of Electronic Packaging, Vol. 117, pp. 241-245, 1995.

[95] D. Attinger, An Investigation of Molten Microdroplet Surface Deposition: Transient Behaviour, Wetting Angle Dynamics and Substrate Melting Phenomenon, Thesis, ETH Zürich, Zürich, 2001.

[96] A. M. Cazabat, N. Fraysse, and F. Heslot, Molecular Wetting Films, Progr. Coll. Polym. Sci., Vol. 83, pp. 52-55, 1990.

[97] A. M. Cazabat, N. Fraysse, and F. Heslot, Thin Wetting Films, Colloids and Surfaces, 52, 1991.

[98] N. Fraysse, M. P. Valignat, A. M. Cazabat, F. Heslot, and P. Levinson, The Spreading of Layered Microdroplets, J. Coll. Inter. Sci., Vol. 158, pp. 27-32, 1993.

[99] W. D. Bascom, R. L. Cottington, and C. R. Singleterry, Dynamic Surface Phenomena in the Spontaneous Spreading of Oils on Solids, in R. F. Gould (ed.), Contact Angle, Wettability and Adhesion, American Chemical Society, 1964.

[100] F. Heslot, A. M. Cazabat, N. Fraysse, and P. Levinson, Experiments on Spreading Droplets and Thin Films, Adv. Coll. Inter. Sci., Vol. 39, pp. 129-145, 1992.

[101] S. Villette, M. P. Valignant, and A. M. Cazabat, Layered Spreading Microdroplets, J. Mol. Liq., Vol. 71, pp. 129-135, 1997.

[102] M. Voué, J. D. Coninck, S. Villette, M. P. Valignat, and A. M. Cazabat, Investigation of Layered Microdroplets using Ellipsometric Techniques, Thin Solid Films, Vol. 313-314, pp. 819-824, 1998.

[103] S. Herminghaus, A. Fery, and D. Reim, Imaging of Droplets of Aqueous Solutions by Tapping-Mode Scanning Force Microscopy, Ultramicroscopy, Vol. 69, pp. 211-217, 1997.

[104] J. Hu, R. W. Carpick, M. Salmeron, and X. Xiao, Imaging and Manipulation of Nanometer-Size Liquid Droplets by Scanning Polarization Force Microscopy, J. Vac. Sci. Technol. B, Vol. 14, pp. 1341-1343, 1995.

[105] S. S. Sheiko, G. Eckert, G. Ignat'eva, A. M. Muzafarov, J. Spickermann, H. J. Räder, and M. Möller, Solid-like States of a Dendrimer Liquid displayed by Scanning Force Microscopy, Macromol. Rapid Commun., Vol. 17, pp. 283-297, 1996.

[106] S. S. Sheiko, A. M. Muzafarov, R. G. Winkler, E. V. Getmanova, G. Eckert, and P. Reineker, Contact Angle Microscopy on a Carbosilane Dendrimer with Hydroxyl End Groups: Method for Mesoscopic Characterization of the Surface Structure, Langmuir, Vol. 13, pp. 4172-4181, 1997.

[107] S. S. Sheiko, A. I. Buzin, A. M. Muzafarov, E. A. Rebrov, and E. V. Getmanova, Spreading of Carbosilane Dendrimers at the Air/Water Interface, Langmuir, Vol. 14, pp. 7468-7474, 1998.

[108] T. Pompe, A. Fery, and S. Herminghaus, Imaging Liquid Structures on Inhomogenous Surfaces by Scanning Force Microscopy, Langmuir, Vol. 14, pp. 2585-2588, 1998.

[109] W. N. Unertl, Wetting and Spreading of Styrene-Butadiene Latexes on Calcite, Langmuir, Vol. 14, pp. 2201-2207, 1998.

[110] J. Tamayo and R. Garcia, Deformation, Contact Time, and Phase Contrast in Tapping Mode Scanning Force Microscopy, Langmuir, Vol. 12, pp. 4430-4435, 1996.

[111] P. C. Wayner, Spreading of a Liquid Film with a Finite Contact Angle by the Evaporation/Condensation Process, Langmuir, Vol. 9, pp. 294-299, 1993.

[112] R. Bevacqua, Computation of the Temperature Distribution of a Microheater, student work, 1998.

[113] H. Knapp, R. Guckenberger, and A. Stemmer, AFM Imaging of Biological Samples Using Hydrophobic Tips, Probe Microscopy, Vol. 1, pp. 247-257, 1998.

[114] H. Knapp, A. Tami, M. Brunner, and A. Stemmer, Hydrophobic Surface Coatings on Tools used for Handling of Micro-Particles, Proc. 4th Internat. Conference on Motion and Vibration Control MOVIC'98, Vol. 3, pp. 1151-1156, 1998.

[115] P. A. Stemmer, private communications, Institute of Robotics, ETH Zurich, 1998.

[116] C. D. Bain, E. B. Troughton, Y. T. Tao, J. Evall, G. M. Whitesides, and R. G. Nuzzo, Formation of Monolayer Films by the Spontaneous Assembly of Organic Thiols from Solution onto Gold, J. Am. Chem. Soc., Vol. 111, pp. 321-335, 1989.

[117] S. Haferl, D. Poulikakos, and Z. Zhao, Employing Scanning Force Microscopy to Investigate the Free Surface of Liquid Microstructures and their Wetting Behaviour on Smooth Surfcaes: Gathered Experiences, Experimental Heat Transfer, Vol. 14, pp. 1-25, 2001.

[118] T. C. R. Company, CRC Handbook of Chemistry and Physics, 81 ed., CRC Press, Boca Raton, 2000.

Acknowledgements

The debts on personal and professional level that I have accumulated throughout the years of my PhD thesis are plenty. It is therefore my honest duty to give my sincere thanks to the many people who supported and helped me throughout this thesis.

To Prof. Dr. D. Poulikakos for his confidence in entrusting me with a fascinating research project but also for his scientific, educational, and personal wisdom which has been a constant source of inspiration.
To Prof. Dr. J. Dual for being my co-examiner, for critically reviewing this dissertation, and for providing pertinent comments.
To Dr. J. Giannakouros and Dr. Z. Zhao for the things they have taught me and for their constant support.
To the people at the Laboratory of Thermodynamics in Emerging Technologies for support and fruitful cooperation.
A special thanks to V. Butty and S. Glod for simply being priceless friends and a continuous source of good laughter as well as ideas and support.
To all my friends inside and outside academia for everything friends are here for.
To my family for personal as well as financial support throughout the years.
Special thanks to all of those at Nordiska Roddfoereningen who shared with me blistering but most unforgettable moments on Lake Zurich.
Last but by far most important to my wife, Simone Bolleter-Haferl, my children, Anne-Sophie, and Finn-Niklas, for simply being everything one can possibly desire.

The work reported herein was supported by NSF Grant No. 21-49183.96

Zurich, July 2001 Stephan Eirik Ligaard Haferl

Curriculum Vitae

Personal Data:

Name	Stephan-Eirik Ligaard Haferl
Date of Birth	08.03.1972
Place of Birth	Fribourg, Switzerland
Nationality	Norwegian, Swiss

Education:

11/1997 – 07/2001	Doctoral Candidate Department of Mechanical and Process Engineering ETH Zürich, Switzerland Advisor: Prof. D. Poulikakos
11/1992 – 11/1997	Graduate and Undergraduate Student in Mechanical and Process Engineering ETH Zürich, Switzerland
4/1987 – 9/1991	Comprehensive Secondary School, Urdorf, Switzerland
4/1985 – 3/1987	Secondary School, Affoltern a/A, Switzerland
4/1979 – 3/1985	Primary School, Affoltern a/A, Switzerland

Professional Experience:

10/1999 – 06/2000	Teaching Assistant in Thermodynamics ETH Zürich, Switzerland

02/1997 – 03/1997	Internship at Bacab SA Sainte-Croix, Switzerland
02/1996 – 10/1996	Graduate Assistant at the Institute of Process Engineering ETH Zürich, Switzerland
07/1995 – 10/1995	Internship at ABB Kraftwerke AG Baden, Switzerland
02/1994 – 12/1994	Undergraduate Assistant at the Institute of Forming Technology ETH Zürich, Switzerland
03/1993 – 04/1993	Internship at SIG AG Neuhausen a.R., Switzerland
11/1991 – 01/1992	Internship at Airex AG Sins, Switzerland